Dunne filmen van tweede-orde-niet-lineaire optische materialen verwerkt bij lage temperaturen voor geïntegreerde fotonische schakelingen in siliciumnitride

Low-Temperature Processed Thin Films of Second-Order Nonlinear Optical Materials for Silicon Nitride Photonic Integrated Circuits

Artur Hermans

Promotoren: prof. dr. ir. R. Baets, prof. dr. S. Clemmen
Proefschrift ingediend tot het behalen van de graad van
Doctor in de ingenieurswetenschappen: fotonica

Vakgroep Informatietechnologie
Voorzitter: prof. dr. ir. B. Dhoedt
Faculteit Ingenieurswetenschappen en Architectuur
Academiejaar 2019 - 2020

UNIVERSITEIT
GENT

ISBN 978-94-6355-288-2
NUR 959
Wettelijk depot: D/2019/10.500/96

Universiteit Gent
Faculteit Ingenieurswetenschappen en Architectuur
Vakgroep Informatietechnologie

Promotoren:
prof. dr. ir. Roel Baets
prof. dr. Stéphane Clemmen

Examencommissie:

em. prof. dr. ir. Daniël De Zutter (voorzitter)	Universiteit Gent
prof. dr. ir. Roel Baets (promotor)	Universiteit Gent
prof. dr. Stéphane Clemmen (promotor)	Universiteit Gent Université Libre de Bruxelles
prof. dr. ir. Dries Van Thourhout (secretaris)	Universiteit Gent
prof. dr. ir. Jeroen Beeckman	Universiteit Gent
prof. dr. Christophe Detavernier	Universiteit Gent
prof. dr. ir. Jan Genoe	KU Leuven imec
prof. dr. Goëry Genty	Tampere University
prof. dr. Klaus-Jochen Boller	Universiteit Twente

Dit werk kwam tot stand in het kader van een aspirantenbeurs van het Fonds voor Wetenschappelijk Onderzoek - Vlaanderen.

Dankwoord
Acknowledgments

Hoewel het nastreven van een doctoraatsdiploma een individuele onderneming is, zouden vele zaken niet mogelijk zijn geweest zonder de ondersteuning en het advies van anderen. In de eerste plaats mijn promotor professor Roel Baets, die mij de mogelijkheid gaf om een doctoraat te starten in de Photonics Research Group. Zonder hem zou van deze thesis geen sprake zijn geweest. Ook mijn co-promotor professor Stéphane Clemmen heeft een grote rol gespeeld. Zijn hulp en advies bij het ontwerpen van meetopstellingen en fotonische circuits, het interpreteren van meetresultaten en het schrijven van manuscripten waren van onmiskenbaar belang.

De resultaten van mijn doctoraatsonderzoek zijn ook in grote mate te danken aan de mensen van de CoCooN Research Group aan de Universiteit Gent, in het bijzonder professor Christophe Detavernier, professor Jolien Dendooven, Eduardo Solano en Michiel Van Daele. Hun expertise op het vlak van de afzetting van atomaire lagen en materiaalkarakterisatie heeft een groot deel van mijn doctoraat mee vormgegeven.

I would like to thank the people from the Large Area Electronics Department at imec, Leuven, for guiding me in the wonderful world of organic crystal growth. Cédric Rolin brought our crystal growth capabilities to new heights with his clever tool design and indispensable help in the lab. Robby Janneck shared his expert knowledge and gave me much needed training for many processing tools. Let me also thank Professor Jan Genoe for his advice and for having me in the ERC project meetings.

I want to express my gratitude towards Professor Martti Kauranen and Kalle Koskinen from Tampere University of Technology, for their helpful advice on second-harmonic generation measurements of second-order nonlinear thin films and the reference measurements they conducted for us. I would also like to thank Professor Christian Koos and Clemens Kieninger from the Karlsruhe Institute of Technology for the fruitful collaboration.

Of course the entire staff (and former staff) of the Photonics Research Group (PRG), arguably amongst the best in the world, cannot be forgotten. During my time in this group, I have met many great people. Since this list of people is end-less, let me simply thank all of my fellow PRG members for their support. Thank you for making the Photonics Research Group such an enjoyable and inspiring place to work. I can hardly imagine a better environment to pursue a PhD degree.

Tot slot zou ik graag mijn familie en vrienden bedanken. Hun steun en aanwezigheid zijn ontzettend belangrijk geweest om de dagelijkse beslommeringen die inherent zijn aan een doctoraat te relativeren.

Gent, juni 2019
Artur Hermans

Contents

List of figures

List of tables

List of abbreviations

A

AC	Alternating current
ALD	Atomic layer deposition

B

BBO	β-BaB_2O_4 (barium borate)
BCB	Bisbenzocyclobutene
BOX	Buried oxide
BNA	*N*-benzyl-2-methyl-4-nitroaniline
BTO	Barium titanate

C

CMOS	Complementary metal-oxide-semiconductor
CVD	Chemical vapor deposition

D

DAST	4-N,N-dimethylamino-4’-N’-methyl-stilbazolium tosylate
DC	Direct current
DEZ	Diethylzinc
DIC	Differential interference contrast (microscopy)

E

e-beam	Electron beam
EO	Electro-optic
ESA	Electrical spectrum analyzer

F

FWHM	Full width at half maximum

G

GPC	Growth per cycle
GSG	Ground-signal-ground

H

HDPCVD	High density plasma chemical vapor deposition

K

KIT	Karlsruhe Institute of Technology

L

LNOI	Lithium-niobate-on-insulator
LPCVD	Low pressure chemical vapor deposition

M

MBE	Molecular beam epitaxy
MLD	Molecular layer deposition
MOCVD	Metalorganic chemical vapor deposition
MOVPE	Metalorganic vapor phase epitaxy

O

OPO	Optical parametric oscillator
OVPD	Organic vapor phase deposition

P

PBSC	Polarizing beamsplitter cube
PE-ALD	Plasma-enhanced atomic layer deposition
PET-ALD	Plasma-enhanced thermal atomic layer deposition
PECVD	Plasma-enhanced chemical vapor deposition
PIC	Photonic integrated circuit
POM	Polarized optical microscopy

PVD	Physical vapor deposition
PZT	Lead zirconate titanate

Q

QPM	Quasi-phase matching

R

RF	Radio frequency

S

SAM	Self-assembled monolayer
SEM	Scanning electron microscope
SH	Second-harmonic
SHG	Second-harmonic generation
SiN	Silicon nitride
SOI	Silicon-on-insulator

T

TE	Tranverse electric
TEM	Transmission electron microscopy
TH-ALD	Thermal atomic layer deposition
TM	Transverse magnetic
TMA	Trimethylaluminum

U

UGent	Ghent University (Universiteit Gent)
UV	Ultraviolet

X

XRD	X-ray diffraction
XRR	X-ray reflectivity

Nederlandstalige samenvatting
Dutch summary

Het integreren van enorme hoeveelheden elektronische componenten op kleine silicium chips zorgde voor een revolutie in de elektronica. Dankzij de ontwikkeling van deze geïntegreerde schakelingen (ICs, van de Engelse benaming *integrated circuits*) maken computers, smartphones, tablets en digitale huishoudtoestellen nu een deel uit van ons dagelijkse leven. Ook in de wereld van de optica is deze integratietendens gaande. De voordelen van integratie zijn talrijk. Optische toestellen kunnen kleiner, sneller, robuuster en energie-efficiënter gemaakt worden. Daarnaast laat integratie op een chip toe om complexere optische systemen te implementeren. Deze geïntegreerde optische systemen kunnen functionaliteit bieden die haast onmogelijk te verwezenlijken is in traditionele systemen bestaande uit discrete componenten. Naar analogie met hun elektronische tegenhangers wordt er naar deze geïntegreerde optische systemen verwezen als geïntegreerde fotonische schakelingen (PICs, van de Engelse benaming *photonic integrated circuits*).

De meest gebruikte technologie in de elektronica voor integratie op grote schaal is de complementaire metaal-oxide-halfgeleidertechnologie (CMOS-technologie, van de Engelse benaming *complementary metal-oxide-semiconductor*). Deze draait rond het gebruik van silicium als substraatmateriaal. Hoewel er verschillende materiaalplatformen gebruikt worden om geïntegreerde fotonische schakelingen te maken, is het siliciumfotonicaplatform één van de meest prominente. Door PIC-technologie gebaseerd op silicium te gebruiken kunnen we voordeel halen uit de decennia aan investeringen in de productie-infrastructuur voor micro-elektronica. Het herbruiken van de apparaten en processen van de CMOS-technologie voor fotonica biedt mogelijkheden voor massaproductie met een hoge opbrengst en een lage kost per chip. Bovendien laat het gebruik van silicium toe om elektronica en fotonica op eenzelfde chip te integreren.

In siliciumfotonica wordt niet enkel silicium maar ook siliciumnitride gebruikt als een materiaal om licht te geleiden. Siliciumnitride (SiN) is een standaardmateriaal in CMOS-technologie. Het is transparant in het zichtbare golflengtebereik (in tegenstelling to silicium) en heeft kleine optische verliezen. Dit maakt siliciumnitride een interessant materiaal voor bijvoorbeeld biosensoren, beeldschermtechnologie en kwantumtoepassingen. Daarnaast kan siliciumnitride afgezet worden bij lage temperaturen via plasma-ondersteunde chemische dampdepositie ($<400\,^{\circ}\mathrm{C}$). Materialen die afgezet kunnen worden bij lage temperaturen zijn geschikt voor de integratie van een fotonicalaag aan het einde van een CMOS-productieproces, waardoor monolithische integratie van elektronische en fotonische schakelingen mogelijk wordt. Hoewel siliciumnitride een uitstekend materiaal is om licht te geleiden, is het een eerder schamel materiaal op het vlak van lichtmodulatie, -voortbrenging en -detectie. Vandaar is het interessant om siliciumnitride met andere materialen te combineren.

In deze doctoraatsthesis worden dunne filmen van tweede-orde-niet-lineaire optische materialen die verwerkt zijn bij lage temperaturen en geïntegreerd kunnen worden met siliciumnitride fotonische schakelingen bestudeerd. In niet-lineaire materialen interageren elektromagnetische golven met elkaar en kan er licht bij nieuwe frequenties gegenereerd worden. Hier worden enkel tweede-orde-niet-lineaire effecten beschouwd. Voorbeelden hiervan zijn frequentieverdubbeling, het Pockels-effect en spontane parametrische neerwaartse conversie. Deze effecten worden in vele toestellen gebruikt, bijvoorbeeld in frequentieverdubbelde lasers, optische parametrische oscillatoren en versterkers, bepaalde bronnen van terahertzstraling, kwantumlichtbronnen en hoge-snelheid elektro-optische modulatoren. Helaas bestaat de meerderheid van de beschikbare tweede-orde-niet-lineaire toestellen uit omvangrijke niet-lineaire kristallen en discrete optische componenten, waardoor zij de voordelen van integratie op een chip mislopen. Het onderzoek dat gepresenteerd wordt in deze thesis is gericht op de integratie van tweede-orde-niet-lineaire optische toestellen in siliciumnitride fotonische schakelingen. Aangezien siliciumnitride zelf geen goed tweede-orde-niet-lineair materiaal is, werden andere tweede-orde-niet-lineaire optische materialen die met siliciumnitride PICs geïntegreerd kunnen worden onderzocht. De volgende materialen worden behandeld in deze thesis: ABC-type nanolaminaten, zinkoxide, zinksulfide en *N*-benzyl-2-methyl-4-nitroaniline (BNA).

Conventionele tweede-orde-niet-lineaire optische materialen zijn inorganische kristallen met een niet-centrosymmetrische materiaalstructuur, zoals lithiumniobaat. De niet-centrosymmetrische kristalstructuur is noodzakelijk aangezien de tweed-orde-niet-lineariteit verdwijnt in een centrosymmetrisch materiaal (in de elektrische-dipoolbenadering). Daarom zijn amorfe materialen, zoals het siliciumnitride en siliciumdioxide gebruikt in PICs, geen goede keuze. Ook kristallijn silicium heeft een centrosymmetrische structuur. De groei van inorganische niet-lineaire monokristallen vereist typisch hoge temperaturen en/of het gebruik van een kristallijn sjabloon. Veelgebruikte productiemethodes zijn de Czochralski- en Bridgman-techniek voor kristallen in bulkvorm, en molecuulbundelepitaxie en metaalorganische dampepitaxie voor dunne filmen. Maar epitaxiale groei rechtstreeks op siliciumnitride PICs is niet mogelijk door siliciumnitrides amorfe aard. Bovendien is het gebruik van hoge temperaturen tijdens de productie ongewenst voor de integratie van een fotonicalaag aan het einde van een CMOS-productieproces. In deze thesis tonen we dat tweede-orde-niet-lineaire optische materialen kunnen worden afgezet bij lage temperaturen via atomaire-laagdepositie (ALD) op amorfe substraten. De bestudeerde ALD-materialen zijn ABC-type nanolaminaten, zinkoxide en zinksulfide. Ook de groei van niet-lineaire organische kristallijne dunne filmen bij lage temperaturen op amorfe substraten wordt gedemonstreerd. De kristallijne filmen worden gegroeid via een techniek die sterk gerelateerd is aan de

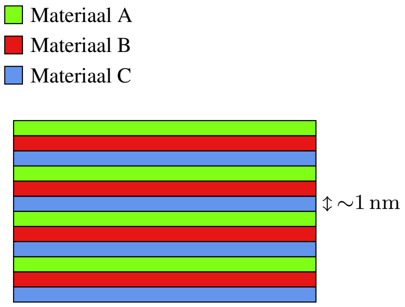

Figuur 1: Schematische voorstelling van een ABC-type nanolaminaat.

Bridgman-methode. Het bestudeerde organisch materiaal is BNA.

Tweede-orde-niet-lineaire materialen afgezet via ALD

ALD is een aantrekkelijke techniek aangezien het een conformeel depositieproces is dat gebeurt bij een lage temperatuur en diktecontrole op het niveau van een monolaag biedt. Daarenboven is ALD al gebruikt in CMOS-technologie.

ABC-type nanolaminaten

Wij hebben ALD gebruikt om ABC-type nanolaminaten met individuele laagdiktes in de grootteorde van $1\,\mathrm{nm}$ af te zetten. Figuur 1 toont een schematische voorstelling van een ABC-type nanolaminaat. Voor de afwisselende, niet-centrosymmetrische stapeling van drie centrosymmetrische materialen A, B en C met laagdiktes op het niveau van een nanometer werd er aangetoond dat dit aanleiding geeft tot een effectieve tweede-order-niet-lineariteit. Voor de materialen A, B en C werden verschillende combinaties van oxides die transparant zijn over het zichtbare en nabij-infrarode golflengtebereik getest. The tweede-orde-niet-lineariteit van de ABC-type nanolaminaten werd geëvalueerd in frequentieverdubbelingsexperimenten. De grootste tweede-orde-niet-lineariteit werd geobserveerd voor een nanolaminaat bestaande uit TiO_2, Al_2O_3 en In_2O_3, met geschatte individuele laagdiktes van $0.9\,\mathrm{nm}$. Transmissie-elektronenmicroscoopbeelden van dit nanolaminaat worden getoond in figuur 2. Een niet-lineaire tensorcomponent $\chi^{(2)}_{zzz} = 1.2\,\mathrm{pm/V}$ bij een fundamentale golflengte van $800\,\mathrm{nm}$ werd gevonden, waarbij z de riching loodrecht op het filmvlak is. Helaas is deze tweede-orde-niet-lineariteit eerder klein en waarschijnlijk onvoldoende voor de verwezenlijking van efficiënte geïntegreerde tweede-order-niet-lineaire optische toestellen.

Om de tweede-orde-niet-lineariteit grootteordes te verbeteren kan het gebruik van zeer niet-lineaire organische moleculen in nanolaminaten een interessante aanpak zijn. Hiervoor kan moleculaire-laagdepositie gebruikt worden, een techniek die zeer sterk gerelateerd is aan atomaire-laagdepositie. Met de recente ontwikkelingen in atomaire- en moleculaire-laagdepositie kan het gebruik van organische

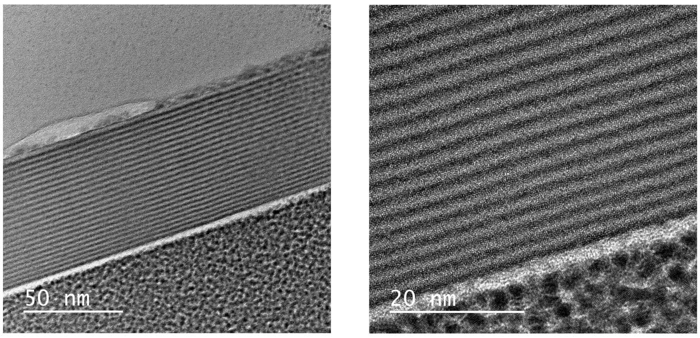

Figuur 2: Transmissie-elektronenmicroscoopbeelden van een $TiO_2/Al_2O_3/In_2O_3$ nanolaminaat met geschatte individuele laagdiktes van $0.9\,\mathrm{nm}$.

en inorganische-organische hybride nanolaminaten voor tweede-orde-niet-lineaire materialen verder verkend worden.

Zinkoxide en zinksulfide

We onderzochten het gebruik van zinkoxide en zinksulfide afgezet door ALD voor geïntegreerde tweede-orde-niet-lineaire toestellen, wat tot nog toe grotendeels onverkend bleef. Niet alleen de resultaten van frequentieverdubbelingsexperimenten worden uit de doeken gedaan, maar ook de resultaten van elektro-optische modulatie-experimenten in siliciumnitride ringresonatoren. Deze geïntegreerde SiN-gebaseerde elektro-optische modulatoren werden verwezenlijkt door SiN golfgeleiders te bedekken met zinkoxide (ZnO) of zinksulfide (ZnS) dunne filmen (zie figuur 3).

Van ZnO en ZnS is het geweten dat ze kristalliseren in niet-centrosymmetrische fasen. Beide materialen zijn transparant in het zichtbare en nabij-infrarode golflengtebereik. Atomaire-laagdepositie van zinkoxide en zinksulfide resulteert bijna altijd in kristallijne filmen. Maar, voor niet-epitaxiale groei zijn deze filmen polykristallijn met typische korrelgroottes die veel kleiner zijn dan de golflengte. Om een grote effectieve tweede-orde-niet-lineariteit te verkrijgen moeten de korrels een zekere voorkeursoriëntatie hebben.

Voor de gepaste verwerkingsparameters hebben onze ALD-ZnO en -ZnS dunne filmen tweede-orde-niet-lineariteiten die een grootteorde groter zijn dan die van de bovengenoemde ABC-type nanolaminaten (verkregen van frequentieverdubbelingsexperimenten). Bovendien zagen we dat het toevoegen van een nanometerschaal kiemlaag gemaakt uit Al_2O_3, afgezet via ALD, leidde tot een significante verbetering in de tweede-orde-niet-lineariteit. Deze vorm van controle over de grootte van de tweede-orde-niet-lineariteit is nuttig voor de quasifaseafstemming van tweede-orde-niet-lineaire processen.

Het voortplantingsverlies in siliciumnitride golfgeleiders met ZnO en ZnS bedekkingen werd geschat door middel van transmissiemetingen in ringresonatoren.

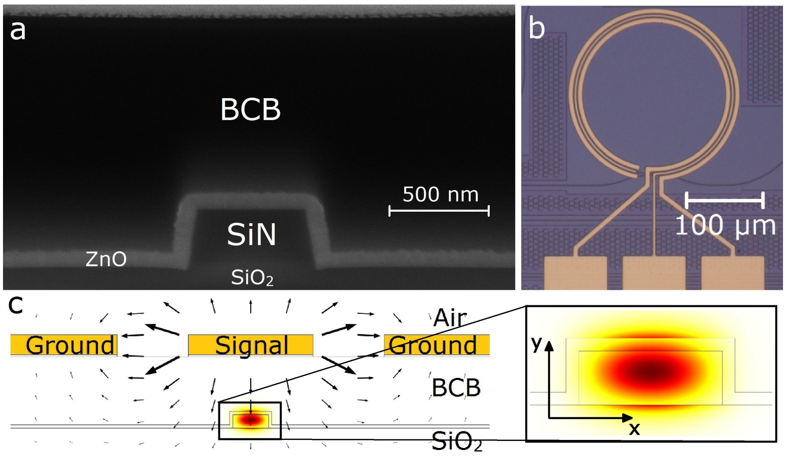

Figuur 3: (a) Rasterelektronenmicroscoopbeeld van een dwarsdoorsnede van een SiN golfgeleider met 6 nm Al_2O_3, 81 nm ZnO en een BCB bekleding. (b) Microscoopbeeld van een afgewerkte modulator. Rechthoekige contactvlakken worden gebruikt voor het landen van een elektrische sonde. (c) Gesimuleerde dwarsdoorsnede van een ZnO-bedekte SiN golfgeleider met elektrodes. De intensiteit van de fundamentele quasi-TM optische mode wordt getoond samen met het elektrische veld opgewekt door de elektrodes (pijlen). 13% van het modale vermogen bevindt zich in de ALD-bedekking.

Verliezen tussen $3\,\mathrm{dB/cm}$ en $12\,\mathrm{dB/cm}$ werden geobserveerd, afhankelijk van het materiaal, het ALD-recept en de golfgeleidermode.

Elektro-optische modulatiemetingen in SiN-gebaseerde ringmodulatoren gaven een $V_\pi L$ product zo klein als $4\,\mathrm{V\,m}$ aan wanneer ZnO bedekkingen werden gebruikten en $20\,\mathrm{V\,m}$ voor ZnS bedekkingen. Voor de SiN/ZnS ringmodulatoren werden modulatiesnelheden groter dan $1\,\mathrm{GHz}$ bereikt, waar we werden gelimiteerd door de caviteitsfotonlevensduur en de weerstand-capaciteit-tijdsconstante. Voor de SiN/ZnO ringen was de bandbreedte beperkt tot $\approx 100\,\mathrm{MHz}$. Vrije ladingsdragers zouden een rol kunnen spelen in het mechanisme van de brekingsindexmodulatie. Om hun rol te onderzoeken en de bandbreedte te vergroten is verder materiaalonderzoek noodzakelijk, zoals gloeibehandelingen en afzettingen bij verschillende temperaturen om de weerstand van de film te wijzigen. Een reductie van het $V_\pi L$ product tot een factor 8 is mogelijk door de ALD-laagdikte te verhogen, de SiN-dikte te verlagen en een optimalere elektrodeconfiguratie te kiezen. Zelfs grotere verbeteringen zijn mogelijk door gebruik te maken van transparante geleidende oxide elektrodes die zeer dicht tegen de golfgeleiderkern geplaatst zijn of door nanoplasmonische SiN-gebaseerde sleufgolfgeleiders te gebruiken.

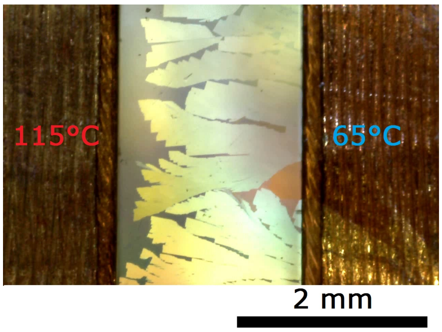

Figuur 4: Beeld van groeiende BNA kristallieten. De kristallieten worden gegroeid door middel van een methode die sterk gerelateerd is aan de Bridgman-techniek: het staal wordt verplaatst van een warm platform ($115\,^{\circ}\mathrm{C}$, linkerkant van de afbeelding) naar een koud platform ($65\,^{\circ}\mathrm{C}$, rechterkant van de afbeelding) aan een snelheid van $0.7\,\mu\mathrm{m\,s^{-1}}$ (het smeltpunt van BNA is $105\,^{\circ}\mathrm{C}$). De opening tussen de twee platformen is $2\,\mathrm{mm}$ breed.

Organische tweede-orde-niet-lineaire kristallijne dunne filmen: BNA

Organische materialen kunnen zeer grote tweede-orde-niet-lineariteiten hebben vergeleken met conventionele inorganische niet-lineaire kristallen. Daarenboven kunnen vele organische materialen bewerkt worden bij lage temperaturen gebruik makende van goedkope oplossingsgebaseerde technieken. Dat terwijl de groei van inorganische tweede-orde-niet-lineaire materialen typisch hoge temperaturen vereist en/of het gebruik van vacuümapparatuur. Maar hoewel grote tweede-orde-niet-lineariteiten werden gerapporteerd voor organische monokristallen in bulkvorm, is de groei van organische niet-lineaire kristallijne dunne filmen van een voldoende hoge optische kwaliteit verre van triviaal.

Wij zijn erin geslaagd om sterk niet-lineaire dunne filmen van het organische materiaal BNA te groeien met een controleerbare kristaloriëntatie en millimetergrote kristallieten. Het productieproces begint met een druppelgegoten BNA film die geherkristalliseerd wordt gebruik makende van een techniek gerelateerd aan de Bridgman-methode (zie figuur 4). De kristallijne filmen worden gegroeid op amorfe substraten met verwerkingstemperaturen die de $115\,^{\circ}\mathrm{C}$ niet overstijgen. Een zeer grote niet-lineariteit van $\chi^{(2)}_{ZZZ} = (153 \pm 70)\,\mathrm{pm/V}$ werd gevonden uit frequentieverdubbelingsexperimenten bij een fundamentele golflengte van $1550\,\mathrm{nm}$. Figuur 5 toont een microscoopbeeld van een afgewerkte kristallijne film.

Om de niet-uniformiteit verbonden aan de druppelgiettechniek te vermijden, kan het nuttig zijn om alternatieve afzettingstechnieken te verkennen, zoals spincoating, sproeibekleding, ultrasonisch-substraat-vibratie-geassisteerd druppelgieten, organische dampdepositie en thermische opdamping. Om de spleten tussen de kristallieten op te vullen kan er een extra laag BNA opgedampt worden. Onder de juiste condities kunnen de onderliggende BNA kristallen als sjablonen voor epi-

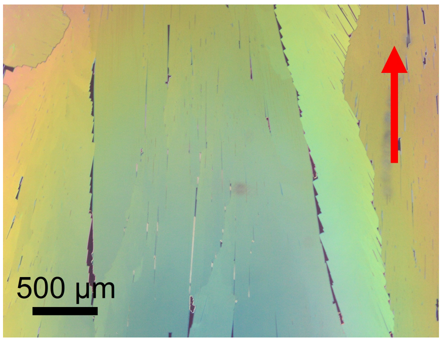

Figuur 5: Microscoopbeeld (differentieel-interferentie-contrast-methode) van een BNA kristallijne film gegroeid op een geoxideerd silicium substraat (met een oxidedikte van 3 µm) volgens de techniek geïllustreerd in figuur 4. De richting waarlangs het staal werd getrokken is aangeduid met een rode pijl.

taxiale groei dienen. Ook mechanisch polijsten kan een interessante aanpak zijn om effen, uniforme filmen te verkrijgen.

De groei van sterk niet-lineaire monokristallijne dunne filmen over grote oppervlaktes opent talrijke mogelijkheden voor de verwezenlijking van geïntegreerde tweede-orde-niet-lineaire optische toestellen.

English summary

The world of electronics has been revolutionized by integrating huge amounts of electronic components on small silicon chips. Thanks to the development of these integrated circuits (ICs), computers, smartphones, tablets, and digital home appliances have become a part of our daily lives. Also in the field of optics, this integration trend is ongoing. The advantages of integration are plentiful. Optical devices can be made smaller, faster, more robust, and energy-efficient. Moreover, on-chip integration allows for the implementation of more complex optical systems which can unlock functionality beyond what is possible in traditional free-space systems. In analogy with their electronic counterparts, these integrated optical systems are called photonic integrated circuits (PICs).

The most used technology for very-large-scale integration in electronics is the complementary metal-oxide-semiconductor (CMOS) technology. It revolves around the use of silicon as a substrate material. While several material platforms are being used to fabricate photonic integrated circuits, the silicon photonics platform is one of the most prominent. By using silicon PIC technology, we can benefit from the decades of investments in the manufacturing infrastructure for microelectronics. Recycling the tools and processes of CMOS technology for photonics, offers a route to high-yield mass manufacturing at a low cost per chip. Moreover, using silicon permits the co-integration of electronics and photonics on a single chip.

In silicon photonics, not only silicon, but also silicon nitride is used as a light guiding material. Silicon nitride (SiN) is a standard material in CMOS technology. It is transparent in the visible wavelength range (as opposed to silicon) and has small optical losses. This makes silicon nitride an interesting material for, e.g., biosensing, display technology, and quantum applications. In addition, silicon nitride can be deposited at low temperatures by plasma-enhanced chemical vapor deposition (<400 °C). Low-temperature deposited materials are suitable for the integration of a photonics layer in the back end of line of a CMOS process, thereby enabling monolithic integration of electronic and photonic circuits. While processing a back-end deposited photonics layer, the temperature needs to be kept low to avoid degradation of the underlying electronics. Although silicon nitride is an excellent light guiding material, it is a rather poor material when it comes to light modulation, generation, and detection. Therefore, it is interesting to combine silicon nitride with other materials.

In this doctoral thesis, low-temperature processed second-order nonlinear optical materials that can be integrated with silicon nitride photonic circuits are stud-

ied. In nonlinear materials, electromagnetic waves interact with one another and light at new frequencies can be generated. Here, only second-order nonlinear optical effects are considered. Examples include second-harmonic generation, the Pockels effect, and spontaneous parametric down-conversion. These effects are used in a variety of devices such as frequency-doubled lasers, optical parametric oscillators and amplifiers, some terahertz radiation sources, quantum light sources, and high-speed electro-optic modulators. Unfortunately, the majority of the available second-order nonlinear devices relies on bulk nonlinear crystals and free-space optical components, therefore missing out on the benefits of on-chip integration. The research presented in this thesis is geared towards the integration of second-order nonlinear optical devices in silicon nitride photonic circuits. As silicon nitride itself is not a very good second-order nonlinear material, other second-order nonlinear optical materials which can be integrated with silicon nitride PICs were investigated. The following materials are treated in this thesis: ABC-type nanolaminates, zinc oxide, zinc sulfide, and *N*-benzyl-2-methyl-4-nitroaniline (BNA).

Conventional second-order nonlinear optical materials are inorganic crystals with a non-centrosymmetric material structure, such as lithium niobate. The non-centrosymmetric crystal structure is necessary for the material to have a non-vanishing second-order nonlinearity (in the electric-dipole approximation). Therefore, amorphous materials, like silicon nitride and silicon dioxide used in PICs, are not a good option. Also crystalline silicon has a centrosymmetric structure. The growth of inorganic nonlinear single crystals typically requires high temperatures and/or the use of a crystalline template. Common fabrication methods are the Czochralski and Bridgman technique for bulk crystals, and molecular beam epitaxy and metalorganic vapor phase epitaxy for thin films. However, epitaxial growth directly on silicon nitride PICs is not an option due to silicon nitride's amorphous nature. Also the involvement of high-temperature processing steps is undesirable for back-end deposited silicon photonics. In this thesis, we show that second-order nonlinear optical materials can be deposited at low temperatures by atomic layer deposition (ALD) on amorphous substrates. The studied atomic layer deposited materials are ABC-type nanolaminates, zinc oxide, and zinc sulfide. Also, the low-temperature growth of highly nonlinear organic crystalline thin films on amorphous substrates is demonstrated. The crystalline films are grown utilizing a Bridgman-type technique. The studied organic material is BNA.

Atomic layer deposited second-order nonlinear materials

ALD is an attractive technique as it is a low-temperature, conformal deposition process that provides thickness control at the monolayer level. Additionally, ALD has been reported to be used in CMOS technology (to deposit the gate dielectric).

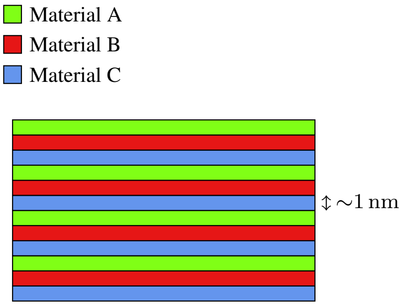

Figure 1: Schematic representation of an ABC-type nanolaminate.

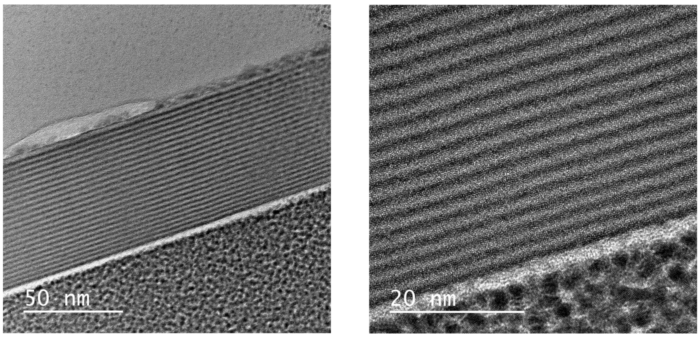

Figure 2: Transmission electron microscopy images of a $TiO_2/Al_2O_3/In_2O_3$ nanolaminate with estimated individual layer thicknesses of $0.9\,\mathrm{nm}$.

ABC-type nanolaminates

We have used ALD to deposit ABC-type nanolaminates with individual layer thicknesses on the order of $1\,\mathrm{nm}$. Figure 1 shows a schematic illustration of an ABC-type nanolaminate. The alternate, non-centrosymmetric stacking of three centrosymmetric materials A, B, and C with nanometer-scale layer thicknesses, was demonstrated to lead to an effective second-order bulk nonlinearity. For the materials A, B, and C, several combinations of oxides that are transparent over the visible and near-infrared wavelength range have been tested. The second-order nonlinearity of the ABC-type nanolaminate thin films was assessed in second-harmonic generation experiments. The largest second-order nonlinearity was observed for a nanolaminate consisting of TiO_2, Al_2O_3, and In_2O_3, with estimated individual layer thicknesses of $0.9\,\mathrm{nm}$. Transmission electron microscopy images of this nanolaminate are shown in figure 2. A nonlinear tensor component $\chi^{(2)}_{zzz} = 1.2\,\mathrm{pm/V}$ at a fundamental wavelength of $800\,\mathrm{nm}$ was obtained, with z the film normal. Unfortunately, the observed second-order nonlinearity is still rather small and likely insufficient for the realization of efficient integrated second-order nonlinear optical devices.

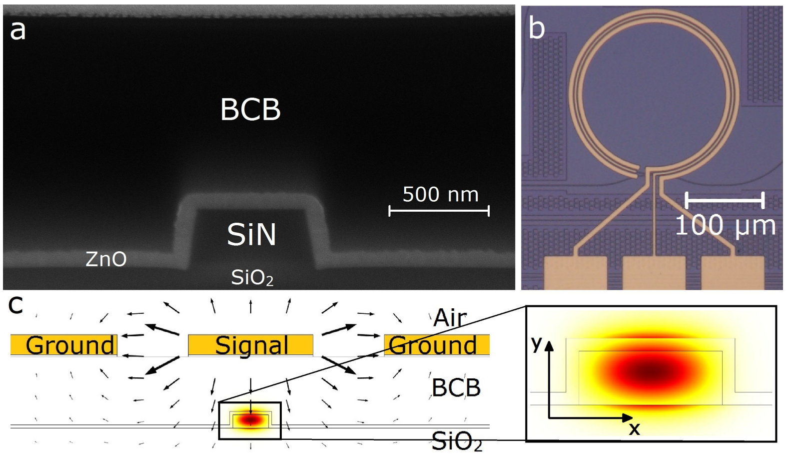

Figure 3: (a) Scanning electron microscopy image of the cross-section of a SiN waveguide with 6 nm Al_2O_3, 81 nm ZnO and a BCB cladding. (b) Microscope image of a fabricated modulator. Rectangular contact pads are used for landing an electrical probe (c) Simulated cross-section of a ZnO covered SiN waveguide with electrodes. The intensity of the fundamental quasi-TM optical mode is shown along with the electric field induced by the electrodes (arrows). 13% of the mode power resides in the ALD overlay.

To get order of magnitude improvements in second-order nonlinearity, the use of highly nonlinear organic molecules in nanolaminates could be an interesting approach. While atomic layer deposition is used for the deposition of inorganic thin films, a related technique known as molecular layer deposition is used for the deposition of organic thin films. With the development of atomic and molecular layer deposition, the use of organic or inorganic-organic nanolaminates for second-order nonlinear optical materials can be explored further.

Zinc oxide and zinc sulfide

We investigated the use of atomic layer deposited zinc oxide and zinc sulfide for integrated second-order nonlinear devices, an area which had remained largely unexplored thus far. Not only the results of second-harmonic generation experiments in thin films are discussed, but also the results of electro-optic modulation experiments in SiN ring resonators. These integrated SiN based electro-optic ring modulators were realized by overlaying SiN waveguides with zinc oxide (ZnO) or zinc sulfide (ZnS) thin films (see figure 3).

Zinc oxide and zinc sulfide are known to crystallize in non-centrosymmetric phases. Both materials are transparent in the visible and near-infrared wavelength range. ALD of zinc oxide and zinc sulfide almost always results in crystalline films. However, for non-epitaxial growth these films are polycrystalline with typical grain sizes much smaller than the wavelength. To get a large effective second-order nonlinearity, the grains need to have a certain preferential orientation.

For the appropriate processing parameters, our ALD zinc oxide and zinc sulfide thin films have second-order nonlinearities which are an order of magnitude larger than those of the aforementioned ABC-type nanolaminates (obtained from second-harmonic generation measurements). Moreover, it was observed that the addition of a nanometer-scale seed layer of Al_2O_3 deposited by ALD, lead to a significant improvement in the second-order nonlinearity. This form of control over the magnitude of the second-order nonlinearity is useful for the quasi-phase matching of second-order nonlinear processes.

The propagation loss in SiN waveguides with ZnO and ZnS overlays was estimated from ring resonator transmission measurements. Losses between $3\,\mathrm{dB/cm}$ and $12\,\mathrm{dB/cm}$ were observed, depending on the material, the ALD recipe, and the waveguide mode.

Electro-optic modulation measurements in SiN based ring modulators indicated $V_\pi L$ products down to $4\,\mathrm{V\,m}$ when using ZnO overlays and $20\,\mathrm{V\,m}$ for ZnS overlays. For the SiN/ZnS ring modulators, modulation speeds over $1\,\mathrm{GHz}$ were reached, where we were limited by the cavity photon lifetime and the resistance-capacitance time constant. For the SiN/ZnO rings, the bandwidth was limited to $\approx 100\,\mathrm{MHz}$. Free charge carriers could play a role in the refractive index modulation mechanism. To investigate their role and extend the bandwidth, a more in-depth material exploration is required, possibly including annealing treatments and depositions at different temperatures to alter the film's resistivity. Up to a factor 8 reduction in $V_\pi L$ is possible by simply increasing the ALD layer thickness, reducing the SiN thickness, and choosing a more optimal electrode configuration. Even larger improvements are possible when using transparent conducting oxide electrodes placed very close to the waveguide core, or by using nanoplasmonic SiN based slot waveguides.

Organic second-order nonlinear crystalline thin films: BNA

Organic materials can have very large second-order nonlinearities compared to conventional inorganic nonlinear crystals. Moreover, many organic materials can be processed at low temperatures using inexpensive solution based techniques. Whereas the growth of inorganic second-order nonlinear materials typically requires high temperatures and/or the use of vacuum equipment. But, while large second-order nonlinearities have been reported for organic bulk single crystals, the growth of organic nonlinear crystalline thin films of sufficient optical quality is far from trivial.

We have managed to grow highly nonlinear thin films of the organic material BNA with a controllable crystal orientation and millimeter-sized crystallites. The fabrication process starts from a drop casted BNA film which is recrystallized utilizing a Bridgman-type method (see figure 4). The crystalline films are grown on amorphous substrates with processing temperatures not exceeding $115\,^\circ\mathrm{C}$. A very large nonlinearity of $\chi^{(2)}_{ZZZ} = (153 \pm 70)\,\mathrm{pm/V}$ has been extracted from second-harmonic generation measurements at a fundamental wavelength of $1550\,\mathrm{nm}$. Figure 5 shows a microscopy image of a fabricated crystalline film.

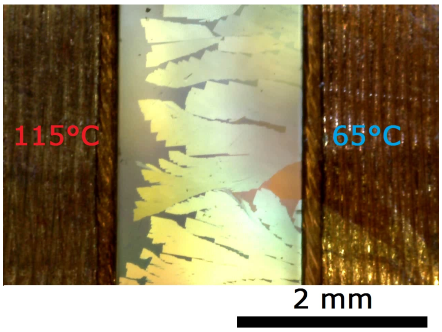

Figure 4: Image of growing BNA crystallites. The crystallites are grown using a Bridgman-type method: the sample is moved from a hot stage ($115\,^{\circ}\mathrm{C}$, left side of image) to a cold stage ($65\,^{\circ}\mathrm{C}$, left side of image) at a speed of $0.7\,\mathrm{\mu m\,s^{-1}}$ (melting point of BNA is $105\,^{\circ}\mathrm{C}$). The gap between the stages is $2\,\mathrm{mm}$.

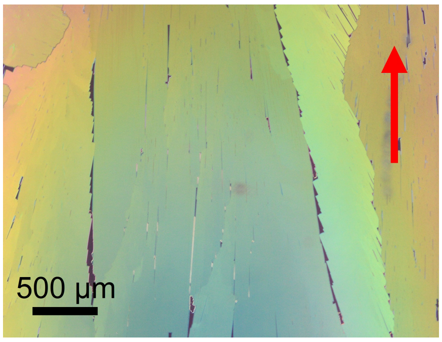

Figure 5: Microscopy image (differential interference contrast mode) of a BNA crystalline film grown on an oxidized silicon substrate (oxide thickness of $3\,\mathrm{\mu m}$) utilizing the method illustrated in figure 4. The direction along which the sample was pulled is indicated by a red arrow.

To avoid the non-uniformity associated with the drop casting technique, the exploration of alternative deposition techniques such as spin coating, spray coating, ultrasonic substrate vibration-assisted drop casting, organic vapor phase deposition (OVPD), and thermal evaporation can prove useful. To fill in the gaps between the crystallites, an extra layer of BNA can be evaporated on top. Under the right conditions, the underlying BNA crystals can act as templates for epitaxial growth. The use of mechanical polishing is also an interesting approach to get smooth, uniform films.

The growth of highly nonlinear single crystal thin films over large areas opens up numerous possibilities for the realization of integrated second-order nonlinear optical devices.

1

Introduction

Contents

1.1 Second-order nonlinear optical effects

The field of optics describes the behavior of light and its interaction with matter. In most materials, at relatively low light intensities, light waves do not seem to interact with one another. Apart from the familiar effects of refraction and diffraction, nothing unusual is observed. However, for some materials and/or sufficiently intense illumination, notable interaction between light beams occurs. Energy can be transferred between light waves through interaction with the material and light at new frequencies can be generated. These effects are studied by the field of nonlinear optics.

Matter consists of negatively charged electrons and positively charged atomic nuclei. Under influence of an electric field, the positive and negative charges will tend to move in opposite directions. In conductors, where free charges are present, this will lead to a flow of charges. Or in other words, an electric current will arise. In dielectric materials, very little free charges are present and the charged particles can be considered as being bound together. An electric field will pull the negative and positive charges apart by some degree and induce an electric dipole moment. Since light waves are oscillating electric and magnetic fields, oscillating dipoles will be created in dielectric media in response to an incident light wave. Also the magnetic field can have an influence on the charged particles. But as this effect is typically much smaller, we will not consider it here. The aforementioned oscillating dipoles will themselves be a source of radiation that interferes with the incident radiation. The whole interplay between electromagnetic radiation and the movement of charged microscopic particles will govern how light propagates through matter and can be translated into macroscopic quantities such as a material's refractive index.

Polarization

To describe light-matter interaction at the macroscopic level, we introduce the electric dipole moment per unit volume or polarization P of a material. The polarization P depends on the electric field E or $P = f(E)$. Yet, this dependency is complex and it is unclear what the function f will look like exactly. Therefore, we write P as a Taylor series at $E = 0$

$$\begin{aligned} P &= P^{(0)} + P^{(1)} + P^{(2)} + P^{(3)} + \cdots \\ &= P^{(0)} + \epsilon_0\chi^{(1)}E + \epsilon_0\chi^{(2)}E^2 + \epsilon_0\chi^{(3)}E^3 + \cdots \end{aligned} \tag{1.1}$$

where ϵ_0 is the vacuum permittivity and $P^{(0)}$ the static or spontaneous polarization. Materials possessing a spontaneous polarization are called polar materials. If the spontaneous polarization can be reversed by the application of a sufficiently strong electric field, we call the material ferroelectric. Ferroelectric materials can be particularly interesting in the context of electro-optic modulation and phase matching for nonlinear wave mixing experiments (see section 2.7 and subsection 4.3.4). The quantity $\chi^{(1)}$ is the linear (electric) susceptibility or first-order susceptibility, $\chi^{(2)}$ is the second-order susceptibility, etc. In nonmagnetic, dielectric media, the linear susceptibility relates to the refractive index as $n = \sqrt{1 + \chi^{(1)}}$. For simplicity, we assumed P and E to be scalar quantities. If we take into account the vector nature of the fields, $\chi^{(1)}$ becomes a second-rank tensor, $\chi^{(2)}$ a third-rank tensor, etc. We also assumed the response of the medium to the electric field to be local and instantaneous, meaning that the polarization at a certain point and time is determined by the electric field at that point and time. In section 2.1, a more rigorous approach will be presented.

In conventional, linear optics, only the first-order term of the polarization is retained and the higher-order terms are neglected. While this description suffices to explain phenomena such as refraction and diffraction, it does not explain how energy can be transferred between light waves at different frequencies. To account for these phenomena, the higher-order terms need to be included. In this doctoral thesis, we will study the effects that arise due to the second-order term $P^{(2)} = \epsilon_0\chi^{(2)}E^2$, so-called second-order nonlinear optical effects.

As a consequence of Neumann's principle (see section 2.2), $\chi^{(2)} = 0$ for materials displaying inversion symmetry (also known as centrosymmetric materials). In fact, all even-order terms in the Taylor series expansion vanish for such materials. Many materials display inversion symmetry: gases, liquids, amorphous solids, and even many crystalline solids. This will have important consequences for the material choices in this thesis.

Second-order nonlinear effects

Now, let us have a look at the effects arising due the second-order nonlinear polarization. Consider a light wave represented by an electric field $E = E_0\cos(\omega t)$ incident on a material with a nonzero second-order susceptibility $\chi^{(2)}$. The second-order nonlinear polarization generated in the material is given by

$$\begin{aligned} P^{(2)} &= \epsilon_0\chi^{(2)}E_0^2\cos^2(\omega t) \\ &= \epsilon_0\chi^{(2)}\left[\frac{E_0^2}{2} + \frac{E_0^2}{2}\cos(2\omega t)\right] \end{aligned} \tag{1.2}$$

The nonlinear polarization contains a DC term (i.e. zero frequency) and term at (angular) frequency 2ω. The DC term leads to the creation of a static electric field in the material, a process known as optical rectification. The second term will lead to the generation of electromagnetic radiation at frequency 2ω. This process is called second-harmonic generation (SHG) and is illustrated in figure 1.1. Part (b) of the figure visualizes the process in an energy level diagram, where the dashed lines represent virtual energy levels. It shows how two photons with frequency ω are annihilated while one photon at frequency 2ω is created simultaneously. If one of these virtual levels is close to a real energy level, we get what is called resonance enhancement. As one or more of the optical frequencies involved in the interaction come close to a resonant frequency of the oscillating dipoles, the coupling between the radiation and the material gets particularly strong and the susceptibility values become very large. However, this also comes at the cost of increased absorption. If we get very close to a material resonance, the approach of writing P as a power series of E becomes unpractical. Many terms in the expansion need to be taken into account to accurately describe the light-matter interaction. The same holds true for very intense fields. For these cases, alternative formalisms are used which will not be described here. The interested reader can consult reference works on nonlinear optics [1, 2].

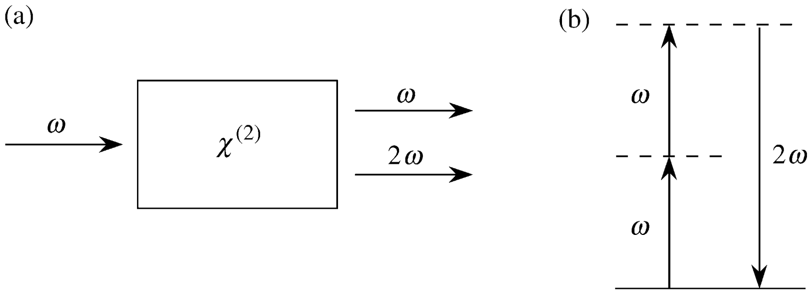

Figure 1.1: (a) Schematic representation of second-harmonic generation (SHG). (b) Energy level diagram describing second-harmonic generation. Figure reproduced from [1].

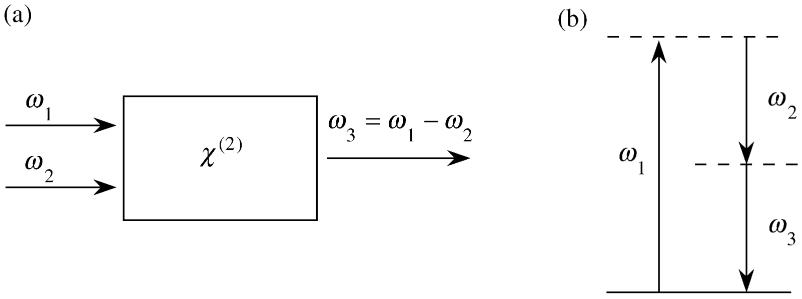

Figure 1.2: (a) Schematic representation of difference-frequency generation. (b) Energy level diagram describing difference-frequency generation. Figure reproduced from [1].

Next, we consider light at two frequencies ω_1 and ω_2 incident upon a second-order nonlinear medium: $E = E_1 \cos(\omega_1 t) + E_2 \cos(\omega_2 t)$. In this case, the second-order nonlinear polarization becomes

$$\begin{aligned} P^{(2)} = \epsilon_0 \chi^{(2)} &\left[\frac{E_1^2 + E_2^2}{2} + \frac{E_1^2}{2} \cos(2\omega_1 t) + \frac{E_2^2}{2} \cos(2\omega_2 t) \right] \\ &+ \epsilon_0 \chi^{(2)} \left[E_1 E_2 \cos((\omega_1 - \omega_2)t) + E_1 E_2 \cos((\omega_1 + \omega_2)t) \right] \end{aligned} \tag{1.3}$$

On the first line we see again the DC and double frequencies terms, but on the second line two new terms are showing up. One term is responsible for generating radiation at frequency $\omega_1 + \omega_2$ and the other at frequency $\omega_1 - \omega_2$ (assuming $\omega_1 > \omega_2$). These processes are called sum-frequency and difference-frequency generation, respectively. The process of difference-frequency generation is illustrated in figure 1.2. When the intensity of the field at frequency ω_1 is large compared to the field at frequency ω_2, difference-frequency generation is often referred to as optical parametric amplification. The annihilation of a photon with frequency

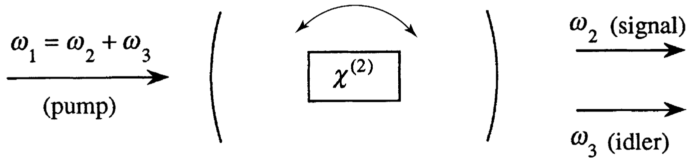

Figure 1.3: Schematic representation of an optical parametric oscillator (OPO). The cavity mirrors have high reflectivities at frequencies ω_2 and/or ω_3. The output frequencies are typically tuned by changing the orientation of the nonlinear material and thus altering the phase matching condition. Figure reproduced from [1].

ω_1 excites the material to the highest virtual energy level. The presence of the field at frequency ω_2 stimulates the material to emit a photon with frequency ω_2 and $\omega_3 = \omega_1 - \omega_2$. This results in an amplification of the field at frequency ω_2, hence the name optical parametric amplification. Since the light wave at frequency ω_1 is very intense, its amplitude is barely altered by the interaction and it will continue to act as a pump for the parametric amplification process. In the absence of a field at frequency ω_2, photons at frequency ω_2 and ω_3 can be emitted spontaneously. In this case, the process is called parametric fluorescence or spontaneous parametric down-conversion. If the nonlinear material is placed inside an optical resonator (see figure 1.3), the stimulated emission/amplification process outlined above can lead to the buildup of strong fields at frequency ω_2 and ω_3 as the light waves oscillate back and forth inside the resonator. This device is called an optical parametric oscillator (OPO). By altering the phase matching condition (see section 3.1) the frequencies at which the OPO emits can be tuned.

Finally, let us consider the case where a static electric field is applied to second-order nonlinear material upon which a light wave is incident: $E = E_0 \cos(\omega t) + E_{DC}$. The second-order polarization is given by

$$P^{(2)} = \epsilon_0 \chi^{(2)} \left[E_0^2 \cos^2(\omega t) + E_{DC}^2 + 2 E_{DC} E_0 \cos(\omega t) \right] \tag{1.4}$$

It contains a term oscillating at the same frequency as the incident optical field. Since the first-order polarization also contains a term oscillating at this frequency, the total polarization oscillating at frequency ω is given by

$$\epsilon_0 \left(\chi^{(1)} + 2\chi^{(2)} E_{DC} \right) E_0 \cos(\omega t) \tag{1.5}$$

This will be perceived as a refractive index n that depends linearly on the applied electric field E_{DC}

$$\begin{aligned} n &= \sqrt{1+\chi^{(1)}+2\chi^{(2)}E_{DC}} \\ &= n_0\sqrt{1+\frac{2\chi^{(2)}E_{DC}}{n_0^2}} \\ &\approx n_0 + \frac{\chi^{(2)}}{n_0}E_{DC} \end{aligned} \tag{1.6}$$

with $n_0 = \sqrt{1+\chi^{(1)}}$, the refractive index for $E_{DC} = 0$. This effect is called the Pockels effect or linear electro-optic effect and it can be used to construct optical modulators.

Applications

Second-order nonlinear optical effects are not merely scientific curiosities. They are used in a whole range of applications, spanning from research oriented tools to widespread commercially available devices. First of all, there are the $\chi^{(2)}$ based light sources, like frequency-doubled lasers, optical parametric oscillators, some terahertz radiation sources (though THz radiation is usually not considered to be light), quantum light sources and frequency comb sources.

Frequency-doubled lasers use second-harmonic generation in nonlinear crystals to access new wavelength ranges [3, 4]. Most green laser pointers rely on the frequency doubling of infrared laser light to generate a green laser beam (see figure 1.4).

Optical parametric oscillators can produce tunable coherent radiation over a very wide wavelength range, making them indispensable tools for spectroscopy. Practically all main laser manufacturers have OPOs on offer. An example is shown in figure 1.5. OPOs usually contain sensitive free-space optical components, are very expensive and bulky. Their use is limited mainly to research environments.

Also THz sources based on difference-frequency generation from infrared laser light are commercially available [5].

In optical quantum computing and communication applications, parametric down-conversion is often used to generate non-classical photon states [6–8].

Even optical frequency comb formation can occur via second-order nonlinear optical effects [9, 10].

Apart from $\chi^{(2)}$ based light generation, electro-optic modulation is another major application of second-order nonlinear effects. Lithium niobate ($LiNbO_3$) modulators are vital components in the fiber-optic communication network. They convert data from the electrical to the optical domain: information, that is stored and processed electronically, is imprinted on an optical carrier wave by means of optical modulators before being sent into a fiber-optic link. Lithium niobate is a popular material for electro-optic modulation and nonlinear wave mixing due to its

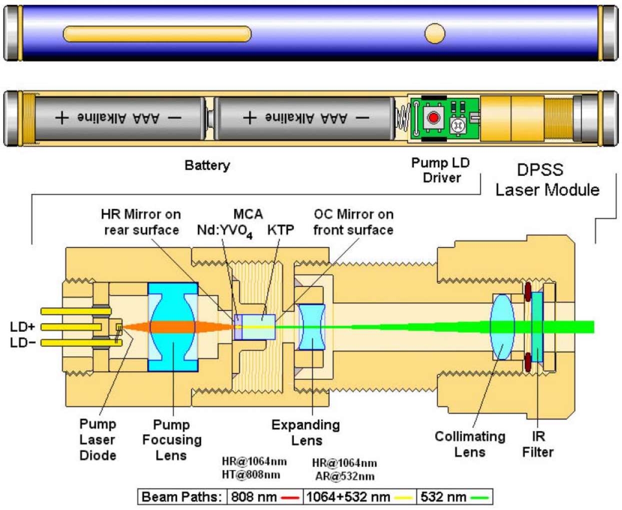

Figure 1.4: Schematic of a green laser pointer. The package contains two batteries that power the unit, a printed circuit board with the laser diode driving circuitry and the diode-pumped solid-state (DPSS) laser module. The laser diode (LD) produces light at a wavelength of 808 nm and pumps a Nd:YVO$_4$ (neodymium-doped yttrium orthovanadate) crystal. The Nd:YVO$_4$ crystal emits light at a wavelength of 1064 nm into a KTP (potassium titanyl phosphate) crystal. In the KTP crystal, light at a wavelength of 532 nm (green light) is generated via a second-harmonic generation process. MCA: multiple-crystal assembly, OC: output coupler, IR: infrared, HR: high reflectivity, HT: high transmittivity, AR: antireflective. Figure reproduced from [4].

Figure 1.5: Optical parametric oscillator, model name Horizon, sold by Continuum. It provides full access to a wavelength range from 192 nm to 2750 nm. Figure reproduced from [11].

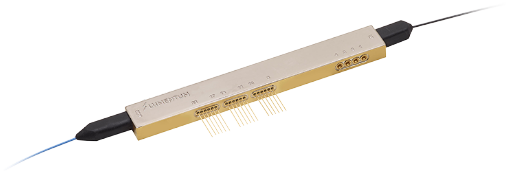

Figure 1.6: A lithium niobate external modulator designed by Lumentum to enable 400 Gbit/s Ethernet and beyond. Figure reproduced from [12].

large second-order susceptibility. An example of a packaged $LiNbO_3$ modulator for fiber-optic networks is shown in figure 1.6.

Finally, several characterization tools and methods are based on $\chi^{(2)}$ nonlinear processes. Second-harmonic generation (SHG) can be used to measure the intensity and phase profiles of ultrashort laser pulses via methods called FROG (frequency-resolved optical gating) and GRENOUILLE (grating-eliminated no-nonsense observation of ultrafast incident laser light E-fields) [13, 14]. Other characterization methods are second-harmonic imaging microscopy [15] and surface second-harmonic generation [16, 17]. Second-harmonic imaging microscopy takes advantage of the fact that biological materials can be highly polarizable and often assemble in non-centrosymmetric structures. Surface second-harmonic generation is a useful technique to study the microscopic structure of material interfaces and the adsorption of molecules. SHG from surfaces is typically weak, so for substrates with a non-zero $\chi^{(2)}$ it will be overpowered by the signal from the bulk. This will not be the case for centrosymmetric substrates. Therefore, surface SHG is an interesting tool to study the nature of interfaces between centrosymmetric media.

1.2 Integrated optics

The world of electronics has been revolutionized by integrating huge amounts of electronic components on a single silicon chip. The integration has lead to the realization of electronic circuits that are many orders of magnitude smaller, cheaper and faster than their counterparts consisting of discrete components. The first computers were massive, expensive and slow machines with limited computational power. But, thanks to the development of integrated circuits (ICs), computers, smartphones, tablets, and digital home appliances have become a part of our daily lives.

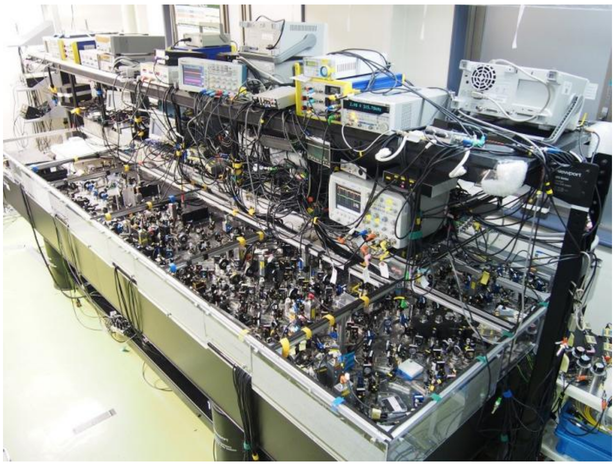

(a)

(b)

Figure 1.7: (a) Example of a free-space optical setup (used for a quantum teleportation experiment) on an optical table of 4.2 m by 1.5 m. The setup contains over 500 lenses and mirrors. (b) Optical chip (about the size of coin) performing a similar function as the free-space optical setup. Both figures are reproduced from [18].

In optics, a similar trend is ongoing, although the number of optical components integrated on a single chip is still small as compared to microelectronics. Figure 1.7(a) shows a free-space optical setup consisting of many mirrors, lenses, beamsplitters, etc. Assembling such a setup and aligning all of the components requires a great deal of time and effort. Clearly, the scalability of free-space optical systems is limited and they are difficult to implement in small, handheld devices. Integrating all of the optical components on a chip (see, e.g., figure 1.7(b)) can reduce the size, cost and power consumption of optical devices, while also making them faster and more robust. Moreover, on-chip integration allows for the implementation of more complex optical systems which can unlock functionality beyond what is possible in traditional free-space systems. In analogy with electronics, these integrated optical systems are called photonic integrated circuits (PICs).

The advancement of photonic integrated circuits is intimately connected with the development of fiber-optic communication networks [19]. The commercial deployment of fiber-optic communication systems took off in the 1970s with the simultaneous availability of low-loss optical fibers and compact gallium arsenide (GaAs) based semiconductor lasers operating continuously at room temperature. With the rise of the internet and the demand for high-speed data transmission, fiber-optic communication technology kept on developing rapidly. This evolution, together with the continuing advancements in microfabrication techniques, has kept on pushing the boundaries of PIC technology. Today, integrated transmitters, receivers and modulators for the telecom and datacom industry are still the primary market for PICs. But, also other applications of PICs are emerging, such as sensing of gases or biomolecules in bodily fluids, 3D holographic display technology, LIDAR (light detection and ranging; e.g., for autonomous cars), and novel computing paradigms like photonic neuromorphic computing (inspired by the human brain) and quantum computing.

While silicon is the substrate material of choice in the microelectronics industry, the landscape of materials for integrated optics is more diverse. PICs for fiber-optic communication networks commonly use lithium niobate or III-V semiconductor substrates, typically indium phosphide (InP) or gallium arsenide (GaAs). Lithium niobate, known for its large Pockels effect, is used to fabricate high-speed low-loss external modulators (see also section 1.1). III-V semiconductors are popular because they make efficient lasers emitting at wavelengths used in optical fiber links (mainly around $850\,\mathrm{nm}$, $1310\,\mathrm{nm}$, and $1550\,\mathrm{nm}$, where the optical fiber attenuation is low), which is challenging in lithium niobate or silicon. III-V compounds like $\mathrm{Ga}_x\mathrm{In}_{1-x}\mathrm{As}_y\mathrm{P}_{1-y}$ (indium gallium arsenide phosphide) or $\mathrm{Al}_x\mathrm{Ga}_{1-x}\mathrm{As}$ (aluminum gallium arsenide) are grown epitaxially on InP or GaAs substrates. The coefficients x and y can be tuned to alter the bandgap and get the desired emission wavelength (or absorption in the case of photodetectors). Also optical modulators are available in III-V material systems, usually based on the Franz-Keldysh effect or the quantum confined Stark effect. The company Infinera, for example, uses InP PIC technology for its optical transceivers [20].

Silicon photonics

If we use silicon PIC technology, we can benefit from the decades of investments in the manufacturing infrastructure for microelectronics [21]. Recycling the tools and processes of CMOS technology (the most used technology for very-large-scale integration in electronics; CMOS stands for complementary metal-oxide-semiconductor [22]) for photonics, offers a route to high-yield mass manufacturing at a low cost per chip. In addition, using silicon permits the co-integration of electronics and photonics on a single chip enabling high data rates with low power consumption [23]. Moreover, the high refractive index contrast in silicon waveguides allows for dense packing of photonic components. The lack of efficient light sources in silicon can be made up for by heterogeneous integration of III-V materials [24]. Alternatively, external light sources can be used, simply acting as optical power supplies [25]. For light detection, germanium photodetectors are typically used, as germanium can be grown on silicon by heteroepitaxy. For light modulation, use of the plasma dispersion effect in silicon is a common approach. Companies like Intel and Luxtera (recently acquired by Cisco [26]) are already selling silicon photonics transceivers [27, 28]. Also outside of the telecom and datacom industry, silicon photonics is finding its way to the market. Indigo is on the road to commercializing glucose sensors based on silicon photonics to improve the life of diabetes patients [29]. Sentea is leveraging silicon photonics to make small, robust and cost-effective interrogators for fiber-optic sensing [30]. Fiber-optic sensors can be used for, e.g., structural health monitoring in bridges, dams, and wind turbines. Xanadu is using silicon photonic chips for quantum computing [31] and Lightelligence utilizes integrated optical neural networks for high-performance computing tasks [32]. Analog Photonics is developing LIDAR sensor solutions (for, e.g., advanced driver-assistance systems) based on optical phased arrays and silicon photonics technology [33].

Use of silicon nitride in silicon photonics

The standard substrates used in silicon photonics are silicon-on-insulator (SOI) wafers. They consist of a thin crystalline silicon light guiding layer (typical thickness of $200\,\mathrm{nm}$ to $400\,\mathrm{nm}$) on a layer of buried oxide (BOX; typical thickness of $2\,\mu\mathrm{m}$), which separates the light guiding layer from the thick crystalline silicon substrate. The BOX layer needs to be sufficiently thick to prevent the light from leaking into the substrate. SOI based waveguides have low absorption losses between a wavelength of $1.1\,\mu\mathrm{m}$ (corresponding to silicon's bandgap) and $\sim 4\,\mu\mathrm{m}$ (onset of mid-infrared absorption in SiO_2) [34]. But, silicon nitride (SiN) is gaining ground as an alternative CMOS-compatible light guiding material. SiN is used in standard CMOS processes for masking and passivation. Using SiN instead of silicon extends the transparency window down to a wavelength of $\sim 400\,\mathrm{nm}$ (though SiN's optical bandgap depends strongly on its chemical composition, which can be tuned by altering the deposition parameters [35]). Moving from the infrared to the visible wavelength region, significantly lowers water's absorption coefficient ($\alpha = 54\,\mathrm{dB/cm}$ for $\lambda = 1.4\,\mu\mathrm{m}$, $\alpha = 2\,\mathrm{dB/cm}$ for $\lambda = 1\,\mu\mathrm{m}$, and $\alpha = 0.01\,\mathrm{dB/cm}$ for $\lambda = 0.6\,\mu\mathrm{m}$ [36]). Therefore, SiN is an appealing platform for the study of substances in aqueous media, as is very often the case for applications in environmental and life sciences. Another possible application domain is display technology, where the use of visible light is a requirement. SiN based PICs have been used for, e.g., on-chip Raman spectroscopy [37], refractive index sensing of disease-related biomarkers [38], and 3D image projection [39]. Also for $\chi^{(3)}$ nonlinear devices operating at telecom wavelengths, SiN is an attractive alternative for silicon, as silicon suffers strongly from two-photon absorption for wavelengths shorter than $\sim 2\,\mu\mathrm{m}$ [40].

Silicon nitride is usually deposited by PECVD (plasma-enhanced chemical vapor deposition) at low temperatures ($<400\,^{\circ}\mathrm{C}$) or LPCVD (low-pressure chemical vapor deposition) at high temperatures ($>700\,^{\circ}\mathrm{C}$). Due to the use of hydrogen-containing precursors, hydrogen will also be incorporated in SiN films. LPCVD SiN tends to contain smaller amounts of hydrogen than PECVD SiN. The presence of Si – H and N – H bonds causes absorption around a wavelength of $1550\,\mathrm{nm}$ [41]. Therefore, LPCVD SiN is typically preferred when working at a wavelength of $1550\,\mathrm{nm}$. Yet, even for PECVD SiN waveguides, waveguide losses as low as $1.5\,\mathrm{dB/cm}$ at $1550\,\mathrm{nm}$ have been reported [42]. This was achieved by using less hydrogen-containing precursors. In addition, high-temperature annealing treatments can be used to reduce waveguide loss [43]. In LPCVD SiN waveguides, losses on the order of 1 dB/m around a wavelength of 1550 nm have been measured [44–46]. In the $532\,\mathrm{nm}$ to $900\,\mathrm{nm}$ wavelength range, waveguide losses $<1\,\mathrm{dB/cm}$ have been reported for PECVD SiN [47].

Compared to the traditional SOI platform, SiN offers more manufacturing flexibility as it can be deposited easily. The fabrication of SOI wafers on the other hand, is a rather complex process, involving oxygen ion implantation, high-temperature annealing and/or direct wafer bonding [48]. Since SiN lends itself for multilayer stacking, it makes 3D device integration possible. Moreover, PECVD SiN is suitable for the integration of a photonics layer in the back end of line of a CMOS process [49], thereby enabling monolithic integration of electronic and photonic circuits. The concept of back-end deposited silicon photonics is illustrated in figure 1.8. While processing the photonics layer, it is important to keep the temperature low (reference [49] proposes to keep the thermal budget below 90 minutes at $450\,^{\circ}\mathrm{C}$) to avoid degradation of the underlying electronics (e.g. copper diffusion can deteriorate transistor characteristics). The traditional SOI substrates used in photonics do no lend themselves very well for monolithic photonic-electronic integration, as mostly bulk silicon wafers are used for CMOS electronics. Yet, silicon-on-insulator CMOS technology exists, but in modern CMOS SOI processes the crystalline silicon layer and buried oxide are very thin ($<100\,\mathrm{nm}$ for the silicon layer and $<200\,\mathrm{nm}$ for the buried oxide). Front-end integration of photonics in modern CMOS SOI technology is possible, but substrate removal is required to optically isolate the crystalline silicon waveguide core from the substrate [23].

Second-order nonlinear optical effects in silicon photonics

Silicon crystallizes in a centrosymmetric structure and therefore exhibits no $\chi^{(2)}$ effects. Also for the SiN and SiO_x thin films used in silicon photonics, no $\chi^{(2)}$ effects are expected to occur because of the materials' amorphous nature. Yet,

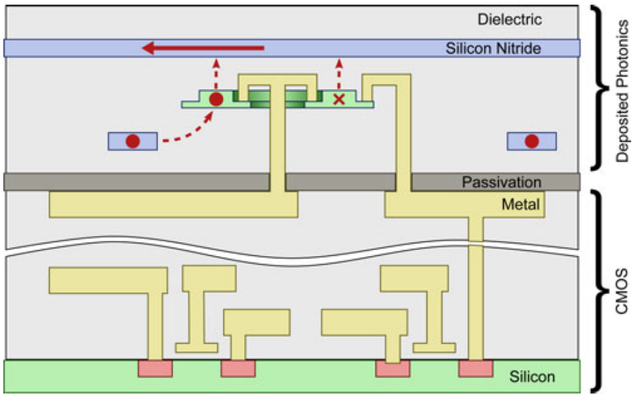

Figure 1.8: Schematic cross-section of a processed silicon wafer with the photonics layer on top of the CMOS electronics. For the photonic circuits, the use of low-loss PECVD SiN and excimer-laser-annealed polycrystalline silicon is envisioned. Figure reproduced from [49].

$\chi^{(2)}$ effects have been observed in each of these materials, but the strength of these effects remains modest.

Highly stressed SiN films have been deposited on top of silicon waveguides to induce a strain gradient in the silicon waveguide core. The presence of a strain gradient breaks the inversion symmetry. Both the Pockels effect [50–53] and second-harmonic generation [54, 55] have been reported in strained silicon waveguides. There has been some debate as to whether the origin of the $\chi^{(2)}$ effects lies in the strained silicon or rather in the SiN cladding [56]. Also the presence of a fixed charge at the silicon-SiN interface, which induces a static electric field near the interface, combined with silicon's strong $\chi^{(3)}$ nonlinearity, has been named as a possible contributor [55]. Moreover, in multiple publications on strained silicon electro-optic modulators, the free carrier effects are not taken into account, leading to an overestimation of the $\chi^{(2)}$ nonlinearity [53, 57].

In silicon ridge waveguides with a p-i-n junction, electric field induced second-harmonic generation (EFISHG) has been demonstrated [58]. Although second-harmonic radiation is generated, this is actually a $\chi^{(3)}$ nonlinear process. Silicon's strong $\chi^{(3)}$ nonlinearity in combination with a static electric field, can create an effective $\chi^{(2)}$ nonlinearity.

Second-harmonic generation has been observed in electron beam (e-beam) deposited SiO_x films with a second-order nonlinearity comparable to that of crystalline quartz [59]. Formation of $Si-H$ dipoles in the direction perpendicular to the surface due to charging of the film during e-beam deposition is suggested as origin of the nonlinearity. SHG has also been reported in thermally poled silica [60–62].

Thermal poling consists of applying strong electric fields ($\sim 50\,\mathrm{kV/cm}$) while the material is heated up ($\sim 300\,^{\circ}\mathrm{C}$). Subsequently, the material is cooled down to room temperature before removing the applied field. The induced nonlinearity is believed to be caused by the migration of impurity ions during the poling process. When the sample is cooled down and the applied field removed, the ions remain in a fixed position and a permanent electric field is present in the material. This electric field can act on silica's $\chi^{(3)}$ nonlinearity to generate an effective $\chi^{(2)}$ nonlinearity.

In silicon nitride, both second-harmonic generation [63–68] and the Pockels effect [69] have been observed. The observations have been attributed to a bulk $\chi^{(2)}$ nonlinearity whose magnitude depends on the material composition, but the exact origin remains elusive.

In references [70, 71], SHG in SiN waveguides with optically induced quasi-phase-matching has been reported. They observe a build-up of SHG over time when a powerful laser beam is injected in the waveguides. This phenomenon cannot be explained by a regular bulk $\chi^{(2)}$ nonlinearity. Instead, it is attributed to the creation of static space-charge field by a third-order nonlinear interaction between an initially weak SH signal and the strong pump laser (coherent photogalvanic effect). The static space-charge field varies periodically along the longitudinal direction of the waveguide with a periodicity corresponding to the phase mismatch between the pump and its second-harmonic. The periodically varying space-charge field combined with SiN's $\chi^{(3)}$ nonlinearity creates a $\chi^{(2)}$ grating. The $\chi^{(2)}$ grating is long-term inscribed and can be used for quasi-phase-matched SHG.

In section 2.7, $\chi^{(2)}$ values for silicon, silica, and silicon nitride are given, together with the $\chi^{(2)}$ values for more traditional materials.

1.3 Rationale and thesis outline

As stated in the title, this doctoral thesis is concerned with low-temperature processed thin films of second-order nonlinear optical materials for silicon nitride photonic integrated circuits.

Section 1.1 showed the importance of second-order nonlinear effects for a wide range of applications. Unfortunately, the majority of $\chi^{(2)}$ devices relies on bulk nonlinear crystals and free-space optical components, therefore missing out on the benefits of on-chip integration listed in section 1.2. Even for the integrated $\mathrm{LiNbO_3}$ modulators used in fiber-optic networks (e.g. figure 1.6), significant improvements are possible. These modulators are based on low-index-contrast waveguides, resulting in large optical mode sizes [72, 73]. This leads to large device footprints, large drive voltages and limited bandwidths.

The research conducted in the context of this doctoral thesis is geared towards

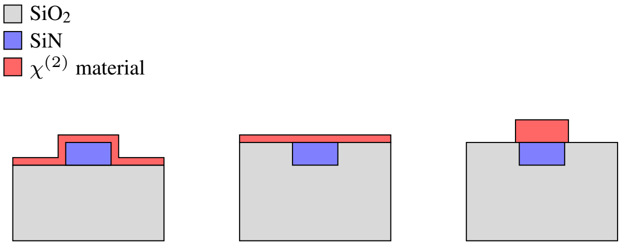

Figure 1.9: Schematic waveguide cross-sections to illustrate how $\chi^{(2)}$ materials can be added to SiN PICs. In the left image, the $\chi^{(2)}$ material is deposited conformally on top of a SiN waveguide. In the middle image, the SiN PIC is planarized before $\chi^{(2)}$ material deposition. In the right image, a thicker layer of $\chi^{(2)}$ material is deposited, which is subsequently patterned into a waveguide. A top cladding can be deposited if desirable.

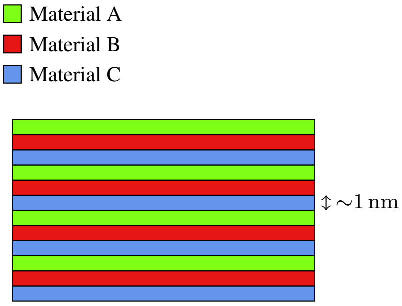

Figure 1.10: Schematic representation of an ABC-type nanolaminate. It consists of three different materials A, B, and C. They are deposited sequentially to create a sequence A, B, C, A, B, C, ... For the ABC-type nanolaminates presented in this work, the individual layers have a thickness on the order of 1 nm.

the integration of $\chi^{(2)}$ devices in silicon photonics, thereby benefiting from not only the integration aspect, but also the compatibility with CMOS fabrication technology and the relative maturity of the silicon photonics platform. Although there have been some demonstrations of $\chi^{(2)}$ effects in silicon, silicon nitride and silica (see section 1.2), this work concentrates on adding new $\chi^{(2)}$ materials to the existing platform. The focus lies on the silicon nitride platform rather than SOI, but most of the thin film processing techniques presented here can easily be applied to SOI waveguide circuits or any other material platform. Figure 1.9 shows some schematic waveguide cross-sections to illustrate how $\chi^{(2)}$ materials can be added to SiN PICs. The $\chi^{(2)}$ materials presented in this thesis are ABC-type nanolaminates (see figure 1.10), zinc oxide, zinc sulfide, and *N*-benzyl-2-methyl-4-nitroaniline (BNA). All of these materials are deposited and processed at low temperatures, thereby allowing for back-end integration on a CMOS chip.

The structure of this doctoral thesis is as follows. Chapter 2 introduces some basic concepts and notational conventions which will help the reader to understand and interpret the results and formulas presented in subsequent chapters. The nonlinear polarization and properties of the second-order susceptibility are discussed. Also an overview of the second-order susceptibility values for a range of materials is given. In chapter 3, several theoretical models for second-harmonic generation in thin films are derived. Second-harmonic generation experiments will be used frequently in subsequent chapters to quantify the second-order susceptibility of thin films, which requires appropriate models. In chapter 4, our results regarding atomic layer deposited (ALD) second-order nonlinear materials are presented. These materials are ABC-type nanolaminates, zinc oxide and zinc sulfide. Second-harmonic generation in thin films as well as electro-optic modulation in ring resonators will be covered. Chapter 5 treats organic second-order nonlinear crystalline thin films. The studied organic material is BNA. Our growth methods are described and the results of second-harmonic generation experiments in thin films are presented. Chapter 6 gives the conclusions and perspectives.

1.4 Publications

The research carried out in the context of this doctoral thesis has lead to multiple publications in international peer-reviewed journals and conference proceedings. A list of these publications is provided below.

1.4.1 Journal publications

- **A. Hermans**, M. Van Daele, J. Dendooven, S. Clemmen, C. Detavernier, and R. Baets. *Integrated silicon nitride electro-optic modulators with atomic layer deposited overlays.* Optics Letters, 44(5):1112, 2019.

- K. Koskinen, R. Czaplicki, A. Slablab, **A. Hermans**, B. Kuyken, V. Mittal, G. S. Murugan, T. Niemi, R. Baets, and M. Kauranen. *Enhancement of bulk second-harmonic generation from silicon nitride films by material composition.* Optics Letters, 42(23):5030, 2017.

- **A. Hermans***, C. Kieninger*, K. Koskinen, A. Wickberg, E. Solano, J. Dendooven, M. Kauranen, S. Clemmen, M. Wegener, C. Koos, and R. Baets. *On the determination of $\chi^{(2)}$ in thin films: a comparison of one-beam second-harmonic generation measurement methodologies.* Scientific Reports, 7:44581, 2017.

- A. Rahim, E. Ryckeboer, A. Z. Subramanian, S. Clemmen, B. Kuyken, A. Dhakal, A. Raza, **A. Hermans**, M. Muneeb, S. Dhoore, Y. Li, U. Dave, P. Bienstman, N. Le Thomas, G. Roelkens, D. Van Thourhout, P. Helin, S.

Severi, X. Rottenberg, and R. Baets. *Expanding the silicon photonics portfolio with silicon nitride photonic integrated circuits.* Journal of Lightwave Technology, 35(4):639, 2017.

- S. Clemmen*, **A. Hermans***, E. Solano, J. Dendooven, K. Koskinen, M. Kauranen, E. Brainis, C. Detavernier, and R. Baets. *Atomic layer deposited second-order nonlinear optical metamaterial for back-end integration with CMOS-compatible nanophotonic circuitry.* Optics Letters, 40(22):5371, 2015.

*These authors contributed equally to this work.

1.4.2 Conference publications

- **A. Hermans**, S. Clemmen, R. Baets, J. Genoe, and C. Rolin. *Growth of organic crystalline thin films with strong second-order nonlinearity for integrated optics.* European Conference on Integrated Optics (ECIO), p. W.A3.3, 2019.
- **A. Hermans**, R. Janneck, C. Rolin, S. Clemmen, P. Heremans, J. Genoe, and R. Baets. *Growth of thin film organic crystals with strong nonlinearity for on-chip second-order nonlinear optics.* Annual Symposium of the IEEE Photonics Society Benelux Chapter, 2018.
- **A. Hermans**, M. Van Daele, C. Kieninger, J. Dendooven, S. Clemmen, C. Detavernier, C. Koos, and R. Baets. *CMOS-compatible ALD zinc oxide coating for on-chip second-order nonlinear optical functionalities.* Conference on Lasers and Electro-Optics (CLEO), p. SM3K.3, 2017.
- **A. Hermans**, M. Van Daele, J. Dendooven, S. Clemmen, C. Detavernier, and R. Baets. *Electro-optic modulation in silicon nitride photonic integrated circuits by means of ALD ZnO overlays.* European Conference on Integrated Optics (ECIO), p. T5.3, 2017.
- **A. Hermans***, S. Clemmen*, E. Solano, J. Dendooven, E. Brainis, C. Detavernier, and R. Baets. *Second-harmonic generation based on symmetry breaking in a periodically layered medium.* Annual Workshop of the IEEE Photonics Society Benelux Chapter, p. 6, 2015.

*These authors contributed equally to this work.

References

[1] R. W. Boyd. *Nonlinear Optics*. Academic Press, 3rd edition, 2008.

[2] P. N. Butcher and D. Cotter. *The Elements of Nonlinear Optics*. Cambridge University Press, Cambridge, 1990.

[3] Coherent. *INNOVA FreD*. `https://www.coherent.com/lasers/laser/innova-fred`. [Accessed 28 February 2019].

[4] J. Galang, A. Restelli, C. W. Clark, and E. Hagley. *The dangerous dark companion of bright green lasers*. SPIE Newsroom, 2011. DOI: 10.1117/2.1201012.003328.

[5] Rainbow Photonics. *TeraTune*®. `http://www.rainbowphotonics.com/prod_teratune.php`. [Accessed 28 February 2019].

[6] P. G. Kwiat, K. Mattle, H. Weinfurter, A. Zeilinger, A. V. Sergienko, and Y. Shih. *New high-intensity source of polarization-entangled photon pairs*. Physical Review Letters, 75(24):4337, 1995.

[7] H. Zhang, X.-M. Jin, J. Yang, H.-N. Dai, S.-J. Yang, T.-M. Zhao, J. Rui, Y. He, X. Jiang, F. Yang, G.-S. Pan, Z.-S. Yuan, Y. Deng, Z.-B. Chen, X.-H. Bao, S. Chen, B. Zhao, and J.-W. Pan. *Preparation and storage of frequency-uncorrelated entangled photons from cavity-enhanced spontaneous parametric downconversion*. Nature Photonics, 5:628, 2011.

[8] M. Bock, A. Lenhard, C. Chunnilall, and C. Becher. *Highly efficient heralded single-photon source for telecom wavelengths based on a PPLN waveguide*. Optics Express, 24(21):23992, 2016.

[9] S. Mosca, M. Parisi, I. Ricciardi, F. Leo, T. Hansson, M. Erkintalo, P. Maddaloni, P. De Natale, S. Wabnitz, and M. De Rosa. *Modulation instability induced frequency comb generation in a continuously pumped optical parametric oscillator*. Physical Review Letters, 121(9):093903, 2018.

[10] M. Zhang, B. Buscaino, C. Wang, A. Shams-Ansari, C. Reimer, R. Zhu, J. M. Kahn, and M. Lončar. *Broadband electro-optic frequency comb generation in a lithium niobate microring resonator*. Nature, 568:373, 2019.

[11] Continuum. *Horizon*^{TM} *OPO*. `http://www.directindustry.com/prod/continuum/product-27505-939357.html`. [Accessed 28 February 2019].

[12] Lumentum Operations LLC. *Modulator, 400G/600G DP-QPMZ*. `https://www.lumentum.com/en/products/modulator-400g-600g-dp-qpmz`. [Accessed 4 March 2019].

[13] Coherent Solutions. *IQFROG - Frequency-Resolved Optical Gating Pulse Analyzer*. `https://www.coherent-solutions.com/frog-optical-pulse-analyzer/`. [Accessed 5 March 2019].

[14] Swamp Optics. *Products*. `http://www.swampoptics.com/products.html`. [Accessed 5 March 2019].

[15] P. J. Campagnola and L. M. Loew. *Second-harmonic imaging microscopy for visualizing biomolecular arrays in cells, tissues and organisms*. Nature Biotechnology, 21(11):1356, 2003.

[16] Y. R. Shen. *Surface properties probed by second-harmonic and sum-frequency generation*. Nature, 337(9):519, 1989.

[17] Y. R. Shen. *Surface nonlinear optics: a historical perspective*. IEEE Journal on Selected Topics in Quantum Electronics, 6(6):1375, 2000.

[18] Centre for Quantum Photonics at the University of Bristol. *Quantum teleportation on a chip*. `https://phys.org/news/2015-04-quantum-teleportation-chip.html`, 2015. [Accessed 5 March 2019].

[19] R. G. Hunsperger. *Integrated Optics: Theory and Technology*. Springer, 6th edition, 2009.

[20] R. Going, M. Lauermann, R. Maher, H. Tsai, M. Lu, N. Kim, S. Corzine, P. Studenkov, J. Summers, A. Hosseini, J. Zhang, B. Behnia, J. Tang, S. Buggaveeti, T. Vallaitis, J. Osenbach, M. Kuntz, X. Xu, K. Croussore, V. Lal, P. Evans, J. Rahn, T. Butrie, A. Karanicolas, K.-T. Wu, M. Mitchell, M. Ziari, D. Welch, and F. Kish. *Multi-channel InP-based Coherent PICs with Hybrid Integrated SiGe Electronics Operating up to 100 GBd, 32QAM*. European Conference on Optical Communication (ECOC), 2017. DOI: 10.1109/ECOC.2017.8346096.

[21] L. Vivien and L. Pavesi, editors. *Handbook of Silicon Photonics*. CRC Press, 2013.

[22] J. P. Uyemura. *Circuit Design for CMOS VLSI*. Springer, 1992.

[23] V. Stojanović, R. J. Ram, M. Popović, S. Lin, S. Moazeni, M. Wade, C. Sun, L. Alloatti, A. Atabaki, F. Pavanello, N. Mehta, and P. Bhargava. *Monolithic silicon-photonic platforms in state-of-the-art CMOS SOI processes [Invited]*. Optics Express, 26(10):13106, 2018.

[24] D. Thomson, A. Zilkie, J. E. Bowers, T. Komljenovic, G. T. Reed, L. Vivien, D. Marris-Morini, E. Cassan, L. Virot, J.-M. Fédéli, J.-M. Hartmann,

J. H. Schmid, D.-X. Xu, F. Boeuf, P. O'Brien, G. Z. Mashanovich, and M. Nedeljkovic. *Roadmap on silicon photonics*. Journal of Optics, 18(7):073003, 2016.

[25] Y. A. Vlasov. *Silicon CMOS-integrated nano-photonics for computer and data communications beyond 100G*. IEEE Communications Magazine, 50(2):S67, 2012.

[26] Cisco. *Cisco Completes Acquisition of Luxtera, Inc.* `https://www.cisco.com/c/en/us/about/corporate-strategy-office/acquisitions/luxtera.html`. [Accessed 7 March 2019].

[27] Intel®. *Intel® Silicon Photonics Optical Transceivers*. `https://www.intel.com/content/www/us/en/products/network-io/high-performance-fabrics/silicon-photonics.html`. [Accessed 7 March 2019].

[28] Luxtera. *Luxtera Silicon Photonics Optical Transceivers*. `http://www.luxtera.com/products/`. [Accessed 7 March 2019].

[29] Indigo. *Giving diabetics the extra sense for health*. `https://indigomed.com/`. [Accessed 7 March 2019].

[30] Sentea. *Fiber optic sensors. Everywhere.* `http://www.senteatech.com/`. [Accessed 7 March 2019].

[31] Xanadu. *Quantum computing powered by light*. `https://www.xanadu.ai/`. [Accessed 7 March 2019].

[32] Lightelligence. *Empower AI with light*. `https://www.lightelligence.ai/`. [Accessed 7 March 2019].

[33] Analog Photonics. *LiDAR*. `http://www.analogphotonics.com/products/`. [Accessed 7 March 2019].

[34] A. Rahim, E. Ryckeboer, A. Z. Subramanian, S. Clemmen, B. Kuyken, A. Dhakal, A. Raza, A. Hermans, M. Muneeb, S. Dhoore, Y. Li, U. Dave, P. Bienstman, N. Le Thomas, G. Roelkens, D. Van Thourhout, P. Helin, S. Severi, X. Rottenberg, and R. Baets. *Expanding the silicon photonics portfolio with silicon nitride photonic integrated circuits*. Journal of Lightwave Technology, 35(4):639, 2017.

[35] C. J. Krückel, A. Fülöp, Z. Ye, P. A. Andrekson, and V. Torres-Company. *Optical bandgap engineering in nonlinear silicon nitride waveguides*. Optics Express, 25(13):15370, 2017.

[36] G. M. Hale and M. R. Querry. *Optical constants of water in the 200-nm to 200-μm wavelength region*. Applied Optics, 12(3):555, 1973.

[37] A. Z. Subramanian, E. Ryckeboer, A. Dhakal, F. Peyskens, A. Malik, B. Kuyken, H. Zhao, S. Pathak, A. Ruocco, A. De Groote, P. Wuytens, D. Martens, F. Leo, W. Xie, U. D. Dave, M. Muneeb, P. Van Dorpe, J. Van Campenhout, W. Bogaerts, P. Bienstman, N. Le Thomas, D. Van Thourhout, Z. Hens, G. Roelkens, and R. Baets. *Silicon and silicon nitride photonic circuits for spectroscopic sensing on-a-chip [Invited]*. Photonics Research, 3(5):B47, 2015.

[38] D. Martens, P. Ramirez-Priego, M. S. Murib, A. A. Elamin, A. B. Gonzalez-Guerrero, M. Stehr, F. Jonas, B. Anton, N. Hlawatsch, P. Soetaert, R. Vos, A. Stassen, S. Severi, W. Van Roy, R. Bockstaele, H. Becker, M. Singh, L. M. Lechuga, and P. Bienstman. *A low-cost integrated biosensing platform based on SiN nanophotonics for biomarker detection in urine*. Analytical Methods, 10:3066, 2018.

[39] M. Raval, A. Yaacobi, D. Coleman, N. M. Fahrenkopf, C. Baiocco, G. Leake, T. N. Adam, D. Coolbaugh, and M. R. Watts. *Nanophotonic phased array for visible light image projection*. In IEEE Photonics Conference, page MG3.4, 2016.

[40] D. J. Moss, R. Morandotti, A. L. Gaeta, and M. Lipson. *New CMOS-compatible platforms based on silicon nitride and Hydex for nonlinear optics*. Nature Photonics, 7:597, 2013.

[41] S. C. Mao, S. H. Tao, Y. L. Xu, X. W. Sun, M. B. Yu, G. Q. Lo, and D. L. Kwong. *Low propagation loss SiN optical waveguide prepared by optimal low-hydrogen module*. Optics Express, 16(25):20809, 2008.

[42] C. Lacava, S. Stankovic, A. Z. Khokhar, T. Dominguez Bucio, F. Y. Gardes, G. T. Reed, D. J. Richardson, and P. Petropoulos. *Si-rich silicon nitride for nonlinear signal processing applications*. Scientific Reports, 7:22, 2017.

[43] L. Wang, W. Xie, D. Van Thourhout, Y. Zhang, Y. Hui, and S. Wang. *Nonlinear silicon nitride waveguides based on PECVD deposition platform*. Optics Express, 26(8):9645, 2018.

[44] J. F. Bauters, M. J. R. Heck, D. John, D. Dai, M.-C. Tien, J. S. Barton, A. Leinse, R. G. Heideman, D. J. Blumenthal, and J. E. Bowers. *Ultra-low-loss high-aspect-ratio Si_3N_4 waveguides*. Optics Express, 19(4):3163, 2011.

[45] X. Ji, F. A. S. Barbosa, S. P. Roberts, A. Dutt, J. Cardenas, Y. Okawachi, A. Bryant, A. L. Gaeta, and M. Lipson. *Ultra-low-loss on-chip resonators with sub-milliwatt parametric oscillation threshold.* Optica, 4(6):619, 2017.

[46] M. H. P. Pfeiffer, J. Liu, A. S. Raja, T. Morais, B. Ghadiani, and T. J. Kippenberg. *Ultra-smooth silicon nitride waveguides based on the Damascene reflow process: fabrication and loss origins*. Optica, 5(7):884, 2018.

[47] A. Z. Subramanian, A. Dhakal, F. Peyskens, S. Selvaraja, R. Baets, P. Neutens, R. Jansen, T. Claes, X. Rottenberg, P. Helin, B. Du Bois, K. Leyssens, S. Severi, P. Deshpande, and P. Van Dorpe. *Low-loss singlemode PECVD silicon nitride photonic wire waveguides for 532-900 nm wavelength window fabricated within a CMOS pilot line*. IEEE Photonics Journal, 5(6):2202809, 2013.

[48] G. T. Reed and A. P. Knights. *Silicon Photonics: An Introduction*. John Wiley & Sons, Ltd, 2004.

[49] Y. H. D. Lee and M. Lipson. *Back-end deposited silicon photonics for monolithic integration on CMOS*. IEEE Journal of Selected Topics in Quantum Electronics, 19(2):8200207, 2013.

[50] R. S. Jacobsen, K. N. Andersen, P. I. Borel, J. Fage-Pedersen, L. H. Frandsen, O. Hansen, M. Kristensen, A. V. Lavrinenko, G. Moulin, H. Ou, C. Peucheret, B. Zsigri, and A. Bjarklev. *Strained silicon as a new electro-optic material.* Nature, 441(7090):199, 2006.

[51] B. Chmielak, M. Waldow, C. Matheisen, C. Ripperda, J. Bolten, T. Wahlbrink, M. Nagel, F. Merget, and H. Kurz. *Pockels effect based fully integrated, strained silicon electro-optic modulator.* Optics express, 19(18):17212, 2011.

[52] P. Damas, X. Le Roux, D. Le Bourdais, E. Cassan, D. Marris-Morini, N. Izard, T. Maroutian, P. Lecoeur, and L. Vivien. *Wavelength dependence of Pockels effect in strained silicon waveguides*. Optics Express, 22(18):22095, 2014.

[53] M. Berciano, G. Marcaud, P. Damas, X. Le Roux, P. Crozat, C. Alonso Ramos, D. Pérez Galacho, D. Benedikovic, D. Marris-Morini, E. Cassan, and L. Vivien. *Fast linear electro-optic effect in a centrosymmetric semiconductor*. Communications Physics, 1:64, 2018.

[54] M. Cazzanelli, F. Bianco, E. Borga, G. Pucker, M. Ghulinyan, E. Degoli, E. Luppi, V. Véniard, S. Ossicini, D. Modotto, S. Wabnitz, R. Pierobon, and L. Pavesi. *Second-harmonic generation in silicon waveguides strained by silicon nitride.* Nature materials, 11:148, 2012.

[55] C. Schriever, F. Bianco, M. Cazzanelli, M. Ghulinyan, C. Eisenschmidt, J. de Boor, A. Schmid, J. Heitmann, L. Pavesi, and J. Schilling. *Second-order optical nonlinearity in silicon waveguides: inhomogeneous stress and interfaces*. Advanced Optical Materials, 3:129, 2015.

[56] J. B. Khurgin, T. H. Stievater, M. W. Pruessner, and W. S. Rabinovich. *On the origin of the second-order nonlinearity in strained Si-SiN structures*. Journal of the Optical Society of America B, 32(12):2494, 2015.

[57] M. Borghi, M. Mancinelli, F. Merget, J. Witzens, M. Bernard, M. Ghulinyan, G. Pucker, and L. Pavesi. *High-frequency electro-optic measurement of strained silicon racetrack resonators*. Optics Letters, 40(22):5287, 2015.

[58] E. Timurdogan, C. V. Poulton, M. J. Byrd, and M. R. Watts. *Electric field-induced second-order nonlinear optical effects in silicon waveguides*. Nature Photonics, 11:200, 2017.

[59] S. V. Andersen and K. Pedersen. *Second-harmonic generation from electron beam deposited SiO films*. Optics Express, 20(13):13857, 2012.

[60] R. A. Myers, N. Mukherjee, and S. R. J. Brueck. *Large second-order nonlinearity in poled fused silica*. Optics Letters, 16(22):1732, 1991.

[61] H. Y. Chen and H. Y. Lin. *Second-order optical nonlinearity in thermally poled phosphorus-doped silicon dioxide thin-film waveguides*. Electronics Letters, 45(11):551, 2009.

[62] K. Yadav, C. L. Callender, C. W. Smelser, C. Ledderhof, C. Blanchetiere, S. Jacob, and J. Albert. *Giant enhancement of the second harmonic generation efficiency in poled multilayered silica glass structures*. Optics Express, 19(27):26975, 2011.

[63] J. S. Levy, M. A. Foster, A. L. Gaeta, and M. Lipson. *Harmonic generation in silicon nitride ring resonators.* Optics express, 19(12):11415, 2011.

[64] T. Ning, H. Pietarinen, O. Hyvärinen, J. Simonen, G. Genty, and M. Kauranen. *Strong second-harmonic generation in silicon nitride films*. Applied Physics Letters, 100(16):161902, 2012.

[65] E. F. Pecora, A. Capretti, G. Miano, and L. Dal Negro. *Generation of second harmonic radiation from sub-stoichiometric silicon nitride thin films*. Applied Physics Letters, 102:141114, 2013.

[66] A. Kitao, K. Imakita, I. Kawamura, and M. Fujii. *An investigation into second harmonic generation by Si-rich SiN_x thin films deposited by RF sputtering over a wide range of Si concentrations*. Journal of Physics D: Applied Physics, 47:215101, 2014.

[67] M. W. Puckett, R. Sharma, H. H. Lin, M. H. Yang, F. Vallini, and Y. Fainman. *Observation of second-harmonic generation in silicon nitride waveguides through bulk nonlinearities*. Optics Express, 24(15):16923, 2016.

[68] K. Koskinen, R. Czaplicki, A. Slablab, T. Ning, A. Hermans, B. Kuyken, V. Mittal, G. S. Murugan, T. Niemi, R. Baets, and M. Kauranen. *Enhancement of bulk second-harmonic generation from silicon nitride films by material composition*. Optics Letters, 42(23):5030, 2017.

[69] S. Miller, Y.-H. D. Lee, J. Cardenas, A. L. Gaeta, and M. Lipson. *Electro-optic effect in silicon nitride*. In Conference on Lasers and Electro-Optics (CLEO), page SF1G.4, 2015.

[70] A. Billat, D. Grassani, M. H. P. Pfeiffer, S. Kharitonov, T. J. Kippenberg, and C.-S. Brès. *Large second harmonic generation enhancement in Si_3N_4 waveguides by all-optically induced quasi-phase-matching*. Nature Communications, 8:1016, 2017.

[71] M. A. G. Porcel, J. Mak, C. Taballione, P. J. M. van der Slot, and K.-J. Boller. *Photo-induced second-order nonlinearity in stoichiometric silicon nitride waveguides*. Optics Express, 25(26):33143, 2017.

[72] R. C. Alferness. *Waveguide Electrooptic Modulators*. IEEE Transactions on Microwave Theory and Techniques, 30(8):1121, 1982.

[73] E. L. Wooten, K. M. Kissa, A. Yi-Yan, E. J. Murphy, D. A. Lafaw, P. F. Hallemeier, D. Maack, D. V. Attanasio, D. J. Fritz, G. J. McBrien, and D. E. Bossi. *A review of lithium niobate modulators for fiber-optic communications systems*. IEEE Journal of Selected Topics in Quantum Electronics, 6(1):69, 2000.

2

The second-order nonlinear susceptibility

This chapter introduces some basic concepts and notational conventions which will help the reader to understand and interpret the results and formulas presented in subsequent chapters. The nonlinear polarization is introduced and the properties of the second-order susceptibility tensor are discussed. Also an overview of the second-order susceptibility values for a range of materials is given.

Contents

2.1 Nonlinear polarization

Electromagnetic phenomena can be described by Maxwell's equations. Maxwell's equations in matter (also known as the macroscopic Maxwell equations) are given by (in SI units) [1]

$$\nabla \cdot \mathbf{D} = \rho \tag{2.1}$$

$$\nabla \cdot \mathbf{B} = 0 \tag{2.2}$$

$$\nabla \times \mathbf{E} = -\frac{\partial \mathbf{B}}{\partial t} \tag{2.3}$$

$$\nabla \times \mathbf{H} = \mathbf{J} + \frac{\partial \mathbf{D}}{\partial t} \tag{2.4}$$

where $\mathbf{E}$ and $\mathbf{B}$ are the (macroscopic) electric and magnetic field. The quantities ρ and $\mathbf{J}$ are the macroscopic averages of the free charge and current densities in the medium. The derived fields $\mathbf{D}$ and $\mathbf{H}$ have components given by

$$D_\alpha = \epsilon_0 E_\alpha + \left(P_\alpha - \sum_\beta \frac{\partial Q_{\alpha\beta}}{\partial x_\beta} + \cdots \right) \tag{2.5}$$

$$H_\alpha = \frac{1}{\mu_0} B_\alpha - (M_\alpha + \cdots) \tag{2.6}$$

with ϵ_0 the vacuum permittivity and μ_0 the vacuum permeability. The quantities $\mathbf{P}$, $\mathbf{Q}$, and $\mathbf{M}$ represent the macroscopically averaged electric dipole, electric quadrupole, and magnetic dipole densities of the material. The higher-order terms are not shown here as they can usually be neglected. $\mathbf{P}$, $\mathbf{Q}$, and $\mathbf{M}$ contain the contributions of the bound charges and currents in the medium. The intricate dependencies of $\mathbf{P}$, $\mathbf{Q}$, and $\mathbf{M}$ on the electric and magnetic field are described by constitutive relations. Substituting $\mathbf{H}$ and $\mathbf{D}$ in equation 2.4 by expressions 2.5 and 2.6, we get

$$\nabla \times \mathbf{B} = \mu_0 \left(\mathbf{J} + \epsilon_0 \frac{\partial \mathbf{E}}{\partial t} + \frac{\partial \mathbf{P}}{\partial t} - \frac{\partial}{\partial t} (\nabla \cdot \mathbf{Q}) + \nabla \times \mathbf{M} + \cdots \right) \tag{2.7}$$

If we take the curl of equation 2.3 and substitute $\nabla \times \mathbf{B}$ with expression 2.7, we find

$$\begin{aligned} \nabla \times (\nabla \times \mathbf{E}) + \frac{1}{c^2} \frac{\partial^2 \mathbf{E}}{\partial t^2} &= -\mu_0 \frac{\partial}{\partial t} \left(\mathbf{J} + \frac{\partial \mathbf{P}}{\partial t} - \frac{\partial}{\partial t} (\nabla \cdot \mathbf{Q}) + \nabla \times \mathbf{M} + \cdots \right) \\ &= -\mu_0 \frac{\partial}{\partial t} \left(\mathbf{J} + \frac{\partial \mathbf{\Pi}}{\partial t} \right) \end{aligned} \tag{2.8}$$

where we have introduced a generalized polarization $\mathbf{\Pi}$ that contains the electric dipole, electric quadrupole, magnetic dipole and all higher-order contributions. Alternatively, one might also include $\mathbf{J}$ in this generalized polarization. Equation 2.8 is the wave equation that will govern how electromagnetic waves propagate.

The conventional formalism is to write $\mathbf{J}$, $\mathbf{P}$, $\mathbf{Q}$, $\mathbf{M}$, and $\mathbf{\Pi}$ as a power series expansion in $\mathbf{E}$ [2–4]. The influence of the magnetic field $\mathbf{B}$ can be neglected for most optical materials. The expansion of $\mathbf{P}$ in $\mathbf{E}$ and the introduction of the susceptibility tensor $\chi^{(i)}$ will be covered below. But in a similar fashion, the power series expansion can be done for $\mathbf{J}$, $\mathbf{Q}$, $\mathbf{M}$, and $\mathbf{\Pi}$. Most often we will only consider the local response of a material to an applied electric field. In that case, the right-hand side of equation 2.8 will not contain spatial derivatives (as these spatial derivatives represent a nonlocal response) and $\mathbf{P}$ will be identical to $\mathbf{\Pi}$. This is known in literature as the electric-dipole approximation. In the context of this doctoral thesis, the nonlocal contributions will only play a role in the process of second-harmonic generation in centrosymmetric media [5, 6].

Now, let us write $\mathbf{P}(\mathbf{r}, t)$ as a power series expansion in $\mathbf{E}(\mathbf{r}, t)$ (we follow the approach outlined in [2])

$$\mathbf{P}(\mathbf{r}, t) = \mathbf{P}^{(0)}(\mathbf{r}, t) + \mathbf{P}^{(1)}(\mathbf{r}, t) + \mathbf{P}^{(2)}(\mathbf{r}, t) + \mathbf{P}^{(3)}(\mathbf{r}, t) + \cdots \tag{2.9}$$

with

$$\begin{aligned}\mathbf{P}^{(i)}(\mathbf{r}, t) = \epsilon_0 \int_{-\infty}^{+\infty} d\tau_1 \cdots \int_{-\infty}^{+\infty} d\tau_i \int_{-\infty}^{+\infty} d\mathbf{r}_1 \cdots \int_{-\infty}^{+\infty} d\mathbf{r}_i \\ \mathbf{R}^{(i)}(\mathbf{r}, \mathbf{r}_1, \tau_1, \ldots, \mathbf{r}_i, \tau_i) | \mathbf{E}(\mathbf{r}_1, t - \tau_1) \cdots \mathbf{E}(\mathbf{r}_i, t - \tau_i)\end{aligned} \tag{2.10}$$

for $i \geq 1$, where $\mathbf{R}^{(i)}(\mathbf{r}, \mathbf{r}_1, \tau_1, \ldots, \mathbf{r}_i, \tau_i)$ is called the polarization response function of the ith-order. Here we have assumed that the response of the material system is time-invariant. Time-invariance means that the dynamical properties of the system are assumed to be unchanged by a translation of the time origin; or in this context, a time-displacement of the driving electric field results only in a time-displacement of the induced polarization. Also, $\mathbf{R}^{(i)}(\mathbf{r}, \mathbf{r}_1, \tau_1, \ldots, \mathbf{r}_i, \tau_i) = 0$ if any $\tau_j < 0$ because of the causality condition: the polarization $\mathbf{P}^{(i)}(\mathbf{r}, t)$ only depends on the electric field at times smaller or equal to t, not on future electric fields. The tensor product $|$ is defined as

$$\begin{aligned}&\mathbf{R}^{(i)}(\mathbf{r}, \mathbf{r}_1, \tau_1, \ldots, \mathbf{r}_i, \tau_i) | \mathbf{E}(\mathbf{r}_1, t - \tau_1) \cdots \mathbf{E}(\mathbf{r}_i, t - \tau_i) = \\ &\sum_{\mu, \alpha_1, \ldots, \alpha_i} R_{\mu \alpha_1 \cdots \alpha_i}(\mathbf{r}, \mathbf{r}_1, \tau_1, \ldots, \mathbf{r}_i, \tau_i) E_{\alpha_1}(\mathbf{r}_1, t - \tau_1) \cdots E_{\alpha_i}(\mathbf{r}_i, t - \tau_i) \mathbf{e}_\mu\end{aligned} \tag{2.11}$$

where the indices μ, α_1, …, α_i need to be replaced by x, y and z (or sometimes the numbers 1, 2, and 3 are used instead) and all the obtained terms summed. The vectors $\mathbf{e}_x$, $\mathbf{e}_y$, and $\mathbf{e}_z$ are the unit vectors of the corresponding coordinate system. The sum consists of $3^{(i+1)}$ terms, or one term for each component of the $(i + 1)$th-rank tensor $\mathbf{R}^{(i)}(\mathbf{r}, \mathbf{r}_1, \tau_1, \ldots, \mathbf{r}_i, \tau_i)$. If we also assume the response of the medium to be local, equation 2.10 can be simplified to

$$\mathbf{P}^{(i)}(\mathbf{r},t) = \epsilon_0 \int_{-\infty}^{+\infty} d\tau_1 \cdots \int_{-\infty}^{+\infty} d\tau_i \\ \mathbf{R}^{(i)}(\mathbf{r},\tau_1,\ldots,\tau_i)|\mathbf{E}(\mathbf{r},t-\tau_1)\cdots\mathbf{E}(\mathbf{r},t-\tau_i) \quad (2.12)$$

Instead of working with polarization response functions in the time domain, a more common approach is to work in the frequency domain and use susceptibility tensors. A well behaving function $\mathbf{X}(\mathbf{r},t)$ and its Fourier transform $\mathbf{X}(\mathbf{r},\omega)$ are related by

$$\mathbf{X}(\mathbf{r},\omega) = \int_{-\infty}^{+\infty} dt\mathbf{X}(\mathbf{r},t)e^{-j\omega t} \quad (2.13)$$

$$\mathbf{X}(\mathbf{r},t) = \frac{1}{2\pi}\int_{-\infty}^{+\infty} d\omega\mathbf{X}(\mathbf{r},\omega)e^{j\omega t} \quad (2.14)$$

Using these Fourier transform relations, we find

$$\mathbf{P}^{(i)}(\mathbf{r},\omega) = \epsilon_0 \left(\frac{1}{2\pi}\right)^{i-1} \int_{-\infty}^{+\infty} d\omega_1 \cdots \int_{-\infty}^{+\infty} d\omega_i \\ \chi^{(i)}(-\omega_\sigma;\omega_1,\ldots,\omega_i)|\mathbf{E}(\mathbf{r},\omega_1)\cdots\mathbf{E}(\mathbf{r},\omega_i)\delta(\omega-\omega_\sigma) \quad (2.15)$$

with δ the Dirac delta function,

$$\chi^{(i)}(-\omega_\sigma;\omega_1,\ldots,\omega_i) = \int_{-\infty}^{+\infty} d\tau_1 \cdots \int_{-\infty}^{+\infty} d\tau_i \\ \mathbf{R}^{(i)}(\tau_1,\ldots,\tau_i)e^{-j\sum_{l=1}^{i}\omega_l\tau_l} \quad (2.16)$$

and

$$\omega_\sigma = \sum_{l=1}^{i}\omega_l \quad (2.17)$$

The quantity $\chi^{(i)}(-\omega_\sigma;\omega_1,\ldots,\omega_i)$ is the ith-order susceptibility. By convention, $-\omega_\sigma$ is written in front of a semicolon. The mentioning of $-\omega_\sigma$ is technically unnecessary, as it is always the negative of the sum of the frequencies following the semicolon. Yet, it is useful when describing the overall permutation symmetry property (see section 2.2).

In many experimental situations, the applied electric field can be considered to be a sum of monochromatic waves

$$\mathbf{E}(\mathbf{r},t) = \sum_{l=1}^{n}\frac{\mathbf{E}_{\tilde{\omega}_l}(\mathbf{r})e^{j\tilde{\omega}_l t} + \mathbf{E}_{-\tilde{\omega}_l}(\mathbf{r})e^{-j\tilde{\omega}_l t}}{2} \quad (2.18)$$

with $\mathbf{E}_{-\tilde{\omega}_l}(\mathbf{r}) = [\mathbf{E}_{\tilde{\omega}_l}(\mathbf{r})]^*$ because $\mathbf{E}(\mathbf{r},t)$ is a real function. The Fourier transform of $\mathbf{E}(\mathbf{r},t)$ is given by

$$\mathbf{E}(\mathbf{r},\omega) = \sum_{l=1}^{n} \frac{\mathbf{E}_{\tilde{\omega}_l}(\mathbf{r})2\pi\delta(\omega-\tilde{\omega}_l) + \mathbf{E}_{-\tilde{\omega}_l}(\mathbf{r})2\pi\delta(\omega+\tilde{\omega}_l)}{2} \tag{2.19}$$

In this case, $\mathbf{P}^{(i)}(\mathbf{r},t)$, or its Fourier transform $\mathbf{P}^{(i)}(\mathbf{r},\omega)$, will also be given by a sum of monochromatic waves according to equation 2.15

$$\mathbf{P}^{(i)}(\mathbf{r},\omega) = \sum_{\omega_\sigma} \frac{\mathbf{P}^{(i)}_{\omega_\sigma}(\mathbf{r})2\pi\delta(\omega-\omega_\sigma) + \mathbf{P}^{(i)}_{-\omega_\sigma}(\mathbf{r})2\pi\delta(\omega+\omega_\sigma)}{2} \tag{2.20}$$

with

$$\mathbf{P}^{(i)}_{\omega_\sigma}(\mathbf{r}) = \\ \epsilon_0 \sum_{\omega} K(-\omega_\sigma;\omega_1,\ldots,\omega_i)\chi^{(i)}(-\omega_\sigma;\omega_1,\ldots,\omega_i)|\mathbf{E}_{\omega_1}(\mathbf{r})\cdots\mathbf{E}_{\omega_i}(\mathbf{r}) \tag{2.21}$$

K is a numerical factor which can be calculated as

$$K(-\omega_\sigma;\omega_1,\ldots,\omega_i) = \frac{p}{2^{i-(j+k)}} \tag{2.22}$$

where p is the number of distinct permutations of $\omega_1,\ldots,\omega_i$, i is the order of the nonlinearity, $j=1$ if $\omega_\sigma \neq 0$ and $j=0$ if $\omega_\sigma = 0$; k is the number of (angular) frequencies in the set $\omega_1,\ldots,\omega_i$ that equal 0. In deriving expression 2.21, we have made use of the intrinsic permutation symmetry of $\chi^{(i)}(-\omega_\sigma;\omega_1,\ldots,\omega_i)$. Intrinsic permutation symmetry implies that $\chi^{(i)}_{\mu\alpha_1\cdots\alpha_i}(-\omega_\sigma;\omega_1,\ldots,\omega_i)$ is invariant under all $i!$ permutations of the i pairs (α_1,ω_1), …, (α_i,ω_i), for example

$$\chi^{(i)}_{\mu\alpha_1\alpha_2\cdots\alpha_i}(-\omega_\sigma;\omega_1,\omega_2,\ldots,\omega_i) = \chi^{(i)}_{\mu\alpha_2\alpha_1\cdots\alpha_i}(-\omega_\sigma;\omega_2,\omega_1,\ldots,\omega_i) \tag{2.23}$$

This symmetry condition is introduced to uniquely define $\chi^{(i)}(-\omega_\sigma;\omega_1,\ldots,\omega_i)$ [2]. Table 2.1 shows the values of K for first- and second-order processes. The summation sign $\sum_\omega$ in equation 2.21 serves as a reminder to sum over all the distinct sets ω_1, …, ω_i (where ω_1, …, ω_i are taken out of the pool of frequencies $-\tilde{\omega}_1$, …, $-\tilde{\omega}_n$, $\tilde{\omega}_1$, …, $-\tilde{\omega}_n$) which satisfy $\omega_\sigma = \omega_1 + \omega_2 + \cdots + \omega_i$. Most experiments are designed to have only one such set.

2.2 Symmetry properties of the susceptibility

Now that we have introduced the nonlinear polarization, let us have a closer look at the properties of the second-order susceptibility $\chi^{(2)}$. Since $\mathbf{E}(\mathbf{r},t)$ and $\mathbf{P}(\mathbf{r},t)$ are real functions, $\mathbf{R}^{(2)}(\mathbf{r},\tau_1,\tau_2)$ is a real function and consequently

$$\left[\chi^{(2)}(-(\omega_1+\omega_2);\omega_1,\omega_2)\right]^* = \chi^{(2)}(\omega_1+\omega_2;-\omega_1,-\omega_2) \tag{2.24}$$

Process	Order i	$-\omega_\sigma; \omega_1, \ldots, \omega_i$	K
Linear absorption/emission and refractive index	1	$-\omega; \omega$	1
Optical rectification	2	$0; \omega, -\omega$	$\frac{1}{2}$
Pockels effect	2	$-\omega; 0, \omega$	2
Second-harmonic generation	2	$-2\omega; \omega, \omega$	$\frac{1}{2}$
Sum- and difference-frequency generation	2	$-\omega_3; \omega_1, \pm\omega_2$	1

Table 2.1: Values of K for first- and second-order processes.

As already introduced in the previous section (see equation 2.23), the susceptibility displays intrinsic permutation symmetry

$$\chi^{(2)}_{\mu\alpha_1\alpha_2}(-(\omega_1+\omega_2); \omega_1, \omega_2) = \chi^{(2)}_{\mu\alpha_2\alpha_1}(-(\omega_1+\omega_2); \omega_2, \omega_1) \tag{2.25}$$

In the case of lossless media (i.e. frequencies of all fields involved in the nonlinear interaction are far from the resonance frequencies of the material), two additional symmetry conditions apply. For lossless media, the components of the $\chi^{(2)}$ tensor are real. Therefore we have

$$\chi^{(2)}(-(\omega_1+\omega_2); \omega_1, \omega_2) = \chi^{(2)}(\omega_1+\omega_2; -\omega_1, -\omega_2) \tag{2.26}$$

where $\omega_1+\omega_2$, ω_1, and ω_2 are from resonance. Secondly, the susceptibility displays full or overall permutation symmetry. This means that all of the frequency arguments of the susceptibility can be freely interchanged (including the frequency in front of the semicolon), as long as the corresponding indices are interchanged simultaneously. Thus, we get

$$\begin{aligned}\chi^{(2)}_{\mu\alpha_1\alpha_2}(-(\omega_1+\omega_2); \omega_1, \omega_2) &= \chi^{(2)}_{\mu\alpha_2\alpha_1}(-(\omega_1+\omega_2); \omega_2, \omega_1)\\ &= \chi^{(2)}_{\alpha_2\mu\alpha_1}(\omega_2; -(\omega_1+\omega_2), \omega_1)\\ &= \chi^{(2)}_{\alpha_2\alpha_1\mu}(\omega_2; \omega_1, -(\omega_1+\omega_2))\\ &= \chi^{(2)}_{\alpha_1\alpha_2\mu}(\omega_1; \omega_2, -(\omega_1+\omega_2))\\ &= \chi^{(2)}_{\alpha_1\mu\alpha_2}(\omega_1; -(\omega_1+\omega_2), \omega_2)\end{aligned} \tag{2.27}$$

These symmetry conditions for lossless media can be proven by verifying the quantum-mechanical expressions of the susceptibility [2].

Another symmetry condition, known as Kleinman's symmetry, applies if the dispersion of the susceptibility can be neglected. It is valid when, not only the involved frequencies are far from resonance, but also there are no resonances in between these frequencies. In this case the susceptibility is essentially frequency independent, so we can permute the indices without permuting the frequencies

$$\begin{aligned}\chi^{(2)}_{\mu\alpha_1\alpha_2}(-(\omega_1+\omega_2);\omega_1,\omega_2) &= \chi^{(2)}_{\mu\alpha_2\alpha_1}(-(\omega_1+\omega_2);\omega_1,\omega_2)\\ &= \chi^{(2)}_{\alpha_2\mu\alpha_1}(-(\omega_1+\omega_2);\omega_1,\omega_2)\\ &= \chi^{(2)}_{\alpha_2\alpha_1\mu}(-(\omega_1+\omega_2);\omega_1,\omega_2)\\ &= \chi^{(2)}_{\alpha_1\alpha_2\mu}(-(\omega_1+\omega_2);\omega_1,\omega_2)\\ &= \chi^{(2)}_{\alpha_1\mu\alpha_2}(-(\omega_1+\omega_2);\omega_1,\omega_2)\end{aligned} \tag{2.28}$$

Although we have limited ourselves here to the second-order susceptibility, the aforementioned properties can be generalized for the ith-order susceptibility.

Finally, the susceptibility tensors will also be subject to restrictions imposed by the spatial symmetry of the material they are describing. The underpinning principle is a postulate known as Neumann's principle. It states that the symmetry elements of any physical property of a material must include the symmetry elements of the point group of the material system. This means that the components of the susceptibility tensor must remain invariant under any coordinate transformation corresponding to a symmetry operation of the material's point group. As a consequence of this principle, some of the tensor components may vanish or be related to each other, thereby reducing the number of independent components. Any coordinate transformation corresponding to a point group symmetry element can be represented by a 3 × 3 transformation matrix $\mathbf{R}$ [2]. The transformation law for $\chi^{(i)}(-\omega_\sigma;\omega_1,\ldots,\omega_i)$ is

$$\begin{aligned}&\chi^{(i)}_{\mu\alpha_1\cdots\alpha_i}{}'(-\omega_\sigma;\omega_1,\ldots,\omega_i) =\\ &\qquad\sum_{u,a_1,\ldots,a_i} R_{\mu u}R_{\alpha_1 a_1}\cdots R_{\alpha_i a_i}\chi^{(i)}_{u\cdots a_i}(-\omega_\sigma;\omega_1,\ldots,\omega_i)\end{aligned} \tag{2.29}$$

If the transformation represented by the matrix $\mathbf{R}$ is a symmetry operation of the material, the susceptibility remains invariant, i.e.

$$\chi^{(i)}_{\mu\alpha_1\cdots\alpha_i}{}'(-\omega_\sigma;\omega_1,\ldots,\omega_i) = \chi^{(i)}_{\mu\alpha_1\cdots\alpha_i}(-\omega_\sigma;\omega_1,\ldots,\omega_i) \tag{2.30}$$

Let us consider the example of centrosymmetric material, i.e. a material having inversion symmetry. The inversion operation is represented by the matrix elements $R_{ij} = -\delta_{ij}$ (with δ_{ij} the Kronecker delta). Thus, we find

$$\chi^{(i)}_{\mu\alpha_1\cdots\alpha_i}(-\omega_\sigma;\omega_1,\ldots,\omega_i) = (-1)^{i+1}\chi^{(i)}_{\mu\alpha_1\cdots\alpha_i}(-\omega_\sigma;\omega_1,\ldots,\omega_i) \tag{2.31}$$

As a consequence, $\chi^{(2)}$ must be zero for centrosymmetric materials. So in the electric-dipole approximation, no second-order effects are allowed in media with inversion symmetry. There are 32 crystallographic point groups or crystal classes.

Crystal system	Crystal class	Non-vanishing tensor components	Examples
Monoclinic	m	xxx, xyy, xzz, xzx, xxz, yyz, yzy, yxy, yyx, zxx, zyy, zzz, zzx, zxz (m $\perp$ y)	DAST(a)
Orthorhombic	mm2	xzx, xxz, yyz, yzy, zxx, zyy, zzz	BNA(b)
Tetragonal	4mm	$xzx = yzy$, $xxz = yyz$, $zxx = zyy$, zzz	$BaTiO_3$ (BTO)
Trigonal	3m	$xzx = yzy$, $xxz = yyz$, $zxx = zyy$, zzz, $yyy = -yxx = -xxy = -xyx$ (m $\perp$ x)	$LiNbO_3$, β-BaB_2O_4 (BBO)
Hexagonal	6mm	$xzx = yzy$, $xxz = yyz$, $zxx = zyy$, zzz	ZnO, AlN, ZnS
Cubic	m3m	All components vanish	Si
	$\bar{4}3$m	$xyz = xzy = yzx = yxz = zxy = zyx$	GaAs, InP, ZnS

Table 2.2: Non-vanishing $\chi^{(2)}$ tensor components for several crystal classes. The tensor components are denoted by their cartesian indices. Examples of materials are included for each of the crystal classes. Note that many materials are known to exist in multiple crystalline phases depending on the temperature and growth conditions, amongst others. The examples given here are how these materials are commonly encountered at room temperature. Sources: [3, 7–11].

(a) DAST stands for 4-N, N-dimethylamino-4'-N'-methyl-stilbazolium tosylate [11].

(b) BNA stands for *N*-benzyl-2-methyl-4-nitroaniline [12].

Among the 32 crystal classes, 21 are non-centrosymmetric. Of these 21 crystal classes, 10 are polar. Crystals belonging to a polar crystal class have a spontaneous polarization $\mathbf{P}^{(0)}$. Table 2.2 gives an overview of the non-vanishing $\chi^{(2)}$ tensor components and their relationships for a few of the 21 non-centrosymmetric crystal classes. A complete overview for all crystal classes can be found in [2, 3].

A material system with in-plane isotropy (also called transverse isotropy), corresponding to symmetry group ∞m, will have the same non-vanishing $\chi^{(2)}$ tensor components as materials with 6mm symmetry [4, 6]. Most thin films with a non-zero $\chi^{(2)}$ deposited by non-epitaxial chemical and physical vapor deposition techniques will display ∞m symmetry. In this case, the non-vanishing $\chi^{(2)}$ tensor components can also be denoted as $\chi^{(2)}_{\perp\perp\perp}$, $\chi^{(2)}_{\perp\|\|}$, $\chi^{(2)}_{\|\perp\|}$, and $\chi^{(2)}_{\|\|\perp}$ where $\perp$ corresponds to the normal (z) direction and $\|$ to the equivalent (x and y) directions in the plane.

2.3 d tensor

An alternative notation is sometimes used to describe $\chi^{(2)}$ processes (often used in literature when describing second-harmonic generation). A d tensor is introduced which relates to $\chi^{(2)}$ as

$$d_{ijk} = \frac{1}{2}\chi^{(2)}_{ijk} \tag{2.32}$$

where the frequency arguments are suppressed for simplicity.

For second-harmonic generation or whenever Kleinman's symmetry is valid, d_{ijk} is symmetric in its last two indices. Therefore, the notation can be simplified by introducing a contracted matrix d_{il} according to the rules

$$\begin{aligned} jk &\to l \\ 11 &\to 1 \\ 22 &\to 2 \\ 33 &\to 3 \\ 23, 32 &\to 4 \\ 13, 13 &\to 5 \\ 12, 21 &\to 6 \end{aligned} \tag{2.33}$$

For example, $d_{111} \equiv d_{11}$ and $d_{123} = d_{132} \equiv d_{14}$. If Kleinman's symmetry is valid, the number of independent matrix elements reduces even further, e.g. $d_{14} \equiv d_{123} = d_{213} \equiv d_{25}$.

2.4 Pockels tensor

The Pockels effect can be described in terms of a second-order nonlinear polarization and the corresponding susceptibility tensor. But because of historical reasons, a different mathematical formalism is traditionally used to describe the Pockels effect. In this section we will make the link between both formalisms.

Consider a monochromatic wave with frequency ω and complex amplitude $\mathbf{E}_\omega(\mathbf{r})$ (see equation 2.18 for the definition of $\mathbf{E}_\omega(\mathbf{r})$) propagating through a material. The linear polarization is given by

$$\mathbf{P}^{(1)}_\omega(\mathbf{r}) = \epsilon_0 \chi^{(1)}(-\omega;\omega)|\mathbf{E}_\omega(\mathbf{r}) \tag{2.34}$$

Consequently, $\mathbf{D}_\omega(\mathbf{r})$ and $\mathbf{E}_\omega(\mathbf{r})$ are related as

$$\begin{aligned} \mathbf{D}_\omega(\mathbf{r}) &= \epsilon_0 \mathbf{E}_\omega(\mathbf{r}) + \epsilon_0 \chi^{(1)}(-\omega;\omega)|\mathbf{E}_\omega(\mathbf{r}) \\ &= \epsilon_0 \epsilon(\omega)|\mathbf{E}_\omega(\mathbf{r}) \end{aligned} \tag{2.35}$$

where $\epsilon(\omega) = I + \chi^{(1)}(-\omega;\omega)$ is the dielectric tensor. In a lossless medium, $\chi^{(1)}(-\omega;\omega)$ and $\epsilon(\omega)$ are symmetric matrices. This means that a coordinate system exists in which the matrices are diagonal with real eigenvalues. The axes of this coordinate system are called the principal (dielectric) axes. In this principal coordinate system, ϵ is given by

$$\begin{pmatrix} n_x^2 & 0 & 0 \\ 0 & n_y^2 & 0 \\ 0 & 0 & n_z^2 \end{pmatrix} \tag{2.36}$$

The impermeability tensor η is defined as the inverse of ϵ: $\eta = \epsilon^{-1}$. Now, the Pockels effect is traditionally described as a change in the impermeability which is proportional to the applied DC electric field $\mathbf{E}_0$

$$\eta_{ij} = \eta_{ij}^{(0)} + \sum_k r_{ijk} E_{0,k} \tag{2.37}$$

where $\eta^{(0)}$ is the impermeability tensor when no field is applied and r is the Pockels tensor.

The Pockels effect can also be described in the susceptibility formalism. Consider again a medium (with a non-zero second-order susceptibility) through which a monochromatic wave with frequency ω and complex amplitude $\mathbf{E}_\omega(\mathbf{r})$ is propagating. A DC electric field $\mathbf{E}_0(\mathbf{r})$ is applied to this medium. In this case, the total polarization at frequency ω is

$$\begin{aligned} \mathbf{P}_\omega(\mathbf{r}) &= \mathbf{P}_\omega^{(1)}(\mathbf{r}) + \mathbf{P}_\omega^{(2)}(\mathbf{r}) \\ &= \epsilon_0 \chi^{(1)}(-\omega;\omega)|\mathbf{E}_\omega(\mathbf{r}) + \epsilon_0 2\chi^{(2)}(-\omega;\omega,0)|\mathbf{E}_\omega(\mathbf{r})\mathbf{E}_0(\mathbf{r}) \end{aligned} \tag{2.38}$$

Consequently, the components of the dielectric tensor are given by

$$\epsilon_{ij} = \delta_{ij} + \chi_{ij}^{(1)}(-\omega;\omega) + 2\sum_k \chi_{ijk}^{(2)}(-\omega;\omega,0) E_{0,k} \tag{2.39}$$

Consider the dielectric tensor in the principal axes (established for $\mathbf{E}_0 = 0$). In the principal axes $\chi_{ij}^{(1)}(-\omega;\omega)$ is diagonal. The last term in expression 2.39 will give rise to small non-zero off-diagonal components in ϵ. Since these off-diagonal components are small compared to the diagonal components, the diagonal components of the impermeability tensor can be approximated as [7]

$$\eta_{ii} \approx \frac{1}{\epsilon_{ii}} \tag{2.40}$$

and the off-diagonal components as

$$\eta_{ij} \approx -\frac{\epsilon_{ij}}{\epsilon_{ii}\epsilon_{jj}} \quad (i \neq j) \tag{2.41}$$

Expressions 2.40 and 2.41 can be established by calculating $\epsilon^{-1} = \frac{adj(\epsilon)}{det(\epsilon)}$, where $adj(\epsilon)$ is the adjugate of ϵ and $det(\epsilon)$ the determinant. Substituting expression 2.39 in 2.40 and 2.41, we finally get

$$\eta_{ii} \approx \frac{1}{n_i^2} - \frac{2\sum_k \chi^{(2)}_{iik}(-\omega;\omega,0)E_{0,k}}{n_i^4} \tag{2.42}$$

$$\eta_{ij} \approx -\frac{2\sum_k \chi^{(2)}_{ijk}(-\omega;\omega,0)E_{0,k}}{n_i^2 n_j^2} \tag{2.43}$$

where $n_i = \sqrt{1+\chi^{(1)}_{ii}(-\omega;\omega)}$ are the principal indices of refraction.

If we compare equation 2.37 with equations 2.42 and 2.43, we find the following relationship between the Pockels tensor and the second-order susceptibility

$$r_{ijk} \approx -\frac{2\chi^{(2)}_{ijk}(-\omega;\omega,0)}{n_i^2 n_j^2} \tag{2.44}$$

Provided that the medium is lossless, the Pockels coefficients r_{ijk} are invariant for the permutation of the indices i and j. Therefore, a contracted notation is often used whereby the indices i and j are replaced by one index running from 1 to 6 (according to the scheme shown in 2.33). For example, $r_{231} = r_{321} \equiv r_{41}$.

The Pockels tensor formalism is not only used for DC applied electric fields, but also for AC electric fields with frequency Ω, where Ω is small compared to the optical field frequency ω. The values of the Pockels coefficients will depend both on Ω and ω, which can be indicated notationally as $r_{ijk}(\omega,\Omega)$.

2.5 Electronic and ionic contributions

As matter consists of charged particles, these particles will tend to move under influence of electromagnetic fields. The nature of this interaction at the microscopic level will determine the macroscopic electromagnetic properties of the medium, such as the susceptibility. In solid media, two types of particle movements are generally considered: the motion of the electrons, and the ionic movements or lattice vibrations [13]. In second-harmonic, sum- and difference-frequency generation experiments, the frequencies of the electromagnetic waves involved in the interaction are typically lying in the near-infrared and/or visible part of the spectrum. At these high optical frequencies, it is the motion of the electrons that is most significant, as the heavy ions have much greater inertia. But, for the Pockels effect, a (quasi-)static electric field (typical frequencies below 100 GHz, so very small compared to optical frequencies) is involved next to the optical field. Therefore, the ionic movements will also play a role. This will be reflected in the frequency dependency of the second-order susceptibility, or equivalently, the

Pockels tensor. In literature, the susceptibility is sometimes used to refer only to the electronic contributions, while the Pockels tensor will contain both electronic and ionic contributions.

Figure 2.1 schematically illustrates how $\epsilon(\Omega)$ and $r(\omega, \Omega)$ vary with frequency Ω for a solid dielectric medium. The susceptibility at low frequencies contains three different contributions: a contribution from acoustic lattice vibrations (acoustic phonons), from optical lattice vibrations (optical phonons), and from electron movements. For the Pockels coefficients, this can be expressed as

$$r^T = r^a + r^o + r^e = r^a + r^S \tag{2.45}$$

where r^T is the Pockels coefficient for low frequencies or the unclamped Pockels coefficient (also described as constant stress condition). The name ”unclamped” refers to the fact that the material needs to be free to expand and contract. The coefficients r^a, r^o, and r^e correspond to the contributions from acoustic phonons, optical phonons, and electrons, respectively. The coefficients r^o and r^e can be grouped in r^S, the clamped Pockels coefficient (also described as constant strain condition). The acoustic phonon contribution can be expressed in terms of piezoelectric and elasto-optic coefficients. The different contributions can have opposite signs, e.g., it is possible that $r^T < r^S$. Acoustic phonon resonances for bulk materials usually occur in the 10^4 Hz to 10^6 Hz range. The mechanical resonance frequencies are determined both by the material and the sample geometry. Optical phonon resonances typically lie in the 10^{12} Hz to 10^{13} Hz range (infrared region of spectrum) and electronic resonances in the 10^{15} Hz to 10^{16} Hz range (visible and ultraviolet region of spectrum).

2.6 Microscopic model of the second-order susceptibility and Miller’s rule

The Drude-Lorentz model is a classical model to describe the microscopic origin of the linear susceptibility. In this section, we will briefly show how the model can be extended to explain the origin of the second-order susceptibility and how this relates to Miller’s rule. We follow the approach outlined in [3].

Consider a light wave propagating through a dielectric medium, represented by an electric field $E(t)$ (we neglect the vector nature of the field). The movement of a bound electron can be described by the following differential equation

$$m\frac{d^2x}{dt^2} = -2m\gamma\frac{dx}{dt} + f(x) - eE(t) \tag{2.46}$$

where $x(t)$ is the displacement of the electron from its equilibrium position and m the mass of the electron. The term $-2m\gamma\frac{dx}{dt}$ represents a damping force, $f(x)$ is

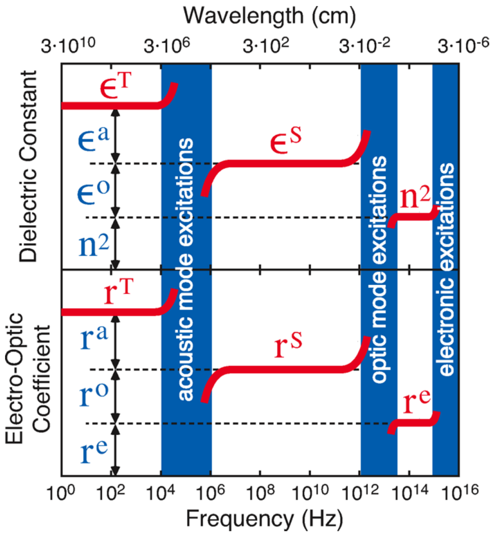

Figure 2.1: General behavior of $\epsilon(\Omega)$ and $r(\omega, \Omega)$ as a function of frequency Ω. Although the figure shows $r^T > r^S > r^e$, this is not necessarily true for all materials. At optical frequencies the susceptibility formalism is typically used, rather than the Pockels tensor formalism shown here. Figure reproduced from [11].

the restoring force, and $-eE(t)$ is the force exerted on the electron by the electric field ($-e$ is the charge of the electron). $f(x)$ can be written as a Taylor series expansion in x. In the traditional Drude-Lorentz model, only the linear term in x is taken into account, but here we will retain both the linear and quadratic term

$$f(x) = -m\omega_0^2 x - max^2 \tag{2.47}$$

where ω_0 is the resonance frequency of the atom. This corresponds to a potential energy function of the form

$$U(x) = -\int f(x)\,dx = \frac{1}{2}m\omega_0^2 x^2 + \frac{1}{3}max^3 \tag{2.48}$$

where the term in x^2 corresponds to the usual harmonic potential and the term in x^3 is an anharmonic correction term. The addition of these correction terms allows us to better approximate the actual potential well the electron is sitting in (see figure 2.2). Here, we have made the assumption that the medium is non-centrosymmetric, as for a centrosymmetric medium we should have $U(x) = U(-x)$. Therefore, only even powers of x are allowed for centrosymmetric media.

Assume an electric field given by

$$E(t) = \frac{E_{\omega_1} e^{j\omega_1 t} + E_{\omega_1}^* e^{-j\omega_1 t}}{2} + \frac{E_{\omega_2} e^{j\omega_2 t} + E_{\omega_2}^* e^{-j\omega_2 t}}{2} \tag{2.49}$$

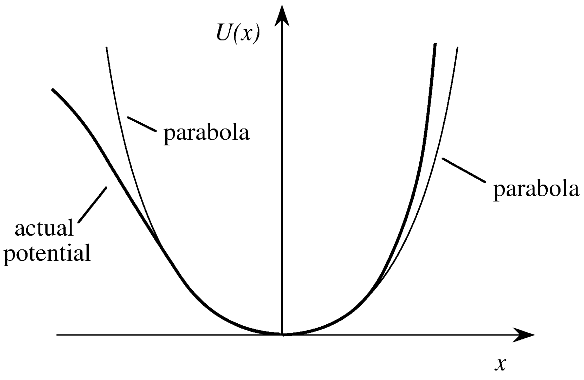

Figure 2.2: Potential well for a non-centrosymmetric medium and the parabolic approximation. Figure reproduced from [3].

If the applied field is sufficiently weak, the nonlinear term ax^2 will be much smaller than the linear term $\omega_0^2 x$ for each displacement x induced by the electric field. In that case, equation 2.46 can be solved by means of a perturbation approach. The details of the calculation can be found in [3]; here we will only present the outcome.

The steady-state solution $x(t)$ will contain terms oscillating with frequencies $\omega_1, \omega_2, 2\omega_1, \omega_1+\omega_2$, etc. This solution can be connected to the macroscopic properties of the medium by calculating the electric dipole moment per unit volume, i.e. the polarization

$$P(t) = -Nex(t) \tag{2.50}$$

where N is the number of electrons per unit volume. By comparing expression 2.50 with the relationships

$$\begin{aligned} P^{(1)}_{\omega_1} &= \epsilon_0 \chi^{(1)}(-\omega_1;\omega_1) E_{\omega_1} \\ P^{(2)}_{\omega_1+\omega_2} &= \epsilon_0 \chi^{(2)}(-(\omega_1+\omega_2);\omega_1,\omega_2) E_{\omega_1} E_{\omega_2} \end{aligned} \tag{2.51}$$

we can find

$$\begin{aligned} \chi^{(1)}(-\omega_1;\omega_1) &= \frac{Ne^2}{m\epsilon_0}\frac{1}{D(\omega_1)} \\ \chi^{(2)}(-(\omega_1+\omega_2);\omega_1,\omega_2) &= \frac{Ne^3 a}{m^2\epsilon_0}\frac{1}{D(\omega_1+\omega_2)D(\omega_1)D(\omega_2)} \end{aligned} \tag{2.52}$$

with

$$D(\omega_l) = \omega_0^2 - \omega_l^2 + j2\gamma\omega_l \tag{2.53}$$

Material	Δ_{ijk} (pm/V)
BNA	$\Delta_{333} = 28.2$
GaAs	$\Delta_{321} = 0.172$
LiNbO$_3$	$\Delta_{333} = 1.02$
Quartz	$\Delta_{111} = 0.372$

Table 2.3: Δ_{ijk} coefficients for a selection of materials, calculated from the d coefficients and refractive index data (for $\lambda_\omega = 1064\,\text{nm}$) presented in table 2.5 and 2.6.

We see the expected resonance behavior when one of the frequencies involved in the interaction approaches ω_0. The magnitude of $\chi^{(2)}$ is proportional to a, or in other words, it depends on the asymmetry of the potential well. Note that this derivation only accounts for the electron movements, not the lattice vibrations which can play an important role in the Pockels effect.

In 1964, R. C. Miller published a paper in which he reported that the quantity

$$\Delta_{ijk} = \frac{\chi^{(2)}_{ijk}(-(\omega_1+\omega_2);\omega_1,\omega_2)}{\chi^{(1)}_{ii}(-(\omega_1+\omega_2);\omega_1+\omega_2)\chi^{(1)}_{jj}(-\omega_1;\omega_1)\chi^{(1)}_{kk}(-\omega_2;\omega_2)} \tag{2.54}$$

is nearly constant ($\sim 0.5\,\text{pm/V}$) for a variety of inorganic crystals (GaAs, quartz, BTO, etc.) [14]. This is known as Miller's rule. If we calculate Δ using the expressions in 2.52, we get

$$\Delta = \frac{ma\epsilon_0^2}{N^2e^3} \tag{2.55}$$

The parameters m, e and ϵ_0 are constants and N is nearly constant for all condensed matter ($\sim 10^{22}\,\text{cm}^{-3}$) [3]. However, a is not necessarily the same for all non-centrosymmetric materials. Table 2.3 shows the calculated Δ_{ijk} coefficients for a selection of materials. Although Δ might be nearly constant for a limited selection of inorganic crystals, table 2.3 shows that Δ can fluctuate quite strongly when including other materials. We see, for example, that Δ is more than two orders of magnitude larger for the organic crystal BNA than it is for GaAs. Therefore, Miller's rule might not be very suitable to estimate a material's second-order susceptibility solely from the knowledge of the linear susceptibility. Yet, if the second-order susceptibility of a material is known for a certain set of frequencies, Miller's rule might be used to estimate the second-order susceptibility for a different set of frequencies (provided that the linear susceptibility is known for these frequencies), since expression 2.55 is constant for a certain material.

2.7 Some materials

In the previous sections, the general properties of the second-order susceptibility and the relation between $\chi^{(2)}$, d, and r have been covered. Here, some values

Material	ϵ^T	n^2	r^T (pm/V)	r^S (pm/V)	r^e (pm/V)
$LiNbO_3$	28	4.5	30	30	5.8
DAST	5.2	4.6	47	48	36

Table 2.4: Overview of the ionic and electronic contributions to ϵ and r for $LiNbO_3$ and DAST. Data reproduced from [11].

of the d and r tensor components for various materials are listed. Table 2.5 and 2.6 list the d values determined from second-harmonic generation experiments for several crystals, along with the bandgap and the refractive index. Table 2.7 and 2.8 show some values of the r tensor components (determined via electro-optic modulation experiments) and the dielectric constant ϵ (at low frequencies).

The linear and second-order nonlinear properties are shown for two organic crystals, BNA and DAST, two ferroelectric inorganic crystals, barium titanate (BTO) and lithium niobate ($LiNbO_3$), and some other inorganic crystals.

The ferroelectric materials are characterized by large Pockels coefficients compared to the non-ferroelectric inorganic crystals (especially BTO, with r coefficients on the order of $10^3\,\mathrm{pm/V}$). But, also the organic crystals have large Pockels coefficients, exceeding those of $LiNbO_3$. Moreover, the ferroelectric materials have large dielectric constants at low frequencies. A dielectric constant at low frequencies which is considerably larger than the dielectric constant at optical frequencies will cause bandwidth limitations in traveling wave modulators due to the velocity mismatch [15]. In lumped modulators, a larger dielectric constant leads to a larger capacitance, which also limits the bandwidth and increases the energy consumption required for switching. The large difference in ϵ at low and optical frequencies for the ferroelectric materials is due to the ionic contributions. This large contribution of the ionic movements is also visible for the second-order susceptibility. For example, $LiNbO_3$ has a $\chi^{(2)}_{zzz}(-2\omega;\omega,\omega) = 54\,\mathrm{pm/V}$ (for $\lambda_\omega = 1064\,\mathrm{nm}$) and a $\chi^{(2)}_{zzz}(-\omega;\omega,0) \approx 400\,\mathrm{pm/V}$ (for $\lambda = 633\,\mathrm{nm}$) [7, 13, 16, 17]. The organic crystals, on the other hand, have large second-order susceptibilities both at low and optical frequencies. This is also illustrated in table 2.4, which compares the ionic and electronic contributions to the Pockels coefficients and dielectric constants for $LiNbO_3$ and DAST. The large ionic contributions for $LiNbO_3$ and BTO can be understood as being related to their ferroelectric nature, since the presence of mobile ionic charge allows for the switching of the spontaneous polarization [18]. Organic $\chi^{(2)}$ materials are usually based on π-conjugated molecules, with the associated delocalized electrons, with strong electron donor and acceptor groups at the ends of the π-conjugated structure [11] (see, e.g., figure 2.3). The electrons will feel a strongly asymmetric potential, giving rise to a large second-order nonlinearity.

The III-V semiconductors InP and GaAs have rather small Pockels coeffi-

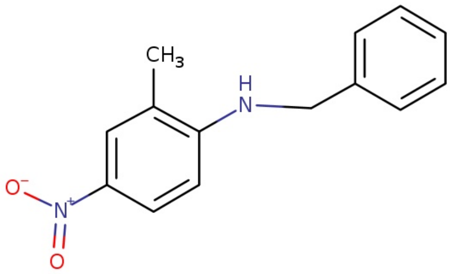

Figure 2.3: Chemical structure of a BNA molecule. Figure reproduced from [19].

cients but large d coefficients. However, for most of the reported d coefficients, the second-harmonic frequency is larger than the frequency corresponding to the bandgap, which might lead to resonance enhancement. Yet, GaAs also exhibits large d coefficients for $\lambda_\omega = 10.6\,\mu\mathrm{m}$, though there is quite some discrepancy between the reported values.

AlN, ZnO, and ZnS are characterized by fairly small Pockels coefficients and moderately large d coefficients. Cubic ZnS, for instance, has a value $d_{36} = 24.6\,\mathrm{pm/V}$, compared to $d_{33} = 27.2\,\mathrm{pm/V}$ for $LiNbO_3$ and $d_{15} = 19.33\,\mathrm{pm/V}$ for BTO.

So far we have focused on bulk nonlinear crystals. To make photonic integrated circuits out of these materials, we need to somehow define waveguides, preferably with a high refractive index contrast. The definition of these waveguides typically requires the use of thin films of materials combined with advanced patterning techniques. Therefore, the integration of $\chi^{(2)}$ materials on a photonic chip is far from a trivial task. Over the past years, many materials and fabrication techniques have been explored for the integration of $\chi^{(2)}$ devices.

Recently, $LiNbO_3$-on-insulator wafers have become commercially available [29]. They consist of a sub-micrometer layer of monocrystalline $LiNbO_3$ on SiO_2 on top of a substrate of choice (silicon, $LiNbO_3$, fused silica, etc.). The $LiNbO_3$-on-insulator (LNOI) wafers are fabricated using the ion slicing technique [30], which is also used for the fabrication of SOI wafers. In this platform, high-index-contrast waveguides can be defined with considerably smaller optical mode sizes than in the traditional bulk $LiNbO_3$ platform. The availability of LNOI technology has lead to a surge of interest in $LiNbO_3$ based PICs [31–36].

Material	E_g (eV)	λ_ω (nm)	n	d (pm/V)	Ref.
AlN (6mm)	6.2	1064	$n_{o,\omega} = 1.431$ $n_{e,\omega} = 1.447$ $n_{o,2\omega} = 1.445$ $n_{e,2\omega} = 1.463$	$d_{33} = 7.4$ $d_{31} = 0.2$	[7, 9]
BBO (3m)	6.2	1064	$n_{o,\omega} = 1.6544$ $n_{e,\omega} = 1.5422$ $n_{o,2\omega} = 1.6743$ $n_{e,2\omega} = 1.5548$	$d_{22} = 2.2$ $d_{33} = 0.04$ $d_{31} = 0.04$ $d_{15} = 0.03$	[16, 20]
BNA (mm2)	$\lambda_c \sim 500\,\mathrm{nm}^{(a)}$	1064	$n_{X,\omega} = 1.558$ $n_{Y,\omega} = 1.717$ $n_{Z,\omega} = 1.798$ $n_{X,2\omega} = 1.621$ $n_{Y,2\omega} = 1.827$ $n_{Z,2\omega} = 2.081$	$d_{33} = 234 \pm 31$ $d_{32} = 15.6 \pm 0.9$ $d_{31} \sim 0$	[12]
		1550		$d_{33} \sim 80$	[21]
BTO (4mm)	3.1	1064.2	$n_\omega \sim 2.3$ $n_{2\omega} \sim 2.4$	$d_{15} = 19.33 \pm 2.0$ $d_{31} = 17.85 \pm 2.0$ $d_{33} = 7.79 \pm 1.17$	[16, 17]
DAST (m)	$\lambda_c \sim 700\,\mathrm{nm}^{(a)}$	1542	$n_{1,\omega} \sim 2.1$ $n_{2,\omega} \sim 1.6$ $n_{3,\omega} \sim 1.6$ $n_{1,2\omega} \sim 2.4$ $n_{2,2\omega} \sim 1.7$ $n_{3,2\omega} \sim 1.6$	$d_{11} = 290 \pm 15$ $d_{12} = 41 \pm 3$ $d_{26} = 39 \pm 2$	[11, 22]

Table 2.5: Overview of d values determined from second-harmonic generation experiments for several crystals. The crystal class is given for each material. Also the bandgap E_g, the fundamental wavelength λ_ω at which the experiment was performed, and the refractive index n are given (both at the fundamental and SH wavelength if available). n_o and n_e stand for the ordinary and extraordinary refractive index, respectively (for uniaxial crystals $n_x = n_y = n_o$ and $n_z = n_e$).

(a) For BNA and DAST the absorption edge determined from absorption/transmission spectra is given instead of E_g.

Material	E_g (eV)	λ_ω (nm)	n	d (pm/V)	Ref.
GaAs ($\bar{4}3$m)	1.4	1064	$n_\omega = 3.4785$ $n_{2\omega} = 4.1300$	$d_{36} = 170$	[16, 23]
		1533		$d_{36} = 119$	[23]
		10600	$n_\omega = 3.27$ $n_{2\omega} = 3.30$	$d_{36} = 368.7$	[7]
		10600		$d_{36} = 83$	[16]
InP ($\bar{4}3$m)	1.4	1058	$n_\omega = 3.44$ $n_{2\omega} = 4.24$	$d_{14} = 143.5$	[7, 9]
$LiNbO_3$ (3m)	4	1064	$n_{o,\omega} = 2.23$ $n_{e,\omega} = 2.16$ $n_{o,2\omega} = 2.33$ $n_{e,2\omega} = 2.23$	$d_{33} = -27.2 \pm 2.7$ $d_{31} = -4.35 \pm 0.44$ $d_{22} = 2.10 \pm 0.21$	[7, 16]
α-$SiO_2$$^{(a)}$ (32)	9	1064.2	$n \sim 1.5$	$d_{11} = 0.364 \pm 0.04$	[9, 17]
		1058.2		$d_{14} = 0.009$	[17]
ZnO (6mm)	3.4	1058.2	$n_\omega \sim 1.9$ $n_{2\omega} \sim 2.0$	$d_{33} = 7.0 \pm 0.2$ $d_{15} = 2.32 \pm 0.2$ $d_{31} = 2.1 \pm 0.2$	[17, 24]
ZnS (6mm)	3.9	1064.2	$n_\omega \sim 2.3$ $n_{2\omega} \sim 2.4$	$d_{33} = 15.72 \pm 1.9$ $d_{15} = 7.59 \pm 1.2$ $d_{31} = 8.65 \pm 1.7$	[9, 17]
ZnS ($\bar{4}3$m)	3.7	1058	$n_\omega = 2.289$ $n_{2\omega} = 2.40$	$d_{36} = 24.6 \pm 1.5$	[9, 17]

Table 2.6: Table 2.5 continued.
$^{(a)}$$\alpha$-quartz or α-SiO_2 is crystalline silicon dioxide.

Material	λ (nm)	r (pm/V)	ϵ (low frequency)	Ref.
AlN	633	$r_{33} = -0.59^{(a)}$	$\epsilon_{11} = 8.3$	[9, 25]
(6mm)		$r_{31} = 0.67^{(a)}$	$\epsilon_{33} = 8.9$	
BBO	633	$r^T_{22} = 2.7$	$\epsilon^T_{11} = 6.7$	[13]
(3m)			$\epsilon^T_{33} = 8.1$	
	632.8	$r^S_{22} = 2.1 \pm 0.1$		[16]
BNA	1550	$r_{33} = 43 \pm 5^{(b)}$	-	[26]
BTO	633	$r^T_{33} = 103$	$\epsilon^T_{11} = 3700$	[13]
(4mm)		$r^T_{13} = 14.5$	$\epsilon^T_{33} = 135$	
		$r^T_{42} = 1700$		
	632.8	$r^S_{33} = 28$		[16]
		$r^S_{13} = 8$		
	546.1	$r^S_{42} = 820$		[16]
DAST	1535	$r^T_{11} = 47 \pm 8$	$\epsilon^T_{11} = 5.2 \pm 0.4$	[11, 27]
(m)		$r^T_{21} = 21 \pm 4$	$\epsilon^T_{22} = 4.1 \pm 0.4$	
		$r^T_{13} = 5 \pm 1$	$\epsilon^T_{33} = 3.0 \pm 0.3$	
		$r^T_{33} < 0.1$		
		$r^T_{31} < 0.1$		
		$r^T_{23} < 0.1$		
GaAs	1060	$r^T_{41} = -1.17$	$\epsilon = 13.2$	[13]
($\bar{4}3m$)				
	1064.2	$r^S_{42} = -1.33$		[16]
InP	1060	$r^T_{41} = -1.32$	$\epsilon = 12.6$	[13]
($\bar{4}3m$)				

Table 2.7: Pockels coefficients measured at a wavelength λ for several crystals. Also the dielectric constants (measured at low frequencies) are shown.

$^{(a)}$These are the Pockels coefficients for a polycrystalline film. No data on single crystals was found.

$^{(b)}$This is the Pockels coefficient for an evaporated poled film. No data on single crystals was found.

Material	λ (nm)	r (pm/V)	ϵ (low frequency)	Ref.
LiNbO$_3$	633	$r_{13}^T = 10.0$	$\epsilon_{11}^T = 85$	[13]
(3m)		$r_{33}^T = 32.6$	$\epsilon_{33}^T = 29$	
		$r_{22}^T = 6.8$		
		$r_{51}^T = 32.6$		
	633	$r_{13}^S = 8.6$	$\epsilon_{11}^S = 43$	[17]
		$r_{33}^S = 30.8$	$\epsilon_{33}^S = 28$	
		$r_{22}^S = 3.4$		
		$r_{51}^S = 28$		
α-SiO$_2$	633	$r_{11}^T = -0.5$	$\epsilon_{11}^T = 4$	[13]
(32)		$r_{41}^T = 0.2$	$\epsilon_{33}^T = 4$	
ZnO	633	$r_{33}^S = 2.6$	$\epsilon \approx 8.15$	[17]
(6mm)		$r_{13}^S = -1.4$		
ZnS	633	$r_{33}^S = 1.8$	$\epsilon_{11}^T = \epsilon_{33}^T = 8.7$	[17]
(6mm)		$r_{13}^S = 0.9$	$\epsilon_{11}^S = 8.7$	
ZnS	650	$r_{41}^T = 2.1$	$\epsilon^T = 16$	[28]
($\bar{4}$3m)			$\epsilon^S = 12.5$	
	633	$r_{41}^S = 1.6$		[17]

Table 2.8: Table 2.7 continued.

Epitaxial growth of BTO on silicon for high-speed integrated electro-optic modulators has been developed by several research groups, with in-device r_{42} coefficients up to $(923 \pm 215)\,\mathrm{pm/V}$ (at $\lambda = 1.55\,\mu\mathrm{m}$) [37–40].

The ferroelectric material lead zirconate titanate (PZT) has been combined with SiN waveguide circuits for high-speed modulation [41]. The fabrication process involves the spin coating and annealing of an intermediate seed layer (on top of the planarized SiN waveguides), followed by the spin coating and annealing (at $620\,^{\circ}\mathrm{C}$) of the PZT film (a sol-gel method). This leads to highly textured polycrystalline films [42]. The PZT films in the modulators are poled prior to device operation. In-device r_{eff} coefficients of the PZT layer up to $70\,\mathrm{pm/V}$ have been demonstrated (for wavelengths around $1.31\,\mu\mathrm{m}$ and $1.55\,\mu\mathrm{m}$).

Organic second-order nonlinear molecules have been used in silicon-organic and plasmonic-organic hybrid modulators [43]. The molecules are spin coated on silicon slot or plasmonic slot waveguides. The organic material fills up the slot where the optical mode resides. However, after spin coating the material is amorphous, therefore showing no macroscopic $\chi^{(2)}$ effects. A poling procedure is required to align the molecules. In-device r_{33} coefficients of $390\,\mathrm{pm/V}$ (at $\lambda = 1.55\,\mu\mathrm{m}$) have been reported for the organic molecule JRD1 [44].

Also organic crystals have been used in integrated modulators. Exploiting capillary flow, silicon slot waveguides have been filled with molten BNA, both for horizontal [45] and vertical slot waveguides [46]. To crystallize the material, the samples are slowly cooled down to room temperature utilizing a non-uniform temperature profile to prevent multiple nucleation. In the horizontal slot waveguide design, the crystal orientation did not allow to use the largest tensor component r_{33} of BNA. Instead, the r_{42} component was used and a value of $\sim 3\,\mathrm{pm/V}$ was measured (at $\lambda = 1.55\,\mu\mathrm{m}$). Due to the large capacitance of the devices, the speed was limited to modulation frequencies below $1\,\mathrm{kHz}$. Waveguide losses of $(10.0 \pm 2.4)\,\mathrm{dB/cm}$ were reported. For the vertical slot waveguide design, high-speed modulation at $12.5\,\mathrm{Gbit/s}$ was demonstrated and an in-device r_{33} coefficient of $\sim 10\,\mathrm{pm/V}$ estimated (at $\lambda = 1.55\,\mu\mathrm{m}$). However, the losses are rather high with an estimated $16\,\mathrm{dB}$ over a length of $1.5\,\mathrm{mm}$. This is possibly related to the silicon waveguide sidewall roughness and incomplete filling of the slots.

A near-infrared optical parametric oscillator has been demonstrated based on GaAs/AlGaAs waveguides grown by molecular beam epitaxy (MBE) on GaAs substrates [47]. Also other III-V semiconductor platforms are being developed which could be interesting for $\chi^{(2)}$ applications, like AlGaAs-on-insulator [48], AlGaAs-on-sapphire [49], and GaN-on-sapphire [50]. GaN has a bandgap of $3.4\,\mathrm{eV}$ and could therefore be interesting for applications in the visible wavelength region. In bulk GaN, the largest d tensor component is $d_{33} = (-3.8 \pm 0.2)\,\mathrm{pm/V}$ (at a fundamental wavelength of $1.064\,\mu\mathrm{m}$) [51].

Second-harmonic generation, electro-optic modulation, and parametric down-conversion have been demonstrated in textured polycrystalline AlN waveguides [52–55]. The AlN films are sputtered on oxidized silicon wafers. The crystallites or grains have a preferential orientation, namely with their c axis normal to the film plane. This allows the use of AlN's largest nonlinear tensor component d_{33}. d values of $(2.4 \pm 1.5)\,\mathrm{pm/V}$ are reported (at a fundamental wavelength of $1.55\,\mu\mathrm{m}$) [54].

As already discussed in section 1.2, $\chi^{(2)}$ effects have been observed in crystalline silicon, amorphous SiN and silica, despite their centrosymmetric nature. Some $\chi^{(2)}$ values are given below so they can be compared with traditional $\chi^{(2)}$ materials (see also table 2.9).

In strained silicon waveguides, the Pockels effect has been demonstrated in the high-speed regime, with a clear distinction between free carrier effects and the Pockels effect [56]. An effective value of $(-1.8 \pm 0.2)\,\mathrm{pm/V}$ for the $\chi^{(2)}_{xxy}$ component was reported (for $\lambda = 1550\,\mathrm{nm}$). It is claimed that values of $100\,\mathrm{pm/V}$ can be reached by increasing the stress in the overlay material and optimizing the strain gradient distribution [56]. In multimode strained silicon waveguides, second-harmonic generation has been shown with $\chi^{(2)}$ values of $(40 \pm 30)\,\mathrm{pm/V}$ at a fundamental wavelength of $2300\,\mathrm{nm}$ [57].

Silicon's strong $\chi^{(3)}$ nonlinearity combined with a static electric field can induce a $\chi^{(2)}$ nonlinearity. This can be used for electric field induced second-harmonic generation (EFISHG). Based on this method, effective second-order susceptibilities $\chi^{(2)}_{xxx,eff}$ of $(41.0 \pm 1.5)\,\mathrm{pm/V}$ (at $\lambda_\omega = 2.29\,\mu\mathrm{m}$) have been demonstrated in silicon ridge waveguides with p-i-n junctions [58].

In thermally poled silica, typical $\chi^{(2)}_{zzz}$ values (with z direction along poling field) of $1\,\mathrm{pm/V}$ are measured (at $\lambda_\omega = 1.06\,\mu\mathrm{m}$) [59, 60].

From second-harmonic generation experiments in ring resonators, an effective $\chi^{(2)}$ value between $0.003\,\mathrm{pm/V}$ and $0.04\,\mathrm{pm/V}$ (at $\lambda_\omega = 1.55\,\mu\mathrm{m}$) has been estimated for LPCVD SiN [61]. In PECVD SiN films, second-harmonic generation experiments indicate $\chi^{(2)}_{zzz}$ values (with z normal to the film plane) up to $5\,\mathrm{pm/V}$ (at $\lambda_\omega = 1064\,\mathrm{nm}$) [62]. In sputtered SiN films, $\chi^{(2)}_{xxx}$ values (with x along the film plane) up to $69\,\mathrm{pm/V}$ have been reported (via second-harmonic generation at a fundamental wavelength of $800\,\mathrm{nm}$) [63]. But, these films have an optical bandgap of only $2.5\,\mathrm{eV}$, therefore resonance enhancement plays a role. In addition, the deposited films are expected to have ∞m symmetry, consequently $\chi^{(2)}_{xxx}$ should be vanishing. In LPCVD SiN waveguides, Pockels coefficients of $(0.008\,31 \pm 0.005\,60)\,\mathrm{pm/V}$ have been reported (at $\lambda = 1.55\,\mu\mathrm{m}$) [64].

It has been shown that a $\chi^{(2)}$ nonlinearity can be induced in SiN waveguides by the coherent photogalvanic effect [65, 66]. Based on this approach, equivalent $\chi^{(2)}$ values up to $(3.7 \pm 0.2)\,\mathrm{pm/V}$ have been achieved in LPCVD SiN (at a fundamental wavelength of $1064\,\mathrm{nm}$).

Material	Effect	$\chi^{(2)}$	Ref.
Crystalline Si, strained	Pockels	$\chi^{(2)}_{xxy,eff} = (-1.8 \pm 0.2)\,\mathrm{pm/V}$ at $\lambda = 1.55\,\mu\mathrm{m}$	[56]
Crystalline Si, strained	SHG	$\chi^{(2)}_{eff} = (40 \pm 30)\,\mathrm{pm/V}$ at $\lambda_\omega = 2.3\,\mu\mathrm{m}$	[57]
Crystalline Si	EFISHG	$\chi^{(2)}_{xxx,eff} = (41.0 \pm 1.5)\,\mathrm{pm/V}$ at $\lambda_\omega = 2.29\,\mu\mathrm{m}$	[58]
Fused silica, poled	SHG	$\chi^{(2)}_{zzz} \sim 1\,\mathrm{pm/V}$ at $\lambda_\omega = 1.06\,\mu\mathrm{m}$	[59]
P-doped SiO_2, poled	SHG	$\chi^{(2)}_{zzz} \sim 0.58\,\mathrm{pm/V}$ at $\lambda_\omega = 1.06\,\mu\mathrm{m}$	[60]
LPCVD SiN	SHG	$\chi^{(2)}_{eff}$ between $0.003\,\mathrm{pm/V}$ and $0.04\,\mathrm{pm/V}$ at $\lambda_\omega = 1.55\,\mu\mathrm{m}$	[61]
LPCVD SiN	Pockels	$\chi^{(2)} \sim 0.07\,\mathrm{pm/V}$ at $\lambda = 1.55\,\mu\mathrm{m}$	[64]
LPCVD SiN, optically poled	SHG	$\chi^{(2)}_{eff} \sim 0.3\,\mathrm{pm/V}$ at $\lambda_\omega = 1.55\,\mu\mathrm{m}$	[65]
LPCVD SiN, optically poled	SHG	$\chi^{(2)}_{eff} = (3.7 \pm 0.2)\,\mathrm{pm/V}$ at $\lambda_\omega = 1.064\,\mu\mathrm{m}$	[66]
PECVD SiN	SHG	$\chi^{(2)}_{zzz} = 5\,\mathrm{pm/V}$ at $\lambda_\omega = 1.064\,\mu\mathrm{m}$	[62]
Sputtered SiN	SHG	$\chi^{(2)}_{xxx} = 68.79\,\mathrm{pm/V}$ at $\lambda_\omega = 0.8\,\mu\mathrm{m}$	[63]

Table 2.9: $\chi^{(2)}$ values reported for silicon, silicon nitride, and silica.

References

[1] J. D. Jackson. *Classical Electrodynamics*. John Wiley & Sons, Inc., 3rd edition, 1999.

[2] P. N. Butcher and D. Cotter. *The Elements of Nonlinear Optics*. Cambridge University Press, Cambridge, 1990.

[3] R. W. Boyd. *Nonlinear Optics*. Academic Press, 3rd edition, 2008.

[4] P.-F. Brevet. *Surface Second Harmonic Generation*. Presses polytechniques et universitaires romandes, Lausanne, 1997.

[5] Y. R. Shen. *The Principles of Nonlinear Optics*. Wiley, 1984.

[6] T. F. Heinz. *Second-Order Nonlinear Optical Effects at Surfaces and Interfaces*. In H.-E. Ponath and G. I. Stegeman, editors, Nonlinear Surface Electromagnetic Phenomena. Elsevier Science Publishers B.V., 1991.

[7] R. L. Sutherland. *Handbook of Nonlinear Optics*. Marcel Dekker, Inc., 2nd edition, 2003.

[8] L. Vivien and L. Pavesi, editors. *Handbook of Silicon Photonics*. CRC Press, 2013.

[9] C. Kasap and P. Capper, editors. *Springer Handbook of Electronic and Photonic Materials*. Springer, 2006.

[10] M. Fujiwara, K. Yanagi, M. Maruyama, M. Sugisaki, K. Kuroyanagi, H. Takahashi, S. Aoshima, Y. Tsuchiya, A. Gall, and H. Hashimoto. *Second order nonlinear optical properties of the single crystal of N-benzyl 2-methyl-4-nitroaniline: anomalous enhancement of the d_{333} component and its possible origin*. Japanese Journal of Applied Physics, 45(11):8676, 2006.

[11] M. Jazbinsek, L. Mutter, and P. Günter. *Photonic applications with the organic nonlinear optical crystal DAST*. IEEE Journal of Selected Topics in Quantum Electronics, 14(5):1298, 2008.

[12] M. Fujiwara, M. Maruyama, M. Sugisaki, H. Takahashi, S. I. Aoshima, R. J. Cogdell, and H. Hashimoto. *Determination of the d-tensor components of a single crystal of N-benzyl-2-methyl-4-nitroaniline*. Japanese Journal of Applied Physics, 46(4A):1528, 2007.

[13] F. Agulló-López, J. Manuel Cabrera, and F. Agulló-Rueda. *Electrooptics: Phenomena, Materials and Applications*. Academic Press, 1994.

[14] R. C. Miller. *Optical second harmonic generation in piezoelectric crystals*. Applied Physics Letters, 5(1):17, 1964.

[15] M. Lee, H. E. Katz, C. Erben, D. M. Gill, P. Gopalan, J. D. Heber, and D. J. McGee. *Broadband modulation of light by using an electro-optic polymer*. Science, 298(5597):1401, 2002.

[16] D. N. Nikogosyan. *Nonlinear Optical Crystals: A Complete Survey*. Springer, 2005.

[17] J. R. Pressley, editor. *Handbook of Lasers with Selected Data on Optical Technology*. The Chemical Rubber Co., 1971.

[18] R. Ulrich, L. Schaper, D. Nelms, and M. Leftwich. *Comparison of paraelectric and ferroelectric materials for aplications as dielectrics in thin film integrated capacitors*. The International Journal of Microcircuits and Electronic Packaging, 23(2):172, 2000.

[19] MolPort. *N-benzyl-2-methyl-4-nitroaniline*. `https://www.molport.com/shop/moleculelink/N-benzyl-2-methyl-4-nitroaniline/2116341?searchtype=text-search&searchkey=47IBPQKPOFENS1D22LRI07`. [Accessed 25 March 2019].

[20] I. Shoji, H. Nakamura, K. Ohdaira, T. Kondo, R. Ito, T. Okamoto, K. Tatsuki, and S. Kubota. *Absolute measurement of second-order nonlinear-optical coefficients of β-BaB_2O_4 for visible to ultraviolet second-harmonic wavelengths*. Journal of the Optical Society of America B, 16(4):620, 1999.

[21] T. Notake, M. Takeda, T. Hosobata, Y. Yamagata, and H. Minamide. *Ultraprecise processing and Maker fringe measurements of organic N-benzyl-2-methyl-4-nitroaniline crystal*. In International Conference on Infrared, Millimeter, and Terahertz Waves (IRMMW-THz), 2018.

[22] S. R. Marder, J. W. Perry, and C. P. Yakymyshyn. *Organic salts with large second-order optical nonlinearities*. Chemistry of Materials, 6(8):1137, 1994.

[23] I. Shoji, T. Kondo, A. Kitamoto, M. Shirane, and R. Ito. *Absolute scale of second-order nonlinear-optical coefficients*. Journal of the Optical Society of America B, 14(9):2268, 1997.

[24] M. C. Larciprete and M. Centini. *Second harmonic generation from ZnO films and nanostructures*. Applied Physics Reviews, 2(3):031302, 2015.

[25] P. Gräupner, J. C. Pommier, A. Cachard, and J. L. Coutaz. *Electro-optical effect in aluminum nitride waveguides*. Journal of Applied Physics, 71(9):4136, 1992.

[26] Z. Wang, W. Sun, A. Chen, I. Kosilkin, D. Bale, and L. R. Dalton. *Organic electro-optic thin films by simultaneous vacuum deposition and laser-assisted poling*. Optics Letters, 36(15):2853, 2011.

[27] F. Pan, G. Knöpfle, Ch. Bosshard, S. Follonier, R. Spreiter, M. S. Wong, and P. Günter. *Electro-optic properties of the organic salt 4-N,N-dimethylamino-4'-N'-methyl-stilbazolium tosylate*. Applied Physics Letters, 69(1):13, 1996.

[28] I. P. Kaminow and E. H. Turner. *Electrooptic light modulators*. Proceedings of the IEEE, 54(10):1374, 1966.

[29] Ltd. Jinan Jingzheng Electronics Co. *NanoLN*. `http://www.nanoln.com/`. [Accessed 26 March 2019].

[30] A. Boes, B. Corcoran, L. Chang, J. Bowers, and A. Mitchell. *Status and potential of lithium niobate on insulator (LNOI) for photonic integrated circuits*. Laser & Photonics Reviews, 12:1700256, 2018.

[31] L. Chang, Y. Li, N. Volet, L. Wang, J. Peters, and J. E. Bowers. *Thin film wavelength converters for photonic integrated circuits*. Optica, 3(5):531, 2016.

[32] L. Chang, M. H. P. Pfeiffer, N. Volet, M. Zervas, J. D. Peters, C. L. Manganelli, E. J. Stanton, Y. Li, T. J. Kippenberg, and J. E. Bowers. *Heterogeneous integration of lithium niobate and silicon nitride waveguides for wafer-scale photonic integrated circuits on silicon*. Optics Letters, 42(4):803, 2017.

[33] C. Wang, Z. Li, M.-H. Kim, X. Xiong, X.-F. Ren, G.-C. Guo, N. Yu, and M. Lončar. *Metasurface-assisted phase-matching-free second harmonic generation in lithium niobate waveguides*. Nature Communications, 8:2098, 2017.

[34] C. Wang, M. Zhang, X. Chen, M. Bertrand, A. Shams-Ansari, S. Chandrasekhar, P. Winzer, and M. Lončar. *Integrated lithium niobate electro-optic modulators operating at CMOS-compatible voltages*. Nature, 562:101, 2018.

[35] C. Wang, C. Langrock, A. Marandi, M. Jankowski, M. Zhang, B. Desiatov, M. M. Fejer, and M. Lončar. *Ultrahigh-efficiency wavelength conversion in nanophotonic periodically poled lithium niobate waveguides*. Optica, 5(11):1438, 2018.

[36] M. Zhang, B. Buscaino, C. Wang, A. Shams-Ansari, C. Reimer, R. Zhu, J. M. Kahn, and M. Lončar. *Broadband electro-optic frequency comb generation in a lithium niobate microring resonator*. Nature, 568:373, 2019.

[37] S. Abel, T. Stöferle, C. Marchiori, C. Rossel, M. D. Rossell, R. Erni, D. Caimi, M. Sousa, A. Chelnokov, B. J. Offrein, and J. Fompeyrine. *A strong electro-optically active lead-free ferroelectric integrated on silicon*. Nature Communications, 4:1671, 2013.

[38] C. Xiong, W. H. P. Pernice, J. H. Ngai, J. W. Reiner, D. Kumah, F. J. Walker, C. H. Ahn, and H. X. Tang. *Active silicon integrated nanophotonics: Ferroelectric* $BaTiO_3$ *devices*. Nano Letters, 14:1419, 2014.

[39] M.-H. M. Hsu, D. Van Thourhout, M. Pantouvaki, J. Meersschaut, T. Conard, O. Richard, H. Bender, P. Favia, M. Vila, R. Cid, J. Rubio-Zuazo, G. R. Castro, J. Van Campenhout, P. Absil, and C. Merckling. *Controlled orientation of molecular-beam-epitaxial* $BaTiO_3$ *on Si(001) using thickness engineering of* $BaTiO_3$ *and* $SrTiO_3$ *buffer layers*. Applied Physics Express, 10:065501, 2017.

[40] S. Abel, F. Eltes, J. E. Ortmann, A. Messner, P. Castera, T. Wagner, D. Urbonas, A. Rosa, A. M. Gutierrez, D. Tulli, P. Ma, B. Baeuerle, A. Josten, W. Heni, D. Caimi, L. Czornomaz, A. A. Demkov, J. Leuthold, P. Sanchis, and J. Fompeyrine. *Large Pockels effect in micro- and nanostructured barium titanate integrated on silicon*. Nature Materials, 18:42, 2019.

[41] K. Alexander, J. P. George, J. Verbist, K. Neyts, B. Kuyken, D. Van Thourhout, and J. Beeckman. *Nanophotonic Pockels modulators on a silicon nitride platform*. Nature Communications, 9:3444, 2018.

[42] J. P. George, P. F. Smet, J. Botterman, V. Bliznuk, W. Woestenborghs, D. Van Thourhout, K. Neyts, and J. Beeckman. *Lanthanide-assisted deposition of strongly electro-optic PZT thin films on silicon: toward integrated active nanophotonic devices*. ACS Applied Materials and Interfaces, 7:13350, 2015.

[43] C. Koos, J. Leuthold, W. Freude, M. Kohl, L. Dalton, W. Bogaerts, A. L. Giesecke, M. Lauermann, A. Melikyan, S. Koeber, S. Wolf, C. Weimann, S. Muehlbrandt, K. Koehnle, J. Pfeifle, W. Hartmann, Y. Kutuvantavida, S. Ummethala, R. Palmer, D. Korn, L. Alloatti, P. C. Schindler, D. L. Elder, T. Wahlbrink, and J. Bolten. *Silicon-organic hybrid (SOH) and plasmonic-organic hybrid (POH) integration*. Journal of Lightwave Technology, 34(2):256, 2016.

[44] C. Kieninger, Y. Kutuvantavida, D. L. Elder, S. Wolf, H. Zwickel, M. Blaicher, J. N. Kemal, M. Lauermann, S. Randel, W. Freude, L. R. Dalton, and C. Koos. *Ultra-high electro-optic activity demonstrated in a silicon-organic hybrid modulator*. Optica, 5(6):739, 2018.

[45] H. Figi, D. H. Bale, A. Szep, L. R. Dalton, and A. Chen. *Electro-optic modulation in horizontally slotted silicon/organic crystal hybrid devices*. Journal of the Optical Society of America B, 28(9):2291, 2011.

[46] D. Korn, M. Jazbinsek, R. Palmer, M. Baier, L. Alloatti, H. Yu, W. Bogaerts, G. Lepage, P. Verheyen, P. Absil, P. Guenter, C. Koos, W. Freude, and J. Leuthold. *Electro-optic organic crystal silicon high-speed modulator*. IEEE Photonics Journal, 6(2):2700109, 2014.

[47] M. Savanier, C. Ozanam, L. Lanco, X. Lafosse, A. Andronico, I. Favero, S. Ducci, and G. Leo. *Near-infrared optical parametric oscillator in a III-V semiconductor waveguide*. Applied Physics Letters, 103(26):261105, 2013.

[48] L. Ottaviano, M. Pu, E. Semenova, and K. Yvind. *Low-loss high-confinement waveguides and microring resonators in AlGaAs-on-insulator*. Optics Letters, 41(17):3996, 2016.

[49] Y. Zheng, M. Pu, H. K. Sahoo, E. Semenova, and K. Yvind. *High-quality-factor AlGaAs-on-sapphire microring resonators*. Journal of Lightwave Technology, 37(3):868, 2019.

[50] E. Stassen, M. Pu, E. Semenova, E. Zavarin, W. Lundin, and K. Yvind. *High-confinement gallium nitride-on-sapphire waveguides for integrated nonlinear photonics*. Optics letters, 44(5):1064, 2019.

[51] M. Abe, H. Sato, I. Shoji, J. Suda, M. Yoshimura, Y. Kitaoka, Y. Mori, and T. Kondo. *Accurate measurement of quadratic nonlinear-optical coefficients of gallium nitride*. Journal of the Optical Society of America B, 27(10):2026, 2010.

[52] C. Xiong, W. H. P. Pernice, X. Sun, C. Schuck, K. Y. Fong, and H. X. Tang. *Aluminum nitride as a new material for chip-scale optomechanics and nonlinear optics*. New Journal of Physics, 14(9):095014, 2012.

[53] C. Xiong, W. H. P. Pernice, and H. X. Tang. *Low-loss, silicon integrated, aluminum nitride photonic circuits and their use for electro-optic signal processing*. Nano Letters, 12(7):3562, 2012.

[54] W. H. P. Pernice, C. Xiong, C. Schuck, and H. X. Tang. *Second harmonic generation in phase matched aluminum nitride waveguides and micro-ring resonators*. Applied Physics Letters, 100(22):223501, 2012.

[55] X. Guo, C. Zou, C. Schuck, H. Jung, R. Cheng, and H. X. Tang. *Parametric down-conversion photon-pair source on a nanophotonic chip*. Light: Science and Applications, 6:e16249, 2017.

[56] M. Berciano, G. Marcaud, P. Damas, X. Le Roux, P. Crozat, C. Alonso Ramos, D. Pérez Galacho, D. Benedikovic, D. Marris-Morini, E. Cassan, and L. Vivien. *Fast linear electro-optic effect in a centrosymmetric semiconductor*. Communications Physics, 1:64, 2018.

[57] M. Cazzanelli, F. Bianco, E. Borga, G. Pucker, M. Ghulinyan, E. Degoli, E. Luppi, V. Véniard, S. Ossicini, D. Modotto, S. Wabnitz, R. Pierobon, and L. Pavesi. *Second-harmonic generation in silicon waveguides strained by silicon nitride.* Nature materials, 11:148, 2012.

[58] E. Timurdogan, C. V. Poulton, M. J. Byrd, and M. R. Watts. *Electric field-induced second-order nonlinear optical effects in silicon waveguides*. Nature Photonics, 11:200, 2017.

[59] R. A. Myers, N. Mukherjee, and S. R. J. Brueck. *Large second-order nonlinearity in poled fused silica*. Optics Letters, 16(22):1732, 1991.

[60] H. Y. Chen and H. Y. Lin. *Second-order optical nonlinearity in thermally poled phosphorus-doped silicon dioxide thin-film waveguides*. Electronics Letters, 45(11):551, 2009.

[61] J. S. Levy, M. A. Foster, A. L. Gaeta, and M. Lipson. *Harmonic generation in silicon nitride ring resonators.* Optics express, 19(12):11415, 2011.

[62] K. Koskinen, R. Czaplicki, A. Slablab, T. Ning, A. Hermans, B. Kuyken, V. Mittal, G. S. Murugan, T. Niemi, R. Baets, and M. Kauranen. *Enhancement of bulk second-harmonic generation from silicon nitride films by material composition*. Optics Letters, 42(23):5030, 2017.

[63] E. F. Pecora, A. Capretti, G. Miano, and L. Dal Negro. *Generation of second harmonic radiation from sub-stoichiometric silicon nitride thin films*. Applied Physics Letters, 102:141114, 2013.

[64] S. Miller, Y.-H. D. Lee, J. Cardenas, A. L. Gaeta, and M. Lipson. *Electro-optic effect in silicon nitride*. In Conference on Lasers and Electro-Optics (CLEO), page SF1G.4, 2015.

[65] A. Billat, D. Grassani, M. H. P. Pfeiffer, S. Kharitonov, T. J. Kippenberg, and C.-S. Brès. *Large second harmonic generation enhancement in Si_3N_4 waveguides by all-optically induced quasi-phase-matching*. Nature Communications, 8:1016, 2017.

[66] M. A. G. Porcel, J. Mak, C. Taballione, P. J. M. van der Slot, and K.-J. Boller. *Photo-induced second-order nonlinearity in stoichiometric silicon nitride waveguides*. Optics Express, 25(26):33143, 2017.

3

Second-harmonic generation in thin films

In this chapter, several theoretical models to describe second-harmonic generation in thin films are presented. These models have been used to quantify the second-order susceptibility $\chi^{(2)}$ of the materials treated in this doctoral thesis. The measurement methods and results are given in chapters 4 and 5.

Contents

3.1 Second-harmonic generation in the presence of an interface

In this section, second-harmonic generation in the geometry shown in figure 3.1 will be described. Medium 1 will be assumed linear and medium 2 nonlinear (i.e. having a non-zero $\chi^{(2)}$). Both media are optically isotropic. A monochromatic plane wave with frequency ω is incident on medium 2. In the second-harmonic generation process, waves at the double frequency 2ω will be created and these

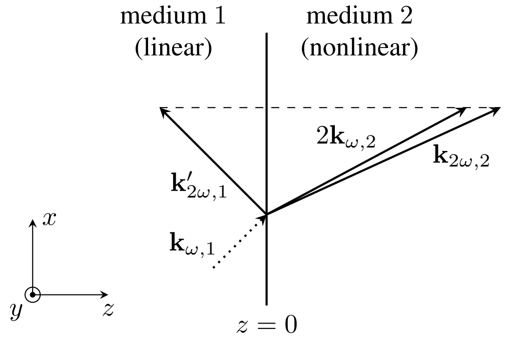

Figure 3.1: Second-harmonic generation in the presence of an interface.

will propagate through medium 1 and 2. The derivation presented here will provide insights in how second-harmonic generation happens in the presence of an interface, of which we will have multiple when dealing with thin films, and how the generated waves will propagate. More complex situations dealing with stacks of thin films and anisotropic materials will be discussed later in this chapter.

In our derivation we follow the approach outlined in [1].

Consider the wave equation 2.8 for a nonmagnetic, dielectric medium in the electric-dipole approximation

$$\nabla \times (\nabla \times \mathbf{E}) + \frac{1}{c^2}\frac{\partial^2 \mathbf{E}}{\partial t^2} = -\mu_0 \frac{\partial^2 \mathbf{P}}{\partial t^2} \tag{3.1}$$

For monochromatic fields, we can rewrite this as

$$\nabla \times (\nabla \times \mathbf{E}_{\omega_l}(\mathbf{r})) - \frac{\omega_l^2}{c^2}\mathbf{E}_{\omega_l}(\mathbf{r}) = \mu_0 \omega_l^2 \mathbf{P}_{\omega_l}(\mathbf{r}) \tag{3.2}$$

Here, we will only consider the first-order and second-order polarization

$$\mathbf{P}_{\omega_l}(\mathbf{r}) = \mathbf{P}^{(1)}_{\omega_l}(\mathbf{r}) + \mathbf{P}^{(2)}_{\omega_l}(\mathbf{r}) \tag{3.3}$$

Now, equation 3.2 can be rewritten as

$$\nabla \times (\nabla \times \mathbf{E}_{\omega_l}(\mathbf{r})) - \frac{\omega_l^2}{c^2}\epsilon(\omega_l)|\mathbf{E}_{\omega_l}(\mathbf{r}) = \frac{\omega_l^2}{\epsilon_0 c^2}\mathbf{P}^{(2)}_{\omega_l}(\mathbf{r}) \tag{3.4}$$

where $\epsilon(\omega_l) = I + \chi^{(1)}(-\omega_l;\omega_l)$ is the dielectric tensor (see also section 2.4).

Consider the second-harmonic generation process shown in figure 3.1. A monochromatic plane wave with frequency ω is incident on a nonlinear medium (medium 2). The coordinate system is chosen such that the wave vector of the incident wave lies in the plane defined by the x and z axes. Medium 1 is linear (in experimental situations medium 1 is usually air). In medium 2, a field at frequency

2ω will be generated. Media 1 and 2 are assumed to be optically isotropic and homogeneous. Since both media are optically isotropic, their dielectric tensors can be reduced to the constants ϵ_1 (for medium 1) and ϵ_2 (for medium 2). The nonlinear interaction is governed by the following equations (obtained by substituting expression 2.21 in equation 3.4, for both ω and 2ω)

$$\nabla \times (\nabla \times \mathbf{E}_{\omega}(\mathbf{r})) - \frac{\omega^2}{c^2}\epsilon(\omega)\mathbf{E}_{\omega}(\mathbf{r}) = \frac{\omega^2}{c^2}\chi^{(2)}(-\omega; 2\omega, -\omega)|\mathbf{E}_{2\omega}(\mathbf{r})\mathbf{E}_{-\omega}(\mathbf{r}) \tag{3.5}$$

$$\nabla \times (\nabla \times \mathbf{E}_{2\omega}(\mathbf{r})) - \frac{4\omega^2}{c^2}\epsilon(2\omega)\mathbf{E}_{2\omega}(\mathbf{r}) = \frac{2\omega^2}{c^2}\chi^{(2)}(-2\omega; \omega, \omega)|\mathbf{E}_{\omega}(\mathbf{r})\mathbf{E}_{\omega}(\mathbf{r}) \tag{3.6}$$

where the electric fields and material constants need to be evaluated in the medium of interest. In medium 1, the terms on the right-hand side will obviously vanish. Assuming that the conversion of the fundamental into the second-harmonic (SH) field is small, equation 3.5, evaluated in medium 2, can be approximated by the familiar equation

$$\nabla^2\mathbf{E}_{\omega,2}(\mathbf{r}) + \frac{\omega^2}{c^2}\epsilon_2(\omega)\mathbf{E}_{\omega,2}(\mathbf{r}) = 0 \tag{3.7}$$

which has the usual plane wave solutions. Consider the plane wave

$$\mathbf{E}_{\omega,2}(\mathbf{r}) = \mathbf{A}_{\omega,2}e^{-j\mathbf{k}_{\omega,2}\cdot\mathbf{r}} \tag{3.8}$$

in medium 2, which is related to the incident wave

$$\mathbf{E}_{\omega,1}(\mathbf{r}) = \mathbf{A}_{\omega,1}e^{-j\mathbf{k}_{\omega,1}\cdot\mathbf{r}} \tag{3.9}$$

by the Fresnel coefficients. The following relations hold for the wave vectors

$$k_{\omega,1,x} = k_{\omega,2,x} \tag{3.10}$$

$$\mathbf{k}_{\omega,1}\cdot\mathbf{k}_{\omega,1} = \frac{\omega^2}{c^2}\epsilon_1(\omega) \tag{3.11}$$

$$\mathbf{k}_{\omega,2}\cdot\mathbf{k}_{\omega,2} = \frac{\omega^2}{c^2}\epsilon_2(\omega) \tag{3.12}$$

Equation 3.6, evaluated in medium 2, can now be written as

$$\nabla \times (\nabla \times \mathbf{E}_{2\omega,2}(\mathbf{r})) - \frac{4\omega^2}{c^2}\epsilon_2(2\omega)\mathbf{E}_{2\omega,2}(\mathbf{r}) = \frac{2\omega^2}{c^2}\chi^{(2)}|\mathbf{A}_{\omega,2}\mathbf{A}_{\omega,2}e^{-j2\mathbf{k}_{\omega,2}\cdot\mathbf{r}} \tag{3.13}$$

where the frequency arguments of the susceptibility are omitted for simplicity. The formal solution to this equation consists of the solution of the homogeneous equation (i.e. right-hand side set to zero) plus a particular solution of the inhomogeneous equation [1]. The solution to the homogeneous equation can be written as a superposition of plane waves. In general, the boundary conditions will determine which plane waves need to be considered to have a completely defined problem. In this particular case, we can satisfy all of the appropriate boundary conditions by assuming a homogeneous solution $\mathbf{A}_{2\omega,2}e^{-j\mathbf{k}_{2\omega,2}\cdot\mathbf{r}}$ with $\mathbf{k}_{2\omega,2}\cdot\mathbf{k}_{2\omega,2} = \frac{4\omega^2}{c^2}\epsilon_2(2\omega)$, $\mathbf{k}_{2\omega,2}$ lying in the xz plane, and $\mathbf{k}_{2\omega,2}\cdot\mathbf{A}_{2\omega,2} = 0$. Thus, the solution to equation 3.13 is written as

$$\begin{aligned}\mathbf{E}_{2\omega,2}(\mathbf{r}) &= \mathbf{A}_{2\omega,2}e^{-j\mathbf{k}_{2\omega,2}\cdot\mathbf{r}} \\ &\quad + \frac{1}{\epsilon_2(\omega)-\epsilon_2(2\omega)}\left[\mathbf{p} - \frac{(\mathbf{p}\cdot\mathbf{k}_{\omega,2})\mathbf{k}_{\omega,2}}{\frac{\omega^2}{c^2}\epsilon_2(2\omega)}\right]e^{-j2\mathbf{k}_{\omega,2}\cdot\mathbf{r}}\end{aligned} \tag{3.14}$$

with

$$\mathbf{p} = \frac{\chi^{(2)}}{2}|\mathbf{A}_{\omega,2}\mathbf{A}_{\omega,2} \tag{3.15}$$

Now, the boundary conditions for electromagnetic fields at the interface can only be fulfilled if we presume the existence of a reflected second-harmonic wave in medium 1

$$\mathbf{E}_{2\omega,1}(\mathbf{r}) = \mathbf{A}'_{2\omega,1}e^{-j\mathbf{k}'_{2\omega,1}\cdot\mathbf{r}} \tag{3.16}$$

with $\mathbf{k}'_{2\omega,1}$ lying in the xz plane. In addition, the following relationship for the wave vector components needs to be met

$$k'_{2\omega,1,x} = k_{2\omega,2,x} = 2k_{\omega,2,x} = 2k_{\omega,1,x} \tag{3.17}$$

Finally, also the the expressions for $\mathbf{A}'_{2\omega,1}$ and $\mathbf{A}_{2\omega,2}$ can be found by applying the boundary conditions at the interface (continuity of the tangential components of $\mathbf{E}$ and $\mathbf{H} = \frac{1}{\mu_0}\mathbf{B}$ across the interface [2])

$$
\begin{aligned}
A'_{2\omega,1,y} &= A_{2\omega,2,y} + \frac{p_y}{\epsilon_2(\omega) - \epsilon_2(2\omega)} \qquad (3.18)\\
A'_{2\omega,1,x} &= A_{2\omega,2,x}\\
&\quad + \frac{p_x - \frac{(\mathbf{p}\cdot\mathbf{k}_{\omega,2})k_{\omega,2,x}}{\frac{\omega^2}{c^2}\epsilon_2(2\omega)}}{\epsilon_2(\omega) - \epsilon_2(2\omega)} \qquad (3.19)\\
k'_{2\omega,1,z}A'_{2\omega,1,y} &= k_{2\omega,2,z}A_{2\omega,2,y}\\
&\quad + 2k_{\omega,2,z}\frac{p_y}{\epsilon_2(\omega) - \epsilon_2(2\omega)} \qquad (3.20)\\
k'_{2\omega,1,z}A'_{2\omega,1,x} - k'_{2\omega,1,x}A'_{2\omega,1,z} &= k_{2\omega,2,z}A_{2\omega,2,x} - k_{2\omega,2,x}A_{2\omega,2,z}\\
&\quad + 2k_{\omega,2,z}\frac{p_x - \frac{(\mathbf{p}\cdot\mathbf{k}_{\omega,2})k_{\omega,2,x}}{\frac{\omega^2}{c^2}\epsilon_2(2\omega)}}{\epsilon_2(\omega) - \epsilon_2(2\omega)}\\
&\quad - 2k_{\omega,2,x}\frac{p_z - \frac{(\mathbf{p}\cdot\mathbf{k}_{\omega,2})k_{\omega,2,z}}{\frac{\omega^2}{c^2}\epsilon_2(2\omega)}}{\epsilon_2(\omega) - \epsilon_2(2\omega)} \qquad (3.21)
\end{aligned}
$$

combined with

$$
\begin{aligned}
k'_{2\omega,1,x}A'_{2\omega,1,x} + k'_{2\omega,1,z}A'_{2\omega,1,z} &= 0 \qquad (3.22)\\
k_{2\omega,2,x}A_{2\omega,2,x} + k_{2\omega,2,z}A_{2\omega,2,z} &= 0 \qquad (3.23)
\end{aligned}
$$

Solving this set of equations, gives us the expression for the transmitted SH wave in medium 2

$$
\begin{aligned}
\mathbf{E}_{2\omega,2}(\mathbf{r}) = \Bigg[&\mathbf{A}'_{2\omega,1} + \left(\frac{k'_{2\omega,1,z}}{k_{2\omega,2,z}} - 1\right)A'_{2\omega,1,z}\mathbf{e}_z\\
&+ \left(\frac{k_{2\omega,2,x}}{k_{2\omega,2,z}}\frac{p_x - \frac{(\mathbf{p}\cdot\mathbf{k}_{\omega,2})k_{\omega,2,x}}{\frac{\omega^2}{c^2}\epsilon_2(2\omega)}}{\epsilon_2(\omega) - \epsilon_2(2\omega)} + \frac{p_z - \frac{(\mathbf{p}\cdot\mathbf{k}_{\omega,2})k_{\omega,2,z}}{\frac{\omega^2}{c^2}\epsilon_2(2\omega)}}{\epsilon_2(\omega) - \epsilon_2(2\omega)}\right)\mathbf{e}_z\\
&+ \frac{\frac{4\omega^2}{c^2}}{2k_{\omega,2,z} + k_{2\omega,2,z}}\left(\mathbf{p} - \frac{(\mathbf{p}\cdot\mathbf{k}_{\omega,2})\mathbf{k}_{\omega,2}}{\frac{\omega^2}{c^2}\epsilon_2(2\omega)}\right)\frac{e^{-j\Delta kz} - 1}{\Delta k}\Bigg]e^{-j\mathbf{k}_{2\omega,2}\cdot\mathbf{r}}
\end{aligned}
\tag{3.24}
$$

with $\Delta k = 2k_{\omega,2,z} - k_{2\omega,2,z}$. We can rewrite expression 3.24 as

$$
\begin{aligned}
\mathbf{E}_{2\omega,2}(\mathbf{r}) &= \mathbf{A}_{2\omega,2}(z)e^{-j\mathbf{k}_{2\omega,2}\cdot\mathbf{r}}\\
&= \Bigg[\mathbf{A}_{2\omega,2}(0) + \frac{\frac{4\omega^2}{c^2}}{2k_{\omega,2,z} + k_{2\omega,2,z}}\\
&\quad \left(\mathbf{p} - \frac{(\mathbf{p}\cdot\mathbf{k}_{\omega,2})\mathbf{k}_{\omega,2}}{\frac{\omega^2}{c^2}\epsilon_2(2\omega)}\right)\frac{e^{-j\Delta kz} - 1}{\Delta k}\Bigg]e^{-j\mathbf{k}_{2\omega,2}\cdot\mathbf{r}}
\end{aligned}
\tag{3.25}
$$

This equation has the form of a plane wave with a spatially varying amplitude. The varying amplitude is a manifestation of the interference between the solutions of the homogeneous and inhomogeneous wave equation, also called the free and bound waves, respectively. If the wave vector mismatch $\Delta k = 0$ (a condition known as phase matching), the second term in expression 3.25 will become proportional to the distance z.

3.2 Slowly varying amplitude approximation

In this section the slowly varying amplitude approximation will be introduced and applied to a second-harmonic generation process. The results will be compared to those obtained in section 3.1. The slowly varying amplitude approximation is treated in many textbooks on nonlinear optics [3–5].

Consider the wave equation 3.4 for a homogeneous, optically isotropic medium.

$$\nabla \times (\nabla \times \mathbf{E}_{\omega_l}(\mathbf{r})) - \frac{\omega_l^2}{c^2}\epsilon(\omega_l)\mathbf{E}_{\omega_l}(\mathbf{r}) = \frac{\omega_l^2}{\epsilon_0 c^2}\mathbf{P}^{(2)}_{\omega_l}(\mathbf{r}) \tag{3.26}$$

In the absence of a nonlinear source term, the solutions are given by transverse plane waves. Such a plane wave, propagating in the z direction, is represented by

$$\mathbf{E}_{\omega_l}(\mathbf{r}) = \mathbf{A}_{\omega_l} e^{-jk_{\omega_l} z} \tag{3.27}$$

with $k_{\omega_l}^2 = \frac{\omega_l^2}{c^2}\epsilon(\omega_l)$. If the nonlinear source term is small, we can expect the solutions of equation 3.26 to be similar to 3.27. But, since we know that nonlinear processes can lead to energy transfer between waves, we adopt the following trial solution

$$\mathbf{E}_{\omega_l}(\mathbf{r}) = \mathbf{A}_{\omega_l}(z) e^{-jk_{\omega_l} z} \tag{3.28}$$

where the amplitude varies with the distance z. If we now substitute this expression in equation 3.4, we get

$$\begin{aligned}
&\frac{\partial^2}{\partial z^2}\left(\mathbf{A}_{\omega_l}(z) - A_{\omega_l,z}(z)\mathbf{e}_z\right) e^{-jk_{\omega_l} z} \\
&\qquad - 2jk_{\omega_l}\frac{\partial}{\partial z}\left(\mathbf{A}_{\omega_l}(z) - A_{\omega_l,z}(z)\mathbf{e}_z\right) e^{-jk_{\omega_l} z} \\
&\qquad\qquad + k_{\omega_l}^2 A_{\omega_l,z}(z)\mathbf{e}_z e^{-jk_{\omega_l} z} = -\frac{\omega_l^2}{\epsilon_0 c^2}\mathbf{P}^{(2)}_{\omega_l}(\mathbf{r})
\end{aligned} \tag{3.29}$$

We can split this up in two equations

$$\frac{\partial^2 \mathbf{A}_{\omega_l,\perp}(z)}{\partial z^2} e^{-jk_{\omega_l} z} - 2jk_{\omega_l}\frac{\partial \mathbf{A}_{\omega_l,\perp}(z)}{\partial z} e^{-jk_{\omega_l} z} = -\frac{\omega_l^2}{\epsilon_0 c^2}\mathbf{P}^{(2)}_{\omega_l,\perp}(\mathbf{r}) \tag{3.30}$$

$$k_{\omega_l}^2 \mathbf{A}_{\omega_l,\parallel}(z) e^{-jk_{\omega_l} z} = -\frac{\omega_l^2}{\epsilon_0 c^2}\mathbf{P}^{(2)}_{\omega_l,\parallel}(\mathbf{r}) \tag{3.31}$$

where $\|$ and $\perp$ indicate the directions along the wave vector and perpendicular to the wave vector, respectively. Next, it is usually assumed that

$$\left|\frac{\partial^2 \mathbf{A}_{\omega_l,\perp}(z)}{\partial z^2}\right| << \left|k_{\omega_l}\frac{\partial \mathbf{A}_{\omega_l,\perp}(z)}{\partial z}\right| \tag{3.32}$$

which is then justified by the fact that the amplitude varies sufficiently slowly with distance [3, 4]. Hence this is known as the slowly varying amplitude approximation. Equation 3.30 now becomes

$$\frac{\partial \mathbf{A}_{\omega_l,\perp}(z)}{\partial z} = -j\frac{\omega_l^2}{2k_{\omega_l}\epsilon_0 c^2}\mathbf{P}^{(2)}_{\omega_l,\perp}(\mathbf{r})e^{jk_{\omega_l}z} \tag{3.33}$$

Now, we will apply the slowly varying amplitude approximation to the SHG process presented in section 3.1 (see also figure 3.1), where a monochromatic plane wave with frequency ω is incident on a nonlinear medium (medium 2). The SH wave in medium 2 is described by (see also equation 3.13)

$$\nabla\times(\nabla\times\mathbf{E}_{2\omega,2}(\mathbf{r})) - \frac{4\omega^2}{c^2}\epsilon_2(2\omega)\mathbf{E}_{2\omega,2}(\mathbf{r}) = \frac{2\omega^2}{c^2}\chi^{(2)}|\mathbf{A}_{\omega,2}\mathbf{A}_{\omega,2}e^{-j2\mathbf{k}_{\omega,2}\cdot\mathbf{r}} \tag{3.34}$$

The first term on the left-hand side equals

$$\nabla\times(\nabla\times\mathbf{E}_{2\omega,2}(\mathbf{r})) = \nabla\left(\nabla\cdot\mathbf{E}_{2\omega,2}(\mathbf{r})\right) - \nabla^2\mathbf{E}_{2\omega,2}(\mathbf{r}) \tag{3.35}$$

In linear, optically isotropic, source-free media, the first term on the right-hand side vanishes since Maxwell's equation 2.1 implies that $\nabla\cdot\mathbf{E}_{2\omega,2}(\mathbf{r}) = 0$. Although the term does not vanish in general, its contribution is often assumed negligible (which is justified if the anisotropy and nonlinearity of the material are not too large) [5]. In that case, equation 3.34 simplifies to

$$\nabla^2\mathbf{E}_{2\omega,2}(\mathbf{r}) + \frac{4\omega^2}{c^2}\epsilon_2(2\omega)\mathbf{E}_{2\omega,2}(\mathbf{r}) = -\frac{2\omega^2}{c^2}\chi^{(2)}|\mathbf{A}_{\omega,2}\mathbf{A}_{\omega,2}e^{-j2\mathbf{k}_{\omega,2}\cdot\mathbf{r}} \tag{3.36}$$

Adopting the trial solution $\mathbf{E}_{2\omega,2}(\mathbf{r}) = \mathbf{A}_{2\omega,2}(z)e^{-j\mathbf{k}_{2\omega,2}\cdot\mathbf{r}}$ and applying the slowly varying amplitude approximation, we get

$$\begin{aligned}\frac{\partial \mathbf{A}_{2\omega,2}(z)}{\partial z} &= -j\frac{\omega^2}{k_{2\omega,2,z}c^2}\chi^{(2)}|\mathbf{A}_{\omega,2}\mathbf{A}_{\omega,2}e^{-j\Delta kz} \\ &= -j\frac{2\omega^2}{k_{2\omega,2,z}c^2}\mathbf{p}e^{-j\Delta kz}\end{aligned} \tag{3.37}$$

Integrating equation 3.37 yields

$$\begin{aligned}\mathbf{A}_{2\omega,2}(z) &= \mathbf{A}_{2\omega,2}(0) + \frac{2\omega^2}{k_{2\omega,2,z}c^2}\mathbf{p}\frac{e^{-j\Delta kz}-1}{\Delta k} \\ &= \frac{2\omega^2}{k_{2\omega,2,z}c^2}\mathbf{p}\frac{e^{-j\Delta kz}-1}{\Delta k}\end{aligned} \tag{3.38}$$

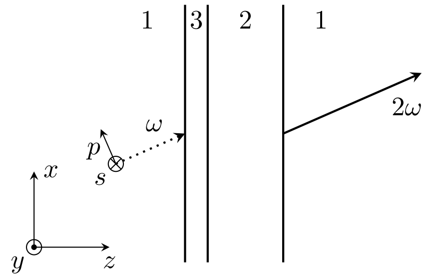

Figure 3.2: Second-harmonic generation in a thin film (3) on top of a substrate (2). The sample is surrounded by medium 1 (typically air). Only medium 3 is assumed to have a non-vanishing $\chi^{(2)}$.

Since no SH wave is incident on medium 2, we have set $\mathbf{A}_{2\omega,2}(0) = 0$ in equation 3.38.

Now let us compare the solution obtained in section 3.1 (expressions 3.24 and 3.25), with the solution following from the slowly varying amplitude approximation (expression 3.38). The treatment of the SHG process by the introduction of the slowly varying amplitude approximation does not naturally yield a reflected SH wave, which does come forward in the more rigorous treatment of section 3.1. In expressions 3.24 and 3.25 we see that $\mathbf{A}_{2\omega,2}(0) \neq 0$ and contains terms in the amplitude of the reflected wave, amongst others. On the other hand, in expression 3.38 we have set $\mathbf{A}_{2\omega,2}(0) = 0$. We could give $\mathbf{A}_{2\omega,2}(0)$ a non-zero value, but which value this should be does not emerge from the slowly varying amplitude approximation approach. Apart from the difference in $\mathbf{A}_{2\omega,2}(0)$, expression 3.25 contains a term in $(\mathbf{p} \cdot \mathbf{k}_{\omega,2})\mathbf{k}_{\omega,2}$, which does not appear in expression 3.38. This can be attributed to the fact that $\nabla \cdot \mathbf{E}_{2\omega,2}(\mathbf{r})$ was not neglected in the calculation in section 3.1. If we take expression 3.25, neglect $\mathbf{A}_{2\omega,2}(0)$, the term in $(\mathbf{p}\cdot\mathbf{k}_{\omega,2})\mathbf{k}_{\omega,2}$ and approximate $2k_{\omega,2,z} + k_{2\omega,2,z}$ by $2k_{2\omega,2,z}$ (which is valid if the dispersion of the refractive index is small), it becomes identical to expression 3.38.

Next, we will have a look at the example of SHG in a thin film with ∞m symmetry. The thin films studied in chapter 4 possess ∞m symmetry. Figure 3.2 depicts the geometry under consideration. We have a thin film (medium 3) on top of a substrate (medium 2) surrounded by medium 1 (typically air). Only the thin film is assumed to have a non-vanishing $\chi^{(2)}$. Since the thin film has ∞m symmetry, the non-zero $\chi^{(2)}$ tensor components are $\chi^{(2)}_{xzx} = \chi^{(2)}_{yzy}$, $\chi^{(2)}_{xxz} = \chi^{(2)}_{yyz}$, $\chi^{(2)}_{zxx} = \chi^{(2)}_{zyy}$, and $\chi^{(2)}_{zzz}$. As we are dealing with SHG, we can say that $\chi^{(2)}_{xzx} = \chi^{(2)}_{yzy} = \chi^{(2)}_{xxz} = \chi^{(2)}_{yyz}$ (see sections 2.2 and 2.3). In our calculation of the transmitted SH wave, we will neglect multiple reflections of the fundamental and SH waves in medium 2 and 3. This is a reasonable approximation if the refractive index contrast between the layers and the angle of incidence are not too large. The materials will be assumed optically isotropic and we will use the slowly varying amplitude approximation. The final solution will be given in terms of the s and p components of the electric fields, rather than the x, y, and z components. s-polarized waves have an electric field parallel to the interface (normal to the plane of incidence; along the y direction in this case) and p-polarized waves have an electric field lying in the plane of incidence (see figure 3.2). We define the corresponding unit vectors as

$$\mathbf{e}_s = -\mathbf{e}_y \tag{3.39}$$

$$\mathbf{e}_p = \frac{\mathbf{k}}{\sqrt{\mathbf{k}\cdot\mathbf{k}}} \times \mathbf{e}_s \tag{3.40}$$

where $\mathbf{k}$ is the wave vector of the plane wave under consideration. Then, the s and p components of a plane wave with electric field amplitude $\mathbf{A}$ are given by

$$A_s = \mathbf{A}\cdot\mathbf{e}_s = -A_y \tag{3.41}$$

$$A_p = \mathbf{A}\cdot\mathbf{e}_p = A_x\frac{k_z}{\sqrt{\mathbf{k}\cdot\mathbf{k}}} - A_z\frac{k_x}{\sqrt{\mathbf{k}\cdot\mathbf{k}}} \tag{3.42}$$

The decomposition in s and p components allows us to use the well known Fresnel coefficients. Starting from expression 3.38, we find for the electric field amplitude of the transmitted SH wave in medium 1

$$A_{2\omega,1out,p} = fA^2_{\omega,1in,p} + gA^2_{\omega,1in,s} \tag{3.43}$$

$$A_{2\omega,1out,s} = hA_{\omega,1in,s}A_{\omega,1in,p} \tag{3.44}$$

with $A_{\omega,1in,p}$ and $A_{\omega,1in,s}$ the p and s components of the electric field amplitude of the incident plane wave at frequency ω, and

$$\begin{aligned} f = &-\frac{\omega^2}{k_{2\omega,3,z}c^2}\frac{e^{-j\Delta kd}-1}{\Delta k}t^2_{p13}T_{p32}T_{p21}\left(2\chi^{(2)}_{xxz}\frac{k_{2\omega,3,z}}{\sqrt{\mathbf{k}_{2\omega,3}\cdot\mathbf{k}_{2\omega,3}}}\frac{k_{\omega,3,x}k_{\omega,3,z}}{\mathbf{k}_{\omega,3}\cdot\mathbf{k}_{\omega,3}}\right. \\ &+\chi^{(2)}_{zxx}\frac{k_{2\omega,3,x}}{\sqrt{\mathbf{k}_{2\omega,3}\cdot\mathbf{k}_{2\omega,3}}}\frac{k^2_{\omega,3,z}}{\mathbf{k}_{\omega,3}\cdot\mathbf{k}_{\omega,3}} \\ &\left.+\chi^{(2)}_{zzz}\frac{k_{2\omega,3,x}}{\sqrt{\mathbf{k}_{2\omega,3}\cdot\mathbf{k}_{2\omega,3}}}\frac{k^2_{\omega,3,x}}{\mathbf{k}_{\omega,3}\cdot\mathbf{k}_{\omega,3}}\right) \end{aligned} \tag{3.45}$$

$$g = -\frac{\omega^2}{k_{2\omega,3,z}c^2}\frac{e^{-j\Delta kd}-1}{\Delta k}t^2_{s13}T_{p32}T_{p21}\chi^{(2)}_{zyy}\frac{k_{2\omega,3,x}}{\sqrt{\mathbf{k}_{2\omega,3}\cdot\mathbf{k}_{2\omega,3}}} \tag{3.46}$$

$$h = -\frac{2\omega^2}{k_{2\omega,3,z}c^2}\frac{e^{-j\Delta kd}-1}{\Delta k}t_{s13}t_{p13}T_{s32}T_{s21}\chi^{(2)}_{yyz}\frac{k_{\omega,3,x}}{\sqrt{\mathbf{k}_{\omega,3}\cdot\mathbf{k}_{\omega,3}}} \tag{3.47}$$

where d is the thickness of the thin film, $\Delta k = 2k_{\omega,3,z} - k_{2\omega,3,z}$, t_{sij} and t_{pij} are the Fresnel transmission coefficients at frequency ω for s- and p-polarization in propagating from medium i to medium j

$$t_{sij} = \frac{2k_{\omega,i,z}}{k_{\omega,i,z} + k_{\omega,j,z}} \tag{3.48}$$

$$t_{pij} = \frac{2\sqrt{\epsilon_i(\omega)\epsilon_j(\omega)}k_{\omega,i,z}}{\epsilon_i(\omega)k_{\omega,j,z} + \epsilon_j(\omega)k_{\omega,i,z}} \tag{3.49}$$

and T_{sij} and T_{pij} are the Fresnel transmission coefficients at frequency 2ω for s- and p-polarization in propagating from medium i to medium j. If we write the refractive index of medium i at frequency $\omega(2\omega)$ as $n_i(N_i)$ and use the relations $k_{\omega,3,x} = \frac{\omega}{c}n_3 \sin\theta_3$, $k_{\omega,3,z} = \frac{\omega}{c}n_3 \cos\theta_3$, $k_{2\omega,3,x} = \frac{2\omega}{c}N_3 \sin\Theta_3$, and $k_{2\omega,3,z} = \frac{2\omega}{c}N_3 \cos\Theta_3$, we get for f, g, and h

$$\begin{aligned} f = &-\frac{\omega}{2N_3c}\frac{e^{-j\Delta kd}-1}{\Delta k}t_{p13}^2T_{p32}T_{p21}\left(\chi_{xxz}^{(2)}\sin(2\theta_3)\right. \\ &+\chi_{zxx}^{(2)}\tan\Theta_3\cos^2\theta_3 \\ &\left.+\chi_{zzz}^{(2)}\tan\Theta_3\sin^2\theta_3\right) \end{aligned} \tag{3.50}$$

$$g = -\frac{\omega}{2N_3c}\frac{e^{-j\Delta kd}-1}{\Delta k}t_{s13}^2T_{p32}T_{p21}\chi_{zyy}^{(2)}\tan\Theta_3 \tag{3.51}$$

$$h = -\frac{\omega}{N_3c\cos\Theta_3}\frac{e^{-j\Delta kd}-1}{\Delta k}t_{s13}t_{p13}T_{s32}T_{s21}\chi_{yyz}^{(2)}\sin\theta_3 \tag{3.52}$$

where $\theta_i(\Theta_i)$ is the angle between the positive z axis and $\mathbf{k}_{\omega,i}(\mathbf{k}_{2\omega,i})$.

Expressions 3.43, 3.44, 3.50, 3.51, and 3.52 can also be obtained by using a simplified version of the Green's function formalism for nonlinear optics where multiple reflections in the layer stack are neglected [6–8].

If $|\Delta kd| << 1$, we can make the following approximation

$$\frac{e^{-j\Delta kd}-1}{\Delta k} \approx -jd \tag{3.53}$$

For optically isotropic materials, $\frac{1}{|\Delta k|}$ is typically on the order of $1\,\mu\mathrm{m}$. Therefore, for thin films with thicknesses on the order of $100\,\mathrm{nm}$ or below, the above-mentioned approximation can often be used. In that case, one might also include the thickness d in the second-order susceptibility, resulting in a surface second order-susceptibility $\chi_s^{(2)} = \chi^{(2)}d$.

3.3 Surface second-harmonic generation

In this section, we will consider second-harmonic radiation generated by a thin layer (i.e. thickness much smaller than the wavelength) at the interface between two centrosymmetric media (in which $\chi^{(2)}$ vanishes). In the previous section, we

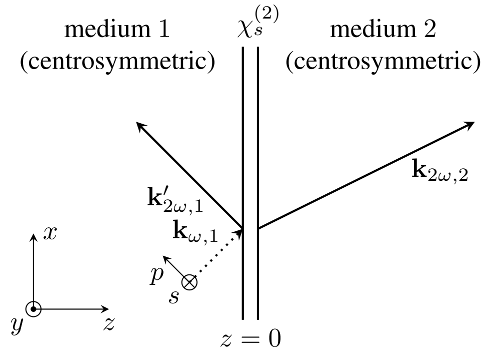

Figure 3.3: Surface second-harmonic generation from an interface between two centrosymmetric media.

already briefly touched upon the concept of a surface second order-susceptibility. Here, this will be treated more rigorously. We follow the derivation outlined in [9].

Consider the geometry depicted in figure 3.3. Media 1 and 2 are assumed to be linear, while the thin layer at the interface is nonlinear. The interfacial layer has a (generalized) nonlinear polarization at frequency ω_l given by $\mathbf{\Pi}_{\omega_l}^{NL}(\mathbf{r})$. In the limit of zero thickness, we introduce a surface nonlinear polarization $\mathbf{\Pi}_{\omega_l,s}^{NL}(x,y) = \int_{0-}^{0+} \mathbf{\Pi}_{\omega_l}^{NL}(\mathbf{r})\,dz$. In the presence of a polarization sheet $\mathbf{\Pi}_{\omega_l,s}^{NL}(x,y)$ at the interface ($z = 0$), the usual boundary conditions for electromagnetic fields are no longer valid. Instead, they are given by

$$[(\epsilon\mathbf{E}_{\omega_l}(\mathbf{r}))\cdot\mathbf{e}_z]_{0-}^{0+} = -\frac{1}{\epsilon_0}\nabla_t\cdot\mathbf{\Pi}_{\omega_l,s}^{NL}(x,y) \tag{3.54}$$

$$[E_{\omega_l,x}(\mathbf{r})\mathbf{e}_x + E_{\omega_l,y}(\mathbf{r})\mathbf{e}_y]_{0-}^{0+} = -\frac{1}{\epsilon_0\epsilon'}\nabla_t\Pi_{\omega_l,s,z}^{NL}(x,y) \tag{3.55}$$

$$[B_{\omega_l,z}(\mathbf{r})]_{0-}^{0+} = 0 \tag{3.56}$$

$$\left[\left((\mu^{-1}\mathbf{B}_{\omega_l}(\mathbf{r}))\cdot\mathbf{e}_x\right)\mathbf{e}_x + \left((\mu^{-1}\mathbf{B}_{\omega_l}(\mathbf{r}))\cdot\mathbf{e}_y\right)\mathbf{e}_y\right]_{0-}^{0+} = j\mu_0\omega_l\mathbf{\Pi}_{\omega_l,s}^{NL}(x,y)\times\mathbf{e}_z \tag{3.57}$$

with $[f]_{0-}^{0+} = f(z=0+) - f(z=0-)$ and $\nabla_t = \mathbf{e}_x\frac{\partial}{\partial x} + \mathbf{e}_y\frac{\partial}{\partial y}$ [9, 10]. The interfacial layer is assumed to be optically isotropic with dielectric constant ϵ'. The above-mentioned boundary conditions are also valid for an anisotropic interfacial layer if its dielectric tensor is diagonal in the xyz coordinate system. In that case ϵ' needs to be replaced by ϵ'_{zz}. For the remainder of this section we will assume $\mu = 1$ (most materials are nonmagnetic at optical frequencies).

For the case of second-harmonic generation, the surface nonlinear polarization can be written as

$$\mathbf{P}^{(2)}_{2\omega,s}(x,y) = \epsilon_0 \frac{1}{2}\chi^{(2)}_s(-2\omega;\omega,\omega)|\mathbf{E}_\omega(x,y,z=0)\mathbf{E}_\omega(x,y,z=0) \tag{3.58}$$

where we are evaluating the electric fields inside the interfacial layer. The electric field $\mathbf{E}_\omega(x,y,z=0)$ can be found from the regular boundary conditions for electromagnetic fields (there is no surface polarization at frequency ω)

$$E_{\omega,x}(x,y,z=0) = E_{\omega,x}(x,y,z=0+) = E_{\omega,x}(x,y,z=0-) \tag{3.59}$$

$$E_{\omega,y}(x,y,z=0) = E_{\omega,y}(x,y,z=0+) = E_{\omega,y}(x,y,z=0-) \tag{3.60}$$

$$\begin{aligned}(\epsilon'\mathbf{E}_\omega(x,y,z=0))\cdot\mathbf{e}_z &= (\epsilon_2\mathbf{E}_\omega(x,y,z=0+))\cdot\mathbf{e}_z \\ &= (\epsilon_1\mathbf{E}_\omega(x,y,z=0-))\cdot\mathbf{e}_z \end{aligned} \tag{3.61}$$

The interfacial layer can be a thin film of a certain material, a monolayer of adsorbed molecules, but it can also simply be the bare interface between medium 1 and 2 (e.g. an air/glass interface, as will be encountered in chapter 4). Since $E_{\omega,z}$ is discontinuous across an interface, the values of $\chi^{(2)}_s$ will depend on the choice of ϵ' (e.g. for a bare interface one might choose $\epsilon' = \epsilon_1$ or $\epsilon' = \epsilon_2$). To remove this arbitrariness, alternative definitions of $\chi^{(2)}_s$, involving $D_{\omega,z}$, exist [11]. It can be shown that $\chi^{(2)}_s(-2\omega;\omega,\omega)$ contains both local and nonlocal contributions [11–14]. The local or dipole contributions arise from the fact that the inversion symmetry is necessarily broken at an interface (as opposed to the bulk of media 1 and 2) and, in some cases, from the presence of a non-centrosymmetric film at the interface. The nonlocal contributions arise from the discontinuity of the normal electric field component across an interface. Because of these rapid spatial variations, the higher-order multipole terms can contribute significantly.

Now, let us calculate the SH fields generated by the surface polarization. Media 1 and 2 have dielectric constants ϵ_1 and ϵ_2, respectively. The interfacial layer will be assumed anisotropic with a dielectric tensor ϵ_3 that is diagonal in the xyz coordinate system. The incident wave at frequency ω is given by

$$\mathbf{E}_{\omega,1}(\mathbf{r}) = \mathbf{A}_{\omega,1}e^{-j\mathbf{k}_{\omega,1}\cdot\mathbf{r}} \tag{3.62}$$

where $\mathbf{k}_{\omega,1}$ lies in the xz plane (see figure 3.3). The polarization sheet will generate a reflected SH beam in medium 1

$$\mathbf{E}_{2\omega,1}(\mathbf{r}) = \mathbf{A}'_{2\omega,1}e^{-j\mathbf{k}'_{2\omega,1}\cdot\mathbf{r}} \tag{3.63}$$

and a transmitted SH beam in medium 2

$$\mathbf{E}_{2\omega,2}(\mathbf{r}) = \mathbf{A}_{2\omega,2}e^{-j\mathbf{k}_{2\omega,2}\cdot\mathbf{r}} \tag{3.64}$$

By applying the boundary conditions, we find following relationship for the wave vector components.

$$k'_{2\omega,1,x} = k_{2\omega,2,x} = 2k_{\omega,1,x} = 2k_{\omega,2,x} \tag{3.65}$$

The surface polarization can be written as

$$\mathbf{P}^{(2)}_{2\omega,s}(x,y) = \epsilon_0 \mathbf{p}^s e^{-j2k_{\omega,1,x}x} \tag{3.66}$$

By applying the boundary conditions, making use of $\mathbf{k}'_{2\omega,1} \cdot \mathbf{A}'_{2\omega,1} = 0$ and $\mathbf{k}_{2\omega,2} \cdot \mathbf{A}_{2\omega,2} = 0$, we find

$$A'_{2\omega,1,x} = j\frac{k'_{2\omega,1,z}k_{2\omega,2,z}}{\epsilon_1 k_{2\omega,2,z} - \epsilon_2 k'_{2\omega,1,z}}p^s_x + j\frac{\epsilon_2}{\epsilon_{3,zz}}\frac{k'_{2\omega,1,x}k'_{2\omega,1,z}}{\epsilon_1 k_{2\omega,2,z} - \epsilon_2 k'_{2\omega,1,z}}p^s_z \tag{3.67}$$

$$A'_{2\omega,1,y} = j\frac{4\omega^2}{c^2}\frac{p^s_y}{k'_{2\omega,1,z} - k_{2\omega,2,z}} \tag{3.68}$$

$$A'_{2\omega,1,z} = -j\frac{k'_{2\omega,1,x}k_{2\omega,2,z}}{\epsilon_1 k_{2\omega,2,z} - \epsilon_2 k'_{2\omega,1,z}}p^s_x - j\frac{\epsilon_2}{\epsilon_{3,zz}}\frac{k'^2_{2\omega,1,x}}{\epsilon_1 k_{2\omega,2,z} - \epsilon_2 k'_{2\omega,1,z}}p^s_z \tag{3.69}$$

$$A_{2\omega,2,x} = j\frac{k'_{2\omega,1,z}k_{2\omega,2,z}}{\epsilon_1 k_{2\omega,2,z} - \epsilon_2 k'_{2\omega,1,z}}p^s_x + j\frac{\epsilon_1}{\epsilon_{3,zz}}\frac{k'_{2\omega,1,x}k_{2\omega,2,z}}{\epsilon_1 k_{2\omega,2,z} - \epsilon_2 k'_{2\omega,1,z}}p^s_z \tag{3.70}$$

$$A_{2\omega,2,y} = j\frac{4\omega^2}{c^2}\frac{p^s_y}{k'_{2\omega,1,z} - k_{2\omega,2,z}} \tag{3.71}$$

$$A_{2\omega,2,z} = -j\frac{k_{2\omega,2,x}k'_{2\omega,1,z}}{\epsilon_1 k_{2\omega,2,z} - \epsilon_2 k'_{2\omega,1,z}}p^s_x - j\frac{\epsilon_1}{\epsilon_{3,zz}}\frac{k'^2_{2\omega,1,x}}{\epsilon_1 k_{2\omega,2,z} - \epsilon_2 k'_{2\omega,1,z}}p^s_z \tag{3.72}$$

where the frequency arguments of ϵ_1, ϵ_2 and $\epsilon_{3,zz}$ are omitted for simplicity (they need to be evaluated at frequency 2ω).

As in section 3.2, we can also write the electric fields in terms of their s and p components (see expressions 3.39, 3.40, 3.41, and 3.42)

$$A'_{2\omega,1,s} = j\frac{4\omega^2}{c^2}\frac{p^s_y}{k_{2\omega,2,z} - k'_{2\omega,1,z}} \tag{3.73}$$

$$A'_{2\omega,1,p} = j\sqrt{\mathbf{k}'_{2\omega,1} \cdot \mathbf{k}'_{2\omega,1}}\frac{k_{2\omega,2,z}p^s_x + \frac{\epsilon_2(2\omega)}{\epsilon_{3,zz}(2\omega)}k'_{2\omega,1,x}p^s_z}{\epsilon_1(2\omega)k_{2\omega,2,z} - \epsilon_2(2\omega)k'_{2\omega,1,z}} \tag{3.74}$$

$$A_{2\omega,2,s} = j\frac{4\omega^2}{c^2}\frac{p^s_y}{k_{2\omega,2,z} - k'_{2\omega,1,z}} \tag{3.75}$$

$$A_{2\omega,2,p} = j\sqrt{\mathbf{k}_{2\omega,2} \cdot \mathbf{k}_{2\omega,2}}\frac{k'_{2\omega,1,z}p^s_x + \frac{\epsilon_1(2\omega)}{\epsilon_{3,zz}(2\omega)}k'_{2\omega,1,x}p^s_z}{\epsilon_1(2\omega)k_{2\omega,2,z} - \epsilon_2(2\omega)k'_{2\omega,1,z}} \tag{3.76}$$

For an interface with ∞m symmetry, $\mathbf{p}^s$ will have the following components

$$\begin{aligned}
p_x^s &= -\chi^{(2)}_{s,xxz} \frac{\epsilon_2(\omega)}{\epsilon_{3,zz}(\omega)} \frac{k_{\omega,2,z}k_{\omega,2,x}}{\mathbf{k}_{\omega,2}\cdot\mathbf{k}_{\omega,2}} A^2_{\omega,2,p} && (3.77)\\
&= -\chi^{(2)}_{s,xxz} \frac{\epsilon_2(\omega)}{\epsilon_{3,zz}(\omega)} \frac{k_{\omega,2,z}k_{\omega,2,x}}{\mathbf{k}_{\omega,2}\cdot\mathbf{k}_{\omega,2}} t^2_{p12} A^2_{\omega,1,p} && (3.78)\\
p_y^s &= \chi^{(2)}_{s,yyz} \frac{\epsilon_2(\omega)}{\epsilon_{3,zz}(\omega)} \frac{k_{\omega,2,x}}{\sqrt{\mathbf{k}_{\omega,2}\cdot\mathbf{k}_{\omega,2}}} A_{\omega,2,p} A_{\omega,2,s} && (3.79)\\
&= \chi^{(2)}_{s,yyz} \frac{\epsilon_2(\omega)}{\epsilon_{3,zz}(\omega)} \frac{k_{\omega,2,x}}{\sqrt{\mathbf{k}_{\omega,2}\cdot\mathbf{k}_{\omega,2}}} t_{p12} t_{s12} A_{\omega,1,p} A_{\omega,1,s} && (3.80)\\
p_z^s &= \frac{\chi^{(2)}_{s,zxx}}{2} \frac{k^2_{\omega,2,z}}{\mathbf{k}_{\omega,2}\cdot\mathbf{k}_{\omega,2}} A^2_{\omega,2,p} \\
&\quad + \frac{\chi^{(2)}_{s,zyy}}{2} A^2_{\omega,2,s} \\
&\quad + \frac{\chi^{(2)}_{s,zzz}}{2} \left(\frac{\epsilon_2(\omega)}{\epsilon_{3,zz}(\omega)}\right)^2 \frac{k^2_{\omega,2,x}}{\mathbf{k}_{\omega,2}\cdot\mathbf{k}_{\omega,2}} A^2_{\omega,2,p} && (3.81)\\
&= \frac{\chi^{(2)}_{s,zxx}}{2} \frac{k^2_{\omega,2,z}}{\mathbf{k}_{\omega,2}\cdot\mathbf{k}_{\omega,2}} t^2_{p12} A^2_{\omega,1,p} \\
&\quad + \frac{\chi^{(2)}_{s,zyy}}{2} t^2_{s12} A^2_{\omega,1,s} \\
&\quad + \frac{\chi^{(2)}_{s,zzz}}{2} \left(\frac{\epsilon_2(\omega)}{\epsilon_{3,zz}(\omega)}\right)^2 \frac{k^2_{\omega,2,x}}{\mathbf{k}_{\omega,2}\cdot\mathbf{k}_{\omega,2}} t^2_{p12} A^2_{\omega,1,p} && (3.82)
\end{aligned}$$

Using the same notational conventions as in section 3.2, we find for the transmitted SH wave in medium 2

$$\begin{aligned}
A_{2\omega,2,p} &= f A^2_{\omega,1,p} + g A^2_{\omega,1,s} && (3.83)\\
A_{2\omega,2,s} &= h A_{\omega,1,s} A_{\omega,1,p} && (3.84)
\end{aligned}$$

with

$$
\begin{aligned}
f = j\frac{\omega}{2N_2c}t_{p12}^2 \Bigg(& \frac{n_2^2}{n_{3,z}^2}\frac{N_2}{N_1}T_{p12}\chi_{s,xxz}^{(2)}\sin(2\theta_2) \\
& + \frac{N_1N_2}{N_{3,z}^2}T_{p21}\chi_{s,zxx}^{(2)}\tan\Theta_2\cos^2\theta_2 \\
& + \frac{n_2^4}{n_{3,z}^4}\frac{N_1N_2}{N_{3,z}^2}T_{p21}\chi_{s,zzz}^{(2)}\tan\Theta_2\sin^2\theta_2\Bigg)
\end{aligned} \tag{3.85}
$$

$$
g = j\frac{\omega}{2N_2c}t_{s12}^2\frac{N_1N_2}{N_{3,z}^2}T_{p21}\chi_{s,zyy}^{(2)}\tan\Theta_2 \tag{3.86}
$$

$$
h = j\frac{\omega}{N_2c\cos\Theta_2}\frac{n_2^2}{n_{3,z}^2}t_{s12}t_{p12}T_{s21}\chi_{s,yyz}^{(2)}\sin\theta_2 \tag{3.87}
$$

These expressions take into account the multiple reflections of the fundamental and SH waves in the interfacial layer with infinitesimal thickness. If the reflections are small and the anisotropy of the interfacial layer limited, we can approximate the expressions above by the expressions obtained from the slowly varying amplitude approximation for the thickness $d \to 0$ (see section 3.2).

So far we have treated the surface second-order nonlinearity of an interface between centrosymmetric media. In centrosymmetric media, the electric dipole contributions to the (generalized) bulk second-order polarization vanish, but the leading-order nonlocal contributions (magnetic dipole and electric quadrupole) do not [15]. Therefore, SHG from the bulk might still interfere with SHG from the interface. For SHG in homogeneous isotropic media with a single incident plane wave, the leading-order nonlocal contributions to the bulk polarization will behave as a surface polarization [9]. Consequently, these bulk contributions cannot be separated from the surface contributions and in a measurement of the surface second-order susceptibility they will always be included [14, 16, 17]. The sum of the surface second-order susceptibility $\chi_s^{(2)}$ and the inseparable bulk contributions, is sometimes called the effective surface second-order susceptibility $\chi_{s,eff}^{(2)}$. For the remainder of this thesis we will simply refer to $\chi_{s,eff}^{(2)}$ as $\chi_s^{(2)}$ and it should be understood that bulk contributions are included.

3.4 Second-harmonic generation in a stack of thin films

In section 3.2 a model was developed for SHG in a stack of materials, but only for optically isotropic materials and multiple reflections were neglected. Section 3.3 dealt with SHG in very thin films, including all reflections and allowing for

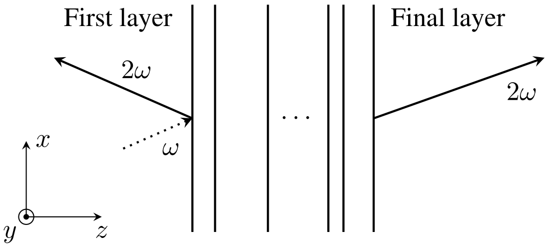

Figure 3.4: Second-harmonic generation in a multilayer medium.

an anisotropic film (provided its dielectric tensor is diagonal in the xyz coordinate system).

But, many nonlinear materials are anisotropic with an orientation that does not lead to a diagonal dielectric tensor in the xyz coordinate system shown in figures 3.2 and 3.3. Moreover, in many cases we will deal with film thicknesses on the order of a wavelength or thicker. Also, for larger refractive index contrasts or larger angles of incidence, neglecting the multiple reflections and the associated Fabry-Pérot type resonances will lead to inaccuracies.

D. S. Bethune developed a model for SHG in a stack of thin films that can handle anisotropic media with arbitrarily oriented principal axes [18]. The model is based on a transfer matrix method that accounts for all of the reflections of the fundamental and SH waves. The considered geometry is sketched in figure 3.4. From the knowledge of the incident wave at frequency ω, the layer thicknesses, the dielectric tensors and the second-order susceptibility tensor(s), the transmitted and reflected waves at frequency 2ω can be calculated. The model is applicable for a low SH conversion efficiency (i.e. no pump depletion). The transfer matrix method allows for convenient numerical implementation and easy addition or removal of layers. We have implemented the model in MATLAB and used it, e.g., to model SHG in biaxial organic crystalline thin films (see chapter 5). In a first step, the electric field distribution at the fundamental frequency ω throughout the multilayer medium is determined. In a second step, the knowledge of the fields at frequency ω is used to calculate the bound waves at the SH frequency 2ω in the nonlinear layer(s) (i.e. solution of inhomogeneous wave equation, see section 3.1). In a final step, the free waves at frequency 2ω (i.e. solution of homogeneous wave equation) are determined taking into account all of the boundary conditions. More details can be found in appendix A.

References

[1] N. Bloembergen and P. S. Pershan. *Light waves at the boundary of nonlinear media*. Physical Review, 128(2):606, 1962.

[2] J. D. Jackson. *Classical Electrodynamics*. John Wiley & Sons, Inc., 3rd edition, 1999.

[3] Y. R. Shen. *The Principles of Nonlinear Optics*. Wiley, 1984.

[4] P. N. Butcher and D. Cotter. *The Elements of Nonlinear Optics*. Cambridge University Press, Cambridge, 1990.

[5] R. W. Boyd. *Nonlinear Optics*. Academic Press, 3rd edition, 2008.

[6] T. Ning, H. Pietarinen, O. Hyvärinen, J. Simonen, G. Genty, and M. Kauranen. *Strong second-harmonic generation in silicon nitride films*. Applied Physics Letters, 100(16):161902, 2012.

[7] J. E. Sipe. *New Green-function formalism for surface optics*. Journal of the Optical Society of America B, 4(4):481, 1987.

[8] J. J. Maki, M. Kauranen, and A. Persoons. *Surface second-harmonic generation from chiral materials*. Physical Review B, 51(3):1425, 1995.

[9] T. F. Heinz. *Second-Order Nonlinear Optical Effects at Surfaces and Interfaces*. In H.-E. Ponath and G. I. Stegeman, editors, Nonlinear Surface Electromagnetic Phenomena. Elsevier Science Publishers B.V., 1991.

[10] B. U. Felderhof and G. Marowsky. *Linear optics of polarization sheets*. Applied Physics B, 43:161, 1987.

[11] P. Guyot-Sionnest, W. Chen, and Y. R. Shen. *General considerations on optical second-harmonic generation from surfaces and interfaces*. Physical Review B, 33(12):8254, 1986.

[12] P. Guyot-Sionnest and Y. R. Shen. *Local and nonlocal surface nonlinearities for surface optical second-harmonic generation*. Physical Review B, 35(9):442, 1987.

[13] J. E. Sipe, D. J. Moss, and H. M. van Driel. *Phenomenological theory of optical second- and third-harmonic generation from cubic centrosymmetric crystals*. Physical Review B, 35(3):1129, 1987.

[14] P. Guyot-Sionnest and Y. R. Shen. *Bulk contribution in surface second-harmonic generation*. Physical Review B, 38(12):7985, 1988.

[15] F. Wang. *Multipolar Nonlinear Optics of Surfaces and Bulk Materials*. PhD thesis, Tampere University of Technology, 2010.

[16] J. E. Sipe, V. Mizrahi, and G. I. Stegeman. *Fundamental difficulty in the use of second-harmonic generation as a strictly surface probe*. Physical Review B, 35(17):9091, 1987.

[17] F. J. Rodriguez, F. X. Wang, and M. Kauranen. *Calibration of the second-order nonlinear optical susceptibility of surface and bulk of glass*. Optics Express, 16(12):8704, 2008.

[18] D. S. Bethune. *Optical harmonic generation and mixing in multilayer media: extension of optical transfer matrix approach to include anisotropic materials*. Journal of the Optical Society of America B, 8(2):367, 1991.

4

Atomic layer deposited second-order nonlinear materials

Traditional second-order nonlinear materials are inorganic, non-centrosymmetric crystals (see section 2.7). The growth of inorganic single crystals typically requires high temperatures and/or the use of a crystalline template/seed. Common fabrication methods are the Czochralski and Bridgman technique for bulk crystals [1, 2], and molecular beam epitaxy (MBE) and metalorganic chemical vapor deposition (MOCVD; also known as metalorganic vapor phase epitaxy (MOVPE)) for thin films [2]. However, epitaxial growth directly on SiN PICs is not an option due to SiN's amorphous nature (and the same holds true for the SiO_x cladding). Also the involvement of high-temperature processing steps is undesirable for back-end deposited silicon photonics (see section 1.2). Therefore, alternative film growth techniques for $\chi^{(2)}$ materials are required.

In this chapter, it will be shown that atomic layer deposition (ALD) can be used for the low-temperature deposition of $\chi^{(2)}$ materials on amorphous substrates. The materials that will be discussed are ABC-type nanolaminates, zinc oxide, and zinc sulfide. Second-harmonic generation as well as electro-optic modulation experiments will be covered. A large part of the results presented in this chapter has been published in [3–8]. For the ALD, we collaborate with the CoCooN (Conformal Coating of Nanomaterials) research group at Ghent University [9].

Contents

4.1 Atomic layer deposition

Atomic layer deposition (ALD) is a chemical vapor deposition (CVD) technique for the growth of uniform, highly conformal thin films at low temperatures with excellent thickness control [10–13]. Typical substrate temperatures range from room temperature to $350\,^{\circ}\mathrm{C}$. Layer thicknesses on the order of a nanometer can readily be achieved. A conformal film is a film that covers 3D structures with an even thickness (irrespective of the orientations of the surfaces). ALD thin films show a high degree of conformality, even for high-aspect ratio structures such as the deep trenches shown in figure 4.1. The excellent conformality achievable with ALD has also been exploited for film deposition on powders/(nano)particles [14], deposition inside nanometer-sized pores [15], on silicon nitride slotted waveguides [16], and 3D woodpile photonic crystals [17]. Moreover, Intel Corporation has reported using ALD to deposit the gate dielectric in its $45\,\mathrm{nm}$ CMOS technology [18].

ALD is a self-limiting film growth technique in which the sample is alternately exposed to different chemical reactants (also called precursors). Each exposure leads to the deposition of a (sub-)monolayer of material. A typical ALD process utilizing two precursors is depicted in figure 4.2. In step 1a, the substrate is exposed to precursor A and a gas-solid reaction between this precursor and the substrate occurs. An essential characteristic of ALD is that this reaction is saturating and irreversible [10], meaning that the reaction is self-terminating or self-limiting. This self-limiting behavior entails that no more than a single layer of molecules is deposited during each precursor pulse. After the first precursor exposure, the reactor is purged to remove the unreacted precursor and reaction by-products (step 1b). In step 2a, precursor B is introduced into the chamber and a

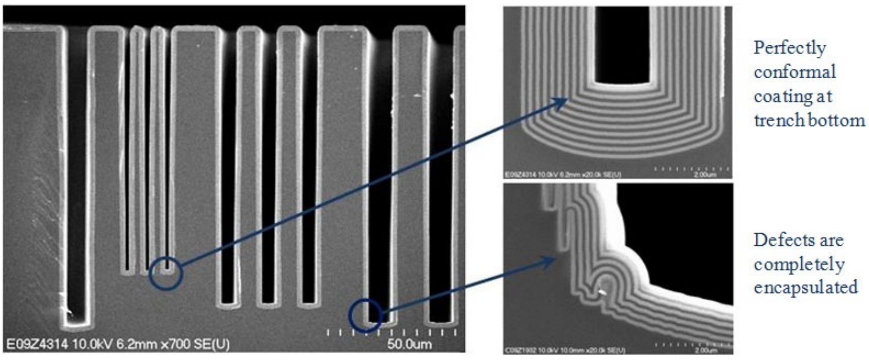

Figure 4.1: Alternating layers of Ta_2O_5 and Al_2O_3 deposited by ALD in deep silicon trenches. Figure reproduced from [19].

second chemisorption reaction occurs. This is again followed by a purge step (step 2b). Step 1a to 2b comprise one ALD cycle. This ALD cycle is repeated over and over until the desired film thickness is reached. The utilization of sequential, self-saturating gas-solid reactions enables the deposition of highly conformal, uniform thin films with angstrom-level thickness control. This degree of conformality and thickness control is hard to achieve with traditional CVD techniques, where the precursors are simultaneously present inside the reactor, or common physical vapor deposition (PVD) techniques, such as sputtering, thermal evaporation and e-beam evaporation.

The temperature range over which the above-mentioned self-limiting, saturated growth occurs is called the ALD window [13]. The ALD window depends on the specific process. It has a typical width of a couple tens of degrees to over 100 °C. Within the ALD window, the growth rate is only weakly temperature dependent [10]. For ALD processes, the growth rate is usually expressed as the growth per cycle (GPC), rather than the growth per time unit.

ALD is used to deposit inorganic thin films. A related technique known as molecular layer deposition (MLD) exists for organic thin films [20]. ALD and MLD can be combined for the deposition of hybrid inorganic-organic materials.

Non-epitaxial atomic layer deposition results in amorphous or polycrystalline films (as-deposited). Grain sizes typically do not exceed the film thickness, but there are exceptions [10]. The higher the substrate temperature, the thicker the film, and the purer the resulting material, the more likely the resulting film will be crystalline. The use of plasma enhancement usually also increases the probability of having a crystalline film. However, one has to keep in mind that the aforementioned behaviors are only trends. Particular ALD processes might contradict some or all of these simplified trends.

Amorphous or centrosymmetric crystalline films are undesirable for $\chi^{(2)}$ ap-

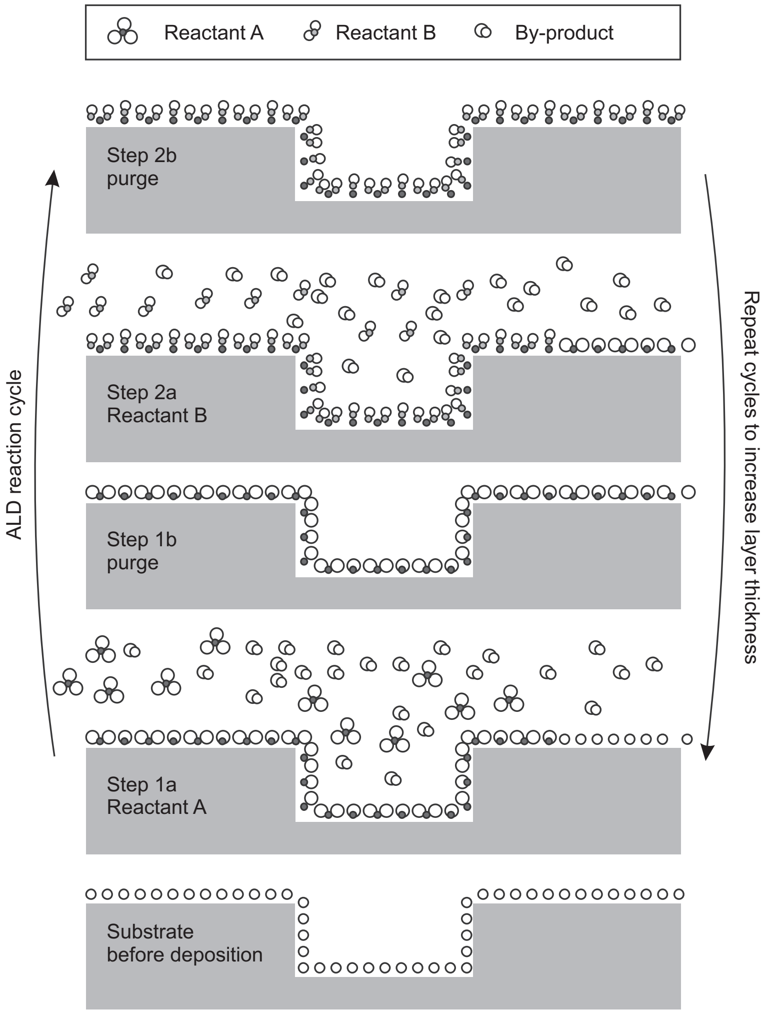

Figure 4.2: Schematic illustration of an ALD process utilizing two precursors. For instance, for the deposition of Al_2O_3, trimethylaluminum (TMA) is often used as aluminum precursor and H_2O as oxygen precursor. Figure reproduced from [10].

plications. Unfortunately, many ALD materials fall into this category. Yet, as will be shown in the next section, even with centrosymmetric materials we can get an effective bulk $\chi^{(2)}$ nonlinearity by layering three of them in an ABC-type nanolaminate. Apart from the ABC-type nanolaminates, this chapter will treat zinc oxide (ZnO) and zinc sulfide (ZnS) thin films. ALD of ZnO and ZnS almost always results in crystalline films [10]. Moreover, these films crystallize in a non-centrosymmetric phase. Yet, this is not sufficient to get a bulk $\chi^{(2)}$ nonlinearity. In a polycrystalline film with small grain sizes (typically they will be much smaller than the wavelength), a random orientation of the crystallites/grains can lead to a vanishing bulk $\chi^{(2)}$ nonlinearity. Therefore, films where the grains have a preferential orientation are desirable (also known as textured films).

4.2 ABC-type nanolaminates

Consider several materials combined in a periodically layered medium. If the periodicity is much smaller than the wavelength, we can treat the multilayer medium as a homogeneous medium possessing certain effective optical properties. These optical properties can be very different from the properties of the constituents. For instance, a periodic multilayer consisting of optically isotropic materials behaves as an anisotropic, uniaxial medium (this phenomenon is known as form birefringence) [21]. Also the nonlinear optical properties can be manipulated utilizing layered media with sub-wavelength periodicity. By combining materials with appropriate linear optical properties and a non-vanishing nonlinear susceptibility (for at least one of the constituents), the effective nonlinear susceptibility can exceed that of the constituents [22, 23]. Crystalline superlattices of germanium and silicon can have a non-vanishing effective $\chi^{(2)}$ nonlinearity, even though bulk silicon and germanium possess inversion symmetry [24, 25]. Epitaxially grown multi-quantum-well structures can be engineered to produce a huge resonant nonlinear response [26, 27]. In multilayer silica-metal nanocomposites, an effective bulk $\chi^{(2)}$ nonlinearity has been observed as well, albeit small ($\chi^{(2)}_{zzz} = 4\,\mathrm{fm/V}$, measured in SHG experiments at a fundamental wavelength of $1064\,\mathrm{nm}$) [28]. Also for organic $\chi^{(2)}$ materials, the concept of multilayer stacks can be useful. Many organic molecules possess a strong second-order nonlinearity on the molecular level, but crystallize into a centrosymmetric structure. Utilizing a Langmuir-Blodgett technique, alternating layers of two molecules, with one highly nonlinear molecule, have been deposited in a non-centrosymmetric structure, thereby allowing for bulk $\chi^{(2)}$ effects [29].

In this section, we will show how alternate stacking of three centrosymmetric materials A, B, and C, with individual layer thicknesses on the order of a nanometer, can lead to an effective $\chi^{(2)}$ nonlinearity. We call this type of material an ABC-type nanolaminate (see figure 4.3 for illustration). These ABC-type nanolaminates

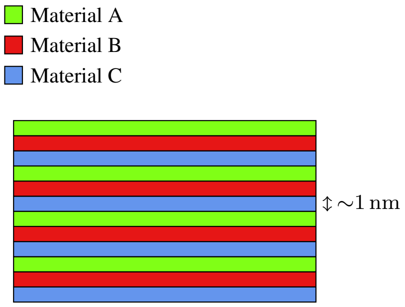

Figure 4.3: Schematic representation of an ABC-type nanolaminate.

are deposited by ALD at low temperatures on amorphous substrates. The origin of the non-zero effective $\chi^{(2)}$ nonlinearity in ABC-type nanolaminates can be explained as follows. The nanolaminate consists of a sequence of interfaces. Each interface is associated with a surface second-order susceptibility $\chi_s^{(2)}$ (see section 3.3). Because of the non-centrosymmetric ABCABC... stacking sequence, the contributions of the A/B, B/C, and C/A interfaces to the nonlinear polarization do not add up to zero, as would be expected for an AB-type nanolaminate.

The demonstration of atomic layer deposited ABC-type nanolaminates with an effective $\chi^{(2)}$ nonlinearity was reported almost simultaneously by our research group [4] and a research group at the Karlsruhe Institute of Technology (KIT) [30]. Following these publications, a collaboration was set up for an in-depth analysis and comparison of the results. The results of this collaboration were published in [5]. The largest $\chi^{(2)}$ tensor component observed in second-harmonic generation experiments was $\chi_{zzz}^{(2)} = 1.2\,\mathrm{pm/V}$ at a fundamental wavelength of $800\,\mathrm{nm}$.

4.2.1 Materials and deposition

The materials A, B, and C are chosen from table 4.1. These materials are chosen because of the availability of well established ALD processes, the possibility of deposition in the same reactor, the overlapping of the ALD windows, and the transparency of the materials down to the visible wavelength range. When deposited by ALD on amorphous substrates, these materials are typically amorphous or polycrystalline with a centrosymmetric phase [10].

The largest effective $\chi^{(2)}$ nonlinearity was found for a nanolaminate with A = TiO_2, B = Al_2O_3, and C = In_2O_3. This is the nanolaminate reported in [4] and [5]. For this nanolaminate and the nanolaminate fabricated at KIT, consisting of TiO_2, Al_2O_3, and HfO_2 [5, 30], a detailed error analysis of the $\chi^{(2)}$ tensor components measured in SHG experiments has been performed [5]. Other material combinations have been tested, but without improvements in the $\chi^{(2)}$ nonlinearity. Also these results will briefly be discussed below.

Material	E_g (eV)	n (at $\lambda = 633\,\mathrm{nm}$)	
		Literature	Measured
Al_2O_3	6.7-8.7 [2]	1.6-1.8 [31]	1.5
HfO_2	5.5-6.0 [2]	1.7-2.1 [32]	2.2
In_2O_3	3.5-3.7 [33]	1.8-2.2 [34]	2.1
SiO_2	8.9-9.0 [2]	~ 1.5 [2]	1.4
TiO_2	3.05-3.3 [2]	1.8-2.6 [2, 35]	2.4

Table 4.1: Bandgap energies E_g and refractive indices n for several oxides. For the refractive index, both literature values and values obtained from ellipsometry measurements are given. The measured oxides were deposited by plasma-enhanced ALD at 120 °C.

The fabrication procedures for our (referred to as UGent's) and KIT's ABC-type nanolaminate with the largest $\chi^{(2)}$ nonlinearity, as reported in [5], are as follows.

UGent sample fabrication The UGent nanolaminates are deposited through plasma-enhanced atomic layer deposition on $500\,\mu\mathrm{m}$ BOROFLOAT® 33 substrates (a type of glass). The materials A, B and C are TiO_2, Al_2O_3 and In_2O_3. After cleaning the glass substrate in O_2 plasma, the deposition is done by alternating $10\,\mathrm{s}$ pulses of the corresponding metal-organic precursor at a pressure of $6.0 \times 10^{-5}\,\mathrm{bar}$ and O_2 plasma pulses at $1.2 \times 10^{-5}\,\mathrm{bar}$. The substrate temperature is 120 °C throughout the full deposition process. The plasma is generated at an RF (radio frequency) power of 200 W and a frequency of $13.56\,\mathrm{MHz}$. The precursors used for Ti, Al and In are tetrakis(dimethylamino)titanium 99% (Strem Chemicals P.Nr. 93-2240), trimethylaluminum 97% (Strem Chemicals P.Nr. 93-1360) and tris(2,2,6,6-tetramethyl-3,5-heptanedionato)indium 99% (Strem Chemicals P.Nr. 49-2200). The number of cycles for each TiO_2, Al_2O_3 and In_2O_3 layer are 12, 7 and 70. This gives individual layer thicknesses of about $0.9\,\mathrm{nm}$. The ABC period is repeated 24 times which gives a total of $24 \times (12 + 7 + 70) = 2136$ ALD cycles. Ellipsometry and transmission electron microscopy (TEM) measurements indicate a total nanolaminate thickness of $66\,\mathrm{nm}$.

KIT sample fabrication The substrates for the KIT samples are borosilicate glass of the first hydrolytic class with a thickness of $170\,\mu\mathrm{m}$ for SHG measurements and silicon wafers for ellipsometry measurements. Before deposition, the substrates are cleaned with acetone and dry-blown by N_2. In order to limit deposition on the substrate front side, the back surface is covered with high temperature resistant masking tape. The films are fabricated by ALD using a Savannah 100 system by Cambridge Nanotech at a deposition temperature of 150 °C. The precursors for Al, Hf and Ti and O are trimethyaluminum 97% (Sigma-Aldrich P.Nr. 257222), tetrakis(dimethylamido)hafnium(IV) $\geq$99.99% (Sigma-Aldrich P.Nr. 455199), titanium(IV) isopropoxide 99.999% (Sigma-Aldrich P.Nr. 377996) and hydrogen peroxide 30% (Merck P.Nr. 107209), respectively. The reaction chamber is constantly flushed with $20\,\mathrm{sccm}$ of Ar, unless differently specified. Further parameters are given in table 4.2. The sample consists of 32 ABC macrocycles. The numbers of growth cycles for the individual layers in each macrocycle are 8, 8 and 12 for Al_2O_3, HfO_2 and TiO_2 corresponding to estimated layer thicknesses of $0.9\,\mathrm{nm}$, $0.9\,\mathrm{nm}$ and $0.3\,\mathrm{nm}$, respectively. Ellipsometry measurements indicate a total nanolaminate thickness of $75\,\mathrm{nm}$.

Precursor for	Aluminum	Titanium	Hafnium	Oxygen
Temperature (°C)	not heated	80	75	not heated
Pulse duration (s)	0.015	0.1	0.15	0.015
Wait time after pulse (s)	20	see below	20	20

Table 4.2: Parameters used for ALD. The vacuum valve was closed before the insertion of the titanium precursor and reopened two seconds later; subsequently the chamber was flushed for $20\,\mathrm{s}$ with $100\,\mathrm{sccm}$ of argon.

TEM images of UGent's TiO_2/Al_2O_3/In_2O_3 nanolaminate are shown in figure 4.4. A layered structure is visible. The nanolaminate has also been subjected to an X-ray analysis. X-ray reflectivity (XRR) measurements and X-ray diffraction (XRD) θ-2θ scans have been performed. Although different tools are used for the XRR and XRD θ-2θ scans, the principle of operation is the same and is illustrated in figure 4.5. X-rays are incident onto a sample with an angle θ between the sample plane and the incident X-rays (note that this angle θ is different from the usual definition in optics, where the angle of incidence is defined with respect to the surface normal). The reflected X-rays at the same angle θ are being detected. In a measurement, the angle θ will be varied, and the reflected X-ray intensity measured as a function of this varying angle. In XRR measurements, only small angles θ (up to a couple degrees) are considered. From the reflectivity measurement, layer thicknesses, roughness, refractive indices, and electron densities can be inferred (when using the proper model). The XRR technique has similarities with ellipsometry. Standard X-ray diffractometers typically do not allow for accurate measurements at the small angles θ considered in XRR measurements. XRD measurements are used to identify the crystalline phases in a sample. At particular angles θ, the X-rays reflecting off the lattice planes will interfere constructively, resulting in a sharp peak in the XRD spectrum. This phenomenon can be described by the Bragg equation [36]

$$2d\sin\theta = n\lambda \tag{4.1}$$

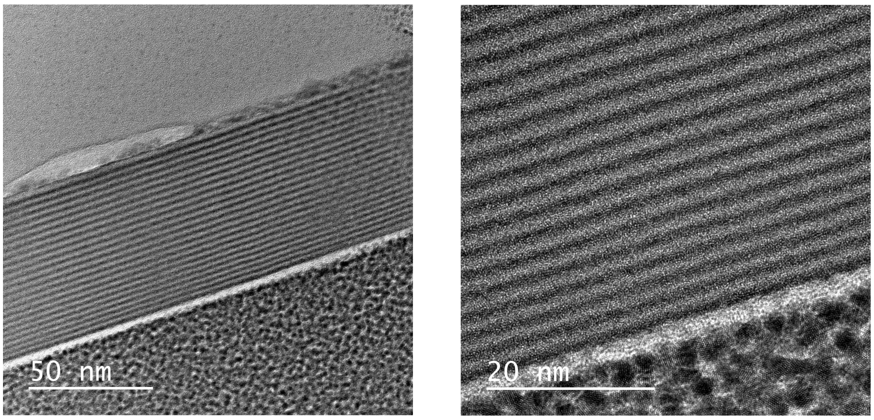

Figure 4.4: TEM images of a $TiO_2/Al_2O_3/In_2O_3$ nanolaminate with estimated individual layer thicknesses of $0.9\,\mathrm{nm}$. Credits to Prof. Katarzyna Komorowska from the Wroclaw Research Centre EIT+.

where d is the lattice spacing, λ the X-ray wavelength, and n an integer. In standard XRD θ-2θ scans, only the lattice planes parallel to the sample plane can be identified. The K_α lines of copper are often used for monochromatic X-ray sources, corresponding to a wavelength of $1.54\,\text{Å}$. The results of the XRR and XRD measurements on the $TiO_2/Al_2O_3/In_2O_3$ nanolaminate are shown in figure 4.6(a) and 4.6(b), respectively. The small fringes in figure 4.6(a) result from the interference of the X-rays reflected off the nanolaminate/glass interface and the nanolaminate/air interface. The fringe spacing $\Delta(2\theta)$ is approximately $0.13°$ or $0.0023\,\mathrm{rad}$. This gives a nanolaminate thickness of

$$d \approx \frac{\lambda}{\Delta(2\theta)} \approx \frac{0.154\,\mathrm{nm}}{0.0023} \approx 68\,\mathrm{nm} \tag{4.2}$$

which corresponds well to the thickness of $66\,\mathrm{nm}$ obtained from ellipsometry measurements. The peak at $2\theta = 3.22°$ corresponds to a lattice spacing $d = \frac{\lambda}{2\sin\theta} \approx 2.7\,\mathrm{nm}$. This peak can be attributed to the periodically repeated ABC unit cell with thickness $3 \times 0.9\,\mathrm{nm}$. The presence of the peak in the XRR spectrum is a good indication that the nanolaminate has well defined layers. In the XRD θ-2θ scan in figure 4.6(b), no sharp peaks, which would indicate the presence of a crystalline phase, are visible. The broad peaks around $23°$ and $44°$ are coming from the amorphous glass substrate.

The refractive index of the $TiO_2/Al_2O_3/In_2O_3$ nanolaminate (and other nanolaminates) has been extracted from ellipsometry measurements. For these measurements, the nanolaminate was deposited on silicon substrates with a $100\,\mathrm{nm}$ oxide layer. The use of a silicon substrate for ellipsometry instead of glass enhances the signal and allows for easier modeling (due to silicon's large well known re-

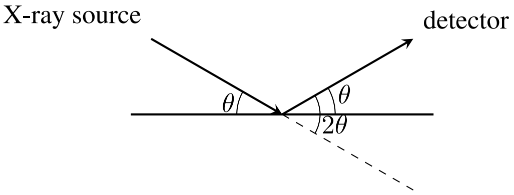

Figure 4.5: Geometry for X-ray analysis.

	Refractive index at			
	$980\,\mathrm{nm}$	$800\,\mathrm{nm}$	$490\,\mathrm{nm}$	$400\,\mathrm{nm}$
ITA (UGent)	$n_o = 2.0119$	$n_o = 2.0300$	$n_o = 2.1323$	$n_o = 2.2260$
	$n_e = 1.8993$	$n_e = 1.9276$	$n_e = 2.0626$	$n_e = 2.1610$
HTA (KIT)	$n = 1.901$	$n = 1.9242$	$n = 1.996$	$n = 2.0194$
UGent glass	$n = 1.4633$	$n = 1.4661$	$n = 1.4766$	$n = 1.4839$
KIT glass	$n = 1.513$	$n = 1.5163$	$n = 1.5297$	$n = 1.5405$

Table 4.3: Refractive indices for UGent's $In_2O_3/TiO_2/Al_2O_3$ nanolaminate (indicated as ITA), KIT's $HfO_2/TiO_2/Al_2O_3$ nanolaminate (indicated as HTA), BOROFLOAT$^{®}$ 33 (UGent glass), and borosilicate glass of the first hydrolytic class (KIT glass). Only the real parts of the refractive index are shown (imaginary part is negligible). The refractive indices of the nanolaminates are determined from ellipsometry measurements (utilizing silicon substrates). The refractive indices of the glass substrates are found in their respective datasheets. For the HTA sample, the use of an anisotropic model for the fitting of the ellipsometry data did not give significant improvements, therefore a simple isotropic model was used.

fractive index and the absence of backside reflections in the visible and part of the near-infrared wavelength region). This improves the quality of the data fitting. The real and imaginary part of the refractive index for the $TiO_2/Al_2O_3/In_2O_3$ nanolaminate are shown in figure 4.7(a) and 4.7(b), respectively. Table 4.3 summarizes the refractive indices of UGent's $TiO_2/Al_2O_3/In_2O_3$ nanolaminate and KIT's $TiO_2/Al_2O_3/HfO_2$ nanolaminate at several wavelengths of interest for the SHG measurements presented hereafter. Also the refractive indices of the glass substrates are shown (as found in the datasheets supplied by the manufacturer).

4.2.2 Second-harmonic generation in thin films

In this subsection the results of second-harmonic generation experiments on the ABC-type nanolaminates (from UGent and KIT) will be presented. The setups, models, and calibration methods used both by the KIT and UGent research groups will be discussed.

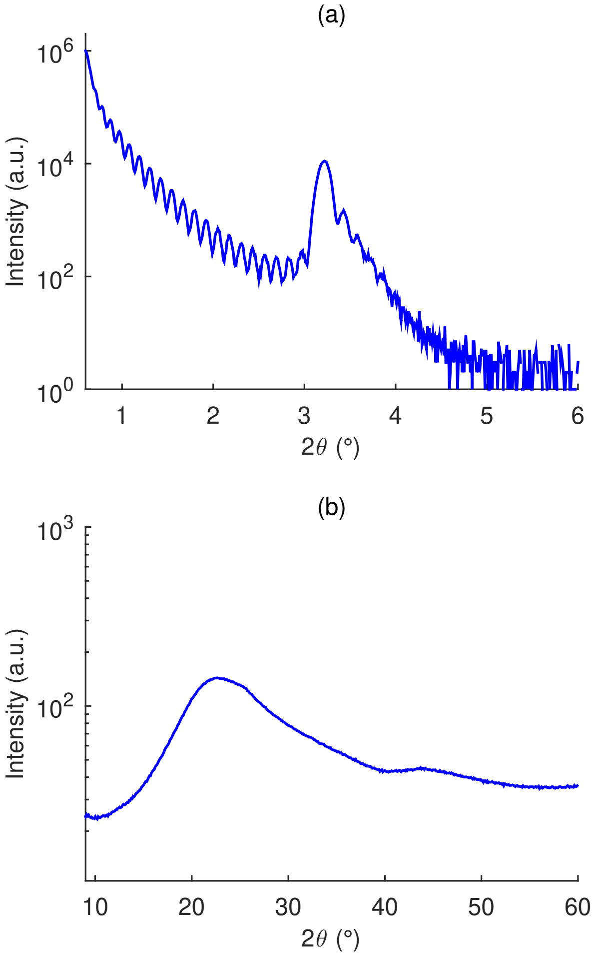

Figure 4.6: (a) XRR scan (using Cu K_α radiation) of a $TiO_2/Al_2O_3/In_2O_3$ nanolaminate with estimated individual layer thicknesses of $0.9\,\mathrm{nm}$. (b) XRD θ-2θ scan (using Cu K_α radiation) of a $TiO_2/Al_2O_3/In_2O_3$ nanolaminate with estimated individual layer thicknesses of $0.9\,\mathrm{nm}$.

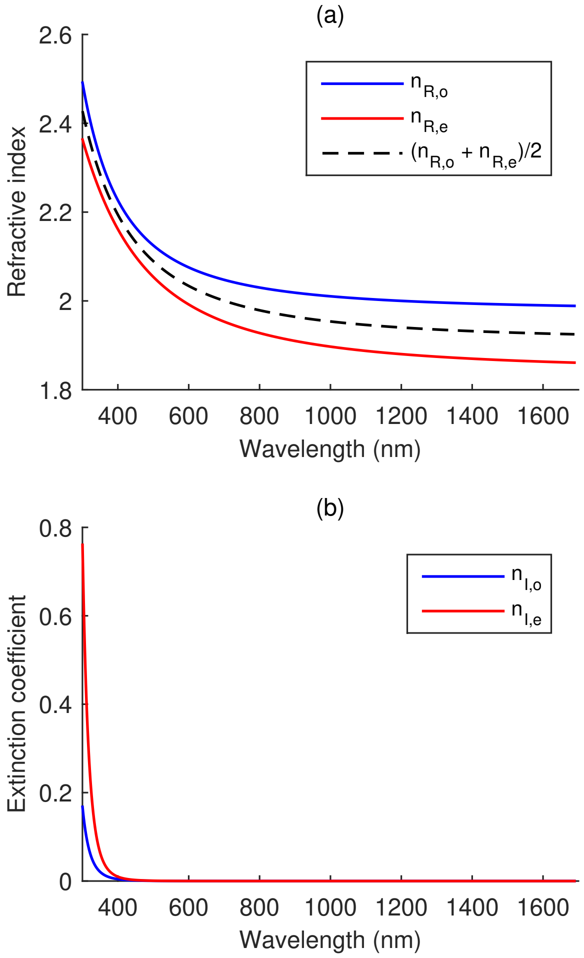

Figure 4.7: Real (a) and imaginary part (b) of the refractive index for a $TiO_2/Al_2O_3/In_2O_3$ nanolaminate extracted from ellipsometry data using a uniaxial Cauchy model. The subscripts o and e stand for ordinary and extraordinary, which refer to the in-plane and out-of-plane directions, respectively. Also the average of the real part of the extraordinary and ordinary index is plotted. For the fitting of the second-harmonic generation measurements, either the average refractive index or the ordinary and extraordinary index will be used, depending on the model being considered.

4.2.2.1 Setups

Due to the limited thickness of the nanolaminates, the generated SH power is quite small, which means a powerful laser combined with sufficiently sensitive detection is necessary for generating and detecting the SH power.

The UGent and KIT setups are shown in figures 4.8(a) and 4.8(b), respectively. In the UGent setup the light source is a commercial Ti:Sapphire laser (Mai Tai HP from Spectra-Physics) emitting $100\,\mathrm{fs}$ pulses at a wavelength of $980\,\mathrm{nm}$, with a repetition rate of $80\,\mathrm{MHz}$ and an average power close to $1\,\mathrm{W}$. A half-wave plate is used to rotate the polarization direction of the linearly polarized laser light to p-polarization. Two parabolic mirrors of $5\,\mathrm{cm}$ focal length are used to focus the laser beam on the sample and to collimate it again after passing through the sample. The focusing brings the beam diameter $(1/e^2)$ down from $1.2\,\mathrm{mm}$ to $52\,\mathrm{\mu m}$. This leaves us with a depth of focus, i.e. $2\times$Rayleigh length, of $4.5\,\mathrm{mm}$, giving enough tolerance for the alignment of the sample in the focal plane. Surrounding the sample there is a long- and shortpass filter. The former filters out any spurious light at wavelengths below $800\,\mathrm{nm}$, while the latter suppresses the laser light at the fundamental wavelength and lets the SH light through. It is important to place these filters right before and after the sample to eliminate parasitic SHG originating in the beam path. The sample is placed on a motorized rotation stage (Thorlabs CR1-Z7) and allows for measurement automation. A lens is placed in front of the femtowatt detector (Thorlabs PDF10A) which compensates for beam displacements induced by the rotation of the sample. There is also a bandpass filter that removes part of the stray light. Moreover it allows to check that the detected light is truly SHG: by tuning the fundamental wavelength until the SH wavelength falls out of the passband of the filter and checking that the detected signal vanishes. During a measurement the sample is rotated and the SH power is measured as a function of the incidence angle.

In the KIT setup, the nonlinear samples are excited using laser pulses from a Ti:Sapphire mode-locked oscillator (*Tsunami* from Spectra-Physics) operating at a repetition rate of $80.5\,\mathrm{MHz}$, a pulse duration of $165\,\mathrm{fs}$ FWHM (full width at half maximum), a center wavelength of $800\,\mathrm{nm}$ and an average power of around $2\,\mathrm{W}$. The excitation power can be set by rotating a half-wave plate which is followed by a polarizing beamsplitter cube. A quarter-wave plate is used to get a circularly polarized beam. Subsequently, a wire-grid polarizer sets the beam at a constant power to a linear polarization at an angle tunable between $0°$ (s-polarized) and $90°$ (p-polarized). The laser beam is chopped to allow for lock-in detection and passes a longpass filter that removes potential parasitic SHG prior to the sample. The fundamental pump beam is then loosely focused onto the sample to a spot diameter $(1/e^2)$ of about $50\,\mathrm{\mu m}$ using a lens with a focal length of $200\,\mathrm{mm}$. The diverging light is collimated by a lens with a focal length of $100\,\mathrm{mm}$ and filtered by a shortpass (cut-off wavelength $700\,\mathrm{nm}$) and a bandpass filter (center wavelength

(a) UGent setup

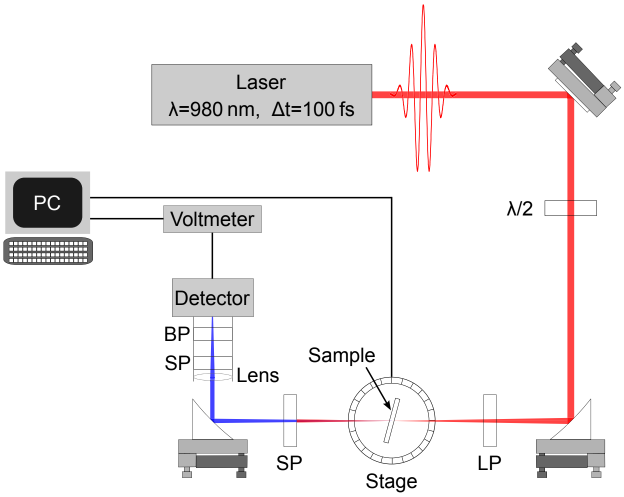

(b) KIT setup

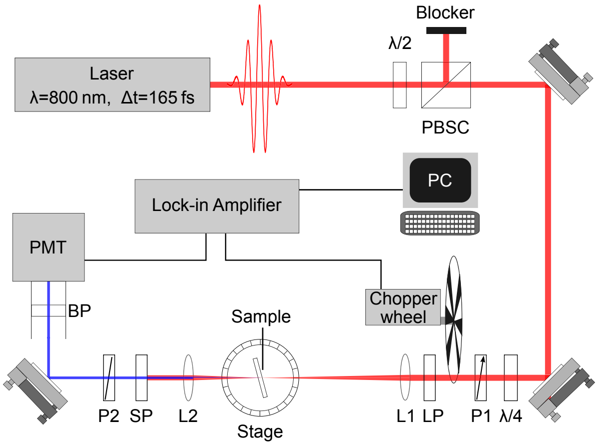

Figure 4.8: Schematic representation of the experimental setups at (a) UGent and (b) KIT for characterizing the second-order nonlinearity of the nanolaminates by means of second-harmonic generation (SHG). PBSC: polarizing beamsplitter cube, P1, P2: wire-grid polarizers, $\lambda/2$, $\lambda/4$: half- and quarter-wave plate, LP: longpass filter, L1, L2: lenses, SP: shortpass filter, BP: bandpass filter, PMT: photomultiplier tube.

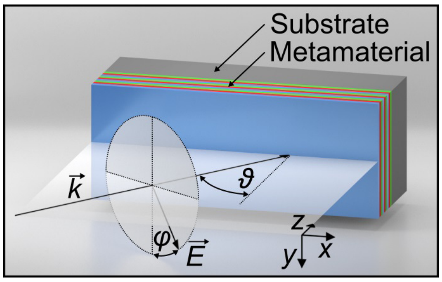

Figure 4.9: Illustration of the excitation geometry including the angle of incidence ϑ and the polarization angle φ. Incident s-polarization corresponds to $\varphi = 0°$, p-polarization to $\varphi = 90°$. Figure reproduced from [30].

$400\,\mathrm{nm}$, spectral width $40\,\mathrm{nm}$). Finally, the SH power is detected using a Hamamatsu R4332 photomultiplier tube. To distinguish between s- and p-polarized SH light, a wire-grid polarizer is placed in the beam path between the sample and the photomultiplier tube. The sample is mounted on a rotation stage which allows to set the angle of incidence. In addition, the sample mount features two goniometers that can be used to correct for tilt of the sample relative to the fundamental beam and relative to the rotation axis of the rotation stage.

4.2.2.2 Models and calibration

The individual A, B and C layers of the nanolaminate are not considered in the analysis, instead an effective medium approach is used. Since these ABC-type materials have ∞m symmetry with respect to the film normal, the non-vanishing $\chi^{(2)}$ tensor components for SHG are $\chi^{(2)}_{xxz} = \chi^{(2)}_{yyz} = \chi^{(2)}_{xzx} = \chi^{(2)}_{yzy}$, $\chi^{(2)}_{zxx} = \chi^{(2)}_{zyy}$ and $\chi^{(2)}_{zzz}$, where z is the film normal and x and y are two orthogonal in-plane directions, see figure 4.9. We assume that these tensor elements are real as we are working at wavelengths far from resonance.

The SH electric field components generated in a thin film with in-plane isotropy (∞m symmetry) can be expressed as

$$A_{2\omega,\mathrm{out},p} = fA^2_{\omega,\mathrm{in},p} + gA^2_{\omega,\mathrm{in},s} \tag{4.3}$$

$$A_{2\omega,\mathrm{out},s} = hA_{\omega,\mathrm{in},s}A_{\omega,\mathrm{in},p} \tag{4.4}$$

where p and s stand for the p- and s-polarized components and $A_{\omega,\mathrm{in}}$ refers to the electric field amplitude of the incident fundamental beam (see sections 3.2 and 3.3). The quantities f, g and h are coefficients that depend on the nonlinear susceptibility tensor components, the angle of incidence ϑ, the linear optical properties, the frequency and layer thicknesses. In the UGent setup, we are working with p-polarized laser light, therefore the generated SH waves are also p-polarized. In the KIT setup, a mixture of p- and s-polarized light is used.

In the UGent model, two contributions to the total SH signal are considered: SH waves generated at the front interface of the sample, where the thin film is deposited, and SH waves generated at the back glass/air interface. Furthermore, the thin film is assumed to have zero thickness. This translates into a physical model where polarized sheets are located at the front and back interface of the sample. The nonlinearities are described by surface second-order susceptibility tensors χ_s^i for the air/thin film/glass ($i = \mathrm{ABC}$) and the glass/air interface ($i = \mathrm{glass}$). In our definition of χ_s^i, the nonlinear polarization is defined with respect to the electric fields inside the thin film (for the front interface) and inside the glass (for the back interface). The surface susceptibility of the thin film is converted to a bulk susceptibility by dividing χ_s^{ABC} by the thin film thickness. We neglect multiple reflections (inside thin film and glass substrate) and we also do not take into account the birefringent character of the thin films. Instead we use an average refractive index. To justify these simplifications, we compared this model to a more advanced model taking into account reflections, anisotropy and finite film thickness, see section B.4, showing the limited impact of these factors. When including these effects, the involved equations become cumbersome and less straightforward to interpret physically. Intuitively, one can understand that the zero film thickness is a good approximation for films much thinner than the wavelength and the coherence length. As we are dealing with small refractive index contrasts ($n_{\mathrm{glass}} \approx 1.5$ and $n_{\mathrm{ABC}} \approx 2$), reflections will also be small as long as the incidence angle is not too large. For p-polarized light, the reflection only rises significantly once Brewster's angle is passed. Our analysis shows that we can safely neglect reflections if we keep the incidence angle below 70°. For a monochromatic p-polarized plane wave at the fundamental frequency with electric field amplitude $A_{\omega,\mathrm{in}}$ incident on the sample, we can find the following expression for the transmitted electric field at the SH frequency (see section 3.2)

$$\begin{aligned}
A_{2\omega,\mathrm{total}} &= A_{2\omega,\mathrm{front}} + A_{2\omega,\mathrm{back}} \\
&= j\frac{\omega}{2c} t_{\mathrm{air,ABC}}^2 A_{\omega,\mathrm{in}}^2 \\
&\quad \left[\frac{T_{\mathrm{ABC,glass}} T_{\mathrm{glass,air}}}{N_{\mathrm{ABC}} \cos\left(\Theta_{\mathrm{ABC}}\right)} \chi_{s,\mathrm{eff}}^{\mathrm{ABC}} \exp\left(-j \frac{2\omega N_{\mathrm{glass}} \cos\left(\Theta_{\mathrm{glass}}\right)}{c} L_{\mathrm{glass}} \right) \right. \\
&\quad - \left. \frac{t_{\mathrm{ABC,glass}}^2 T_{\mathrm{glass,air}}}{N_{\mathrm{glass}} \cos\left(\Theta_{\mathrm{glass}}\right)} \chi_{s,\mathrm{eff}}^{\mathrm{glass}} \exp\left(-2j \frac{\omega n_{\mathrm{glass}} \cos\left(\theta_{\mathrm{glass}}\right)}{c} L_{\mathrm{glass}} \right) \right]
\end{aligned} \tag{4.5}$$

with $\chi^i_{s,\mathrm{eff}}$ the effective surface second-order susceptibility defined as

$$\begin{aligned}\chi^i_{s,\mathrm{eff}} &= \chi^i_{s,xxz}\sin(2\theta_i)\cos(\Theta_i) + \chi^i_{s,zxx}\sin(\Theta_i)\cos^2(\theta_i)\\ &\quad + \chi^i_{s,zzz}\sin^2(\theta_i)\sin(\Theta_i)\\ &\approx \left(\chi^i_{s,zxx} + 2\chi^i_{s,xxz}\right)\sin(\Theta_i)\cos^2(\theta_i) + \chi^i_{s,zzz}\sin^2(\theta_i)\sin(\Theta_i)\end{aligned} \tag{4.6}$$

In these relations, parameters specified at the fundamental frequency ω (SH frequency 2ω) are written in lower case letters (capital letters). The quantities $T_{i,j}$ and $t_{i,j}$ are the Fresnel transmission coefficients (for p-polarized light) propagating from medium i to j, N_i and n_i are the refractive indices of medium i, Θ_i and θ_i are the propagation angles with respect to the surface normal z, L_{glass} is the thickness of the glass substrate and c is the speed of light. The approximation in equation 4.6 can be done because $\theta_i \approx \Theta_i$ for samples with low dispersion. This also means that $\chi^{\mathrm{ABC}}_{s,zxx}$ and $\chi^{\mathrm{ABC}}_{s,xxz}$ cannot be determined separately in the UGent measurement. Instead, we use the combined value $A^{\mathrm{ABC}}_{s,zx} = \chi^{\mathrm{ABC}}_{s,zxx} + 2\chi^{\mathrm{ABC}}_{s,xxz}$ as a fitting parameter. Using the non-approximated version of equation 4.6 in the regression analyis of the data leads to diverging results. In principle, $\chi^{\mathrm{ABC}}_{s,zxx}$ and $\chi^{\mathrm{ABC}}_{s,xxz}$ can be determined separately even for low-dispersion materials by studying the polarization signature of carefully chosen polarization combinations for the input and/or output beams. For example, if an s-polarized fundamental beam is used, only $\chi^{\mathrm{ABC}}_{s,zxx}$ will be probed. But in practice, it is difficult to obtain reliable information from this type of measurements in the UGent setup, as the SH powers are close to the detection limit for the considered samples.

As we rotate the sample and detect the SH power, the front and back contributions will interfere resulting in an angle-dependent fringe pattern. These interference fringes form the basis of the UGent calibration method and can be used for $\chi^{(2)}$ extraction. A reference measurement needs to be done on a blank glass substrate to determine its surface second-order susceptibility $\chi^{(2)}_s$. For BOROFLOAT® 33, this measurement and the obtained $\chi^{(2)}_s$ values are shown in section B.1. For several other types of glass, the surface nonlinear susceptibility can be found in [37]. The average detected power is given by $P_{2\omega} = K_1 \left|A_{2\omega,\mathrm{total}}\right|^2$, where K_1 is a function of the pulse duration, the repetition rate of the laser, the spot size and the transmission of the optics. As it can be difficult to know all these properties accurately, it is often preferred to determine K_1 from a calibration measurement. In the UGent calibration method, we use the known nonlinear susceptibility of the back glass/air interface, to fit K_1 and the unknown susceptibility tensor elements of the thin film simultaneously. However, this calibration method cannot be used for films with a very strong nonlinear response, since the interference fringes will no longer be discernible.

Equation 4.5 is only strictly valid for monochromatic waves. When working with short laser pulses, there will be a temporal walk-off between the SH pulse generated at the front and back surface of the sample which equation 4.5 does not account for. The pulse at the fundamental wavelength will travel at a different group velocity through the substrate than the SH pulse generated at the front and thus there will be a small delay between both generated SH pulses. This reduces the depth of the interference fringes. If this effect is not taken into account, it will result in an overestimation of $\chi^{(2)}$ of the thin film. The temporal walk-off effect is implemented in the model by introducing sech^2 pulses [38]

$$P_{2\omega} = K_2 \int_{-\infty}^{+\infty} \left| A_{2\omega,\mathrm{front}} \mathrm{sech}^2 \left(\frac{t}{\frac{\Delta t}{2\ln(1+\sqrt{2})}} \right) + A_{2\omega,\mathrm{back}} \mathrm{sech}^2 \left(\frac{t + t_{\mathrm{walk-off}}}{\frac{\Delta t}{2\ln(1+\sqrt{2})}} \right) \right|^2 \mathrm{d}t \tag{4.7}$$

with Δt the FWHM pulse duration, $t_{\mathrm{walk-off}}$ the walk-off time and K_2 again a calibration constant. The walk-off time increases for increasing incidence angles and can be expressed as $t_{\mathrm{walk-off}} = t_{\mathrm{walk-off},0}/\cos(\theta_{\mathrm{glass}})$, with $t_{\mathrm{walk-off},0}$ the walk-off time for normal incidence.

The KIT model is based on the approach of Herman and Hayden [39] which solves the nonlinear wave equation and satisfies the boundary conditions for the SH wave at all interfaces of the sample: at the air/film, the film/substrate, and the substrate/air interface. The approach has been generalized for arbitrary polarization of the fundamental pump beam [30]. The model takes into account the thickness of the nanolaminate and therefore also the phase mismatch between fundamental and SH wave which becomes of importance for thick or very dispersive nonlinear films. However, the effect of multiple reflections inside the nanolaminate as well as inside the glass substrate at both the fundamental and SH frequency are neglected due to the small index difference. In addition, the birefringence of the nanolaminate is neglected. Also, the formalism does not take into account the SH wave that is generated by the second-order nonlinearity of the substrate/air interface. For the p/s-polarized peak SH power which is generated in the sample the following expression is derived

$$P_{2\omega}^{p/s,\mathrm{peak}} = \underbrace{\frac{1}{S \Delta t^2 f_{\mathrm{rep}}^2}}_{\alpha} \frac{2 \left((\sin(\varphi))^2 \, (t^p_{\mathrm{air,ABC}})^2 + (\cos(\varphi))^2 \, (t^s_{\mathrm{air,ABC}})^2 \right)^2 (T^{p/s}_{\mathrm{ABC,glass}})^2 (T^{p/s}_{\mathrm{glass,air}})^2}{\epsilon_0 c (N_{\mathrm{ABC}} \cos(\Theta_{\mathrm{ABC}}))^2} \left(\chi^{p/s}_{\mathrm{eff}} \frac{2\pi L}{\lambda} P^2_{\omega,\mathrm{in}} \frac{\sin(\Psi)}{\Psi} \right)^2 \tag{4.8}$$

Parameters specified at the fundamental frequency ω (SH frequency 2ω) are written in lower (upper) case letters. $t_{i,j}^{p/s}$ and $T_{i,j}^{p/s}$ are the Fresnel transmission coefficients (for p/s-polarized light) propagating from medium i to j, and n_i and N_i are the refractive indices of medium i. The constant c is the vacuum speed of light, S is the spot size of the laser at the focus, Δt is the FWHM of the temporal pulse and f_{rep} is the repetition rate of the laser. The quantity $P_{\omega,\text{in}}$ corresponds to the average incident laser power outside the nonlinear film, L is the thickness of the nonlinear film, λ is the vacuum wavelength of the fundamental beam and φ is the pump polarization angle in air with $\varphi = 0°, 90°$ for s- and p-polarization, respectively. Possible phase mismatch between fundamental and SH waves is accounted for by the quantity $\Psi = \frac{2\pi L}{\lambda}(n_{\text{ABC}}\cos(\theta_{\text{ABC}}) - N_{\text{ABC}}\cos(\Theta_{\text{ABC}}))$, where θ_{ABC} and Θ_{ABC} are given by Snell's law $\sin(\theta_{\text{ABC}}) = \frac{1}{n_{\text{ABC}}}\sin(\vartheta)$ and $\sin(\Theta_{\text{ABC}}) = \frac{1}{N_{\text{ABC}}}\sin(\vartheta)$ with the angle of incidence ϑ (see section 3.1). The quantity α is independently determined by a reference measurement. This is advantageous because of the potentially inaccurately determined spot size S and pulse width Δt of the fundamental beam. The parameter $\chi_{\text{eff}}^{p/s}$ is the effective second-order susceptibility for p/s-polarized SHG, which takes the following form for ∞m symmetry

$$\begin{aligned}
\chi_{\text{eff}}^{p} = &-\frac{1}{2}\big[\chi_{xxz}\cos(\Theta_{\text{ABC}})\sin(2\theta_{\text{ABC}})\sin^2(\varphi') \\
&+\chi_{zxx}\sin(\Theta_{\text{ABC}})\big(\cos^2(\theta_{\text{ABC}})\sin^2(\varphi')+\cos^2(\varphi')\big) \\
&+\chi_{zzz}\sin(\Theta_{\text{ABC}})\sin^2(\theta_{\text{ABC}})\sin^2(\varphi')\big] \\
\chi_{\text{eff}}^{s} = &-\frac{1}{2}\chi_{xxz}\sin(\theta_{\text{ABC}})\sin(2\varphi')
\end{aligned} \tag{4.9}$$

In this relation, the quantity φ' is the polarization angle of the pump inside the nonlinear material which is defined by $\tan(\varphi') = \frac{t^p_{\text{air,ABC}}}{t^s_{\text{air,ABC}}}\tan(\varphi)$. The excitation geometry is depicted in figure 4.9 where also φ and ϑ are defined.

To determine the second-order nonlinearity of a sample, the s- and p-polarized SH power is recorded as a function of the polarization of the fundamental beam φ for a fixed angle of incidence. The detected s- and p-polarized SH power are fitted simultaneously with the theoretical expressions presented in equation 4.8, where the three independent tensor elements of $\chi^{(2)}$ are the corresponding fitting parameters. The parameter α is determined in an independent SHG measurement of a Y-cut quartz crystal with known second-order nonlinearity of $\chi_{XXX}^{\text{SiO}_2} = 0.6\,\text{pm/V}$ [40] (see section B.2). This is done immediately after the $\chi^{(2)}$ measurement on the nanolaminate in order to avoid the influence of possible laser fluctuations.

4.2.2.3 Measurement results and discussion

Before determining the values of the second-order susceptibility, we will show that the ABC-type nanolaminates indeed have an effective bulk $\chi^{(2)}$ nonlinear-

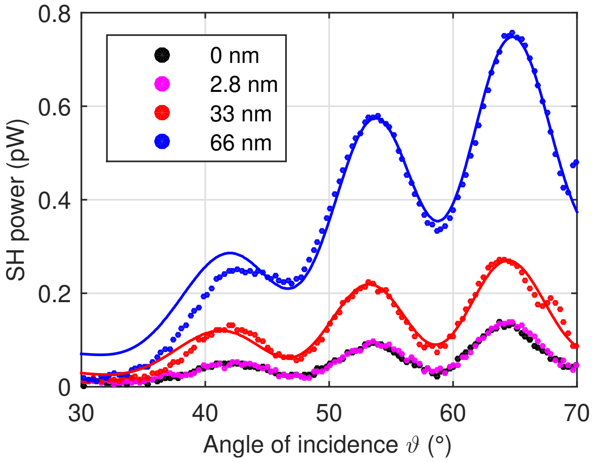

Figure 4.10: Detected second-harmonic power (average) as a function of the angle of incidence ϑ for UGent $TiO_2/Al_2O_3/In_2O_3$ nanolaminates with varying total thicknesses (individual layer thicknesses of approximately $0.9\,\mathrm{nm}$). The corresponding nanolaminate thicknesses are indicated in the figure legend. $0\,\mathrm{nm}$ corresponds to a blank BOROFLOAT® 33 glass substrate. The dots are the measurement data and the full lines the fitted curves. SHG measurements are done on the UGent setup.

ity. Figure 4.10 shows the measured SH power as a function of the angle of incidence ϑ for UGent $TiO_2/Al_2O_3/In_2O_3$ nanolaminates with varying total thicknesses (individual layer thicknesses remain fixed at approximately $0.9\,\mathrm{nm}$). The SH power clearly goes up with increasing thickness, as expected for a bulk $\chi^{(2)}$ nonlinearity. In addition, the fitting of the data for the $33\,\mathrm{nm}$ and $66\,\mathrm{nm}$ thick nanolaminate gives $\chi^{(2)}_{s,zzz}(66\,\mathrm{nm}) \approx 2\chi^{(2)}_{s,zzz}(33\,\mathrm{nm})$ for the surface nonlinearity, or $\chi^{(2)}_{zzz}(66\,\mathrm{nm}) \approx \chi^{(2)}_{zzz}(33\,\mathrm{nm})$ for the corresponding bulk nonlinearity.

The KIT research group also demonstrated that the effective bulk $\chi^{(2)}$ nonlinearity of ABC-type nanolaminates is proportional to the density of interfaces (i.e. thinner individual layers result in a larger nonlinearity). This is illustrated in figure 4.11. However, for very thin individual layers, the nonlinearity starts going down again. This could be related to not having a closed film for a very small number of ALD cycles. In an attempt to increase the $\chi^{(2)}$ nonlinearity of UGent's $TiO_2/Al_2O_3/In_2O_3$ nanolaminate, the individual layer thickness was decreased to approximately $0.5\,\mathrm{nm}$. Unfortunately, this resulted in negligible SHG (i.e. SH signal similar to a bare glass substrate).

Control samples of simple AB-type nanolaminates or films of a single material also yielded negligible SHG.

Next, the second-order susceptibility of UGent's and KIT's optimized nanolaminates (for which the fabrication details were given in subsection 4.2.1) will be de-

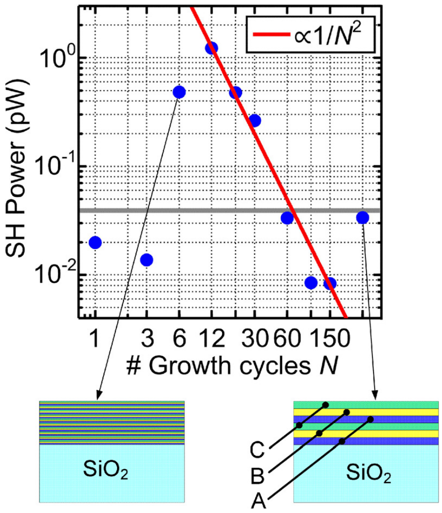

Figure 4.11: Second-harmonic power versus the number of ALD cycles N for each layer of material A = Al_2O_3, B = TiO_2, and C = HfO_2. The deposition of N ALD cycles of material A, B, and C is repeated M times. The total number of ALD cycles $M \times 3 \times N$ is kept constant to 900, so the total thickness of the nanolaminate is approximately equal for all samples. The gray horizontal line represents the SH signal from a bare glass substrate. The SH power shows a maximum for $N = 12$. This corresponds to layer thicknesses of about $1.4\,\mathrm{nm}$, $0.3\,\mathrm{nm}$, and $1.4\,\mathrm{nm}$ for Al_2O_3, TiO_2, and HfO_2, respectively. For $N > 12$ the SH signal decreases approximately like $1/N^2$ until the noise floor is reached. The observed decrease in signal for $N < 12$ is attributed to the fact that the ALD layer of at least one material may not have formed a closed film. The SH signal could be increased further by keeping the number of ALD cycles N for TiO_2 fixed at 12, and reducing it to 8 for Al_2O_3 and HfO_2. Figure reproduced from [30].

termined. UGent's $In_2O_3/TiO_2/Al_2O_3$ nanolaminate will be referred to as ITA, and KIT's $HfO_2/TiO_2/Al_2O_3$ nanolaminate as HTA. Apart from the $\chi^{(2)}$ determination, the weaknesses and strengths of the UGent and KIT measurement techniques will be discussed and the most important sources of errors in the deduction of $\chi^{(2)}$ will be identified. Both the ITA and HTA samples are measured by the UGent and KIT research groups, thus allowing for cross-checking of the obtained values.

Quantifying the second-order susceptibility

The fitting of the measurement data is carried out in MATLAB using a nonlinear least-squares algorithm. The nonlinear regression is done assuming a constant error, i.e. equal weights for all data points.

UGent measurements and fitting The reference measurement to determine the nonlinear surface susceptibility of a blank glass substrate was performed at Tampere University of Technology using a picosecond laser, see section B.1. From this reference measurement, which was calibrated against a Y-cut quartz crystal, we get: $\chi^{\mathrm{glass}}_{s,zzz} = 43 \times 10^{-22}\,\mathrm{m}^2/\mathrm{V}$ and $2\chi^{\mathrm{glass}}_{s,xxz} + \chi^{\mathrm{glass}}_{s,zxx} = 18 \times 10^{-22}\,\mathrm{m}^2/\mathrm{V}$. To find the walk-off time $t_{\mathrm{walk-off},0}$, the measurement of a blank substrate needs to be repeated with the UGent setup, see figure 4.12. The data is fitted using the model with and without walk-off (see equations 4.5 and 4.7, except the ABC-type coating on the front surface needs to be replaced with glass). The fitting parameters are the substrate thickness L_{glass}, the constants K_1 and K_2 and the walk-off time $t_{\mathrm{walk-off},0}$. The fitting of the substrate thickness is necessary to ensure that the extrema of the fringes in the fitted curve are positioned at the right incidence angles. Incidence angles greater than 70° are not considered, since the theoretical model does not hold any more due to the unaccounted reflections. Section B.3 illustrates the consequences for the fitting when larger incidence angles are included. In figure 4.12 we see that the visibility of the fringes is lower for the measurement data than it is for the fitted curve when walk-off is not included in the model. Including the temporal walk-off effect clearly improves the agreement between the measurement and the fitted curve. The regression analysis gives a walk-off time of $t_{\mathrm{walk-off},0} = 45.3\,\mathrm{fs}$. This result will be used later in the fitting of the data of the ABC-type thin films. From the refractive index versus wavelength graph in the datasheet [41] we get 37 fs as a very rough estimate (estimating $\frac{\mathrm{d}n}{\mathrm{d}\lambda}$ graphically), which agrees well with the fitted value.

The measured SH powers and corresponding fitted curves for both the ITA and HTA sample are shown in figure 4.13. The theoretical model is described by equation 4.7, where K_2, L_{glass}, $A^{\mathrm{ABC}}_{s,zx}$ and $\chi^{\mathrm{ABC}}_{s,zzz}$ are the fitting parameters. The fitting results for the ITA sample are: $A^{\mathrm{ABC}}_{zx} = (0.211 \pm 0.011)\,\mathrm{pm/V}$, $\chi^{\mathrm{ABC}}_{zzz} = (0.974 \pm 0.054)\,\mathrm{pm/V}$ and $L_{\mathrm{glass}} = (498.26 \pm 0.16)\,\mu\mathrm{m}$. For the HTA sample we get: $A^{\mathrm{ABC}}_{zx} = (0.6045 \pm 0.0081)\,\mathrm{pm/V}$, $\chi^{\mathrm{ABC}}_{zzz} = (0.6970 \pm 0.0098)\,\mathrm{pm/V}$

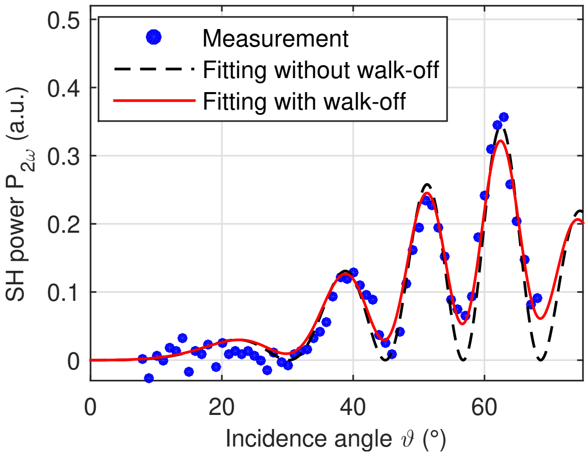

Figure 4.12: Fitting the measurement data for a blank BOROFLOAT® 33 substrate without temporal walk-off (black dashed line) and with walk-off (red full line). Negative SH powers for the measurement data are obtained due to subtraction of background noise. The regression analysis gives us a walk-off of $45.3\,\mathrm{fs}$ and a substrate thickness of $484.97\,\mu\mathrm{m}$. The thickness agrees well with the specified thickness of $(500 \pm 20)\,\mu\mathrm{m}$.

and $L_{\mathrm{glass}} = (170.310 \pm 0.040)\,\mu\mathrm{m}$. The quoted uncertainties are the standard deviations following from nonlinear regression analysis; these only reflect the uncertainty due to statistical intensity fluctuations. The standard deviations are kept low by averaging over many read-outs for a single angle of incidence.

There is also an uncertainty on the incidence angle which can impact the final results. Since we are working with an motorized rotation stage, the relative angle setting is very precise (repeatability $< 1'$ according to specifications). The main uncertainty originates in the setting of the reference angle: after we have placed the sample, we need to manually set the angle corresponding to normal incidence. We estimate that this results in a maximum systematic error of $2°$. Table 4.4 illustrates how this systematic error will influence the retrieved $\chi^{(2)}$ values. The uncertainties are several times larger than the standard deviations following from the nonlinear regression, and they are the main source of uncertainty in the UGent measurements.

Another aspect that needs to be stressed is the importance of proper alignment in this type of measurements. The depth of focus is only $4.5\,\mathrm{mm}$, so care must be taken to avoid the sample from moving out of the laser focus while rotating it. We achieve this by aligning at two widely spaced incidence angles: we maximize the signal for both angles by iteratively adjusting the mirrors in our setup. When the rotation axis of the sample is not positioned in the laser focus, it will cause an apparent shift in the weights of the fitted nonlinear tensor elements, i.e. cer-

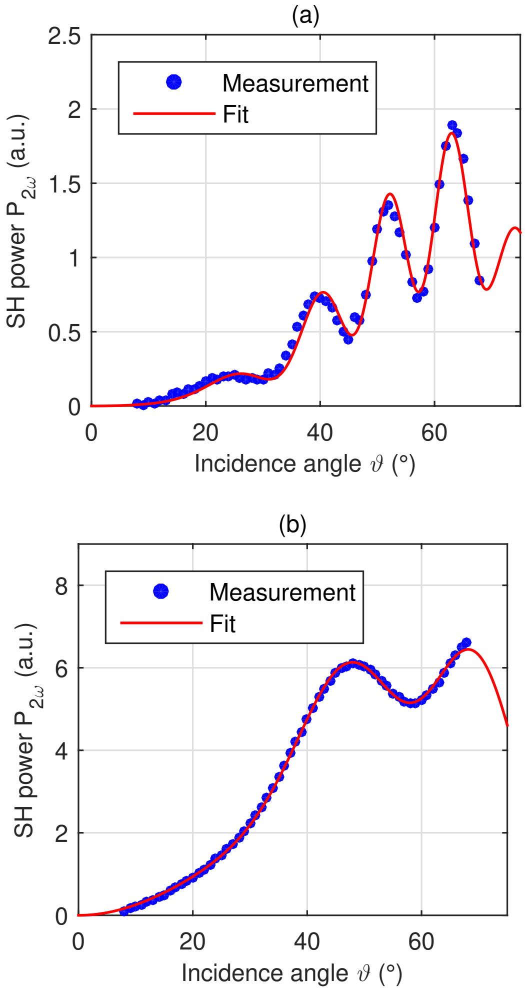

Figure 4.13: Measured and fitted SH power vs incidence angle for (a) ITA sample and (b) HTA sample in the UGent setup (laser wavelength of $980\,\mathrm{nm}$). As the substrate is thinner for the HTA sample, there are fewer interference fringes.

	ITA sample	HTA sample
A_{zx}^{ABC} (pm/V)	0.21 ± 0.04	0.60 ± 0.07
$\chi_{zzz}^{\mathrm{ABC}}$ (pm/V)	1.0 ± 0.2	0.7 ± 0.3
L_{glass} (µm)	498 ± 5	170 ± 1

Table 4.4: Error margins on the bulk susceptibilities and substrate thicknesses as a consequence of the systematic error on the incidence angle ($\pm 2^{\circ}$) for the UGent measurement technique. Results are shown both for the ITA and HTA sample.

tain elements will become smaller, others larger. From simulations we estimated that displacements of the rotation axis with respect to the focus on the order of $1\,\mathrm{mm}$ can cause the tensor elements to change by several 10s of percent, which would make the induced error of similar magnitude to the error due to uncertainty on the incidence angle. To avoid possible alignment issues one can choose to focus the laser beam less tightly, but again this requires a more sensitive detection mechanism.

The reproducibility of the measurements was tested by doing multiple measurements on the same sample. In between measurements the sample was removed from the sample holder and put back into place. The setup was also intentionally misaligned and realigned. Including error boundaries, these measurements gave identical results.

KIT measurements and fitting An advantage of the KIT approach is the simplicity in sample alignment. Since ϑ is constant during a measurement, there is no risk of rotating the sample out of focus. Moreover, the influence of the slightly inhomogeneous sensitivity of the active region of the PMT is eliminated since the SH light spot on the PMT does not move during the measurement.

The most important source of error for the KIT technique is the fact that the KIT model does not take into account interference effects between SH waves emanated from the nanolaminate and the glass back surface. In fact, these interference fringes are also visible in the KIT setup as depicted in figure 4.14 where the p-polarized SH power is plotted as a function of the angle of incidence ϑ for a p-polarized fundamental beam for the HTA and ITA sample. Note that in the KIT setup, a fundamental wavelength of $800\,\mathrm{nm}$ instead of $980\,\mathrm{nm}$ in the UGent setup is used. This is why the interference patterns are different from the ones measured with the UGent setup. In order to estimate the error that is introduced by neglecting the influence of interference, several measurements at different angles of incidence are performed for both the HTA and ITA sample. These angles are chosen such that constructive interference ($\vartheta_{\mathrm{constr.}}$) or destructive interference ($\vartheta_{\mathrm{destr.}}$) occurs. For these two extreme cases the determined value for $\chi^{(2)}$ will be overestimated or underestimated, respectively. An additional measurement at an intermediate angle

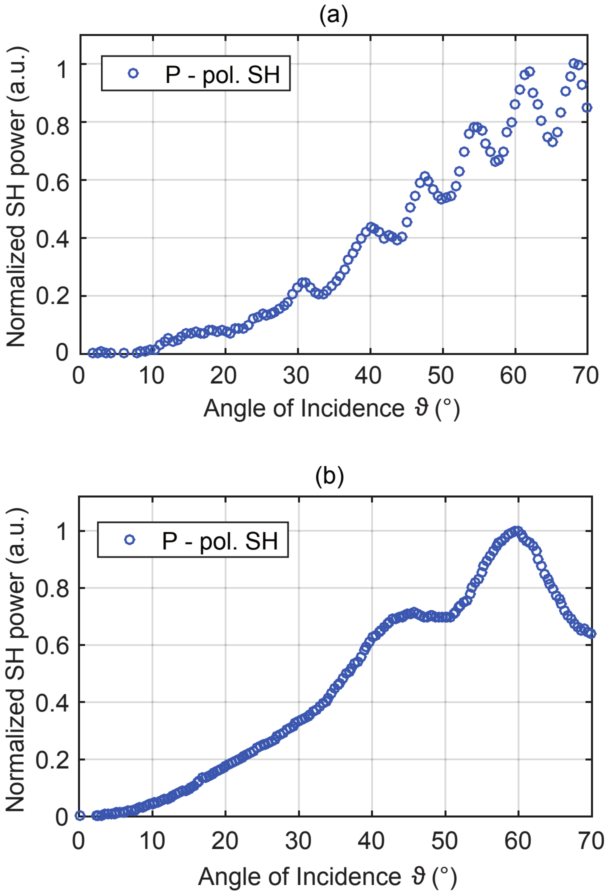

Figure 4.14: p-polarized SH power as a function of the angle of incidence ϑ for p-polarized fundamental beam obtained from (a) the ITA sample and (b) the HTA sample. These measurements are done using the KIT setup (laser wavelength of 800 nm). Both measurements show oscillations in the SH power which can be attributed to interference effects between SH waves generated in the nanolaminate and SH waves generated at the back surface of the glass substrate.

($\vartheta_{\mathrm{inter.}}$) between those two specified angles will give a good indicator of the true value of $\chi^{(2)}$.

HTA	$\vartheta_{\mathrm{constr.}}$ $= 59.8°$	$\vartheta_{\mathrm{inter.}}$ $= 55.8°$	$\vartheta_{\mathrm{destr.}}$ $= 51.1°$	Average
χ_{zzz} (pm/V)	0.862	0.685	0.450	0.667 ± 0.207
χ_{xxz} (pm/V)	0.264	0.262	0.236	0.254 ± 0.016
χ_{zxx} (pm/V)	0.216	0.231	0.227	0.225 ± 0.008

ITA	$\vartheta_{\mathrm{constr.}}$ $= 68.4°$	$\vartheta_{\mathrm{inter.}}$ $= 66.0°$	$\vartheta_{\mathrm{destr.}}$ $= 63.9°$	Average
χ_{zzz} (pm/V)	1.252	1.155	1.088	1.165 ± 0.082
χ_{xxz} (pm/V)	0.168	0.144	0.132	0.148 ± 0.018
χ_{zxx} (pm/V)	0.063	0.030	0.049	0.047 ± 0.017

Table 4.5: Deduced $\chi^{(2)}$ tensor components for different angles of incidence $\vartheta_{\mathrm{constr.}}$, $\vartheta_{\mathrm{destr.}}$ and $\vartheta_{\mathrm{inter.}}$ corresponding to constructive interference, destructive interference and an intermediate case respectively. Results are shown for the HTA and ITA sample. Because the interference from the substrate is not accounted for, different results are obtained for different angles of incidence. The last column shows the average values and the corresponding standard deviations for each tensor component.

Figure 4.15 shows three separate measurements of the s- (triangles) and p-polarized (circles) SH power and the corresponding fitted theoretical expressions (lines) as a function of φ obtained for the ITA and the HTA sample. The measurements are performed for three different angles of incidence where the blue, magenta and red markers and lines correspond respectively to $\vartheta^{\mathrm{ITA}}_{\mathrm{constr.}} = 68.4°$, $\vartheta^{\mathrm{ITA}}_{\mathrm{inter.}} = 66.0°$ and $\vartheta^{\mathrm{ITA}}_{\mathrm{destr.}} = 63.9°$ for the ITA sample and $\vartheta^{\mathrm{HTA}}_{\mathrm{constr.}} = 59.8°$, $\vartheta^{\mathrm{HTA}}_{\mathrm{inter.}} = 55.8°$ and $\vartheta^{\mathrm{HTA}}_{\mathrm{destr.}} = 51.1°$ for the HTA sample. For better visibility of the s-polarized SH power the data sets and corresponding fitting curves are multiplied by a factor of 10. The determined values of the $\chi^{(2)}$ tensor components depend significantly on the angle of incidence ϑ, as summarized in table 4.5 where the last column contains the average value of the determined tensor elements and the corresponding standard deviation. Note that for all deduced tensor elements the error following from curve fitting is well below 10%. It is interesting to observe that for the HTA sample the decrease of the determined value of $\chi^{\mathrm{HTA}}_{zzz}$ is very pronounced when going from constructive to destructive interference. On the other hand, the determined off-diagonal tensor elements vary only little for the three different angles. This finding suggests that the off-diagonal tensor elements of the HTA nanolaminate are much larger than the off-diagonal tensor elements of the glass surface, which would result in ϑ-independent values of these tensor components. Indeed, only minor interference occurs for s-polarized SH power when the fundamental beam polarization is defined by $\varphi = 45°$, in this case only $\chi^{\mathrm{HTA}}_{xxz}$ is addressed, see section B.5. Furthermore, no interference effects are visible for

p-polarized SH power when the fundamental beam is s-polarized, in this case only $\chi_{zxx}^{\mathrm{HTA}}$ is addressed, see section B.6. For the ITA sample the deduced value for $\chi_{zzz}^{\mathrm{ITA}}$ decreases more moderately when changing the angle of incidence from $\vartheta_{\mathrm{constr.}}$ to $\vartheta_{\mathrm{destr.}}$. Additionally, also the calculated value of the off-diagonal tensor element $\chi_{xxz}^{\mathrm{ITA}}$ decreases with decreasing ϑ. In fact, s-polarized SH power for a fundamental beam polarization of $\varphi = 45°$ exhibits major interference effects which can explain this decrease in $\chi_{xxz}^{\mathrm{ITA}}$, see section B.5. The large variation of $\chi_{zxx}^{\mathrm{ITA}}$ is attributed to the fact that the low level of p-polarized generated SH power for s-polarized fundamental beam is close to the detection limit. Note that the visibility of the fringes and therefore this source of error is eliminated for thicker or more strongly nonlinear films.

As an additional source of error, an imprecisely calibrated angle of incidence is investigated. The angle calibration is done by studying the back reflected fundamental beam close to normal incidence and trying to make it overlap with the incident beam by rotating the sample. In order to illustrate the effect on the deduction of $\chi^{(2)}$, an error of $\Delta\vartheta = \pm 1.0°$ will be assumed. Note that using the same technique in the UGent setup gives larger errors, as a focusing element with a smaller focal length is used. The effect is quantified by performing $\chi^{(2)}$ measurements on the ITA and HTA sample at angles of incidence of $\vartheta_0^{\mathrm{ITA}} = 68.4°$ and $\vartheta_0^{\mathrm{HTA}} = 59.8°$ (blue data in figure 4.15) while the data is evaluated at angles of incidence of ϑ_0 and $\vartheta_0 \pm \Delta\vartheta$. The fitting results for $\Delta\vartheta = \pm 1.0°$ are $\chi_{zzz} = (0.86 \mp 0.05)\,\mathrm{pm/V}$, $\chi_{xxz} = (0.264 \pm 0.004)\,\mathrm{pm/V}$ and $\chi_{zxx} = (0.216 \pm 0.004)\,\mathrm{pm/V}$ for the HTA sample and $\chi_{zzz} = (1.25 \mp 0.02)\,\mathrm{pm/V}$, $\chi_{xxz} = (0.169 \pm 0.008)\,\mathrm{pm/V}$ and $\chi_{zxx} = (0.063 \pm 0.003)\,\mathrm{pm/V}$ for the ITA sample. It can be seen that the values for the tensor elements change by roughly 5%. This can be understood as an upper error bound since the error in the angle of incidence of $\Delta\vartheta = \pm 1.0°$ is chosen pessimistically.

The reproducibility of the measurements was also checked by doing multiple measurements on the same sample. The setup was deliberately misaligned and realigned before each measurement. The results of these measurements were in very good agreement with one another.

Lastly, the SHG reference measurement on a Y-cut quartz plate that is necessary for the determination of the quantity α in equation 4.8 is briefly discussed. To validate the stability of the calibration measurement and the corresponding fit, a set of SHG measurements is performed, see section B.2. The fitting results vary by less than 1% for consecutive measurements. Therefore it can be assumed that the calibration technique does not introduce any significant error.

Comparison UGent and KIT measurements The UGent methodology takes into account the interference from the backside of the substrate and it even exploits this for calibration purposes. During a measurement, the sample needs to

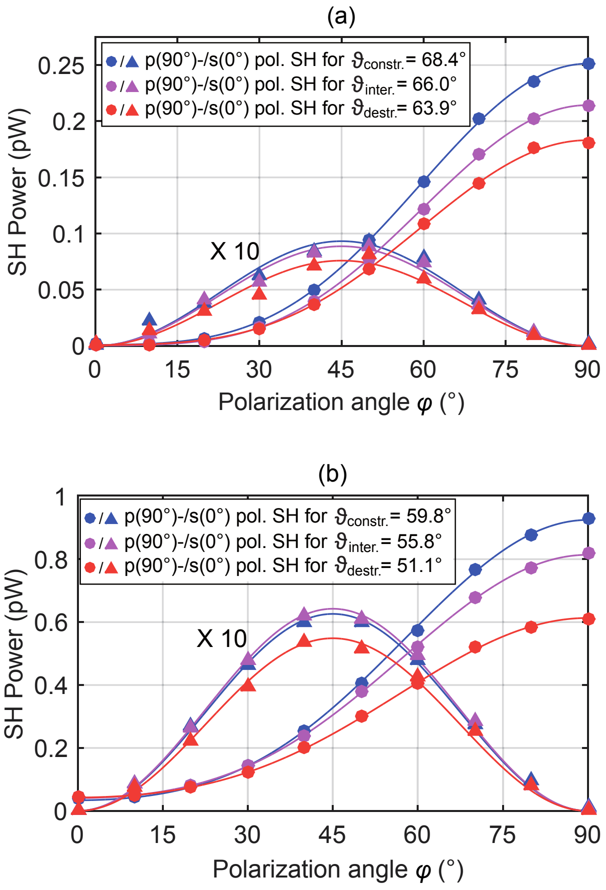

Figure 4.15: s- (triangles) and p-polarized SH power (circles) and corresponding fitting curves (lines) as a function of the polarization angle φ for an average excitation power of $P_{\omega,\mathrm{in}} = 200\,\mathrm{mW}$ obtained from (a) the ITA sample at $(\vartheta^{\mathrm{ITA}}_{\mathrm{constr.}}, \vartheta^{\mathrm{ITA}}_{\mathrm{inter.}}, \vartheta^{\mathrm{ITA}}_{\mathrm{destr.}}) = (68.4^\circ, 66.0^\circ, 63.9^\circ)$ and (b) the HTA sample at $(\vartheta^{\mathrm{HTA}}_{\mathrm{constr.}}, \vartheta^{\mathrm{HTA}}_{\mathrm{inter.}}, \vartheta^{\mathrm{HTA}}_{\mathrm{destr.}}) = (59.8^\circ, 55.8^\circ, 51.1^\circ)$. Here, $\varphi = 0^\circ, 90^\circ$ corresponds to incident s- and p-polarization, respectively. To quantify the impact of interference we perform three measurements at different angles of incidence where $\vartheta_{\mathrm{constr.}}$ and $\vartheta_{\mathrm{destr.}}$ denote the angles of incidence under which constructive and destructive interference occurs, respectively and $\vartheta_{\mathrm{inter.}}$ denotes an intermediate angle of incidence. Note that data and fit of the s-polarized SH power is multiplied by a factor 10 for better visibility.

be rotated, and thus care must be taken when aligning the sample such that it stays in the laser focus. The main source of error in the UGent method is related to the setup rather than the theoretical model, namely the systematic error on the incidence angle. The obtained $\chi^{(2)}$ values and associated overall error margins are $\chi_{zzz}^{\mathrm{ITA}} = (1.0 \pm 0.2)\,\mathrm{pm/V}$ and $A_{zx}^{\mathrm{ITA}} = (0.21 \pm 0.05)\,\mathrm{pm/V}$ for the ITA sample. For the HTA sample we have $\chi_{zzz}^{\mathrm{HTA}} = (0.7 \pm 0.3)\,\mathrm{pm/V}$ and $A_{zx}^{\mathrm{HTA}} = (0.60 \pm 0.08)\,\mathrm{pm/V}$. These overall error margins include the error listed in table 4.4 and the error introduced by curve fitting. By improving the sensitivity of the current setup, the off-diagonal tensor components could be identified separately. This could also allow to focus the beam more loosely, which eases the alignment and leads to a reduced error on the angle.

The KIT technique for $\chi^{(2)}$ determination is very robust against misalignment between the sample and the fundamental beam, since the sample is not moved during the measurement. Additionally, the high detection sensitivity allows to determine the three tensor components individually. The main source of error is due to the fact that the KIT formalism used for the evaluation does not take into account interference effects of the SH waves generated in the nonlinear film and at the glass back surface. The deduced values and corresponding overall error bounds for the tensor components are $\chi_{zzz}^{\mathrm{HTA}} = (0.7 \pm 0.2)\,\mathrm{pm/V}$, $A_{zx}^{\mathrm{HTA}} = (0.73 \pm 0.04)\,\mathrm{pm/V}$ and $\chi_{zzz}^{\mathrm{ITA}} = (1.2 \pm 0.1)\,\mathrm{pm/V}$, $A_{zx}^{\mathrm{ITA}} = (0.34 \pm 0.06)\,\mathrm{pm/V}$ for the HTA and the ITA sample, respectively. The specified error bounds include the error due to interference effects, the errors introduced by curve fitting and the errors due to an imprecise setting of the angle of incidence. The interference effect, the main source of error, is reduced significantly if thicker samples are examined or if samples with higher nonlinearity are introduced.

Finally, we compare the $\chi^{(2)}$ values obtained in the UGent and KIT measurements. Since, the two presented setups use lasers at different wavelengths, we compensate for the dispersion of $\chi^{(2)}$ by considering Miller's rule (see section 2.6). As a reference wavelength we choose the fundamental wavelength used in the KIT setup, i.e. $800\,\mathrm{nm}$. Therefore we need to scale the tensor components determined in the UGent setup by using the relation

$$\chi^{(2)}(800\,\mathrm{nm}) = \frac{(N_{\mathrm{ABC}}(800\,\mathrm{nm})^2 - 1)((n_{\mathrm{ABC}}(800\,\mathrm{nm})^2 - 1))^2}{(N_{\mathrm{ABC}}(980\,\mathrm{nm})^2 - 1)((n_{\mathrm{ABC}}(980\,\mathrm{nm})^2 - 1))^2}\chi^{(2)}(980\,\mathrm{nm}) \tag{4.10}$$

where $\chi^{(2)}$ can be χ_{zzz} or A_{zx}. The $\chi^{(2)}$ values at the reference wavelength of $800\,\mathrm{nm}$ are summarized graphically in figure 4.16. The values for the relevant tensor component χ_{zzz} determined with the different techniques match very well for both the ITA and HTA sample and also for the off-diagonal components the error bounds overlap.

It is interesting to compare these values with the reported values in references [30] and [4]. For the ITA sample, we reported a value of $\chi_{zzz}^{\mathrm{ITA}} = (5 \pm 2)\,\mathrm{pm/V}$

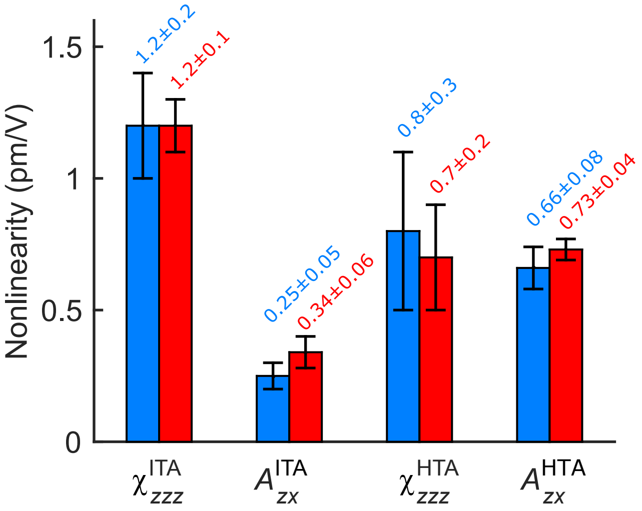

Figure 4.16: Overview of the $\chi^{(2)}$ tensor components of the ITA and HTA nanolaminates obtained from the UGent (blue) and the KIT measurements (red). The tensor components determined in the UGent measurements are scaled according to Miller's rule in order to fairly compare the values at a reference wavelength of $800\,\mathrm{nm}$.

in [4], compared to a value of $\chi_{zzz}^{\mathrm{ITA}} = (1.0 \pm 0.2)\,\mathrm{pm/V}$ presented here (and in [5]). On the one hand, this is caused by the use of a larger reference surface nonlinearity for the glass substrate in [4] (the surface nonlinearity of BK7 calibrated against $\chi_{XYZ}^{(2)}$ of quartz was used). Additionally, the thin film thickness was underestimated. Our ellipsometry measurements indicate a thickness of $66\,\mathrm{nm}$ (confirmed by TEM and XRR) while the initial estimate of $50\,\mathrm{nm}$ used in [4] was based on given ALD growth rates. The remaining discrepancy can be explained by all the factors discussed above with a dominant impact of the temporal walk-off. The HTA sample reported here is nominally identical to the ACB sample with inverted order of growth and adapted thicknesses of the individual layers reported in the main text of [30] for which a dominant $\chi^{(2)}$ tensor element of $\chi_{zzz} = 0.43\,\mathrm{pm/V}$ can be estimated. This is in fair agreement with the value of $\chi_{zzz}^{\mathrm{HTA}} = (0.7 \pm 0.2)\,\mathrm{pm/V}$ reported here (and in [5]). The discrepancy is due to the fact that the effect of SHG from the back surface was not accounted for in [30]. Additionally, in [30] the $\chi^{(2)}$ deduction was done without the reference measurement on quartz which led to an underestimation of $\chi^{(2)}$.

Other material combinations and deposition temperatures

Figure 4.17 shows SHG measurements of ABC-type nanolaminates with different material combinations (and deposition temperatures). The SH power of the tested

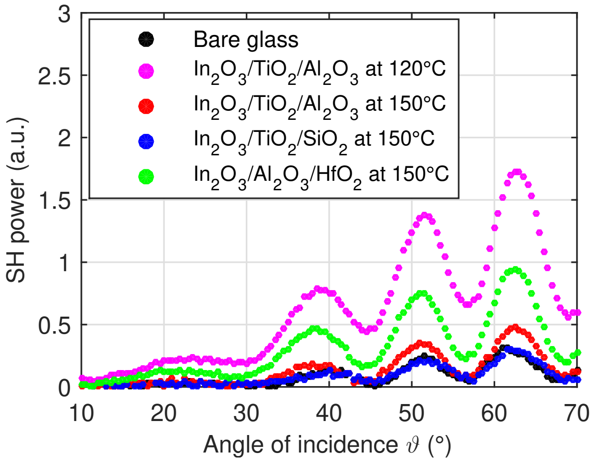

Figure 4.17: SH power versus the angle of incidence for ABC-type nanolaminates with different material combinations. The measurements were conducted on the UGent setup described above. The black dots correspond to a bare glass substrate. The magenta dots correspond to the $In_2O_3/TiO_2/Al_2O_3$ nanolaminate that is described and characterized in detail above (deposited by plasma-enhanced ALD at a substrate temperature of $120\,^{\circ}\mathrm{C}$ with individual layer thicknesses of approximately $0.9\,\mathrm{nm}$ and a total thickness of $66\,\mathrm{nm}$). The other ABC-type nanolaminates are deposited by plasma-enhanced ALD at a substrate temperature of $150\,^{\circ}\mathrm{C}$ with individual layer thicknesses of approximately $0.7\,\mathrm{nm}$. The $In_2O_3/TiO_2/Al_2O_3$ nanolaminate (red) has a total thickness of $49\,\mathrm{nm}$ (determined via ellipsometry), the $In_2O_3/TiO_2/SiO_2$ nanolaminate (blue) has a total thickness of $47\,\mathrm{nm}$, the $In_2O_3/Al_2O_3/HfO_2$ nanolaminate (green) has a total thickness of $51\,\mathrm{nm}$.

ABC-type nanolaminates does not exceed the SH power of the In_2O_3/TiO_2/Al_2O_3 nanolaminate that is described and characterized in detail above (shown in magenta in figure 4.17), also not when compensating for the differences in total thickness. Interestingly, the SH response from the In_2O_3/TiO_2/Al_2O_3 nanolaminate deposited at $150\,^{\circ}\mathrm{C}$ is much smaller (close to response of bare glass) than the response from the In_2O_3/TiO_2/Al_2O_3 nanolaminate deposited at $120\,^{\circ}\mathrm{C}$. The combination of a higher deposition temperature and slightly thinner individual layers ($0.7\,\mathrm{nm}$ versus $0.9\,\mathrm{nm}$) leads to a significant decrease in SH power. Apart from the possibility of not having closed films for thinner layers, the higher substrate temperature can lead to layer intermixing due to diffusion processes, and consequently lead to a smaller SH response. Materials with higher melting temperatures are expected to be less susceptible to intermixing. For the oxides listed in table 4.1, HfO_2 has the highest melting temperature ($\sim$2800 °C), followed by Al_2O_3 ($\sim$2000 °C), In_2O_3 ($\sim$1900 °C), TiO_2 ($\sim$1800 °C), and SiO_2 ($\sim$1700 °C) [42]. For the three nanolaminates in figure 4.17 that were deposited at $150\,^{\circ}\mathrm{C}$, only the In_2O_3/Al_2O_3/HfO_2 nanolaminate gave a SH response significantly larger than the response of a bare substrate. The constituent materials of this nanolaminate correspond to the materials with the highest melting temperatures. Also note that all of the nanolaminates in figure 4.17 contain In_2O_3. The growth rate of In_2O_3 (GPC of $\sim 0.1\,\mathrm{\AA/cycle}$) is roughly an order of magnitude lower than the growth rate of the other oxides used (this is related to the large precursor molecules for indium causing steric hindrance [13]). Longer deposition times could also lead to more intermixing.

4.2.3 Conclusions

A material with an effective bulk $\chi^{(2)}$ nonlinearity can be created from three centrosymmetric materials A, B, and C that lack a bulk $\chi^{(2)}$ nonlinearity. This can be done by layering these materials periodically in an ABCABC... stack, where the thickness of an ABC period is much smaller than the wavelength. We have demonstrated this concept utilizing atomic layer deposition, a low-temperature conformal film growth technique with angstrom-level thickness control that works for virtually any substrate. Thus, these atomic layer deposited ABC-type nanolaminates are suitable for back-end photonic integration and deposition of $\chi^{(2)}$ materials on amorphous SiN waveguide circuits as opposed to traditional nonlinear crystals.

In second-harmonic generation experiments at a fundamental wavelength of $800\,\mathrm{nm}$, a second-order nonlinearity of $\chi^{(2)}_{zzz} = 1.2\,\mathrm{pm/V}$ has been observed for a In_2O_3/TiO_2/Al_2O_3 nanolaminate with individual layer thicknesses of approximately $0.9\,\mathrm{nm}$. The constituent oxides are transparent over the visible and near-infrared wavelength range. Unfortunately, the observed second-order nonlinearity is still quite small and likely insufficient for the realization of efficient integrated $\chi^{(2)}$ devices.

The $\chi^{(2)}$ nonlinearity of atomic layer deposited ABC-type nanolaminates increases with decreasing thickness of the ABC period up to certain point, whereafter it goes down. This limit is thought to be related to the disappearing of the material interfaces due to not having closed films. Also layer intermixing can be a limiting factor. Not considering fabrication issues, the ultimate limit in layer thickness is a monolayer of material, which we are likely already quite close to (a single layer of MoS_2 has a thickness of approximately 3 Å [43]). Therefore, not a lot of gain is expected on this part.

Several combinations of oxides were tested, with no signs of significant improvements in $\chi^{(2)}$. It is thought that high refractive index contrasts between the constituent materials will lead to a larger effective $\chi^{(2)}$ nonlinearity (due to the electric field discontinuity at the interfaces, see section 3.3). The refractive indices of the used materials vary between 1.4 and 2.4 (see table 4.1). Most materials that are transparent in the visible and near-infrared wavelength range have a refractive index that falls within this range or is not far off. If transparency in the visible wavelength range is not a requirement, several other high index materials (e.g. silicon, germanium) could also be included in the layer stack.

In fact, more recently an effective $\chi^{(2)}$ nonlinearity has been reported for sputtered $Al_2O_3(10\,\mathrm{nm})$/a-Si$(25\,\mathrm{nm})$/$SiO_2(10\,\mathrm{nm})$ stacks (layer thicknesses indicated in parentheses) [44]. But the origin of the effective $\chi^{(2)}$ nonlinearity is ascribed to the existence of a non-zero built-in electric field coupling with silicon's strong $\chi^{(3)}$ nonlinearity, rather than the interface nonlinearities. The built-in electric field arises from fixed charges with opposite signs at the Al_2O_3/a-Si and a-Si/SiO_2 interfaces. From SHG measurements at a fundamental wavelength of $800\,\mathrm{nm}$, a nonlinearity of $\chi^{(2)}_{zzz} = 2\,\mathrm{pm/V}$ has been extracted. After annealing for 15 minutes at $400\,°\mathrm{C}$, this value could be increased to $\chi^{(2)}_{zzz} = 8.5\,\mathrm{pm/V}$. Similarly, a $\chi^{(2)}$ nonlinearity has been induced by placing a layer of silicon between two metals with different work functions [45]. From SHG measurements at a fundamental wavelength of $800\,\mathrm{nm}$, a nonlinearity of $\chi^{(2)}_{zzz} = (8.9 \pm 1.6)\,\mathrm{pm/V}$ has been extracted for a $25\,\mathrm{nm}$ a-Si film surrounded by a layer of Pt and Al (all of them deposited by magnetron sputtering). By applying a voltage, the effective $\chi^{(2)}_{zzz}$ component could be increased up to $15.6\,\mathrm{pm/V}$ (limited by breakdown).

The use of atomic layer deposited Al_2O_3/ZnO nanolaminates has also proven useful to control the crystal orientation of the grains in polycrystalline ZnO and therefore control the effective $\chi^{(2)}$ nonlinearity [46] (see section 4.3). From SHG measurements at a fundamental wavelength of $800\,\mathrm{nm}$, a nonlinearity of $\chi^{(2)}_{zzz} = -4\,\mathrm{pm/V}$ was extracted.

To get order of magnitude improvements in $\chi^{(2)}$ nonlinearity, the use of highly nonlinear organic molecules in nanolaminates could be an interesting approach. In bulk materials, these polar nonlinear molecules tend to arrange in a centrosymmetric structure. This centrosymmetric arrangement can be avoided by combining the nonlinear molecules with another material in a nanolaminate. This has already been demonstrated for a limited amount of layers using a Langmuir-Blodgett technique [29]. With the development of atomic and molecular layer deposition [20], the use of organic or inorganic-organic nanolaminates for $\chi^{(2)}$ materials can be explored further.

4.3 Zinc oxide and zinc sulfide

This section covers the use of atomic layer deposited zinc oxide and zinc sulfide for integrated $\chi^{(2)}$ devices, an area which had remained largely unexplored thus far. Firstly, our results of second-harmonic generation experiments in thin films will be discussed. Both for ALD zinc oxide and zinc sulfide, $\chi^{(2)}$ values exceeding those of the previously discussed ABC-type nanolaminates were observed (up to a factor 10 larger). Secondly, our results of electro-optic modulation experiments in SiN ring resonators will be covered. These integrated SiN based electro-optic ring modulators were realized by overlaying SiN waveguides with zinc oxide or zinc sulfide thin films. A large part of the results has been published in [6–8].

Zinc oxide and zinc sulfide are known to crystallize in non-centrosymmetric phases. Zinc oxide (ZnO) crystallizes preferably in the hexagonal wurtzite structure, point group 6mm [47]. Zinc sulfide (ZnS) exists in two main crystalline phases: the hexagonal wurtzite structure, and the cubic zinc-blende (also known as sphalerite) structure, point group $\bar{4}3$m [2]. Both materials are transparent in the visible and near-infrared wavelength range. An overview of the linear and second-order nonlinear properties of bulk ZnO and ZnS crystals is given in tables 4.6 and 4.7. ALD of ZnO and ZnS almost always results in crystalline films [10]. However, for non-epitaxial growth these films are polycrystalline with typical grain sizes much smaller than the wavelength. To get a large effective $\chi^{(2)}$ nonlinearity, textured films are desirable, i.e. the grains need to have a certain preferential orientation so that the $\chi^{(2)}$ response averaged over many grains does not vanish.

To our knowledge, the first and only prior report on $\chi^{(2)}$ effects in ALD ZnO was given by Wickberg et al. [46]. They investigated second-harmonic generation (for a fundamental wavelength of $800\,\mathrm{nm}$) in three types of samples: pure ZnO films, ZnO films deposited on an ALD Al_2O_3 seed layer, and Al_2O_3/ZnO nanolaminates (all of them deposited on glass substrates). XRD θ-2θ scans and SHG measurements for these samples are shown in figure 4.18. Interestingly, the SH response is the smallest for a pure ZnO film. XRD measurements show strong peaks corresponding to the 100 and 101 reflections of ZnO, indicating that the grains are predominantly oriented with their c axis (or optical axis) parallel to the substrate. For the sample with a $6\,\mathrm{nm}$ Al_2O_3 seed layer, the XRD scan shows a strong peak corresponding to the 002 reflection (i.e. crystallites have their c axis perpendicular to the substrate). The 101 reflection has almost vanished and the

Material	E_g (eV)	λ_ω (nm)	n	d (pm/V)	Ref.
ZnO (6mm)	3.4	1058.2	$n_\omega \sim 1.9$ $n_{2\omega} \sim 2.0$	$d_{33} = 7.0 \pm 0.2$ $d_{15} = 2.32 \pm 0.2$ $d_{31} = 2.1 \pm 0.2$	[47, 48]
ZnS (6mm)	3.9	1064.2	$n_\omega \sim 2.3$ $n_{2\omega} \sim 2.4$	$d_{33} = 15.72 \pm 1.9$ $d_{15} = 7.59 \pm 1.2$ $d_{31} = 8.65 \pm 1.7$	[2, 48]
ZnS ($\bar{4}$3m)	3.7	1058	$n_\omega = 2.289$ $n_{2\omega} = 2.40$	$d_{36} = 24.6 \pm 1.5$	[2, 48]

Table 4.6: Overview of d values determined from second-harmonic generation experiments for ZnO and ZnS bulk crystals. The bandgap E_g, the fundamental wavelength λ_ω at which the experiments were performed, and the refractive index n are given (both at the fundamental and SH wavelength).

Material	λ (nm)	r (pm/V)	ϵ (low frequency)	Ref.
ZnO (6mm)	633	$r_{33}^S = 2.6$ $r_{13}^S = -1.4$	$\epsilon \approx 8.15$	[48]
ZnS (6mm)	633	$r_{33}^S = 1.8$ $r_{13}^S = 0.9$	$\epsilon_{11}^T = \epsilon_{33}^T = 8.7$ $\epsilon_{11}^S = 8.7$	[48]
ZnS ($\bar{4}$3m)	650	$r_{41}^T = 2.1$	$\epsilon^T = 16$ $\epsilon^S = 12.5$	[49]
	633	$r_{41}^S = 1.6$		[48]

Table 4.7: Pockels coefficients measured at a wavelength λ for ZnO and ZnS bulk crystals. Also the dielectric constants (measured at low frequencies) are shown.

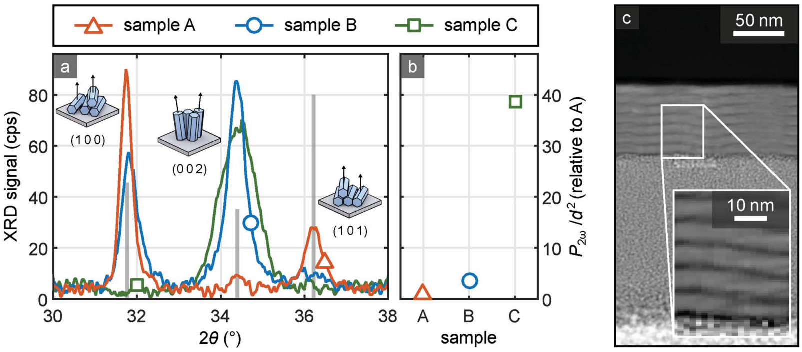

Figure 4.18: (a) XRD measurement showing the effect of seed and intermediate Al_2O_3 layers on the ZnO crystallite orientation and size. Sample A is a pure ALD ZnO film with 700 ZnO ALD cycles ($95.1\,\mathrm{nm}$ thickness); sample B consists of a 50 cycles thick Al_2O_3 seed layer ($6\,\mathrm{nm}$ thickness) underneath 350 cycles of ZnO ($73.3\,\mathrm{nm}$ total thickness). Sample C is a nanolaminate structure where the sequence of sample B is complemented by intermediate layers, which subdivide the ZnO film, resulting in a layer stack of the form $50 \times \mathrm{Al_2O_3} + 7 \times (50 \times \mathrm{ZnO} + 10 \times \mathrm{Al_2O_3})$. In terms of thicknesses this gives $6\,\mathrm{nm}$ $\mathrm{Al_2O_3}\ +7 \times (9.3\,\mathrm{nm}\ \mathrm{ZnO} + 1.2\,\mathrm{nm}\ \mathrm{Al_2O_3})$. The three dominant peaks in the measurement curves are ascribed to the ZnO crystallites with (100), (002), and (101) orientation (see the three different insets). The seed and intermediate Al_2O_3 layers have a huge impact enhancing the growth of crystallites with (002) orientation and the optical axis perpendicular to the substrate. At the same time, the intermediate layers limit the crystallite size perpendicular to the substrate, leading to a broadening of the (002) peak. For comparison, the gray bars indicate relative intensities obtained from ZnO-powder diffraction measurements. (b) $P_{2\omega}/d^2$ is normalized to the value obtained for sample A. This quantity is used as an indicator for the second-order bulk susceptibility of the three samples. The nanolaminate structure with intermediate Al_2O_3 layers (sample C) shows an increase by nearly 40 times as compared to the pure ZnO (sample A). (c) Scanning transmission electron image of a sample with a cycle sequence corresponding to sample C. The nanolaminate structure of the sample is clearly visible and shows seven macrocycles on top of the substrate. Figure reproduced from [46].

100 reflection has decreased by roughly one third compared to the pure ZnO film. The SH response (normalized with respect to the film thickness) of this sample is slightly larger. Finally, for the Al_2O_3/ZnO nanolaminate, the XRD scan only shows a strong 002 reflection, indicating ZnO crystallite growth with the c axis normal to the substrate. The SH response of this sample is about 11 times larger than the response of the ZnO film with the Al_2O_3 seed layer, and nearly 40 times larger than the response for a pure ZnO film. For the nanolaminate, a $|\chi^{(2)}_{zzz}|$ value of $4\,\mathrm{pm/V}$ was extracted.

For our ALD ZnO films, we have observed $|\chi^{(2)}_{zzz}|$ values of $4\,\mathrm{pm/V}$ for pure ZnO films, and $15\,\mathrm{pm/V}$ for ZnO films with a $6\,\mathrm{nm}$ ALD Al_2O_3 seed layer [7], which is comparable to the values reported for bulk crystals. This increase in nonlinearity is thought to be related to the use of different ALD process parameters. We use a plasma-enhanced ALD process with a substrate temperature of $300\,^\circ\mathrm{C}$, whereas Wickberg et al. use a thermal ALD process (H_2O as oxygen precursor) at a substrate temperature of $250\,^\circ\mathrm{C}$. The control over the magnitude of the nonlinearity by the absence or presence of an Al_2O_3 seed layer opens up interesting perspectives for quasi-phase matching.

Second-harmonic generation has also been observed in ZnO films prepared by other deposition techniques, such as pulsed laser ablation, laser molecular beam epitaxy, sputtering, and plasma-enhanced chemical vapor deposition [47, 50–52]. Note that in many cases, the films are deposited on crystalline sapphire substrates. These films can behave very differently from those deposited on amorphous substrates. For polycrystalline ZnO films, it is thought that not only the grains themselves, but also the grain boundaries contribute to the total SH signal [47]. Therefore, an increase in grain size can lead to a decrease in $\chi^{(2)}$ nonlinearity. Also an increase in film thickness can sometimes lead to a decreased $\chi^{(2)}$ nonlinearity [51]. Flipping of the c axis during growth has been suggested as a possible mechanism. For epitaxially grown ZnO on sapphire substrates, control of the polarity ($+c$ or $-c$ axis orientation) by using specific buffer layers has been reported [53–55]. This can be of interest for quasi-phase-matched second-order nonlinear processes [56].

Second-harmonic generation has been observed in e-beam deposited and thermally evaporated polycrystalline ZnS thin films [57, 58]. Also phase matched second-harmonic generation in hybrid TiO_2/ZnS/glass slab waveguides has been reported [59].

Furthermore, electro-optic effects have been reported in sputtered ZnO films [60, 61], and in polycrystalline ZnO and ZnS slab waveguides [62, 63], but only for low-frequency AC voltages ($< 100\,\mathrm{kHz}$).

4.3.1 Materials and deposition

Our ALD materials are deposited in a homebuilt setup with a base pressure of $10^{-6}\,\mathrm{mbar}$. A standard ALD cycle consists of a $5\,\mathrm{s}$ exposure for the precursors and a $25\,\mathrm{s}$ purge time between each exposure, with the pressure of the precursors set to $5 \times 10^{-3}\,\mathrm{mbar}$, unless stated otherwise.

For the ZnO deposition, two processes were investigated, both at a substrate temperature of $300\,^\circ\mathrm{C}$: a plasma-enhanced ALD (PE-ALD) process and plasma-enhanced thermal ALD (PET-ALD) process. The PE-ALD process uses diethylzinc (DEZ) and $10\,\mathrm{s}$ oxygen plasma exposures (at $10^{-2}\,\mathrm{mbar}$). In the PET-ALD process, the exposure sequence is DEZ-H_2O-$10\,\mathrm{s}$ O_2 plasma. The O_2 plasma is generated by an RF inductively coupled generator, operated at $13.56\,\mathrm{MHz}$ and $200\,\mathrm{W}$ power. The PET-ALD recipe was used to examine the role of free charge carriers in the electro-optic modulation experiments, as the PET-ALD process is known to increase the resistivity of ZnO films and decrease the carrier concentration [64]. ZnS layers were deposited by a thermal process (TH-ALD) using DEZ and H_2S at a substrate temperature of $150\,°\mathrm{C}$. For the deposition of Al_2O_3 seed layers, we use a standard thermal process (using TMA and H_2O) at a substrate temperature of $120\,°\mathrm{C}$.

XRD measurements of PE-ALD and PET-ALD ZnO samples are shown in figure 4.19. In contrast to the XRD measurements for TH-ALD ZnO shown in figure 4.18, no peaks corresponding to 100 or 101 reflections are visible. Our XRD scans only show a strong 002 reflection. In [46], this could only be achieved by using a ZnO/Al_2O_3 nanolaminate. We can get a preferential 002 orientation of the crystallites for pure PE(T)-ALD ZnO films or PE(T)-ALD ZnO films with a $6\,\mathrm{nm}$ ALD Al_2O_3 seed layer. For both PE-ALD and PET-ALD ZnO, the use of a $6\,\mathrm{nm}$ ALD Al_2O_3 seed layer enhances the crystallinity (increased 002 reflection).

XRD measurements for TH-ALD ZnS samples with and without a $6\,\mathrm{nm}$ Al_2O_3 seed layer are shown in figure 4.20. The samples shown in figure 4.20(a) and 4.20(b) were deposited using the same ALD recipes, but on different substrates. In figure 4.20(a), glass substrates were used. The broad peak around $21°$ is coming from the amorphous glass. This makes it harder to distinguish the peaks around $28°$, coming from the ZnS films. Still, we can see that the sample with a Al_2O_3 seed layer produces a larger peak. For the samples deposited on silicon substrates (with amorphous native oxide on the order of $1\,\mathrm{nm}$ in thickness), the peaks stand out more clearly. The peaks at $32.7°$ can be ascribed to the forbidden 200 reflection of the silicon substrate. The amplitude of this Si 200 reflection depends on the in-plane sample orientation (the height fluctuates as the sample is rotated about the substrate normal) [65]. The rising background for $2\theta > 40°$ is related to the XRD tool configuration. In an XRD analysis performed by Kuhs et al. on ALD ZnS deposited at $80\,°\mathrm{C}$ (utilizing the same ALD process parameters as described above) [66], the crystalline phase of ZnS was identified as the cubic zinc-blende phase. The peaks at $28.2°$ can be ascribed to the 111 reflection of cubic ZnS. However, these peaks can also be assigned to the 002 reflection of hexagonal ZnS [67]. Anyhow, both phases are non-centrosymmetric, having a non-zero $\chi^{(2)}$ nonlinearity (see tables 4.6 and 4.7). In the inset of figure 4.20(b), we can clearly see that the XRD peak at $28.2°$ is largest for the sample with a $6\,\mathrm{nm}$ Al_2O_3 seed layer.

Using the Scherrer equation, we estimate the lower limit for the crystallite size [46]

$$\tau = \frac{0.9\lambda}{\delta(2\theta)\cos\theta} \tag{4.11}$$

where τ denotes the mean size of the crystalline domains, λ the X-ray wavelength, $\delta(2\theta)$ the FWHM of the XRD peak, and θ the Bragg angle. This gives sizes τ of approximately $16\,\mathrm{nm}$ for the ZnO films in figure 4.19(a), and $22\,\mathrm{nm}$ for the

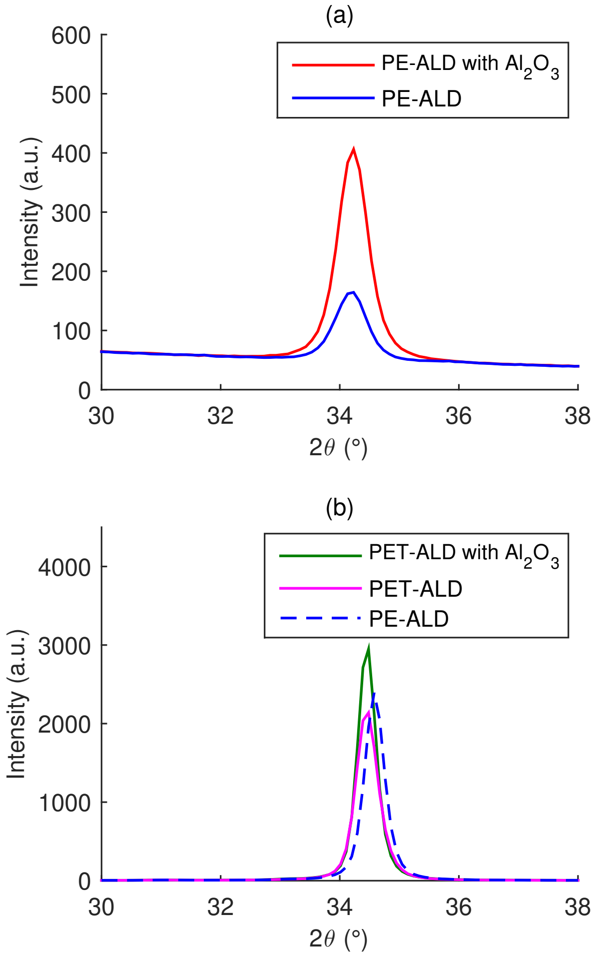

Figure 4.19: XRD θ-2θ scans (using Cu K_α radiation) of ALD ZnO deposited on (a) glass substrates, and (b) silicon substrates with native oxide (oxide thickness on the order of $1\,\mathrm{nm}$). The samples shown in figure (a) are: $37\,\mathrm{nm}$ PE-ALD ZnO on $6\,\mathrm{nm}$ Al_2O_3 (red) and $39\,\mathrm{nm}$ PE-ALD ZnO (blue). The samples shown in figure (b) are: $81\,\mathrm{nm}$ PET-ALD ZnO on $6\,\mathrm{nm}$ Al_2O_3 (green), $81\,\mathrm{nm}$ PET-ALD ZnO (magenta), and $62\,\mathrm{nm}$ PE-ALD ZnO (blue, dashed).

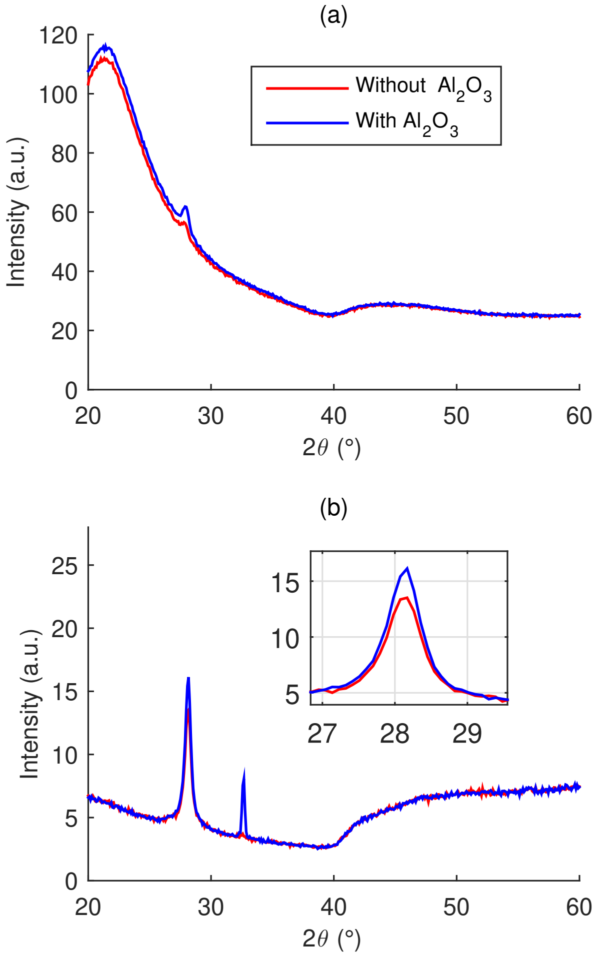

Figure 4.20: XRD θ-2θ scans (using Cu K_α radiation) of TH-ALD ZnS deposited on (a) glass substrates, and (b) silicon substrates with native oxide (oxide thickness on the order of $1\,\mathrm{nm}$). XRD measurements are shown for $27\,\mathrm{nm}$ ZnS (without Al_2O_3 seed layer; shown in red) and $30\,\mathrm{nm}$ ZnS on a $6\,\mathrm{nm}$ Al_2O_3 seed layer (shown in blue). The legend is the same for figure (a) and (b). The inset in figure (b) shows a magnified image of the peaks around 28.2°.

thicker films in figure 4.19(b). For the ZnS films in figure 4.20(b), we get values of approximately $11\,\mathrm{nm}$.

4.3.2 Second-harmonic generation in thin films

In second-harmonic generation measurements on the polycrystalline ZnO and ZnS films described above, the combined response of many crystallites will be detected. As such, the polycrystalline films will be treated as effective media with ∞m symmetry with respect to the surface normal (same as for the ABC-type nanolaminates). Thus, the non-vanishing $\chi^{(2)}$ tensor components for SHG are $\chi^{(2)}_{xxz} = \chi^{(2)}_{yyz} = \chi^{(2)}_{xzx} = \chi^{(2)}_{yzy}$, $\chi^{(2)}_{zxx} = \chi^{(2)}_{zyy}$ and $\chi^{(2)}_{zzz}$, where z is the film normal and x and y are two orthogonal in-plane directions (these non-vanishing components are the same as for materials with 6mm symmetry, like ZnO and hexagonal ZnS).

SHG measurements for PE-ALD ZnO films (with and without Al_2O_3 seed layer) are shown in figures 4.21 (for a fundamental wavelength of $980\,\mathrm{nm}$) and 4.22 (for a fundamental wavelength of $800\,\mathrm{nm}$). The $\chi^{(2)}$ components obtained from these measurements are listed in table 4.8. The use of a Al_2O_3 seed layer clearly enhances the $\chi^{(2)}$ nonlinearity. This enhancement is correlated with an increase in the XRD 002 reflection (see figure 4.19(a)). The $\chi^{(2)}_{zzz}$ component for our PE-ALD ZnO on Al_2O_3 films is identical (within the experimental error) to the $\chi^{(2)}_{zzz}$ component for ZnO single crystals (see table 4.6). The $\chi^{(2)}$ components are larger (in absolute value) than those found for TH-ALD ZnO ($\chi^{(2)}_{zzz} = -4.0\,\mathrm{pm/V}$, $\chi^{(2)}_{xxz} = 1.6\,\mathrm{pm/V}$, and $\chi^{(2)}_{zxx} = 1.5\,\mathrm{pm/V}$ for an optimized TH-ALD ZnO/Al_2O_3 nanolaminate) [46]. This improvement is likely related to the use of a plasma and the slightly elevated substrate temperature (300 °C vs 250 °C), promoting the 002 orientation of the crystallites.

The control over the magnitude of the $\chi^{(2)}$ nonlinearity by adding or removing a thin Al_2O_3 seed layer offers possibilities for quasi-phase matching (QPM) of $\chi^{(2)}$ processes. One could for instance deposit a thin Al_2O_3 layer on top of a silicon nitride waveguide and etch this layer periodically as illustrated in figure 4.23. On top of this, a ZnO layer can be deposited, resulting in a periodic variation of the $\chi^{(2)}$ nonlinearity along the waveguide propagation direction. First-order QPM in a nanophotonic waveguide typically requires lengths of a couple of microns for one QPM period [68, 69]. This can be achieved in standard lithography processes. The refractive index grating caused by the periodically etched $6\,\mathrm{nm}$ Al_2O_3 layer can increase the propagation loss. To avoid this, decreasing the thickness of the Al_2O_3 layer might be worth considering.

Note that the SHG measurements allow us to determine the relative signs of the $\chi^{(2)}$ components for a single sample, but not for different samples. For instance, we do not know whether the $\chi^{(2)}_{zzz}$ components for pure PE-ALD ZnO and PE-ALD

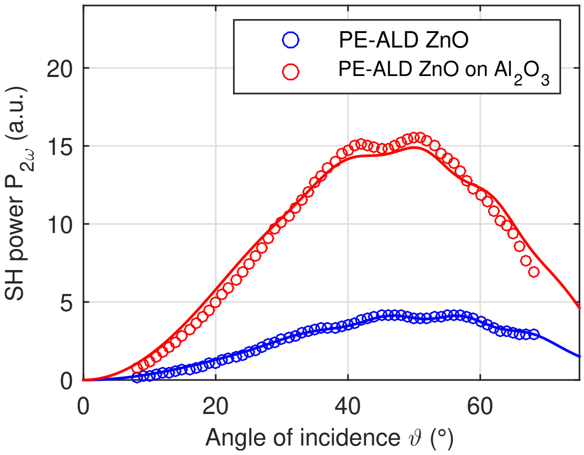

Figure 4.21: SHG measurements of PE-ALD ZnO samples using the UGent setup described in 4.2.2.1 ($\lambda_\omega = 980\,\mathrm{nm}$, incident laser light is p-polarized). The circles are the measurement data and the full lines the fitted curves. For the curve fitting, the model described by equation 4.7 is used (where the parameters corresponding to the ABC-type nanolaminate need to be replaced by the ZnO parameters; for the sample with the Al_2O_3 seed layer, extra Fresnel transmission coefficients corresponding to this layer are included). The blue data corresponds to 39 nm PE-ALD ZnO on glass, the red data to 37 nm PE-ALD ZnO on 6 nm Al_2O_3 on glass. The glass is BOROFLOAT® 33 with 500 µm thickness. Before the actual measurements on the ZnO samples, a reference SHG measurement is conducted on a bare glass substrate. The refractive indices needed for the fitting were determined from ellipsometry measurements and the thicknesses from XRR measurements.

	PE-ALD ZnO	PE-ALD ZnO on Al_2O_3
At $\lambda_\omega = 980\,\mathrm{nm}$:		
$\chi^{(2)}_{zzz}$ (pm/V)	-4 ± 2	-14 ± 5
$2\chi^{(2)}_{xxz} + \chi^{(2)}_{zxx}$ (pm/V)	5.9 ± 0.5	13.1 ± 0.9
At $\lambda_\omega = 800\,\mathrm{nm}$:		
$\chi^{(2)}_{zzz}$ (pm/V)	-4 ± 2	-15 ± 4
$\chi^{(2)}_{xxz}$ (pm/V)	3.4 ± 0.2	5.7 ± 0.3
$\chi^{(2)}_{zxx}$ (pm/V)	3.72 ± 0.03	7.72 ± 0.04

Table 4.8: $\chi^{(2)}$ components for PE-ALD ZnO and PE-ALD ZnO with a Al_2O_3 seed layer extracted from the SHG measurements shown in figures 4.21 and 4.22. The errors are due to an uncertainty on the angle of incidence, as described in 4.2.2.3. If we assume Kleinman's symmetry to be valid, we have $\chi^{(2)}_{xxz} = \chi^{(2)}_{zxx}$ (see section 2.2). For a fundamental wavelength of 800 nm we see this is not truly the case. This can be related to the SH frequency approaching the bandgap frequency.

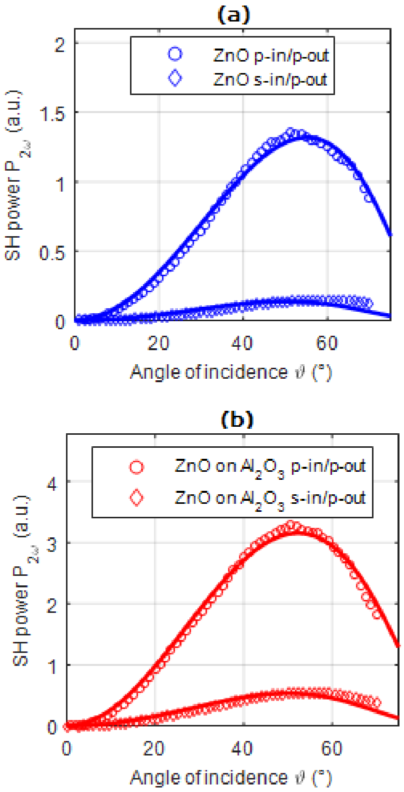

Figure 4.22: SHG measurements of PE-ALD ZnO samples (identical to those in figure 4.21) using the KIT setup described in 4.2.2.1. The circles and diamonds are the measurement data, the full lines the fitted curves. The circles correspond to measurements with p-polarized incident laser light; for the diamonds this is s-polarized. In both cases, the polarizer in front of the detector is oriented to transmit p-polarized SH waves. In (a) the data for the pure PE-ALD ZnO sample is shown, in (b) for the PE-ALD ZnO on $6\,\mathrm{nm}$ Al_2O_3 sample. The model used for the fitting is given by equation 4.8. For the reference SHG measurement, a Y-cut quartz plate with $\chi_{XXX}^{\mathrm{SiO_2}} = 0.6\,\mathrm{pm/V}$ is used.

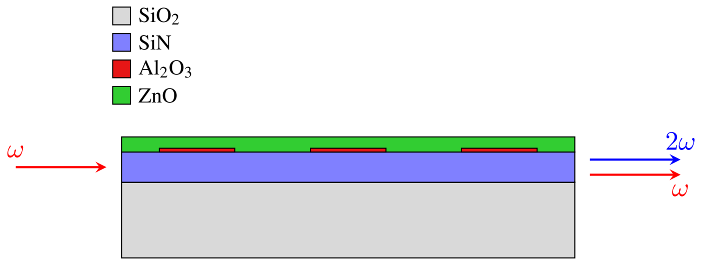

Figure 4.23: Schematic illustration of the longitudinal cross-section of a silicon nitride waveguide with a periodic Al_2O_3/ZnO cladding for quasi-phase-matched $\chi^{(2)}$ processes.

ZnO with a Al_2O_3 seed layer have the same signs or not. In most applications this does not play a role, but for the quasi-phase matching scheme described above it makes a difference in terms of efficiency of the nonlinear process (with opposite signs giving a larger efficiency). We conducted a preliminary SHG measurement where we placed a PE-ALD ZnO sample and a PE-ALD ZnO on Al_2O_3 sample together in the sample holder with the ZnO layers in contact with each other (see figure 4.24). For the fitting of the data, we treated the two ZnO layers as one layer with an unknown nonlinearity. The fitting gave (surface) second-order susceptibility components of $\chi^{(2)}_{s,zzz} = -0.6\,\mathrm{nm}^2/\mathrm{V}$ and $2\chi^{(2)}_{s,xxz} + \chi^{(2)}_{s,zxx} = 1.11\,\mathrm{nm}^2/\mathrm{V}$. Since we know the nonlinearity of the ZnO and ZnO on Al_2O_3 samples separately (see table 4.8), we can calculate what to expect when the samples are placed against each other. For opposite signs, we expect to get values of $\chi^{(2)}_{s,zzz} = (-0.7 \pm 0.2)\,\mathrm{nm}^2/\mathrm{V}$ and $2\chi^{(2)}_{s,xxz} + \chi^{(2)}_{s,zxx} = (1.11 \pm 0.04)\,\mathrm{nm}^2/\mathrm{V}$ (obtained by simply summing the surface nonlinearity of the ZnO and ZnO on Al_2O_3 sample). For identical signs, we expect to get values of $\chi^{(2)}_{s,zzz} = (-0.4 \pm 0.2)\,\mathrm{nm}^2/\mathrm{V}$ and $2\chi^{(2)}_{s,xxz} + \chi^{(2)}_{s,zxx} = (0.29 \pm 0.04)\,\mathrm{nm}^2/\mathrm{V}$ (obtained by taking the difference of the surface nonlinearity of the ZnO and ZnO on Al_2O_3 sample). These results indicate we are getting opposite signs, which would be beneficial for quasi-phase matching. The polarity of the ZnO films can also be determined by piezoresponse force microscopy [54] or advanced X-ray diffraction techniques [70].

SHG measurements for PET-ALD ZnO films (with and without Al_2O_3 seed layer) are shown in figure 4.25. The $\chi^{(2)}$ components obtained from these measurements are listed in table 4.9. These measurements are done at a fundamental wavelength of $1550\,\mathrm{nm}$ instead of the usual $980\,\mathrm{nm}$ or $800\,\mathrm{nm}$. Also the results for a PE-ALD ZnO film (with Al_2O_3 seed layer) are included for comparison. The measurement setup is the same as the UGent setup described in 4.2.2.1, but with the optics adapted to a fundamental wavelength of $1550\,\mathrm{nm}$, and also a different detector and laser. The laser source (Calmar FPL-03CCFPM femtosecond fiber laser) emits $100\,\mathrm{fs}$ pulses at a wavelength of $1550\,\mathrm{nm}$ with a repetition rate of $20\,\mathrm{MHz}$ and an average power of $10\,\mathrm{mW}$. Since the power of this laser is signif-

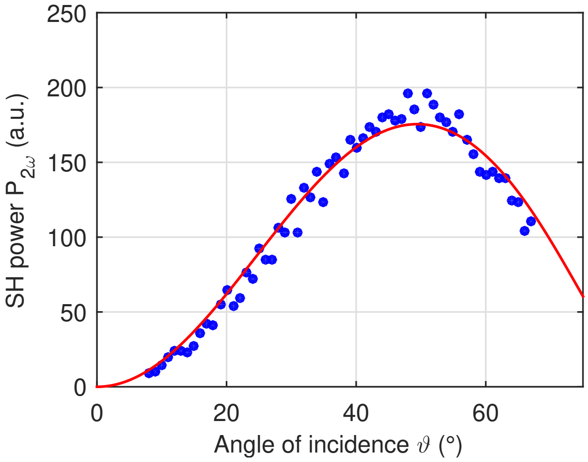

Figure 4.24: SH power versus the angle of incidence for a PE-ALD ZnO sample placed against a PE-ALD ZnO on Al_2O_3 sample (same samples as in figure 4.21). The samples are placed in the sample holder such that the two ZnO layers are in contact with each other. So the laser beam travels through the layers of the samples in the following order: glass, ZnO, ZnO, Al_2O_3, glass. The incident laser light is p-polarized and p-polarized SH waves are measured. The measurements are done at a fundamental wavelength of $800\,\mathrm{nm}$. The blue dots are the measurement data and the red line the fitted curve.

icantly lower than the power of the $980\,\mathrm{nm}$ laser (average power of about $1\,\mathrm{W}$), also a more sensitive detector is needed. Therefore, we use a single-photon detector purchased from IDQ (ID120, based on a silicon avalanche photodiode). This adapted setup was constructed to enable non-resonant SHG measurements of the organic material presented in chapter 5 (the organic crystal BNA has an absorption edge close to $500\,\mathrm{nm}$). Also, working at a fundamental wavelength of $1550\,\mathrm{nm}$ permits SHG measurements on silicon substrates, provided that we let the laser beam pass through the substrate first (to avoid absorption of the generated SH waves in the silicon substrate; in our regular measurements on glass substrates, we let the laser light pass through the thin film(s) first and afterwards through the glass). In this adapted setup, the SH signal from a bare glass substrate is hard to detect and requires long integration times. We therefore do not use it for reference measurements. Instead we use a thin BBO crystal. The reference SHG measurement procedure for this BBO crystal is explained in appendix C.

Also for PET-ALD ZnO, we see that the addition of a $6\,\mathrm{nm}$ Al_2O_3 seed layer gives an enhancement of the $\chi^{(2)}$ nonlinearity, which is correlated with an increase in the XRD 002 reflection.

Figure 4.26 shows the dispersion of the $\chi^{(2)}$ nonlinearity for PE-ALD ZnO on $6\,\mathrm{nm}$ Al_2O_3, as obtained from the above-mentioned SHG measurements. From

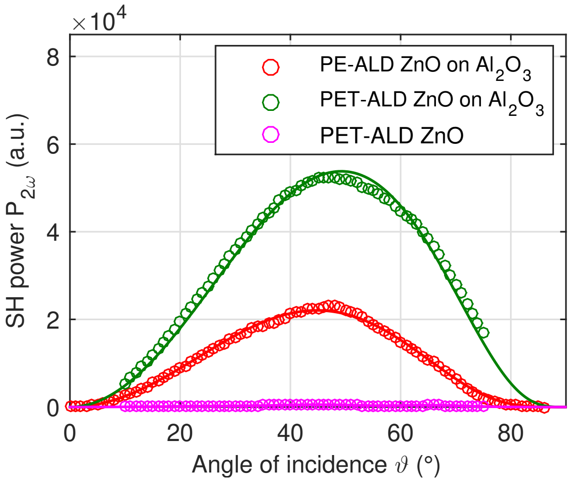

Figure 4.25: SHG measurements of PE(T)-ALD ZnO samples using the UGent setup described in 4.2.2.1, but adapted to operate at a fundamental wavelength of 1550 nm instead of 980 nm (incident laser light is p-polarized, p-polarized SH is measured). The circles are the measurement data and the full lines the fitted curves. The red data corresponds to 37 nm PE-ALD ZnO on 6 nm Al_2O_3 on glass, the green data to 63 nm PET-ALD ZnO on 6 nm Al_2O_3 on glass, and the magenta data to 65 nm PET-ALD ZnO on glass. The glass is BOROFLOAT® 33 with 500 µm thickness. Before the actual measurements on the ZnO samples, a reference SHG measurement is conducted on a BBO crystal.

	PE-ALD ZnO on Al_2O_3	PET-ALD ZnO on Al_2O_3	PET-ALD ZnO
$\chi^{(2)}_{zzz}$ (pm/V)	-10 ± 4	-5 ± 3	-0.7 ± 0.2
$2\chi^{(2)}_{xxz} + \chi^{(2)}_{zxx}$ (pm/V)	8.3 ± 0.5	7.4 ± 0.5	0.84 ± 0.02

Table 4.9: $\chi^{(2)}$ components for PE(T)-ALD ZnO extracted from the SHG measurements shown in figures 4.25 (at $\lambda_\omega = 1550\,\text{nm}$). The errors are due to an uncertainty on the angle of incidence, as described in 4.2.2.3.

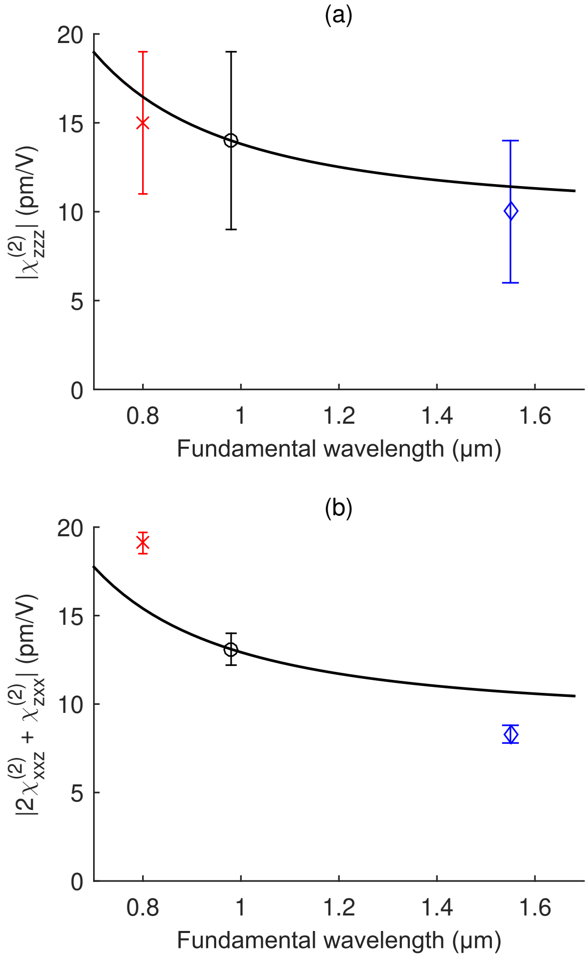

Figure 4.26: Dispersion of the $\chi^{(2)}$ nonlinearity for 37 nm PE-ALD ZnO on 6 nm Al_2O_3 on glass; obtained from SHG measurements. Figure (a) shows $|\chi^{(2)}_{zzz}|$ vs the fundamental wavelength, and (b) $|2\chi^{(2)}_{xxz} + \chi^{(2)}_{zxx}|$ vs the fundamental wavelength. The red crosses, black circles and blue diamonds correspond to the $\chi^{(2)}$ components at 800 nm, 980 nm, and 1550 nm. The black line is obtained by calculating the $\chi^{(2)}$ components utilizing Miller's rule (see section 2.6) from the knowledge of the $\chi^{(2)}$ components at 980 nm and the refractive index.

	TH-ALD ZnS	TH-ALD ZnS on Al_2O_3
$\chi^{(2)}_{zzz}$ (pm/V)	-6 ± 3	-9 ± 4
$2\chi^{(2)}_{xxz} + \chi^{(2)}_{zxx}$ (pm/V)	2.8 ± 0.7	4.8 ± 0.7

Table 4.10: $\chi^{(2)}$ components for TH-ALD ZnS extracted from SHG measurements conducted at a fundamental wavelength of $1550\,\mathrm{nm}$. The measured samples consisted of $27\,\mathrm{nm}$ ZnS on glass and $30\,\mathrm{nm}$ ZnS on $6\,\mathrm{nm}$ Al_2O_3 on glass.

the knowledge of the $\chi^{(2)}$ components at $980\,\mathrm{nm}$ and the refractive index, the $\chi^{(2)}$ components over the wavelength range $700\,\mathrm{nm}$ to $1700\,\mathrm{nm}$ have been calculated utilizing Miller's rule (see section 2.6). The result is plotted as a black line in figure 4.26. The agreement between the measured $\chi^{(2)}_{zzz}$ components and Miller's rule is fairly good. For the off-diagonal $\chi^{(2)}$ components, the measured dispersion is stronger than what is predicted by Miller's rule. Miller's rule is known to not always be accurate in predicting the dispersion of the second-order susceptibility [71].

Finally, table 4.10 shows the $\chi^{(2)}$ components for TH-ALD ZnS (with and without Al_2O_3 seed layer) extracted from SHG measurements at a fundamental wavelength of $1550\,\mathrm{nm}$. The addition of a Al_2O_3 seed layer seemingly enhances the $\chi^{(2)}$ nonlinearity, although the enhancement is not as large as what is observed for ZnO. The values of the $\chi^{(2)}$ tensor components for our ZnS films are still significantly smaller than those observed in ZnS single crystals (see table 4.6). To get closer to the single crystal $\chi^{(2)}$ values, interesting follow-up experiments could include depositions at higher temperatures and post-annealing treatments.

4.3.3 Electro-optic ring modulators

Silicon nitride (SiN) is currently the most prominent CMOS-compatible platform for photonics at wavelengths shorter than $1\,\mu\mathrm{m}$. But realizing fast electro-optic modulators, key components of any integrated optics platform, remains challenging in SiN. Here, we report the back-end CMOS-compatible atomic layer deposition of conventional second-order nonlinear crystalline materials, zinc oxide and zinc sulfide, on existing SiN waveguide circuits. Using these ALD overlays, electro-optic modulation in ring resonators is demonstrated.

With the ever increasing demand for data, cheap, efficient and fast optical modulators are highly wanted. Next to telecom and datacom, other application areas are emerging where integrated phase modulators play an important role: programmable photonic integrated circuits for, e.g., microwave photonics and quantum information processing [72, 73] and optical phased arrays for, e.g., LIDAR (light detection and ranging), free-space communication, and 3D holographic displays [74, 75]; the latter requiring visible wavelength operation.

On the SOI platform, the plasma dispersion effect is exploited to realize fast electro-optic modulators [76]. SiN however, is an insulating material, making the free charge carrier based approach non-viable. Another well known approach to electro-optic modulation is the use of the Pockels effect, e.g., in lithium niobate modulators. Unfortunately, SiN's $\chi^{(2)}$ nonlinearity is expected to vanish due to SiN's amorphous nature. Yet, Pockels effect based modulation has been demonstrated in low-loss LPCVD SiN, albeit with small electro-optic coefficients of maximum $(8.31 \pm 5.60)\,\mathrm{fm/V}$ at a wavelength of $1550\,\mathrm{nm}$ [77]. Also, second-harmonic generation has been observed in SiN films [78–82] and waveguides [81, 83]. Experiments indicate the existence of a bulk $\chi^{(2)}$ nonlinearity which appears to be strongest in silicon-rich SiN films. It is yet unclear whether large Pockels coefficients in low-loss waveguides can be achieved.

As SiN itself offers no clear-cut solutions for optical modulation, apart from the slow and inefficient thermo-optic effect [84], there have been attempts to combine SiN with other materials. Combining graphene with SiN, Phare et al. demonstrated a high-speed electro-absorption modulator at a wavelength of $1550\,\mathrm{nm}$ [85]. The fabrication was done by transferring CVD graphene on copper to a planarized SiN PIC. Mehta et al. showed efficient modulation in SiN-on-$\mathrm{LiNbO_3}$ Mach-Zehnder modulators at a wavelength of $674\,\mathrm{nm}$ [86]. Only DC characterization was performed. The modulators were fabricated by depositing PECVD SiN on a $\mathrm{LiNbO_3}$-on-insulator substrate. Lead zirconate titanate (PZT) thin films have been used to demonstrate high-speed PZT-on-SiN modulators in the O- and C-band, with the possibility of extension to visible wavelengths [87]. However, the PZT deposition involves annealing at a temperature of $620\,^{\circ}\mathrm{C}$, which can cause Cu diffusion in the underlying CMOS electronics for back-end deposited photonic circuits [88]. Additionally, the PZT thin films are poled before the modulators are put to use. Also sputtered AlN has been proposed as an alternative CMOS-compatible platform which is transparent at wavelengths below $1\,\mu\mathrm{m}$ and allows for Pockels effect based electro-optic modulation [89].

Here we demonstrate monolithically integrated SiN based fast electro-optic ring modulators operating at $0.9\,\mu\mathrm{m}$, a wavelength often used in LIDAR systems [90]. The modulators are realized by overlaying SiN waveguides with low-temperature atomic layer deposited ZnO or ZnS. Our approach does not require poling. Poled materials can suffer from long term stability issues, especially at elevated operating temperatures.

4.3.3.1 Fabrication

Our SiN waveguides are patterned in a CMOS pilot line using $193\,\mathrm{nm}$ deep UV lithography. The SiN layer has a thickness of $300\,\mathrm{nm}$ and is deposited by LPCVD on top of a $3.3\,\mu\mathrm{m}$ HDPCVD (high density plasma CVD) $\mathrm{SiO_2}$ layer. On the patterned waveguides, the ALD materials are deposited (thicknesses in 70-$100\,\mathrm{nm}$

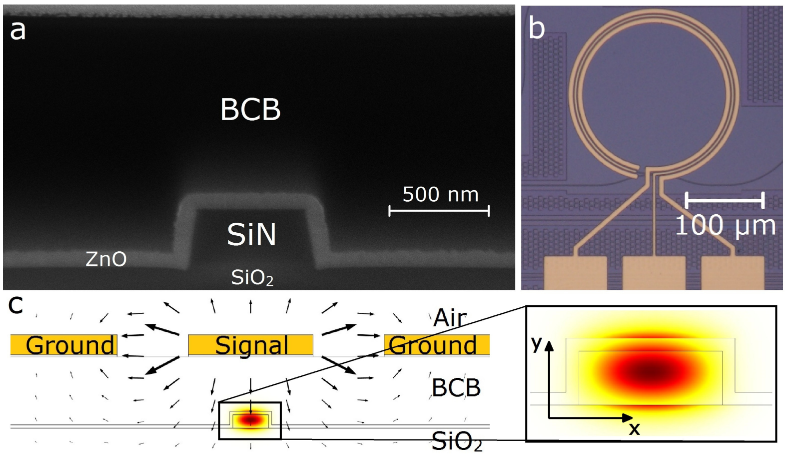

Figure 4.27: (a) SEM image of the cross-section of a SiN waveguide with 6 nm Al_2O_3, 81 nm PET-ALD ZnO and a BCB cladding. (b) Microscope image of a fabricated modulator. Rectangular contact pads are used for landing a GSG probe with a 100 μm pitch. (c) Simulated cross-section of a ZnO covered SiN waveguide with electrodes. The intensity of the fundamental quasi-TM optical mode is shown along with the electric field induced by the electrodes (arrows). 13% of the mode power resides in the ALD overlay.

range) in a homebuilt setup. The details of the ALD processes for ZnO, ZnS and Al_2O_3 can be found in subsection 4.3.1. After ALD, a layer of bisbenzocyclobutene (BCB, brand name CYCLOTENE$^{\text{TM}}$ 3022-35 from DOW) is spin coated and cured to serve as waveguide cladding. Figure 4.27(a) shows a scanning electron microscope (SEM) image of a waveguide cross-section. Next, Ti/Au (40 nm/450 nm, titanium improves adhesion of gold) electrodes are patterned in a ground-signal-ground (GSG) configuration utilizing a lift-off process. Figure 4.27(b) shows a fabricated device. Finally, the chips are cleaved to allow for edge coupling through use of tapered lensed fibers.

4.3.3.2 Design

Consider an optical waveguide with propagation along the z axis and the x and y axis as indicated in figure 4.27(c). A (small, slowly varying) change in the dielectric tensor $\Delta\epsilon(\mathbf{r},t)$ will cause a change in the effective index of an optical waveguide mode given by [91–93]

$$\Delta n_{eff}(\mathbf{r},t) = \frac{c\epsilon_0 \iint_{-\infty}^{+\infty} [\Delta\epsilon(\mathbf{r},t)|\mathbf{E}(x,y)] \cdot \mathbf{E}^*(x,y)\,dx\,dy}{2\iint_{-\infty}^{+\infty} \mathrm{Re}\left(\mathbf{E}(x,y) \times \mathbf{H}^*(x,y)\right) \cdot \mathbf{e}_z\,dx\,dy} \tag{4.12}$$

where $\mathbf{E}(x,y)$ and $\mathbf{H}(x,y)$ are the vectorial modal fields and $\mathbf{e}_z$ the unit vector in the z direction. For the Pockels effect, the change in the dielectric tensor can be expressed as

$$\Delta\epsilon_{i_1 i_2} \approx -\sum_{j_1,j_2} \epsilon^{(0)}_{i_1 j_1} \Delta\eta_{j_1 j_2} \epsilon^{(0)}_{j_2 i_2} = -\sum_{j_1,j_2,j_3} \epsilon^{(0)}_{i_1 j_1} r_{j_1 j_2 j_3} E_{0,j_3} \epsilon^{(0)}_{j_2 i_2} \tag{4.13}$$

with r the Pockels tensor and $\mathbf{E}_0$ the low-frequency applied electric field. In our analysis, the Pockels effect in the ALD overlay and the SiN waveguide core will be considered. Both the ALD overlays and SiN are assumed to be optically isotropic (ellipsometry did not give an improvement in fitting for an anisotropic model). So the change in the dielectric tensor can be written as

$$\Delta\epsilon_{i_1 i_2} \approx -n^4 \sum_{j_3} r_{i_1 i_2 j_3} E_{0,j_3} \tag{4.14}$$

For the fundamental (quasi-)TE and TM mode, which we will excite in our devices, the change in effective index can be approximated as

$$\Delta n_{eff,TE} \approx \frac{c\epsilon_0 \iint_{-\infty}^{+\infty} \Delta\epsilon_{xx} |E_x(x,y)|^2 \, dx\, dy}{2 \iint_{-\infty}^{+\infty} \mathrm{Re}\left(\mathbf{E}(x,y) \times \mathbf{H}^*(x,y)\right) \cdot \mathbf{e}_z \, dx\, dy} \tag{4.15}$$

$$\Delta n_{eff,TM} \approx \frac{c\epsilon_0 \iint_{-\infty}^{+\infty} \Delta\epsilon_{yy} |E_y(x,y)|^2 \, dx\, dy}{2 \iint_{-\infty}^{+\infty} \mathrm{Re}\left(\mathbf{E}(x,y) \times \mathbf{H}^*(x,y)\right) \cdot \mathbf{e}_z \, dx\, dy} \tag{4.16}$$

Since the polycrystalline ALD films and SiN layer possess in-plane isotropy (∞m symmetry), the non-zero Pockels tensor components are $r_{13} = r_{23}$, $r_{51} = r_{42}$, and r_{33}, with 3 referring to the normal to the film plane. By choosing the electrode configuration illustrated in figure 4.27(c), we get an out-of-plane electric field in the film on the waveguide top surface so we can probe r_{13} (for TE modes) and r_{33} (for TM modes) in the ALD overlay (and in the SiN waveguide core). The axis indicated by 3 in this case corresponds to the y axis. From the equations above, it can be seen that the effective index change of the guided mode depends on the electro-optic coefficients, the overlap of the optical mode with the electro-optic active layers and the electric field induced by the electrodes. In choosing the BCB cladding thickness, there is a trade-off between minimal absorption loss by the metal and maximal electric field $\mathbf{E}_0$ in the thin film. We have opted for BCB thicknesses of $\approx 1.6\,\mu\mathrm{m}$ (measured from the top of the SiO_2 layer) for the ZnO based devices and $\approx 1.5\,\mu\mathrm{m}$ for the ZnS based devices. This gives an estimated (from mode simulations) absorption loss on the order of $0.001\,\mathrm{dB/cm}$ for the fundamental quasi-TE mode and $0.01\,\mathrm{dB/cm}$ for the quasi-TM mode, for a SiN waveguide width of $800\,\mathrm{nm}$ at a wavelength of $0.9\,\mu\mathrm{m}$. The signal electrode width is chosen to be $2\,\mu\mathrm{m}$ wider than the waveguide width to have some tolerance against misalignment in the lithography process. The gap between the signal and ground electrodes is $1.6\,\mu\mathrm{m}$. This gap size is limited by the resolution of our contact mask. Smaller gaps would result in larger electric fields, but can give issues during lift-off. Also, smaller gaps increase the probability of dielectric breakdown.

To convert the effective index change induced by the electro-optic effect into a change in optical power, we use $100\,\mu\mathrm{m}$ radius ring resonators (see figure 4.27(b)). The used resonators are all-pass ring resonators, i.e. ring resonators with a single coupling section [94]. The coupling gaps between the ring and bus waveguides vary from $200\,\mathrm{nm}$ to $450\,\mathrm{nm}$ (excluding ALD layer). The transmission of an all-pass ring resonator is given by [94]

$$T = \frac{(r-a)^2 + 4ar\sin^2\frac{\phi}{2}}{(1-ar)^2 + 4ar\sin^2\frac{\phi}{2}} \tag{4.17}$$

where $\phi = \frac{\omega}{c} n_{eff} 2\pi R$ (with R the ring radius), $a = e^{-\alpha\pi R}$ (with α the power attenuation coefficient) is the single-pass amplitude transmission, and r the self-coupling coefficient (which depends on the size of the gap between the ring and bus waveguide). Clearly, a change in n_{eff} will result in a change in the transmission T.

4.3.3.3 Device characterization and discussion

Both transmission and modulation measurements have been conducted on the fabricated devices. In the transmission measurements, light from a tunable laser (New Focus$^{\mathrm{TM}}$ Velocity® TLB-6318, wavelength tunable from $890\,\mathrm{nm}$ to $910\,\mathrm{nm}$, fiber-coupled) is coupled in and out of the chip via tapered lensed fibers (no voltage applied to the modulators). The polarization is controlled with a fiber polarization controller. The resonances in the transmission spectrum can be fitted using expression 4.17, which gives us the self-coupling coefficient r and single-pass amplitude transmission a. Since various coupling gaps are available, r and a can be distinguished from one another, thus allowing us to get an estimate of the propagation loss. Figure 4.28(a) shows an example of a transmission measurement and the fitting of the resonance. Table 4.11 summarizes the estimated propagation losses for a SiN waveguide width of $800\,\mathrm{nm}$ at a wavelength of $0.9\,\mu\mathrm{m}$ for different ALD overlays. The presence of an overlay increases the propagation loss. The loss for the PE-ALD ZnO overlay seems considerably larger than it is for the other overlays.

In the modulation measurements, a small AC voltage $U(t) = U_{peak}\sin(2\pi f t)$ is applied with a GSG probe. The transmitted light is led to a photodetector of which the RF output is connected to an electrical spectrum analyzer (ESA). On the ESA, a peak is observed at the same frequency as the applied voltage. From the ESA peak height, the variation in optical power ΔP_{out} can be calculated ($P_{out}(t) = P_{out,0} + \Delta P_{out}\sin(2\pi f t)$). Figure 4.28(a) shows how ΔP_{out} changes when the laser wavelength is tuned (for a fixed U_{peak} and f). We see maxima on the slopes of the resonance, while ΔP_{out} drops significantly at the bottom of the resonance and when tuning away from resonance. A slight shift in resonance

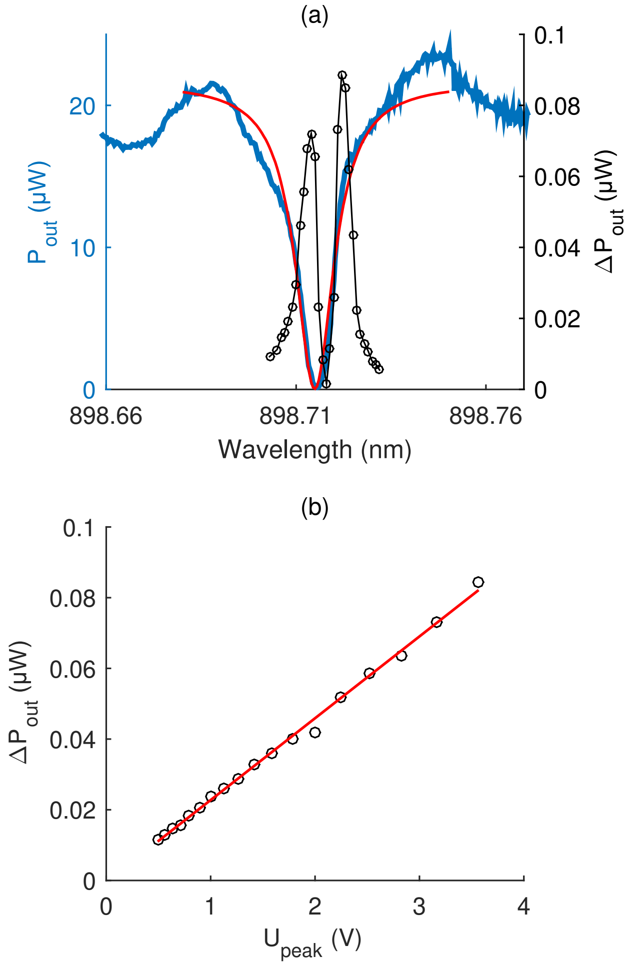

Figure 4.28: Tranmsission and modulation measurements performed on a SiN with ZnS overlay (thickness of $100\,\mathrm{nm}$) ring modulator with a gap size of $350\,\mathrm{nm}$ (without ALD layer) and a waveguide width of $800\,\mathrm{nm}$ for the quasi-TE mode. (a) Blue: Transmitted optical power measured as a function of wavelength. Red: fitting of resonance. Black: modulation amplitude of transmitted optical power ΔP_{out} measured as a function of wavelength for $f = 10\,\mathrm{MHz}$ and $U_{peak} = 3.6\,\mathrm{V}$. (b) Black circles: measurement of ΔP_{out} as a function of U_{peak} for $f = 10\,\mathrm{MHz}$ and a wavelength of $898.721\,\mathrm{nm}$. Red line: linear fitting of data.

ALD overlay	α_{TE} (dB/cm)	α_{TM} (dB/cm)
No ALD overlay	1.1 ± 0.5	0.9 ± 0.2
PE-ALD ZnO	11 ± 4	12 ± 2
PET-ALD ZnO	4 ± 2	3.9 ± 0.6
PET-ALD ZnO + 6 nm Al_2O_3	4.6 ± 0.7	6 ± 2
TH-ALD ZnS	4 ± 1	9 ± 2
TH-ALD ZnS + 6 nm Al_2O_3	3.0 ± 0.8	7.9 ± 0.8

Table 4.11: Propagation loss in a SiN waveguide (width of 800 nm) with different ALD overlays, both for the fundamental quasi-TE and -TM mode (at a wavelength of 0.9 µm).

occurred during the measurements. Figure 4.28(b) illustrates the linear variation of ΔP_{out} with the applied voltage U_{peak}. The aforementioned observations concur with a linear electro-optic effect. The same behavior was observed for all the tested modulators.

A figure of merit that is often used for electro-optic modulators is the $V_\pi L$ product. Consider a waveguide with a phase shift section of length L (i.e. length of waveguide along which there are electrodes to change the effective index). V_π corresponds to the voltage that needs to be applied to induce a π phase shift over this section. An estimate of the $V_\pi L$ product can be derived from the above-mentioned measurements. In case of the Pockels effect, the effective index varies linearly with the applied electric field or voltage, $\Delta n_{eff} = \zeta U$ (with ζ a proportionality constant). Therefore, we have

$$\zeta V_\pi \frac{2\pi}{\lambda} L = \pi \tag{4.18}$$

In a ring resonator with radius R and a phase shift section of length L, a change in effective index Δn_{eff} will result in a shift of the resonance wavelength given by

$$\Delta\lambda_r = \frac{\Delta n_{eff} L}{n_{eff} 2\pi R}\lambda_{r,0} = \frac{\zeta U L}{n_{eff} 2\pi R}\lambda_{r,0} \tag{4.19}$$

Now, assuming the laser wavelength is fixed, a small resonance shift $\Delta\lambda_r$ will lead to a change in transmitted optical power given by

$$\begin{aligned} P_{out} - P_{out,0} &\approx \frac{\partial P_{out,0}}{\partial \lambda}\Delta\lambda_r \\ &\approx \frac{\partial P_{out,0}}{\partial \lambda}\frac{\zeta U L}{n_{eff} 2\pi R}\lambda_{r,0} \\ &\approx \frac{\partial P_{out,0}}{\partial \lambda}\frac{\lambda^2}{n_{eff} 4\pi R}\frac{U}{V_\pi} \end{aligned} \tag{4.20}$$

Consequently, the $V_\pi L$ product can be estimated from the slope of the fitted line in figure 4.28(b) and the first-order derivative of the transmission spectrum at the

ALD overlay	TE	TM
No ALD overlay	1×10^2	2×10^2
PE-ALD ZnO	6	4
PET-ALD ZnO	1×10	2×10
PET-ALD ZnO + 6 nm Al_2O_3	6	5
TH-ALD ZnS	2×10	3×10
TH-ALD ZnS + 6 nm Al_2O_3	3×10	2×10

Table 4.12: $V_\pi L$ estimations (expressed in $\mathrm{V \cdot m}$) for SiN waveguide devices with different ALD overlays, both for the fundamental quasi-TE and -TM mode. These numbers were extracted from transmission measurements and modulation measurements at a frequency of 10 MHz.

bias point (i.e. laser wavelength), using the expression

$$V_\pi L \approx \frac{\lambda^2 L}{n_{eff} 4\pi R} \frac{\frac{\partial P_{out,0}}{\partial \lambda}}{\frac{\Delta P_{out}}{U_{peak}}} \tag{4.21}$$

The estimated $V_\pi L$ products for our SiN based waveguide modulators with different ALD overlays are shown in table 4.12. For the PET-ALD ZnO overlay, the addition of Al_2O_3 improves $V_\pi L$, which can be related to the improved crystallinity. For the ZnS overlay, no significant improvement was observed with the addition of Al_2O_3. The PE-ALD ZnO overlay gives $V_\pi L$ values similar to the PET-ALD ZnO with Al_2O_3 overlay, but the propagation loss is larger for the PE-ALD ZnO overlay. All of the modulators with ALD overlay have improved $V_\pi L$ products compared to the modulators without ALD overlay.

Also the electro-optic response for increasing modulation frequencies was measured (see figure 4.29). As the Pockels effect is an ultrafast effect, the bandwidth is expected to be limited by the cavity photon lifetime τ and/or the resistance-capacitance time constant. The 3 dB bandwidth can be estimated from $1/f_{3dB}^2 = 1/f_Q^2 + 1/f_{RC}^2 = (2\pi\tau)^2 + (\pi(50\,\Omega + 2R)C)^2$, where $50\,\Omega$ is the output impedance of the signal generator and termination of the probe; R and C are the series resistance and capacitance of the device [95]. From S_{11} parameter measurements, we found $C = 140\,\mathrm{fF}$ and $R = 200\,\Omega$. For each ring resonator, the cavity photon lifetime can be estimated from transmission measurements through use of the formula [89]

$$\tau = \frac{\lambda Q}{2\pi c} = \frac{\lambda^2}{2\pi c \delta\lambda} \tag{4.22}$$

where Q is the Q factor and $\delta\lambda$ the FWHM of the resonance. For the ZnS based modulators and blank SiN modulator measured in figure 4.29(b), we estimated the photon lifetimes and corresponding f_{3dB}: 29 ps, corresponding to 3.7 GHz (red), 37 ps, corresponding to 3.3 GHz (blue), and 97 ps, corresponding to 1.5 GHz

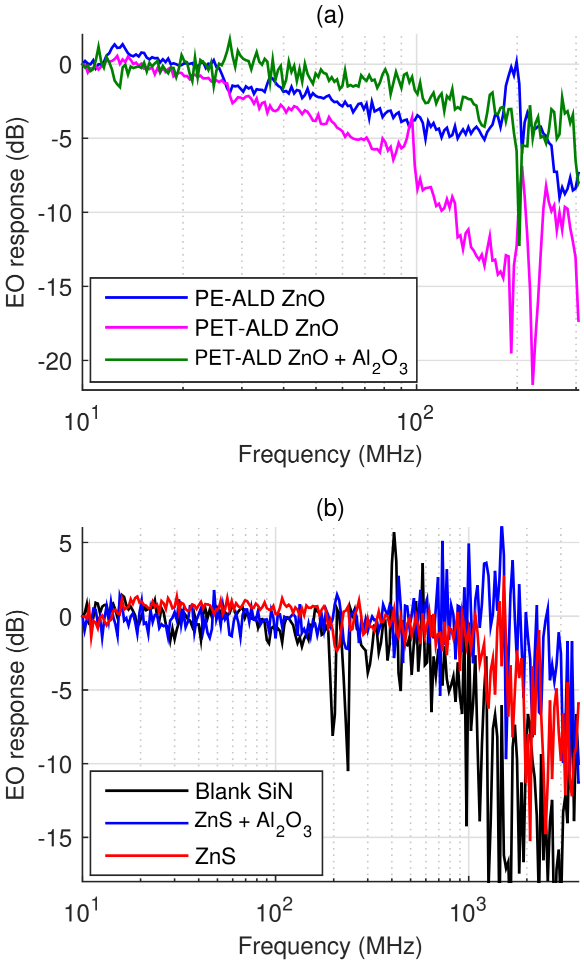

Figure 4.29: Electro-optic response (i.e. normalized ESA peak height) of modulators versus modulation frequency (wavelength fixed on slope of resonance). These measurements are done with a $50\,\Omega$ terminated GSG probe to avoid reflections. (a) PE-ALD ZnO (blue), PET-ALD ZnO (magenta), and PET-ALD ZnO with Al_2O_3 (green). (b) TH-ALD ZnS (red), TH-ALD ZnS with Al_2O_3 (blue), and SiN without ALD overlay (black).

(black). The observed bandwidths are somewhat smaller, however this is not unusual, as the above-mentioned empirical formula does not account for coupling conditions and wavelength [95]. For the ZnO based modulators, none of the above explains the $\approx 100\,\mathrm{MHz}$ bandwidths. ZnO is known to possess n-type conductivity due to the presence of defects and impurities [11]. The free charge carriers could play a role in the modulation mechanism. The resistivity ρ of the ALD films was measured with a 4-point probe. For the PE-ALD ZnO films, we found $\rho \approx 10\,\Omega\,\mathrm{cm}$. For all other ZnO and ZnS films ρ was above the measurement limit ($>10^4\,\Omega\,\mathrm{cm}$). The PET-ALD recipe was used specifically to increase ρ and decrease the carrier concentration [64]. Although ρ was increased by several orders of magnitude, this had no significant influence on the bandwidth. We did observe a decrease in propagation loss for the PET-ALD ZnO overlays compared to PE-ALD ZnO. To investigate the role of free carriers in the modulation mechanism and extend the bandwidth, a more in-depth material exploration is required, including annealing treatments and depositions at different temperatures to alter the film's resistivity [11]. For sputtered ZnO films with a resistivity on the order of $10^8\,\Omega\,\mathrm{cm}$, a free carrier electro-optic response has been reported [61]; though this response relaxed at a frequency of approximately $12\,\mathrm{kHz}$.

From the knowledge of $V_\pi L$, the simulated electrostatic and optical field distributions (using COMSOL), and expressions 4.15 and 4.16, the Pockels coefficients can be estimated. For SiN, we estimate $|r_{33}| \approx 0.01\,\mathrm{pm/V}$ and $|r_{13}| \approx 0.02\,\mathrm{pm/V}$. For ZnS (with Al_2O_3), we find $|r_{33}| \approx 0.3\,\mathrm{pm/V}$ $(0.4\,\mathrm{pm/V})$ and $|r_{13}| \approx 0.2\,\mathrm{pm/V}$ $(0.1\,\mathrm{pm/V})$. These values are smaller than those reported for ZnS single crystals, as expected for polycrystalline films. For PE-ALD ZnO, we estimate $|r_{33}| \approx 3\,\mathrm{pm/V}$ and $|r_{13}| \approx 2\,\mathrm{pm/V}$. For PET-ALD ZnO (with Al_2O_3), we find $|r_{33}| \approx 0.5\,\mathrm{pm/V}$ $(2\,\mathrm{pm/V})$ and $|r_{13}| \approx 0.7\,\mathrm{pm/V}$ $(2\,\mathrm{pm/V})$. Some of these values are larger than those reported for ZnO single crystals, which could also hint to the fact that other mechanisms play a role in the refractive index modulation.

Although the estimated $V_\pi L$ values are large, we do not need a full π phase shift in the ring resonators to realize modulation with a large extinction ratio $P_{out,max}/P_{out,min}$. For a critically coupled ring (i.e. $r = a$), the transmission is given by

$$T = \frac{4a^2 \sin^2 \frac{\phi}{2}}{(1-a^2)^2 + 4a^2 \sin^2 \frac{\phi}{2}} \tag{4.23}$$

So in principle, the transmission drops to 0 at resonance $\phi = m2\pi$ (with m an integer). The maximum transmission is $T_{max} = \frac{4a^2}{(1+a^2)^2}$ for $\phi = (2m+1)\pi$ (with m an integer). Switching between T_{min} and T_{max} requires a voltage V_π; but for sufficiently sharp resonances, we can get close to T_{max} by applying a much smaller voltage. Let's say we choose our wavelength so we are at resonance ($T = T_{min} = 0$) when no voltage is applied. When a voltage V is applied, the

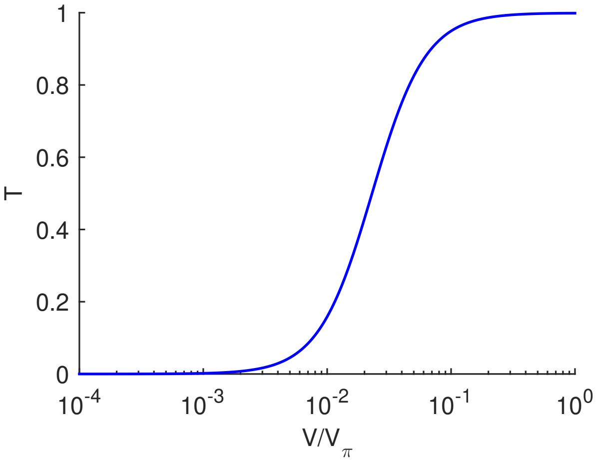

Figure 4.30: The transmission of a critically coupled ring modulator with radius $R = 100\,\mu\mathrm{m}$ and a propagation loss of $5\,\mathrm{dB/cm}$ plotted as a function of V/V_π, where V is the applied voltage. It is assumed that we are at resonance when no voltage is applied.

transmission will rise to

$$\begin{aligned} T &= \frac{4a^2 \sin^2 \frac{\Delta\phi_V}{2}}{(1-a^2)^2 + 4a^2 \sin^2 \frac{\Delta\phi_V}{2}} \\ &= \frac{4a^2 \sin^2 \frac{\pi V}{2V_\pi}}{(1-a^2)^2 + 4a^2 \sin^2 \frac{\pi V}{2V_\pi}} \end{aligned} \tag{4.24}$$

Figure 4.30 plots T as a function of V for a (critically coupled) ring with radius $R = 100\,\mu\mathrm{m}$ and a propagation loss of $5\,\mathrm{dB/cm}$. Switching between minimum transmission and a transmission of $-3\,\mathrm{dB}$ (not including coupling and access waveguide loss) requires only 2% of V_π.

By adapting the waveguide dimensions and electrode configuration, further improvements in $V_\pi L$ can be made. Firstly, the modal overlap with the electro-optic ALD layer can be increased by reducing the SiN thickness and/or increasing the ALD layer thickness. Secondly, the electrostatic field strength can be increased by lowering the ground electrodes (placing them in trenches etched in the SiO_2 next to the waveguide). Such a configuration is illustrated in figure 4.31. A contour plot of the simulated $V_\pi L$ product as a function of the vertical offset of the ground and signal electrodes with respect to the SiN waveguide core for this configuration is shown in figure 4.32 (using the Pockels coefficients found for PET-ALD ZnO on $6\,\mathrm{nm}$ Al_2O_3). The optimal value for the offset of the ground electrodes is around $-0.4\,\mu\mathrm{m}$. The $V_\pi L$ product decreases for a decreasing offset of the signal electrode (i.e. thinner BCB cladding), but this also results in increased absorption

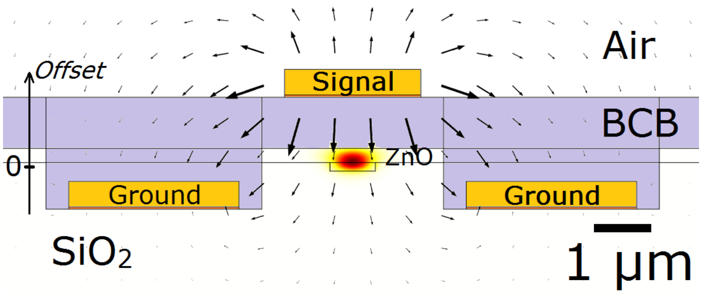

Figure 4.31: Simulated cross-section of a ZnO covered SiN waveguide with lowered ground electrodes. The intensity of the fundamental quasi-TE optical mode is shown along with the electric field induced by the electrodes (arrows). The SiN waveguide core has a width of $800\,\mathrm{nm}$ and a height of $150\,\mathrm{nm}$. The ZnO film has a thickness of $250\,\mathrm{nm}$. The vertical offset of the center of the ground electrodes with respect to the center of the SiN waveguide core is $-0.5\,\mathrm{\mu m}$. For the signal electrode this offset is $1.47\,\mathrm{\mu m}$.

loss. Therefore, it is interesting to define an alternative figure of merit $V_\pi L\alpha$, with α the propagation loss (including the absorption by the metal electrodes and the propagation loss of the waveguide itself). The simulation results for $V_\pi L\alpha$ are shown in figure 4.33. We find optimal values of approximately $370\,\mathrm{V\,dB}$ for the TE mode and $520\,\mathrm{V\,dB}$ for the TM mode, both corresponding to a $V_\pi L$ product of about $80\,\mathrm{V\,cm}$ (and metal absorption losses of $0.09\,\mathrm{dB/cm}$ for TE and $0.3\,\mathrm{dB/cm}$ for TM). So, using this alternative configuration, the $V_\pi L$ product can be reduced by a factor 6 to 8.

Other possible measures to increase the field strength are the use of transparent conducting oxides as electrodes which can be placed very close to the waveguide core [96], or using nanoplasmonic SiN slot waveguides [16].

4.3.4 Conclusions

The $\chi^{(2)}$ properties of back-end CMOS-compatible atomic layer deposited zinc oxide and zinc sulfide have been explored. ALD ZnO and ZnS thin films have been investigated in second-harmonic generation experiments and silicon nitride based electro-optic ring modulators with ALD ZnO and ZnS overlays have been demonstrated.

For PE-ALD ZnO films on a $6\,\mathrm{nm}$ ALD Al_2O_3 seed layer, $\chi^{(2)}$ nonlinearities similar to those of ZnO single crystals have been observed ($|\chi^{(2)}_{zzz}| = 15\,\mathrm{pm/V}$ at $\lambda_\omega = 800\,\mathrm{nm}$). The $\chi^{(2)}$ tensor components are signicantly larger than those reported for optimized TH-ALD ZnO/Al_2O_3 nanolaminates ($|\chi^{(2)}_{zzz}| = 4\,\mathrm{pm/V}$ at $\lambda_\omega = 800\,\mathrm{nm}$) [46]. For pure PE-ALD ZnO films, where no Al_2O_3 seed layer is present, we find a $|\chi^{(2)}_{zzz}|$ value comparable to that of the optimized TH-ALD

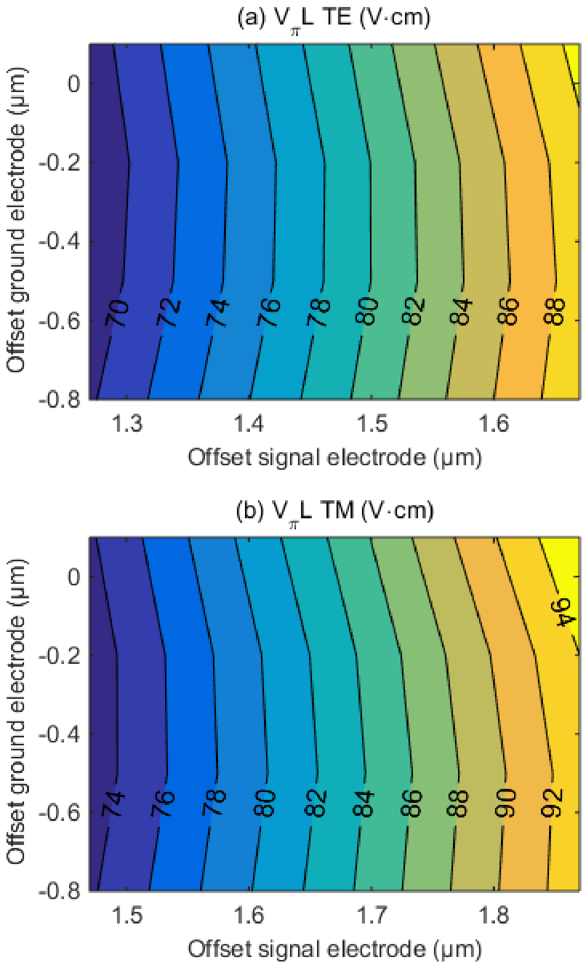

Figure 4.32: Contour plot of the simulated $V_\pi L$ product as a function of the vertical offset of the ground and signal electrodes with respect to the SiN waveguide core for the configuration illustrated in figure 4.31. Results are shown for (a) the fundamental quasi-TE mode and (b) the fundamental quasi-TM mode. In the simulation, the Pockels coefficients found for PET-ALD ZnO on $6\,\mathrm{nm}$ Al_2O_3 are used.

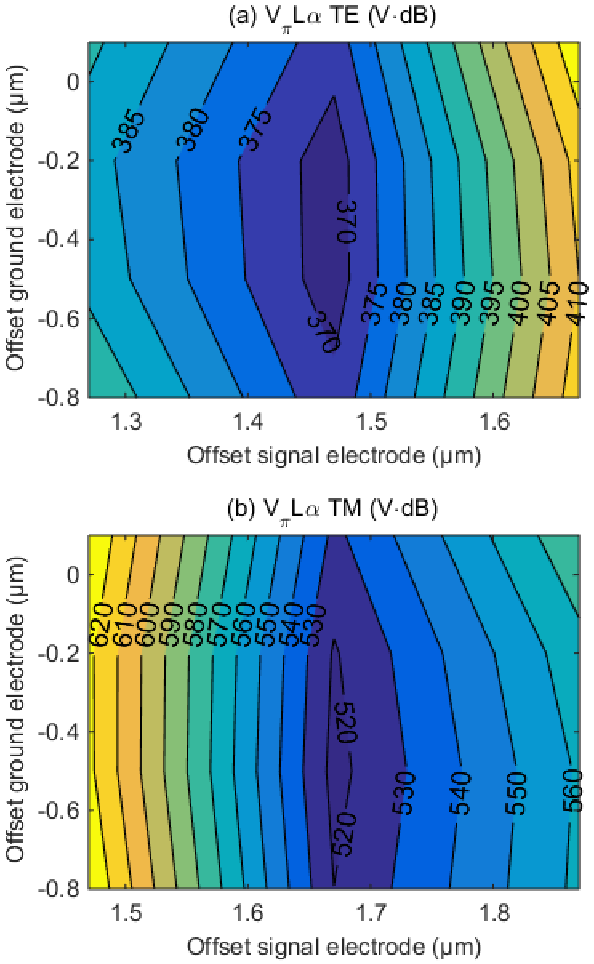

Figure 4.33: Contour plot of the simulated $V_\pi L\alpha$ product as a function of the vertical offset of the ground and signal electrodes with respect to the SiN waveguide core for the configuration illustrated in figure 4.31. Results are shown for (a) the fundamental quasi-TE mode and (b) the fundamental quasi-TM mode. In the simulation, the Pockels coefficients found for PET-ALD ZnO on $6\,\mathrm{nm}$ Al_2O_3 are used. The propagation loss α is calculated as the sum of the experimentally determined propagation loss and the simulated absorption loss induced by the metal electrodes.

ZnO/Al_2O_3 nanolaminate. The control over the magnitude of the $\chi^{(2)}$ nonlinearity by the presence or absence of a nanometer-thickness Al_2O_3 layer can open up possibilities for quasi-phase-matched second-order nonlinear optical processes. Also for PET-ALD ZnO and TH-ALD ZnS, the addition of a Al_2O_3 seed layer led to an enhancement in $\chi^{(2)}$ nonlinearity.

The propagation loss in SiN waveguides with ZnO and ZnS overlays has been estimated from ring resonator transmission measurements. For PE-ALD ZnO overlays, a fairly large loss of approximately $11\,\mathrm{dB/cm}$ has been estimated. For high resistivity PET-ALD ZnO, this goes down to about $5\,\mathrm{dB/cm}$. For TH-ALD ZnS, losses in the range 3 to $9\,\mathrm{dB/cm}$ were observed. The presence of a ZnO or ZnS overlay increases the loss compared to a bare SiN waveguide ($\alpha \approx 1\,\mathrm{dB/cm}$).

Electro-optic modulation measurements in silicon nitride based ring modulators indicated $V_\pi L$ products down to $4\,\mathrm{V\,m}$ when using ZnO overlays and $20\,\mathrm{V\,m}$ for ZnS overlays. This is a significant improvement compared to the $V_\pi L$ product of $\sim 100\,\mathrm{V\,m}$ for SiN waveguides without ALD overlay. For the SiN/ZnS ring modulators, modulation speeds over $1\,\mathrm{GHz}$ were reached, where we were limited by the cavity photon lifetime and the resistance-capacitance time constant. For the SiN/ZnO rings, the bandwidth was limited to $\approx 100\,\mathrm{MHz}$. Free charge carriers could play a role in the refractive index modulation mechanism. To investigate their role and extend the bandwidth, a more in-depth material exploration is required, possibly including annealing treatments and depositions at different temperatures to alter the film's resistivity [11]. Up to a factor 8 reduction in $V_\pi L$ is possible by simply increasing the ALD layer thickness, reducing the SiN thickness, and choosing a more optimal electrode configuration. Even larger improvements are possible when using transparent conducting oxide electrodes placed very close to the waveguide core, or by using nanoplasmonic SiN slot waveguides [16].

Concerning performance, the SiN/ZnO and SiN/ZnS platforms are not as good as the recently developed $LiNbO_3$-on-insulator [97] and PZT-on-SiN platforms [87], both also being transparent in the visible to near-infrared wavelength range. For $LiNbO_3$-on-insulator, $V_\pi L$ products down to $2\,\mathrm{V\,cm}$ have been reported (with $\alpha \approx 0.2\,\mathrm{dB/cm}$) [97] and losses as low as $2.7\,\mathrm{dB/m}$ [98]. Moreover, periodic poling of lithium niobate can be utilized for quasi-phase matching of $\chi^{(2)}$ processes, as has been demonstrated for second-harmonic generation in $LiNbO_3$-on-insulator waveguides [68, 69]. In PZT-on-SiN ring modulators, $V_\pi L$ products of $3.2\,\mathrm{V\,cm}$ have been measured and propagation losses down to $1\,\mathrm{dB/cm}$ [87]. However, the $LiNbO_3$-on-insulator technology requires expensive substrates prepared by wafer bonding. For PZT, the deposition involves annealing at a temperature of $620\,^\circ\mathrm{C}$. Therefore, these technologies are not suitable for monolithic integration on CMOS based on back-end deposited photonics [88], as opposed to low-temperature atomic layer deposited zinc oxide and zinc sulfide.

References

[1] E. L. Wooten, K. M. Kissa, A. Yi-Yan, E. J. Murphy, D. A. Lafaw, P. F. Hallemeier, D. Maack, D. V. Attanasio, D. J. Fritz, G. J. McBrien, and D. E. Bossi. *A review of lithium niobate modulators for fiber-optic communications systems*. IEEE Journal of Selected Topics in Quantum Electronics, 6(1):69, 2000.

[2] C. Kasap and P. Capper, editors. *Springer Handbook of Electronic and Photonic Materials*. Springer, 2006.

[3] A. Hermans, S. Clemmen, E. Solano, J. Dendooven, E. Brainis, C. Detavernier, and R. Baets. *Second-harmonic generation based on symmetry breaking in a periodically layered medium*. In Annual Workshop of the IEEE Photonics Society Benelux Chapter, page 6, 2015.

[4] S. Clemmen, A. Hermans, E. Solano, J. Dendooven, K. Koskinen, M. Kauranen, E. Brainis, C. Detavernier, and R. Baets. *Atomic layer deposited second-order nonlinear optical metamaterial for back-end integration with CMOS-compatible nanophotonic circuitry*. Optics Letters, 40(22):5371, 2015.

[5] A. Hermans, C. Kieninger, K. Koskinen, A. Wickberg, E. Solano, J. Dendooven, M. Kauranen, S. Clemmen, M. Wegener, C. Koos, and R. Baets. *On the determination of* $\chi^{(2)}$ *in thin films: a comparison of one-beam second-harmonic generation measurement methodologies*. Scientific Reports, 7:44581, 2017.

[6] A. Hermans, M. Van Daele, J. Dendooven, S. Clemmen, C. Detavernier, and R. Baets. *Electro-optic modulation in silicon nitride photonic integrated circuits by means of ALD ZnO overlays*. In European Conference on Integrated Optics (ECIO), page T5.3, 2017.

[7] A. Hermans, M. Van Daele, C. Kieninger, J. Dendooven, S. Clemmen, C. Detavernier, C. Koos, and R. Baets. *CMOS-compatible ALD zinc oxide coating for on-chip second-order nonlinear optical functionalities*. In Conference on Lasers and Electro-Optics (CLEO), page SM3K.3, 2017.

[8] A. Hermans, M. Van Daele, J. Dendooven, S. Clemmen, C. Detavernier, and R. Baets. *Integrated silicon nitride electro-optic modulators with atomic layer deposited overlays*. Optics Letters, 44(5):1112, 2019.

[9] CoCooN research group. *Welcome to the CoCooN research group*. `http://www.cocoon.ugent.be/`. [Accessed 5 May 2019].

[10] V. Miikkulainen, M. Leskelä, M. Ritala, and R. L. Puurunen. *Crystallinity of inorganic films grown by atomic layer deposition: overview and general trends*. Journal of Applied Physics, 113:021301, 2013.

[11] T. Tynell and M. Karppinen. *Atomic layer deposition of ZnO: a review*. Semiconductor Science and Technology, 29:043001, 2014.

[12] R. L. Puurunen. *Surface chemistry of atomic layer deposition: a case study for the trimethylaluminum/water process*. Journal of Applied Physics, 97:121301, 2005.

[13] R. W. Johnson, A. Hultqvist, and S. F. Bent. *A brief review of atomic layer deposition: from fundamentals to applications*. Materials Today, 17(5):236, 2014.

[14] D. Longrie, D. Deduytsche, and C. Detavernier. *Reactor concepts for atomic layer deposition on agitated particles: a review*. Journal of Vacuum Science & Technology A, 32(1):010802, 2014.

[15] C. Detavernier, J. Dendooven, S. Pulinthanathu Sree, K. F. Ludwig, and J. A. Martens. *Tailoring nanoporous materials by atomic layer deposition*. Chemical Society Reviews, 40:5242, 2011.

[16] A. Raza, S. Clemmen, P. Wuytens, M. Muneeb, M. Van Daele, J. Dendooven, C. Detavernier, A. Skirtach, and R. Baets. *ALD assisted nanoplasmonic slot waveguide for on-chip enhanced Raman spectroscopy*. APL Photonics, 3:116105, 2018.

[17] A. Wickberg, A. Abass, H.-H. Hsiao, C. Rockstuhl, and M. Wegener. *Second-harmonic generation by 3D laminate metacrystals*. Advanced Optical Materials, page 1801235, 2019.

[18] K. Mistry, C. Allen, C. Auth, B. Beattie, D. Bergstrom, M. Bost, M. Brazier, M. Buehler, A. Cappellani, R. Chau, C.-H. Choi, G. Ding, K. Fischer, T. Ghani, R. Grover, W. Han, D. Hanken, M. Hattendorf, J. He, J. Hicks, R. Huessner, D. Ingerly, P. Jain, R. James, L. Jong, S. Joshi, C. Kenyon, K. Kuhn, K. Lee, H. Liu, J. Maiz, B. McIntyre, P. Moon, J. Neirynck, S. Pae, C. Parker, D. Parsons, C. Prasad, L. Pipes, M. Prince, P. Ranade, T. Reynolds, J. Sandford, L. Shifren, J. Sebastian, J. Seiple, D. Simon, S. Sivakumar, P. Smith, C. Thomas, T. Troeger, P. Vandervoorn, S. Williams, and K. Zawadzki. *A 45nm logic technology with high-k+metal gate transistors, strained silicon, 9 Cu unterconnect layers, 193nm dry patterning, and 100% Pb-free packaging*. In IEEE International Electron Devices Meeting, page 247, 2007.

[19] Lotus Applied Technology. *Conventional ALD*. `http://lotusat.com/conventional-ald/`. [Accessed 17 April 2019].

[20] P. Sundberg and M. Karppinen. *Organic and inorganic-organic thin film structures by molecular layer deposition: a review*. Beilstein Journal of Nanotechnology, 5:1104, 2014.

[21] P. Lalanne and M. Hutley. *Artifical Media Optical Properties - Subwavelength Scale*. In R. G. Driggers, editor, Encyclopedia of Optical Engineering, volume 1, page 62. Marcel Dekker, Inc., 2003.

[22] R. W. Boyd and J. E. Sipe. *Nonlinear optical susceptibilities of layered composite materials*. Journal of the Optical Society of America B, 11(2):297, feb 1994.

[23] G. L. Fischer, R. W. Boyd, R. J. Gehr, S. A. Jenekhe, J. A. Osaheni, J. E. Sipe, and L. A. Weller-Brophy. *Enhanced nonlinear optical response of composite materials*. Physical Review Letters, 74(10):1871, 1995.

[24] E. Ghahramani, D. J. Moss, and J. E. Sipe. *Second-harmonic generation in odd-period, strained,* $(Si)_n(Ge)_n/Si$ *superlattices and at Si/Ge interfaces*. Physical review letters, 64(23):2815, 1990.

[25] E. Ghahramani, D. J. Moss, and J. E. Sipe. *Full-band-structure calculation of second-harmonic generation in odd-period strained* $(Si)_n/(Ge)_n$ *superlattices*. Physical Review B, 43(11):8990, 1991.

[26] M. M. Fejer, S. J. B. Yoo, R. L. Byer, A. Harwit, and J. S. Harris. *Observation of extremely large quadratic susceptibility at* 9.6-10.8 µm. Physical Review Letters, 62(9):1041, 1989.

[27] J. Lee, M. Tymchenko, C. Argyropoulos, P.-Y. Chen, F. Lu, F. Demmerle, G. Boehm, M.-C. Amann, A. Alù, and M. A. Belkin. *Giant nonlinear response from plasmonic metasurfaces coupled to intersubband transitions*. Nature, 511:65, 2014.

[28] M. Zdanowicz, J. Harra, J. M. Mäkelä, E. Heinonen, T. Ning, M. Kauranen, and G. Genty. *Second-harmonic response of multilayer nanocomposites of silver-decorated nanoparticles and silica*. Scientific reports, 4:5745, 2014.

[29] I. R. Girling, P. V. Kolinsky, N. A. Cade, J. D. Earls, and I. R. Peterson. *Second harmonic generation from alternating Langmuir-Blodgett films*. Optics Communications, 55(4):289, 1985.

[30] L. Alloatti, C. Kieninger, A. Froelich, M. Lauermann, T. Frenzel, K. Köhnle, W. Freude, J. Leuthold, M. Wegener, and C. Koos. *Second-order nonlinear*

optical metamaterials: ABC-type nanolaminates. Applied Physics Letters, 107(12):121903, 2015.

[31] K. K. Shih and D. B. Dove. *Deposition of aluminum oxide films with high refractive index*. Journal of Vacuum Science & Technology A, 12(2):321, 1994.

[32] F. L. Martínez, M. Toledano-Luque, J. J. Gandía, J. Cárabe, W. Bohne, J. Röhrich, E. Strub, and I. Mártil. *Optical properties and structure of HfO_2 thin films grown by high pressure reactive sputtering*. Journal of Physics D: Applied Physics, 40:5256, 2007.

[33] R. K. Ramachandran, J. Dendooven, H. Poelman, and C. Detavernier. *Low temperature atomic layer deposition of crystalline In_2O_3 films*. The Journal of Physical Chemistry C, 119:11786, 2015.

[34] F. O. Adurodija, L. Semple, and R. Brüning. *Real-time in situ crystallization and electrical properties of pulsed laser deposited indium oxide thin films*. Thin Solid Films, 492:153, 2005.

[35] W. Shimizu, S. Nakamura, T. Sato, and Y. Murakami. *Creation of high-refractive-index amorphous titanium oxide thin films from low-fractal-dimension polymeric precursors synthesized by a sol-gel technique with a hydrazine monohydrochloride catalyst*. Langmuir, 28:12245, 2012.

[36] W. Massa. *Crystal Structure Determination*. Springer, 2000.

[37] F. J. Rodriguez, F. X. Wang, and M. Kauranen. *Calibration of the second-order nonlinear optical susceptibility of surface and bulk of glass*. Optics Express, 16(12):8704, 2008.

[38] G. P. Agrawal. *Nonlinear Fiber Optics*. Academic Press, 3rd edition, 2001.

[39] W. N. Herman and L. M. Hayden. *Maker fringes revisited: second-harmonic generation from birefringent or absorbing materials*. Journal of the Optical Society of America B, 12(3):416, 1995.

[40] V. G. Dmitriev, G. G. Gurzadyan, and D. N. Nikogosyan. *Handbook of Nonlinear Optical Crystals*. Springer, 3rd edition, 1999.

[41] SCHOTT Technical Glass Solutions GmbH. *SCHOTT BOROFLOAT® 33 Datasheet*. `http://psec.uchicago.edu/glass/borofloat_33_e.pdf`. [Accessed 1 August 2016].

[42] S. J. Schneider. *Compilation of the Melting Points of the Metal Oxides*. National Bureau of Standards, 1963.

[43] R. Addou, L. Colombo, and R. M. Wallace. *Surface defects on natural* MoS_2. ACS Applied Materials & Interfaces, 7:11921, 2015.

[44] H.-H. Lin, M.-H. Yang, R. Sharma, M. W. Puckett, S. Montoya, C. D. Wurm, F. Vallini, E. E. Fullerton, and Y. Fainman. *Synthesis of second-order nonlinearities in dielectric-semiconductor-dielectric metamaterials*. Applied Physics Letters, 110:113103, 2017.

[45] H.-H. Lin, F. Vallini, M.-H. Yang, R. Sharma, M. W. Puckett, S. Montoya, C. D. Wurm, E. E. Fullerton, and Y. Fainman. *Electronic metamaterials with tunable second-order optical nonlinearities*. Scientific Reports, 7:9983, 2017.

[46] A. Wickberg, C. Kieninger, C. Sürgers, S. Schlabach, X. Mu, C. Koos, and M. Wegener. *Second-harmonic generation from* ZnO/Al_2O_3 *nanolaminate optical metamaterials grown by atomic-layer deposition*. Advanced Optical Materials, 4:1203, 2016.

[47] M. C. Larciprete and M. Centini. *Second harmonic generation from ZnO films and nanostructures*. Applied Physics Reviews, 2(3):031302, 2015.

[48] J. R. Pressley, editor. *Handbook of Lasers with Selected Data on Optical Technology*. The Chemical Rubber Co., 1971.

[49] I. P. Kaminow and E. H. Turner. *Electrooptic light modulators*. Proceedings of the IEEE, 54(10):1374, 1966.

[50] H. Cao, J. Y. Wu, H. C. Ong, J. Y. Dai, and R. P. H. Chang. *Second harmonic generation in laser ablated zinc oxide thin films*. Applied Physics Letters, 73(5):572, 1998.

[51] G. Wang, G. T. Kiehne, G. K. L. Wong, J. B. Ketterson, X. Liu, and R. P. H. Chang. *Large second harmonic response in ZnO thin films*. Applied Physics Letters, 80(3):401, 2002.

[52] X. Q. Zhang, Z. K. Tang, M. Kawasaki, A. Ohtomo, and H. Koinuma. *Second harmonic generation in self-assembled ZnO microcrystallite thin films*. Thin Solid Films, 450:320, 2004.

[53] H. Kato, K. Miyamoto, M. Sano, and T. Yao. *Polarity control of ZnO on sapphire by varying the MgO buffer layer thickness*. Applied Physics Letters, 84(22):4562, 2004.

[54] J. S. Park, T. Minegishi, S. H. Lee, I. H. Im, S. H. Park, T. Hanada, T. Goto, M. W. Cho, T. Yao, S. K. Hong, and J. H. Chang. *Effects of interfacial layer structures on crystal structural properties of ZnO films*. Journal of Vacuum Science & Technology A, 26(1):90, 2008.

[55] J. S. Park, Y. Yamazaki, Y. Takahashi, S. K. Hong, J. H. Chang, T. Fujiwara, and T. Yao. *Origin of second-order nonlinear optical response of polarity-controlled ZnO films*. Applied Physics Letters, 94:231118, 2009.

[56] J. Park, Y. Yamazaki, M. Iwanaga, S. Ahn, H. Jeon, T. Fujiwara, and T. Yao. *Second harmonic generation in periodically polarity-inverted zinc oxide*. Optics Express, 18(8):7851, 2010.

[57] S. Enoch and H. Akhouayri. *Second-harmonic specular and scattered generated light: application to the experimental study of zinc-sulfide thin films*. Applied Optics, 36(25):6319, 1997.

[58] K. Christova, I. A. Maslyanitsyn, I. Miloushev, V. D. Shigorin, T. Tenev, and V. Voronov. *Second harmonic generation in thin zinc sulfide films*. Physics of Wave Phenomena, 26(1):9, 2018.

[59] H. Ito and H. Inaba. *Efficient phase-matched second-harmonic generation method in four-layered optical-waveguide structure*. Optics Letters, 2(6):139, 1978.

[60] V. Gulia and S. Kumar. *Electro-optic effect in c-axis oriented ZnO thin films prepared by rf magnetron sputtering*. Optical Materials, 29(7):778, 2007.

[61] L. Dominici, M. Auf der Maur, and F. Michelotti. *Strong free-carrier electro-optic response of sputtered ZnO films*. Journal of Applied Physics, 112:053514, 2012.

[62] D. Persegol, E. Pic, and J. Plantier. *Experimental study of a ZnO modulator using guided wave resonance*. Journal of Applied Physics, 62(6):2563, 1987.

[63] B. Wong, P. E. Jessop, and A. H. Kitai. *Pockels' effect in polycrystalline ZnS planar waveguides*. Journal of Applied Physics, 70(3):1180, 1991.

[64] M. A. Thomas and J. B. Cui. *Highly tunable electrical properties in undoped ZnO grown by plasma enhanced thermal-atomic layer deposition*. ACS Applied Materials & Interfaces, 4:3122, 2012.

[65] P. Zaumseil. *High-resolution characterization of the forbidden Si 200 and Si 222 reflections*. Journal of Applied Crystallography, 48:528, 2015.

[66] J. Kuhs, T. Dobbelaere, Z. Hens, and C. Detavernier. *Plasma enhanced atomic layer deposition of zinc sulfide thin films*. Journal of Vacuum Science & Technology A, 35(1):01B111, 2017.

[67] M. Scocioreanu, M. Baibarac, I. Baltog, I. Pasuk, and T. Velula. *Photoluminescence and Raman evidence for mechanico-chemical interaction of*

polyaniline-emeraldine base with ZnS in cubic and hexagonal phase. Journal of Solid State Chemistry, 186:217, 2012.

[68] L. Chang, Y. Li, N. Volet, L. Wang, J. Peters, and J. E. Bowers. *Thin film wavelength converters for photonic integrated circuits*. Optica, 3(5):531, 2016.

[69] C. Wang, C. Langrock, A. Marandi, M. Jankowski, M. Zhang, B. Desiatov, M. M. Fejer, and M. Lončar. *Ultrahigh-efficiency wavelength conversion in nanophotonic periodically poled lithium niobate waveguides*. Optica, 5(11):1438, 2018.

[70] H. Tampo, P. Fons, A. Yamada, K.-K. Kim, H. Shibata, K. Matsubara, S. Niki, H. Yoshikawa, and H. Kanie. *Determination of crystallographic polarity of ZnO layers*. Applied Physics Letters, 87:141904, 2005.

[71] I. Shoji, T. Kondo, A. Kitamoto, M. Shirane, and R. Ito. *Absolute scale of second-order nonlinear-optical coefficients*. Journal of the Optical Society of America B, 14(9):2268, 1997.

[72] L. Zhuang, C. G. H. Roeloffzen, M. Hoekman, K.-J. Boller, and A. J. Lowery. *Programmable photonic signal processor chip for radiofrequency applications*. Optica, 2(10):854, 2015.

[73] C. Taballione, T. A. W. Wolterink, J. Lugani, A. Eckstein, B. A. Bell, R. Grootjans, I. Visscher, D. Geskus, C. G. H. Roeloffzen, J. J. Renema, I. A. Walmsley, P. W. H. Pinkse, and K.-J. Boller. 8×8 *programmable quantum photonic processor based on silicon nitride waveguides*. arXiv:1805.10999, 2018.

[74] M. Raval, A. Yaacobi, D. Coleman, N. M. Fahrenkopf, C. Baiocco, G. Leake, T. N. Adam, D. Coolbaugh, and M. R. Watts. *Nanophotonic phased array for visible light image projection*. In IEEE Photonics Conference, page MG3.4, 2016.

[75] C. V. Poulton, M. J. Byrd, M. Raval, Z. Su, N. Li, E. Timurdogan, D. Coolbaugh, D. Vermeulen, and M. R. Watts. *Large-scale silicon nitride nanophotonic phased arrays at infrared and visible wavelengths*. Optics Letters, 42(1):21, 2017.

[76] G. T. Reed, G. Mashanovich, F. Y. Gardes, and D. J. Thomson. *Silicon optical modulators*. Nature Photonics, 4:518, 2010.

[77] S. Miller, Y.-H. D. Lee, J. Cardenas, A. L. Gaeta, and M. Lipson. *Electro-optic effect in silicon nitride*. In Conference on Lasers and Electro-Optics (CLEO), page SF1G.4, 2015.

[78] T. Ning, H. Pietarinen, O. Hyvärinen, J. Simonen, G. Genty, and M. Kauranen. *Strong second-harmonic generation in silicon nitride films*. Applied Physics Letters, 100(16):161902, 2012.

[79] E. F. Pecora, A. Capretti, G. Miano, and L. Dal Negro. *Generation of second harmonic radiation from sub-stoichiometric silicon nitride thin films*. Applied Physics Letters, 102:141114, 2013.

[80] A. Kitao, K. Imakita, I. Kawamura, and M. Fujii. *An investigation into second harmonic generation by Si-rich SiN_x thin films deposited by RF sputtering over a wide range of Si concentrations*. Journal of Physics D: Applied Physics, 47:215101, 2014.

[81] M. W. Puckett, R. Sharma, H. H. Lin, M. H. Yang, F. Vallini, and Y. Fainman. *Observation of second-harmonic generation in silicon nitride waveguides through bulk nonlinearities*. Optics Express, 24(15):16923, 2016.

[82] K. Koskinen, R. Czaplicki, A. Slablab, T. Ning, A. Hermans, B. Kuyken, V. Mittal, G. S. Murugan, T. Niemi, R. Baets, and M. Kauranen. *Enhancement of bulk second-harmonic generation from silicon nitride films by material composition*. Optics Letters, 42(23):5030, 2017.

[83] J. S. Levy, M. A. Foster, A. L. Gaeta, and M. Lipson. *Harmonic generation in silicon nitride ring resonators.* Optics express, 19(12):11415, 2011.

[84] J. Joo, J. Park, and G. Kim. *Cost-effective* 2×2 *silicon nitride Mach-Zehnder interferometric (MZI) thermo-optic switch*. IEEE Photonics Technology Letters, 30(8):740, 2018.

[85] C. T. Phare, Y.-H. D. Lee, J. Cardenas, and M. Lipson. *Graphene electro-optic modulator with 30 GHz bandwidth*. Nature Photonics, 9:511, 2015.

[86] K. K. Mehta, G. N. West, and R. J. Ram. *SiN-on-$LiNbO_3$ integrated optical modulation at visible wavelengths*. In Conference on Lasers and Electro-Optics (CLEO), page STu3N.7, 2017.

[87] K. Alexander, J. P. George, J. Verbist, K. Neyts, B. Kuyken, D. Van Thourhout, and J. Beeckman. *Nanophotonic Pockels modulators on a silicon nitride platform*. Nature Communications, 9:3444, 2018.

[88] Y. H. D. Lee and M. Lipson. *Back-end deposited silicon photonics for monolithic integration on CMOS*. IEEE Journal of Selected Topics in Quantum Electronics, 19(2):8200207, 2013.

[89] C. Xiong, W. H. P. Pernice, and H. X. Tang. *Low-loss, silicon integrated, aluminum nitride photonic circuits and their use for electro-optic signal processing*. Nano Letters, 12(7):3562, 2012.

[90] C. V. Poulton, A. Yaacobi, D. B. Cole, M. J. Byrd, M. Raval, D. Vermeulen, and M. R. Watts. *Coherent solid-state LIDAR with silicon photonic optical phased arrays*. Optics Letters, 42(20):4091, 2017.

[91] C. Koos. *Nanophotonic Devices for Linear and Nonlinear Optical Signal Processing*. PhD thesis, Universität Karlsruhe (TH), 2007.

[92] C. Koos, J. Leuthold, W. Freude, M. Kohl, L. Dalton, W. Bogaerts, A. L. Giesecke, M. Lauermann, A. Melikyan, S. Koeber, S. Wolf, C. Weimann, S. Muehlbrandt, K. Koehnle, J. Pfeifle, W. Hartmann, Y. Kutuvantavida, S. Ummethala, R. Palmer, D. Korn, L. Alloatti, P. C. Schindler, D. L. Elder, T. Wahlbrink, and J. Bolten. *Silicon-organic hybrid (SOH) and plasmonic-organic hybrid (POH) integration*. Journal of Lightwave Technology, 34(2):256, 2016.

[93] K. Alexander. *Integrated Silicon Nitride Photonics with Highly Nonlinear Thin Films and 2D Materials: Properties and Devices*. PhD thesis, Ghent University, 2018.

[94] W. Bogaerts, P. De Heyn, T. Van Vaerenbergh, K. De Vos, S. K. Selvaraja, T. Claes, P. Dumon, P. Bienstman, D. Van Thourhout, and R. Baets. *Silicon microring resonators*. Laser and Photonics Reviews, 6(1):47, 2012.

[95] H. Yu, D. Ying, M. Pantouvaki, J. Van Campenhout, P. Absil, Y. Hao, J. Yang, and X. Jiang. *Trade-off between optical modulation amplitude and modulation bandwidth of silicon micro-ring modulators*. Optics Express, 22(12):15178, 2014.

[96] G. Xu, Z. Liu, J. Ma, B. Liu, S.-T. Ho, L. Wang, P. Zhu, T. J. Marks, J. Luo, and A. K. Y. Jen. *Organic electro-optic modulator using transparent conducting oxides as electrodes*. Optics Express, 13(19):7380, 2005.

[97] C. Wang, M. Zhang, X. Chen, M. Bertrand, A. Shams-Ansari, S. Chandrasekhar, P. Winzer, and M. Lončar. *Integrated lithium niobate electro-optic modulators operating at CMOS-compatible voltages*. Nature, 562:101, 2018.

[98] M. Zhang, C. Wang, R. Cheng, A. Shams-Ansari, and M. Lončar. *Monolithic ultra-high-Q lithium niobate microring resonator*. Optica, 4(12):1536, 2017.

5

Organic second-order nonlinear crystalline thin films: BNA

This chapter treats the low-temperature growth of organic crystalline thin films with a large $\chi^{(2)}$ nonlinearity on amorphous substrates. The organic material that has been investigated is *N*-benzyl-2-methyl-4-nitroaniline, or BNA. The $\chi^{(2)}$ nonlinearity of the BNA thin films has been characterized in second-harmonic generation experiments. The results shown here have been published in part in [1, 2].

Contents

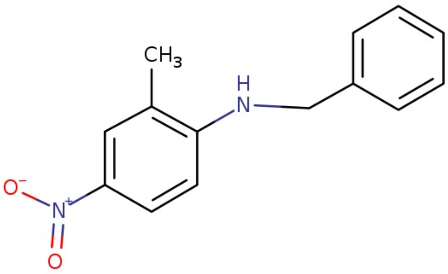

Figure 5.1: Chemical structure of a BNA molecule. Figure reproduced from [12].

5.1 Introduction

Organic materials can have very strong $\chi^{(2)}$ nonlinearities compared to conventional inorganic nonlinear crystals. Table 5.1 compares some organic $\chi^{(2)}$ materials with the ferroelectric inorganic $\chi^{(2)}$ material $LiNbO_3$, one of the benchmark nonlinear crystals, known for its large nonlinearity and wide transparency range. Although the $\chi^{(2)}(-\omega;\omega,0)$ nonlinearity of $LiNbO_3$ is relatively large (i.e. strong Pockels effect), the $\chi^{(2)}(-2\omega;\omega,\omega)$ nonlinearity is significantly smaller than that of the organic $\chi^{(2)}$ materials listed. $LiNbO_3$ thanks its strong $\chi^{(2)}(-\omega;\omega,0)$ nonlinearity to the ionic contributions (see sections 2.5 and 2.7). Due to these strong ionic contributions, there is also a large difference in ϵ at low and optical frequencies, which gives bandwidth limitations in optical modulators. Organic $\chi^{(2)}$ materials are typically based on π-conjugated molecules with strong electron donor and acceptor groups at the ends of the π-conjugated structure (chemical structure of a BNA molecule is shown in figure 5.1). The delocalized electrons associated with this π-conjugated structure are in a strongly asymmetric potential well, giving rise to a large (electronic) $\chi^{(2)}$ nonlinearity. As the $\chi^{(1)}$ and $\chi^{(2)}$ susceptibilities are mostly electronic in origin, ϵ and $\chi^{(2)}$ vary little from DC up to near-infrared or visible light frequencies (see also section 2.7). This makes organic $\chi^{(2)}$ materials particularly interesting both for high-speed electro-optic modulation and nonlinear wave mixing (at optical frequencies).

Moreover, many organic materials can be processed at low temperatures using

Material	λ_c (µm)	$\chi^{(2)}(-2\omega;\omega,\omega)$ (pm/V)	$\chi^{(2)}(-\omega;\omega,0)$ (pm/V)	Ref.
$LiNbO_3$	0.4	54 $(\lambda_\omega = 1.064\,\mu m)$	$\sim$400 $(\lambda_\omega = 0.633\,\mu m)$	[4–6]
DAST	0.7	580 $(\lambda_\omega = 1.542\,\mu m)$	$\sim$500 $(\lambda_\omega = 1.535\,\mu m)$	[7–9]
BNA	0.5	468 $(\lambda_\omega = 1.064\,\mu m)$	$\sim 200^{(a)}$ $(\lambda_\omega = 1.550\,\mu m)$	[3, 10]
HD-BB-OH/ YLD 124	1.1		$\sim$1400 $(\lambda_\omega = 1.310\,\mu m)$	[11]

Table 5.1: Overview of the largest $\chi^{(2)}$ tensor components for the organic crystals DAST and BNA, the poled organic material HD-BB-OH/YLD 124, and the inorganic ferroelectric crystal $LiNbO_3$ (see also section 2.7). The $\chi^{(2)}$ nonlinearity extracted from second-harmonic generation ($\chi^{(2)}(-2\omega;\omega,\omega)$) and electro-optic modulation experiments ($\chi^{(2)}(-\omega;\omega,0)$) is given. $\chi^{(2)}(-\omega;\omega,0)$ is calculated from the Pockels tensor r using formula 2.44. λ_c denotes the wavelength corresponding to the absorption edge obtained from transmission/absorption spectra or ellipsometry measurements.
$^{(a)}$This is the $\chi^{(2)}$ nonlinearity for an evaporated poled film [3]. No data on single crystals was found.

inexpensive solution based techniques. Whereas the growth of inorganic $\chi^{(2)}$ materials typically requires high temperatures and/or the use of vacuum equipment.

Organic $\chi^{(2)}$ materials in the solid phase are usually molecular solids, meaning they consist of discrete molecules being held together by relatively weak intermolecular forces such as van der Waals forces or hydrogen bonds. Even though the molecules can have a strong second-order nonlinearity (known as the molecular hyperpolarizability β [13]), they still need to arrange into a non-centrosymmetric structure to get a non-vanishing bulk $\chi^{(2)}$ nonlinearity. Unfortunately, organic compounds tend to organize in centrosymmetric arrangements [9, 14, 15].

An often used technique to break the inversion symmetry is to pole the material. This approach has led to the realization of efficient, high-speed silicon-organic and plasmonic-organic hybrid integrated electro-optic modulators [16, 17]. In these devices, an organic material is deposited (e.g. by spin coating) on top of silicon slot or plasmonic slot waveguides. After deposition, the nonlinear molecules have random orientations. To get a macroscopic $\chi^{(2)}$ effect, the material is heated to its glass-transition temperature T_g while applying a DC voltage across the slot. Under influence of the applied electric field, the polar nonlinear molecules will align in the slot. This ordered configuration is frozen by cooling the material down to room temperature while keeping the poling voltage constant. Finally, the poling voltage is removed. Unfortunately, the molecules tend to relax over time towards an energetically favored random orientation, thus leading to partial or complete loss of the macroscopic $\chi^{(2)}$ effect [18]. This detrimental effect gets worse when the temperature gets closer to the glass-transition temperature T_g. To reduce the impact of this effect, T_g can be increased by carefully engineering the organic molecules [18].

Although many organic compounds crystallize in centrosymmetric structures, multiple organic nonlinear molecules crystallizing in acentric arrangements have been identified [7, 19–32]. As opposed to poled organic materials, these organic crystals are orientationally stable [9]; furthermore, they show a superior photochemical stability [33]. However, most reports focus on the growth of bulk organic nonlinear crystals. The fabrication of organic crystalline thin films with sub-micron thicknesses and sufficient optical quality for applications in integrated optics is far from trivial [34]. Organic nonlinear thin films with thicknesses in the range 0.1-$4\,\mu\mathrm{m}$, centimeter-scale crystalline domains, and good optical quality have been grown from solution on amorphous substrates, but they take several weeks to grow [35, 36]. Also the patterning of organic films is challenging, since most organic materials dissolve in the solvents used in conventional lithographic processing. In addition, the baking of the photoresist can be a problem for organic materials with low melting points. Organic films that are insoluble in water can be patterned using a water soluble inorganic photoresist [37], or by spin coating a polyvinyl alcohol (dissolved in water) protection layer on top and using low-temperature baked SU-8 as a photoresist [38]. Alternatively, photoresists based on fluorous solvents can be used as these are benign to many organic materials [39, 40]. Even without lithographic patterning of the organic film, organic single crystal waveguides with sub-micron heights have been realized [41, 42]. The fabrication process starts with the patterning of channels on one substrate. Next, a second substrate is bonded on top. Subsequently, the empty channels are filled with molten organic material relying on capillary flow. Finally, the sample is cooled down slowly in a non-uniform temperature profile to crystallize the material while preventing multiple nucleation points. The crystallization process takes several hours to several days.

A widely investigated organic nonlinear crystal with a large $\chi^{(2)}$ nonlinearity (see table 5.1) is DAST (4-N,N-dimethylamino-4'-N'-methyl-stilbazolium tosylate) [9]. But, working with DAST has several disadvantages. DAST dissolves in water and forms a hydrated centrosymmetric phase when grown in a humid environment [9, 34]. Also, DAST decomposes at its melting temperature (256 °C), therefore melt based growth methods are generally undesirable. This is a common problem for nonlinear organic molecules. Typically, the hyperpolarizability of these molecules is increased by elongating the molecules. This elongation often leads to a decrease of the decomposition temperature [34].

Another organic nonlinear crystal with well known properties is BNA (*N*-benzyl-2-methyl-4-nitroaniline). BNA crystals have no hygroscopic character and are therefore stable during water based processing (e.g. BNA crystals can be pol-

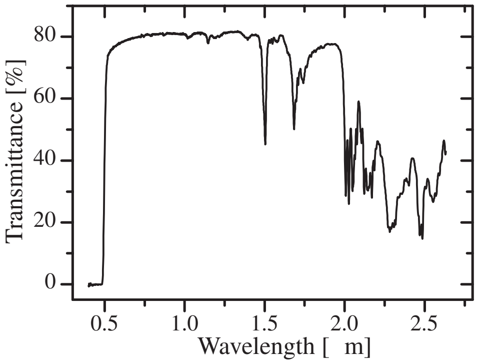

Figure 5.2: Transmission spectrum of a $1\,\mathrm{mm}$ thick cleaved BNA slab recorded at room temperature with non-polarized light. Figure reproduced from [10].

ished using water and alumina powder) [10]. BNA does not decompose at its melting temperature ($105\,°\mathrm{C}$) and can consequently be grown from the melt [19, 43]. In addition, BNA is transparent down to a wavelength of $500\,\mathrm{nm}$ [10] (compared to $700\,\mathrm{nm}$ for DAST, see table 5.1). A transmission spectrum for a bulk BNA crystal is shown in figure 5.2. Most organic materials with a large $\chi^{(2)}$ nonlinearity have longer cut-off wavelengths. Typically, organic nonlinear molecules with longer conjugated structures have a larger hyperpolarizability, but a red-shifted absorption edge. For instance, the poled organic material HD-BB-OH/YLD 124 has a significantly larger $\chi^{(2)}$ nonlinearity than that of BNA or DAST (see table 5.1), but also its cut-off wavelength is considerably larger ($1.1\,\mu\mathrm{m}$) [11]. Yet, there have been reports of molecules with very large hyperpolarizabilities without the associated red-shifted absorption [44]. We have chosen to work with BNA because of the aforementioned properties and the commercial availability of BNA molecules.

BNA is mainly reported to exist in a non-centrosymmetric orthorhombic phase (point group mm2) [19, 42, 43, 45–47], but also a centrosymmetric monoclinic phase has been observed [48]. An irreversible transformation of the metastable monoclinic phase to the orthorhombic phase was reported to take place at $362\,\mathrm{K}$ ($89\,°\mathrm{C}$). The refractive indices and d tensor components for orthorhombic BNA are listed in table 5.2. Since orthorhombic BNA is a biaxial crystal, three refractive indices n_X, n_Y, and n_Z are given. The dielectric axes X, Y, and Z correspond to the crystal axes a, b, and c, and are denoted as 1, 2, and 3 for the d tensor components [43]. The measured wavelength dispersion for the d_{333} coefficient of BNA is shown in figure 5.3. Repeated measurements of the SH intensity on BNA crystals that were freshly grown and 8 weeks after preparation (stored at room temperature) showed no significant changes [19].

Polycrystalline BNA thin films with micrometer-scale grain sizes have been

Refractive index	d (pm/V)
$n_{X,\omega} = 1.558$	$d_{333} = 234 \pm 31$
$n_{Y,\omega} = 1.717$	$d_{322} = 15.6 \pm 0.9$
$n_{Z,\omega} = 1.798$	$d_{311} \sim 0$
$n_{X,2\omega} = 1.621$	
$n_{Y,2\omega} = 1.827$	
$n_{Z,2\omega} = 2.081$	

Table 5.2: Overview of refractive indices and d tensor components determined from second-harmonic generation experiments at $\lambda_\omega = 1064\,\mathrm{nm}$ for bulk BNA crystals [10].

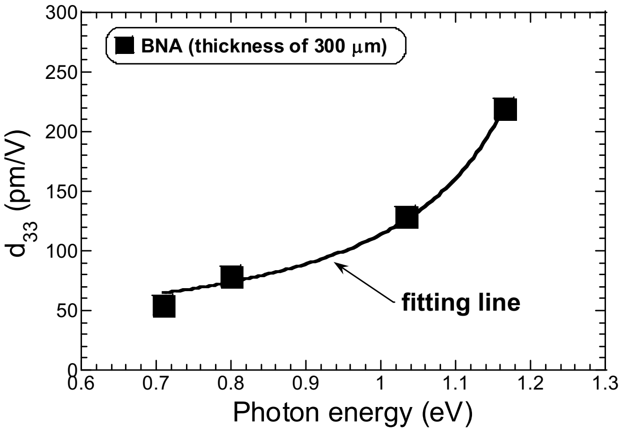

Figure 5.3: Wavelength dispersion of the d_{333} coefficient of BNA. The squares correspond to the experimentally determined values (from SHG measurements at different fundamental wavelengths, indicated as photon energies in the figure). The solid line is the result of fitting based on an oriented gas model combined with a two-level excitation model. Figure reproduced from [49].

deposited by thermal evaporation [3, 50]. Electrodes were patterned on the substrates before deposition. During deposition, a voltage was applied to align the grains [50]. Pockels coefficients r_{33} of approximately $30\,\mathrm{pm/V}$ were measured at a wavelength of $1550\,\mathrm{nm}$. The same procedure has been repeated while illuminating the sample with a laser beam ($\lambda = 473\,\mathrm{nm}$), which resulted in r_{33} coefficients up to $43\,\mathrm{pm/V}$ [3].

Integrated silicon-BNA hybrid modulators have been demonstrated [42, 51]. In these devices, BNA crystals were grown from the melt in horizontal and vertical silicon slot waveguides utilizing capillary methods. For the horizontal slot waveguides, propagation losses of $(10.0 \pm 2.4)\,\mathrm{dB/cm}$ at a wavelength of $1550\,\mathrm{nm}$ have been measured. Due to the device design and crystal orientation, the largest Pockels coefficient r_{33} could not be addressed. Instead, the r_{42} coefficient was probed and a lower limit of $3\,\mathrm{pm/V}$ was estimated. The $V_\pi L$ product was determined to be $(14.7 \pm 2.0)\,\mathrm{V\,cm}$. The measurements were done at a modulation frequency of $272\,\mathrm{Hz}$. No high-speed measurements could be conducted due to the large capacitance of the devices. For the vertical slot waveguides, a loss of $16\,\mathrm{dB}$ over a length of $1.5\,\mathrm{mm}$ at a wavelength of $1550\,\mathrm{nm}$ is reported. A $V_\pi L$ product of $12\,\mathrm{V\,mm}$ and a $3\,\mathrm{dB}$ bandwidth of $7\,\mathrm{GHz}$ were observed. The modulation measurements give an estimated r_{33} coefficient of $10\,\mathrm{pm/V}$, which is significantly lower than the values reported for the polycrystalline evaporated BNA films. Imperfect filling of the slots could have played a role in this.

In the following sections, our results on the growth of highly nonlinear crystalline thin films of BNA with a controllable crystal orientation and millimeter-scale crystallites will be presented. The crystals are grown on amorphous substrates with processing temperatures not exceeding $115\,^\circ\mathrm{C}$. This makes BNA suitable for integration on SiN PICs and allows for back-end integration on a CMOS chip. The growth of nonlinear single crystal thin films over large areas opens up numerous possibilities for the realization of integrated $\chi^{(2)}$ devices.

5.2 BNA crystal growth

The general fabrication process is as follows. The first step consists of the drop casting of a BNA in toluene solution on an oxidized silicon or glass substrate. This results in a polycrystalline BNA film with negligible second-harmonic generation. A glass cover is placed on top of the BNA thin film to avoid dewetting in subsequent processing steps. Next, the BNA thin film is molten and recrystallized in a non-uniform temperature profile to prevent multiple nucleation points and promote the growth of large single crystals. Two different crystallization methods will be discussed below. Finally, the glass cover is removed and the sample characterized.

We use $2\,\mathrm{cm}$ by $2\,\mathrm{cm}$ glass (BOROFLOAT$^{®}$ 33 with $500\,\mu\mathrm{m}$ thickness) and oxidized silicon substrates. Both oxide thicknesses of $100\,\mathrm{nm}$ and $3\,\mu\mathrm{m}$ have been used. The latter being a realistic thickness for photonic integrated circuits (typical thicknesses of the buried oxide layer in SiN PICs are $2\,\mu\mathrm{m}$ to $3\,\mu\mathrm{m}$, thinner layers can cause substrate leakage). Before processing, the substrates are cleaned sequentially in a heated ultrasonic bath using detergent, deionized water, acetone, and isopropanol. This is followed by a 15 minutes UV-ozone treatment. Some glass covers have been treated with 1H,1H,2H,2H-perfluorodecyltrichlorosilane or FDTS (if not mentioned, the glass cover was not treated with FDTS). The FDTS molecules form a self-assembled monolayer which reduces the surface energy [52]. This way, the glass cover can be removed after crystallization without sticking to the BNA film. The FDTS monolayer is deposited from the vapor phase directly after the UV-ozone treatment in a homebuilt system at a temperature of $140\,^{\circ}\mathrm{C}$ and a pressure of approximately $10\,\mathrm{mbar}$. To check the quality of the FDTS deposition, static contact angle measurements with the sessile drop method were performed and analyzed at room temperature (using an OCA-20 contact angle meter from DataPhysics Instruments GmbH). For deionized water, contact angles of approximately 110° were measured, which is in line with the values reported in literature [52].

BNA was purchased as a crystalline powder from MolPort (95% purity). From this powder, a BNA in toluene solution is prepared. Also other solvents can be used [45, 46]. For drop casting on $2\,\mathrm{cm}$ by $2\,\mathrm{cm}$ substrates, we use $100\,\mu\mathrm{l}$ of a $0.4\,\mathrm{wt}\%$ BNA in toluene solution (unless stated otherwise). This gives a BNA film thickness of about $400\,\mathrm{nm}$. After the solvent has evaporated and we are left with a dry film (this takes about 10 minutes), a glass cover (with or without FDTS) is placed on top. With some tweezers, pressure is applied to the cover to ensure good contact. To check whether this is the case, the sample is placed on a hotplate for several minutes to melt the BNA film. If the cover is not applied properly, dewetting over large areas is observed. Once the sample with the glass cover is prepared, we can move on to the crystallization procedure.

5.2.1 Crystallization in a temperature gradient

In a first approach to grow large single crystals, we used a hotplate whose temperature profile over time can be programmed (Unitemp RSS-450-110). The samples were placed on the hotplate such that they extended from the side of the hotplate by several millimeters, as to create a temperature gradient (see figure 5.4). The hotplate was programmed to heat up to $105\,^{\circ}\mathrm{C}$ (BNA's melting point) in 5 minutes, after which it stayed at $105\,^{\circ}\mathrm{C}$ for 1 minute. In the final part of the program, the samples were cooled down to room temperature. Cooling rates of $-1.4\,^{\circ}\mathrm{C}/\mathrm{minute}$ and $-0.1\,^{\circ}\mathrm{C}/\mathrm{minute}$ have been tested.

The second approach is based on the apparatus demonstrated by Schweicher et al. and is illustrated in figure 5.5 [53, 54]. The sample is moved slowly from

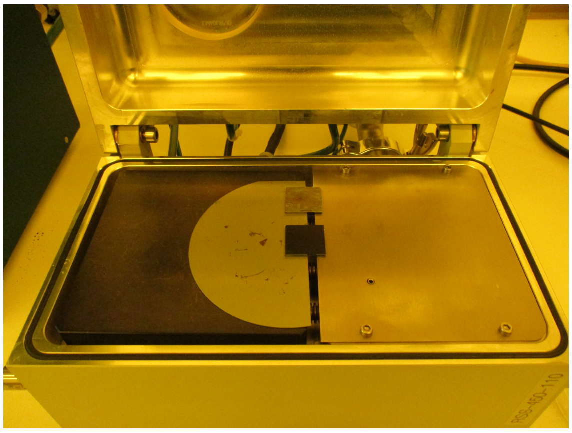

Figure 5.4: Picture of a Unitemp RSS-450-110 hotplate with two samples on it. The black area visible on the left side is the actual hotplate. The samples are sitting on a piece of silicon as a support. The edges of the samples are protruding from the hotplate.

a hot stage, where the BNA film is in the molten state, to a cold stage, where the BNA film is in the solid state. This technique has been used for a long time in the semiconductor industry for the growth of bulk single crystals and is known as the Bridgman technique [55]. Using the type of apparatus illustrated in figure 5.5, thin films of terthiophene (20-50 $\mu\mathrm{m}$ thickness) and poly(ethylene oxide) (220-1500 nm thickness) with millimeter-sized crystalline domains have been grown [53, 54]. A similar method, known as zone melting or zone annealing, has also been used for the growth of organic single crystal thin films [56–58].

Our implementation of the apparatus schematically depicted in figure 5.5, is shown in figure 5.6. This is a homebuilt tool designed by C. Rolin from the Large Area Electronics Department at imec. It consists of two copper blocks acting as the hot and cold stages. In each copper block, heating elements and a thermocouple have been integrated. The heating elements and thermocouples are connected to two temperature controllers (Cole-Parmer® Digi-Sense® temperature controller R/S) to set the temperatures. The copper blocks are encased in an inox structure. The two blocks are supported by spring loaded screws. The spring loaded screws keep the hot and cold stage leveled during heating, and they minimize the contact area between the copper blocks and the inox frame to avoid heat transfer. The sample holder is made of polyether ether ketone (PEEK), a high-temperature resistant polymer with low thermal conductivity. The PEEK sample holder sits in an inox frame which is being pulled by a stepper motor (Nanotec® ST4118M1404). The speed and position is controlled by a LabVIEW program. Above the heated stages, there is a Dino-Lite digital microscope which can be used to make images of the samples while they are on the tool. The gap between the hot and cold stage can be

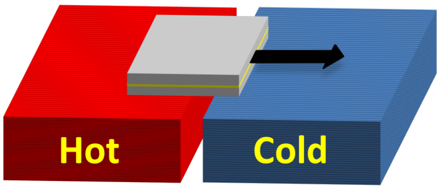

Figure 5.5: Schematic illustration of the apparatus used to grow large single crystals. The sample is moved from the hot side to the cold side. The hot side is set at a temperature above the melting point of BNA, the cold side at a temperature below the melting point.

set between $0\,\mathrm{mm}$ and approximately $3\,\mathrm{mm}$. Unless state otherwise, the gap size is set to $2\,\mathrm{mm}$.

5.3 Characterization methods

A thermogravimetric analysis (TGA) was done on the as-purchased crystalline BNA powder. The thermogravimetric analysis was performed in a TA Instruments Q50 device in air. The material ($7.78\,\mathrm{mg}$ of BNA) was loaded in an open crucible and the weight as a function of increasing temperature was recorded. The temperature was increased from $35\,°\mathrm{C}$ to $800\,°\mathrm{C}$ at a rate of $10\,°\mathrm{C\,min^{-1}}$.

The fabricated samples were checked under an optical microscope using traditional bright field microscopy, differential interference contrast microscopy (DIC), or polarized optical microscopy (POM; also known as polarized light microscopy or PLM). In DIC mode, edges are emphasized, which makes it easier to see defects such as cracks. In polarized optical microscopy, the sample is illuminated with polarized light (by passing the light through a polarizer before sending it to the sample). After interaction with the sample, the light passes trough a second polarizer (analyzer) whose transmission axis is rotated $90°$ compared to the transmission axis of the first polarizer. Therefore, amorphous or optically isotropic samples will appear dark when viewed under the microscope in POM mode. Since BNA crystals are optically anisotropic (biaxial), crystalline regions of the sample will appear brighter or darker depending on the crystal orientation. Thus, by rotating our sample (about the surface normal) under the microscope, crystalline regions can be identified. Also in DIC mode, it is possible to set up the microscope such that good contrast between different crystal orientations is obtained [59].

The crystallinity of the samples was also investigated in X-ray diffraction (XRD) θ-2θ measurements (with a Bruker D8 Discover system utilizing Cu K_α radiation). A contact profilometer (Veeco Dektak 150) was used to study the films' surface profile and estimate the thickness.

The setup which was used for second-harmonic generation (SHG) measure-

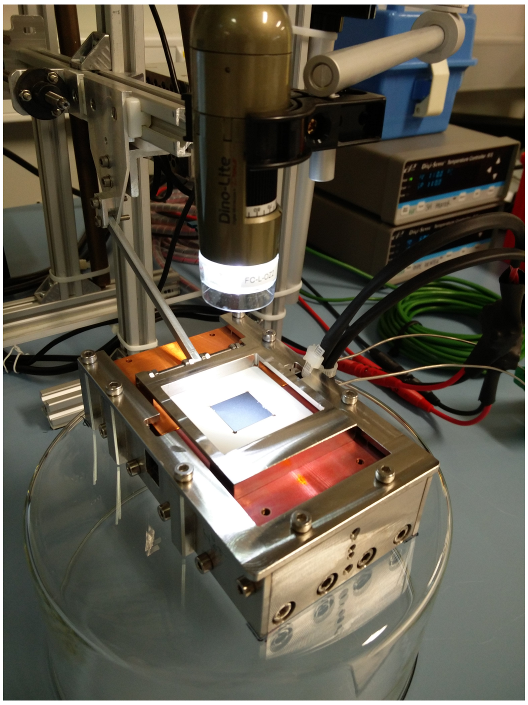

Figure 5.6: Implementation of the apparatus schematically illustrated in figure 5.5. In this picture, we see the backside of a 2 cm by 2 cm sample with a silicon substrate lying on the tool (inside the PEEK sample holder).

ments is schematically depicted in figure 5.7. The laser source (Calmar FPL-03CCFPM femtosecond fiber laser) emits $100\,\mathrm{fs}$ pulses at a wavelength of $1550\,\mathrm{nm}$ with a repetition rate of $20\,\mathrm{MHz}$ and an average power of $10\,\mathrm{mW}$. The laser beam is collimated and sent through a polarizing beamsplitter cube to obtain linearly polarized light. Next, the beam passes through a half-wave plate to alter the polarization direction. Afterwards, the laser light is focused onto the sample with a parabolic mirror (focal length of $5\,\mathrm{cm}$) and a second parabolic mirror directs the light to the detector (IDQ ID120, based on a silicon avalanche photodiode). In front and behind the sample there are a longpass and shortpass filter, to filter out light at the second-harmonic wavelength that is not generated in the sample and to filter out the laser light, respectively. In front of the detector there are also a polarizing beamsplitter cube, to select the polarization of interest, a bandpass filter, to filter out all light not at the SH wavelength, and a lens to focus the light onto the detector. The rotation mount/stage of the half-wave plate/sample holder are motorized and computer controlled. Also the detector is computer controlled, so the SHG measurements can be automated. The setup is calibrated with a thin BBO crystal. The calibration measurement is explained in appendix C. To fit our data, the model described in section 3.4 has been implemented in MATLAB. Since the BNA thin films have a large nonlinearity and are rather thick compared to the thin films studied in chapter 4, the surface nonlinearity of the backside of the samples can be neglected.

5.4 Results and discussion

The TGA results are shown in figure 5.8. Weight loss starts occurring at a temperature of about $200\,^{\circ}\mathrm{C}$. This sets an upper limit for the processing temperature of BNA.

When drop casting BNA in toluene on glass or oxidized silicon substrates, POM images indicate an amorphous film structure right after the solvent has evaporated. After the samples have been lying at room temperature for a while (on the order of 10 minutes), crystalline structures, which are described in literature as spherulites [60], start appearing. This behavior is also observed after melting a BNA film (with a glass cover to avoid dewetting) on a hotplate and letting it solidify at room temperature. The formation of spherulites during crystallization has been observed in many materials [60–62]. Figure 5.9 shows microscopy images of an amorphous BNA film with a growing spherulite (growth rate on the order of $1\,\mathrm{\mu m\,s^{-1}}$). In the POM image of the spherulite (figure 5.9(a)), we see the typical Maltese cross pattern (i.e. the alternation of dark and bright regions) [61]. SHG measurements on BNA samples covered with spherulites yielded negligible signals. This could either be attributed to the spherulites being in the centrosymmetric monoclinic phase of BNA, or to the polycrystalline nature of the spherulites. In

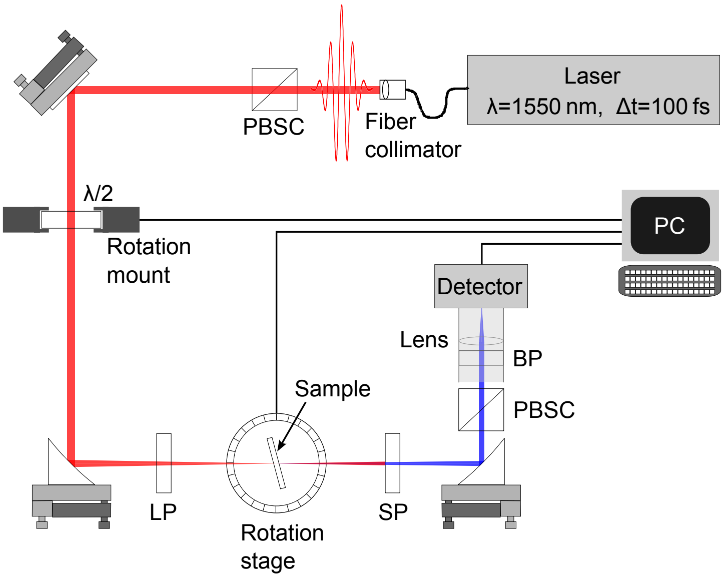

Figure 5.7: Setup for SHG measurements. PBSC: polarizing beamsplitter cube, λ/2: half-wave plate, LP: longpass filter, SP: shortpass filter, BP: bandpass filter.

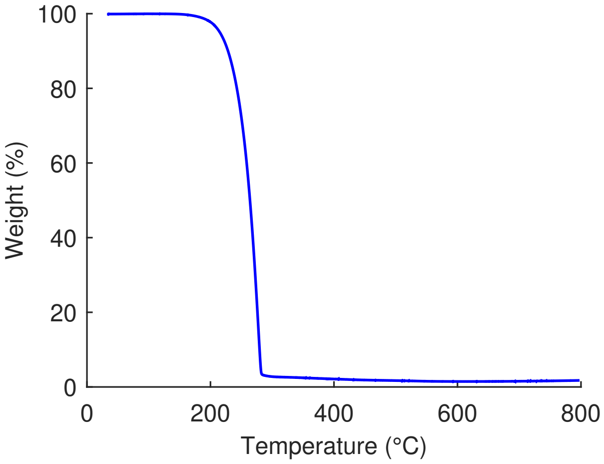

Figure 5.8: Thermogravimetric analysis (TGA) of as-purchased BNA crystalline powder in air.

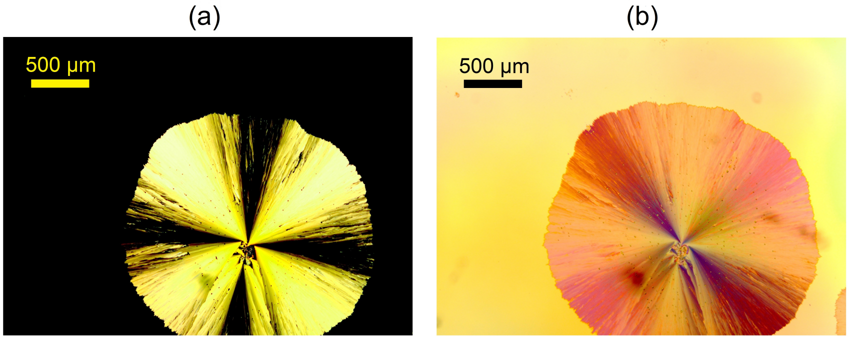

Figure 5.9: Microscopy image of an amorphous BNA film with a growing spherulite (on a silicon substrate with 100 nm SiO_2). Image (a) is taken in POM mode and (b) in DIC mode.

figure 5.10, an XRD θ-2θ measurement of a BNA sample covered with spherulites is shown. The broad peak around 21° is originating from the amorphous SiO_2 layer underneath the BNA thin film. The forbidden 200 reflection of the silicon substrate is expected to occur at an angle 2θ of approximately 33° [63], as explained in subsection 4.3.1. The sharp peaks around 8°, 17°, 27°, and 44° could be ascribed to the higher-order diffraction peaks of the (001) plane of monoclinic BNA (more specifically to the 002, 004, 006, and 0010 reflections, respectively) [48]. But, also the peaks corresponding to the 020, 040, 060, and 0100 reflections of orthorhombic BNA (i.e. the higher-order diffraction peaks of the (010) plane) are expected to be very close to these positions [42, 45, 48].

5.4.1 Crystallization on a simple hotplate

Here, the results are shown for the first approach to the growth of BNA crystals (i.e. the use of the programmable hotplate, see subsection 5.2.1). For all the samples characterized in this subsection, oxidized silicon substrates with 100 nm oxide were used. For the glass covers, no FDTS treatments were done.

If the sample is placed in the middle of the hotplate for the melting and subsequent crystallization, we typically get a polycrystalline film with spherulitic crystalline structures (see figure 5.11). On the other hand, figure 5.12 shows images of samples that were placed on the side of the hotplate with their edges protruding from the hotplate (for a cooling rate of $-1.4\,°\mathrm{C/minute}$). Some plate-like crystals are observed. Figure 5.13 shows what happens if this experiment is repeated with a reduced cooling rate of $-0.1\,°\mathrm{C/minute}$. Millimeter-sized crystals can be seen. The darker regions are gaps or cracks. Figure 5.14 shows a surface profile measured over one of these gaps, which gives an estimate of the film thickness.

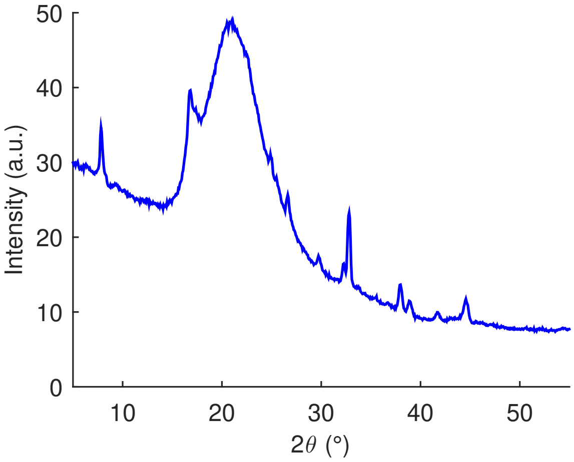

Figure 5.10: XRD θ-2θ scan (utilizing Cu K_α radiation) of a BNA film with spherulitic crystalline structures. The substrate used is oxidized silicon with $3\,\mu\mathrm{m}$ oxide.

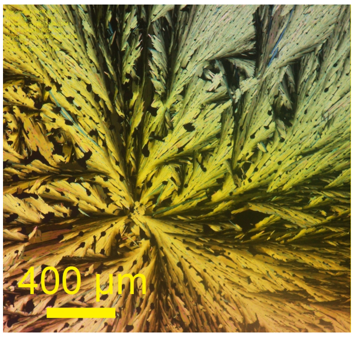

Figure 5.11: POM image of a BNA sample placed in the middle of the hotplate for crystallization (at a cooling rate of $-1.4\,^{\circ}\mathrm{C/minute}$; on a silicon substrate with $100\,\mathrm{nm}$ SiO_2). No SHG was detected for this sample.

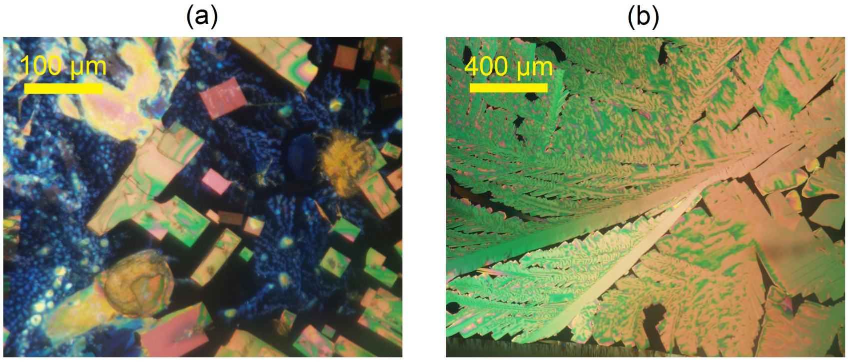

Figure 5.12: POM images of BNA samples placed on the side of the hotplate, for a cooling rate of $-1.4\,^{\circ}\mathrm{C/minute}$ (using silicon substrate with $100\,\mathrm{nm}$ SiO_2). Strong SHG was detected for these samples. Image (a) and (b) show results for two samples with the same processing parameters; sample (a) dewetted considerably during melting.

The drop casting technique results in thicknesses varying from $100\,\mathrm{nm}$ to $700\,\mathrm{nm}$, though locally the variations are small as can be seen from the surface profile. Strong SHG was detected for these millimeter-sized crystals, indicating that the BNA thin film crystallized in the orthorhombic phase. XRD measurements show reflections corresponding to the higher-order diffraction peaks of the (010) plane (see figure 5.15). This indicates that the Y axis (or b axis) of the BNA crystals is perpendicular to the substrate (and the X and Z axes are parallel to the the sample plane). Therefore, the largest nonlinear tensor component $\chi^{(2)}_{ZZZ}$ can be probed at normal incidence. Thus, in the SHG measurements, we keep the angle of incidence fixed at 0° and vary the polarization angle of the incident laser beam by rotating the half-wave plate. Figure 5.16 shows an example of such a measurement. The polarization direction corresponding to a maximal signal depends on the in-plane orientation of the BNA crystals. The polarizing beamsplitter cube (PBSC) in front of the detector is set either with its transmission axis normal or parallel to the optical table. Depending on the in-plane orientation of the BNA crystals, one of the PBSC orientations can give a significantly stronger signal. Fitting of the measurements gives a nonlinearity of $\chi^{(2)}_{ZZZ} = (61 \pm 10)\,\mathrm{pm/V}$. This result is an average of 6 measurements (similar to the one shown in figure 5.16) spread over 3 different samples (fabricated using the same processing parameters). The quoted error is due to the thickness uncertainty. No preferred in-plane direction of the crystals has been observed. The observed $\chi^{(2)}$ nonlinearity is smaller than the value reported for bulk crystals ($\approx 160\,\mathrm{pm/V}$ at a fundamental wavelength of $1550\,\mathrm{nm}$, see figure 5.3). Possibly, this is related to the crystal quality.

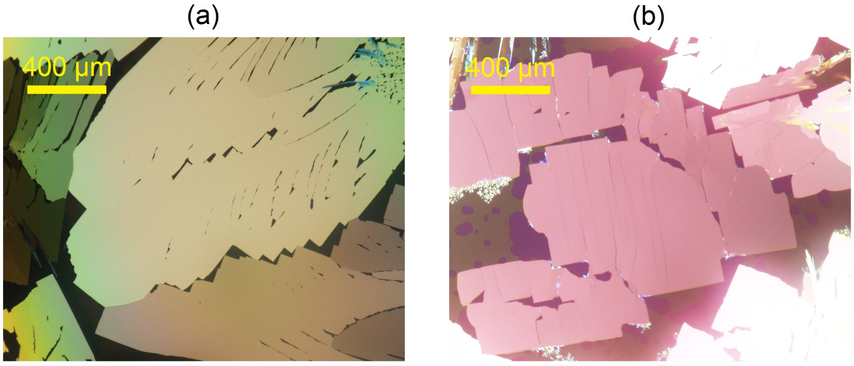

Figure 5.13: POM images of BNA samples placed on the side of the hotplate, for a cooling rate of $-0.1\,^{\circ}\mathrm{C/minute}$ (using silicon substrate with $100\,\mathrm{nm}$ SiO_2). Image (a) and (b) show results for two samples with the same processing parameters.

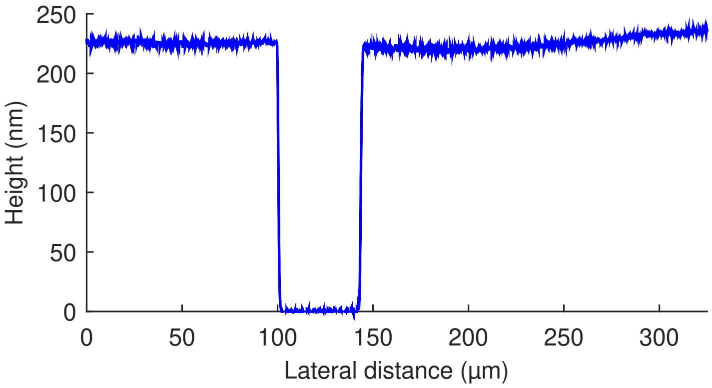

Figure 5.14: Surface profile measured over a gap between BNA crystals (crystals grown by placing sample on the side of the hotplate and using a cooling rate of $-0.1\,^{\circ}\mathrm{C/minute}$).

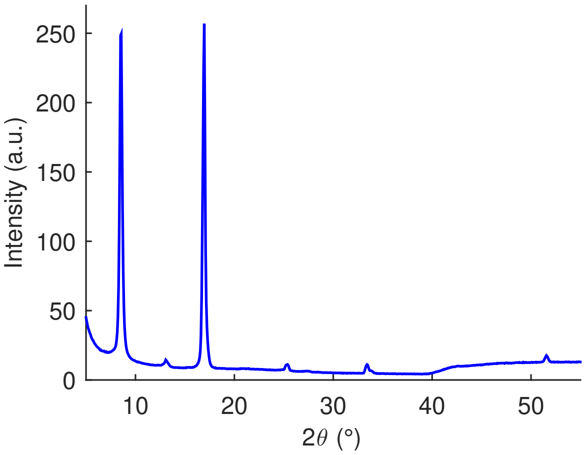

Figure 5.15: XRD θ-2θ scan (utilizing Cu K_α radiation) of a BNA crystalline thin film. The crystalline thin film is grown by placing the sample on the side of the hotplate and using a cooling rate of $-0.1\,^\circ\mathrm{C/minute}$. The substrate used is oxidized silicon with $100\,\mathrm{nm}$ oxide.

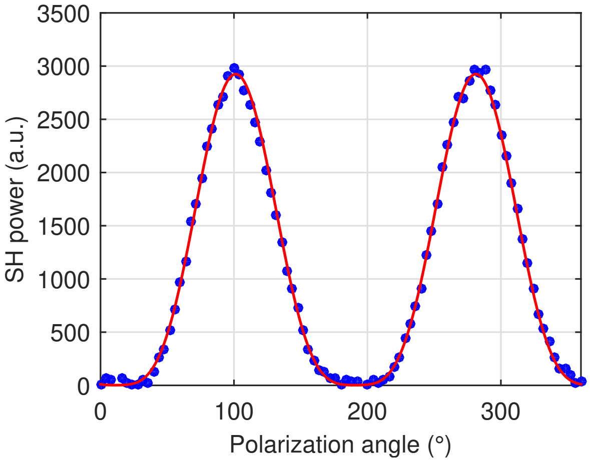

Figure 5.16: Measurement (blue dots) and fitting (red line) of the SH power for normal incidence and varying input polarization (0° corresponds to the electric field of the incident laser beam being normal to the optical table; for 90° it is parallel to the optical table). The PBSC in front of the detector is oriented with its transmission axis parallel to the optical table. The measured BNA crystals are grown on an oxidized silicon substrate with $100\,\mathrm{nm}$ oxide, using the simple hotplate technique with a cooling rate of $-0.1\,^\circ\mathrm{C/minute}$. The laser beam passes first through the silicon, then through the oxide layer, and finally through the BNA thin film.

5.4.2 Crystallization on the homebuilt temperature gradient tool

Although the results presented in the previous subsection look promising, the method with the hotplate offers little freedom for process optimization. Therefore, we investigated a second approach to the growth of BNA crystals, namely the use of the homebuilt tool shown in figure 5.6 (see also subsection 5.2.1).

In our initial tests, we used glass substrates (and glass covers) instead of silicon substrates. The relatively large thermal conductivity of silicon is thought to flatten out the spatial temperature profile, which can negatively impact the crystal growth. But, as we will show later, by using oxidized silicon substrates with a sufficiently thick oxide ($3\,\mu\mathrm{m}$, as is typical for PICs) and placing the sample on the tool with the substrate facing upwards, very good results can be obtained.

Figure 5.17 shows microscopy images of crystalline BNA thin films grown on the homebuilt tool, where the temperature of the hot stage was set to $110\,^{\circ}\mathrm{C}$, the temperature of the cold stage to $60\,^{\circ}\mathrm{C}$, and the sample displacement speed to $5\,\mu\mathrm{m}\,\mathrm{s}^{-1}$. For a hot stage temperature of $110\,^{\circ}\mathrm{C}$, $60\,^{\circ}\mathrm{C}$ for the cold stage is about the lower limit (due to heat flowing through the sample). Lower temperatures would require active cooling of the cold stage. The sample shown in figure 5.17 is grown from a polycrystalline seed. This polycrystalline seed is obtained by drop casting the BNA film, placing the glass cover on top, and letting the film crystallize at room temperature (resulting in typical spherulitic growth patterns). Subsequently, the sample is placed on the homebuilt tool with part of it already on the cold stage, so this part does not melt. The seed area can be seen in the lower part of figure 5.17(a). If no seed was used (i.e. sample starting out completely on the hot stage, so the entire film gets molten), the BNA film remained amorphous upon moving from the hot to the cold side. In the top part of figure 5.17(a) and in figure 5.17(b), we see the crystalline ribbons that were grown. These ribbons have widths on the order of $100\,\mu\mathrm{m}$ and are several millimeters long. The long side of these ribbons is approximately parallel to the direction in which the sample was pulled by the stepper motor (indicated by the red arrow). For the POM image in figure 5.17(b), the sample has been rotated by 45° about the surface normal, since for 0° rotation the entire image was very dark. This indicates that all of the crystalline ribbons have a similar crystal orientation. No significant differences in morphology were observed for samples that were grown with the cold stage temperature set to 70 °C or 80 °C (while the hot stage temperature and speed remained the same).

Figure 5.18 shows the results for the same tool parameters ($T_{hot} = 110\,^{\circ}\mathrm{C}$, $T_{cold} = 60\,^{\circ}\mathrm{C}$, and $v = 5\,\mu\mathrm{m}\,\mathrm{s}^{-1}$, starting from seed), but a thicker BNA film (using $1\,\mathrm{wt\%}$ BNA in toluene solution for drop casting instead of $0.4\,\mathrm{wt\%}$). Again, crystalline ribbons are observed, but the width of these ribbons is reduced to 20-$50\,\mu\mathrm{m}$.

Also the influence of an increased sample displacement speed was tested. Fig-

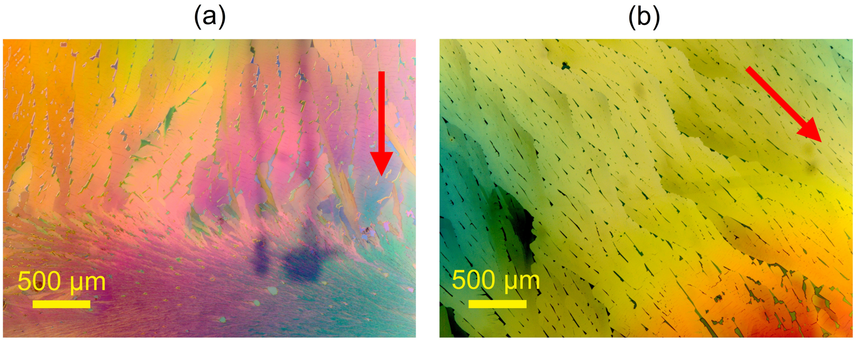

Figure 5.17: BNA crystals grown on glass substrates utilizing the homebuilt tool with following parameters: $T_{hot} = 110\,^{\circ}\mathrm{C}$ (temperature of the hot stage), $T_{cold} = 60\,^{\circ}\mathrm{C}$ (temperature of the cold stage), and $v = 5\,\mu\mathrm{m\,s}^{-1}$ (sample displacement speed). The growth started from a polycrystalline seed. The pulling direction of the tool is indicated by a red arrow in the images. (a) DIC image of boundary between seed and newly grown crystals. The black marks are traces of dirt on the top glass cover which has not been removed yet. (b) POM image of grown crystals. The sample has been rotated 45° to make the crystals visible. The crystalline ribbons grew from the bottom right in the image to the top left.

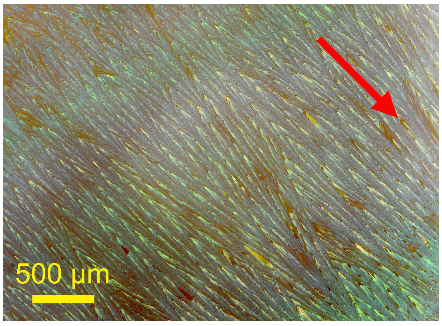

Figure 5.18: POM image of a BNA crystalline film grown on a glass substrate utilizing the homebuilt tool with following parameters: $T_{hot} = 110\,^{\circ}\mathrm{C}$, $T_{cold} = 60\,^{\circ}\mathrm{C}$, and $v = 5\,\mu\mathrm{m\,s}^{-1}$. The pulling direction of the tool is indicated by a red arrow in the image. The growth started from a polycrystalline seed. For this sample, a $1\,\mathrm{wt\%}$ BNA in toluene solution was used for drop casting instead of a $0.4\,\mathrm{wt\%}$ BNA in toluene solution, resulting in a thicker film.

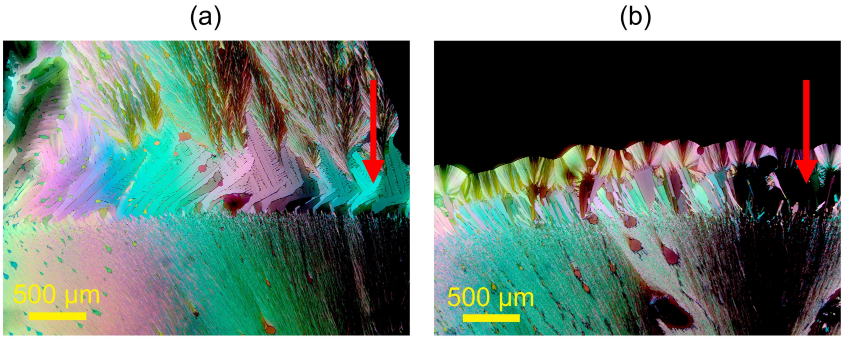

Figure 5.19: POM images of BNA thin films on glass substrates processed with the homebuilt tool using following parameters: (a) $T_{hot} = 110\,°\mathrm{C}$, $T_{cold} = 60\,°\mathrm{C}$, and $v = 25\,\mu\mathrm{m\,s^{-1}}$; (b) $T_{hot} = 110\,°\mathrm{C}$, $T_{cold} = 100\,°\mathrm{C}$, and $v = 25\,\mu\mathrm{m\,s^{-1}}$. The pulling direction of the tool is indicated by a red arrows. The growth started from a polycrystalline seed, which can be seen in the lower part of the images. For the drop casting of the thin films, the usual concentration of $0.4\,\mathrm{wt\%}$ BNA in toluene was used.

ure 5.19(a) shows the resulting morphology for a speed of $25\,\mu\mathrm{m\,s^{-1}}$. In the lower part of the images, the seed can be seen. From this seed, plate-like crystals started growing, but they quickly transitioned in fiber-like structures. For figure 5.19(b), not only the speed was increased ($v = 25\,\mu\mathrm{m\,s^{-1}}$), but also the temperature of the cold stage ($T_{cold} = 100\,°\mathrm{C}$). By increasing this temperature, the effective cooling rate the material experiences decreases [53]. Yet, no crystallization was observed (the upper part of the image remained amorphous, hence the black color). Increasing the temperature of the cold stage, decreases the effective cooling rate, but also decreases the amount of undercooling, which influences the crystallization process as well.

BNA crystalline films have been grown for different sizes of the gap between the two stages: $0.5\,\mathrm{mm}$, $2\,\mathrm{mm}$, and $3\,\mathrm{mm}$ (for $T_{hot} = 110\,°\mathrm{C}$, $T_{cold} = 60\,°\mathrm{C}$, and $v = 5\,\mu\mathrm{m\,s^{-1}}$). No changes in morphology were observed compared to figure 5.17.

So far, only the use of glass substrates for the growth of crystalline films using the homebuilt tool has been treated. In PICs, silicon substrates are used. Figure 5.20 shows a BNA crystalline film grown on a silicon substrate with a $3\,\mu\mathrm{m}$ wet oxide layer. The sample was placed on the tool with the glass cover in direct contact with the heating stages and the silicon substrate facing upwards, to avoid creating a thermal bridge. Crystalline ribbons can be seen, although the direction of these ribbons seems less defined compared to the crystals grown on glass.

To avoid dewetting during melting, the samples a have glass cover. But after crystal growth, it would be desirable to have the cover removed for possible

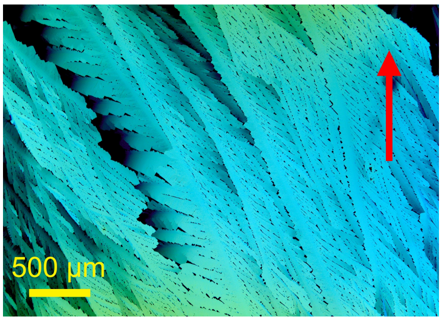

Figure 5.20: POM image of a BNA crystalline film grown on an oxidized silicon substrate (oxide thickness of 3 µm) utilizing the homebuilt tool with following parameters: $T_{hot} = 110\,^{\circ}\mathrm{C}$, $T_{cold} = 60\,^{\circ}\mathrm{C}$, and $v = 5\,\mu\mathrm{m\,s^{-1}}$. The pulling direction of the tool is indicated by a red arrow in the image. The growth started from a polycrystalline seed. The sample was placed on the tool with the glass cover in direct contact with the heating stages and the silicon substrate facing upwards.

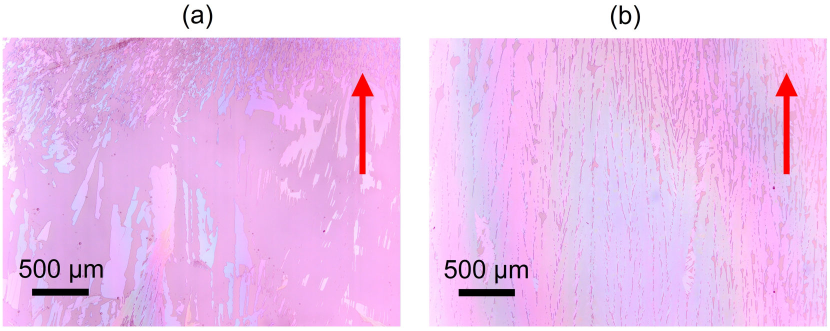

Figure 5.21: Bright field microscopy images of BNA crystalline thin films grown on glass substrates after removal of the glass covers (growth parameters: $T_{hot} = 110\,^{\circ}\mathrm{C}$, $T_{cold} = 60\,^{\circ}\mathrm{C}$, $v = 5\,\mu\mathrm{m\,s^{-1}}$, growth from seed). For sample (a) no FDTS treatment was done on the cover, while sample (b) had a cover with an FDTS monolayer.

additional processing steps and the coupling of light in and out of waveguides. Unfortunately, removal of the glass cover usually results in part of the film sticking to the cover and part to the substrate. By treating the cover with FDTS (see section 5.2), this unwanted behavior can be avoided. Figure 5.21 shows two samples after removal of the glass covers. The sample in figure 5.21(b) had an FDTS treated cover which resulted in a very clean removal.

Finally, the effect of lower displacement speeds was investigated. Figure 5.22 shows a BNA crystalline film grown at a speed of $0.7\,\mu\mathrm{m\,s^{-1}}$ on an oxidized silicon substrate (oxide thickness of 3 µm) with an FDTS treated glass cover. Figure 5.23 shows an image of a sample on the tool as BNA crystals are being grown (at

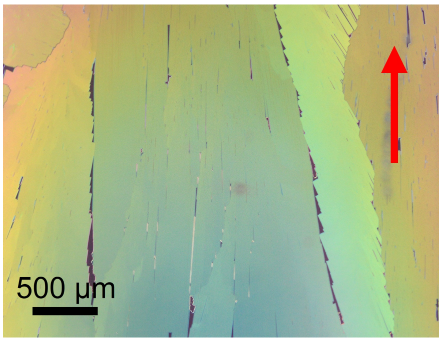

Figure 5.22: DIC image of a BNA crystalline film grown on an oxidized silicon substrate (oxide thickness of 3 µm) utilizing the homebuilt tool with following parameters: $T_{hot} = 115\,°\mathrm{C}$, $T_{cold} = 65\,°\mathrm{C}$, and $v = 0.7\,\mathrm{\mu m\,s^{-1}}$. The pulling direction of the tool is indicated by a red arrow in the image. The growth started from a polycrystalline seed. The sample was placed on the tool with the glass cover in direct contact with the heating stages and the silicon substrate facing upwards. The glass cover was treated with FDTS.

a speed of $0.7\,\mathrm{\mu m\,s^{-1}}$). We observe crystalline ribbons of several millimeters long and hundreds of micrometers wide. These crystalline films have been analyzed further in XRD (see figure 5.24), surface profile (see figure 5.25), and SHG measurements (see figure 5.26). Strong SHG was detected, indicating that the BNA thin films crystallized in the orthorhombic phase. XRD measurements show reflections corresponding to the higher-order diffraction peaks of the (010) plane, as was also observed for the crystals grown using the hotplate technique. Knowing the out-of-plane crystal axis, the film thickness and refractive index [10], the $\chi^{(2)}$ nonlinearity can be estimated from the SHG measurements. For BNA on glass substrates, we found $\chi^{(2)}_{ZZZ} = (153 \pm 70)\,\mathrm{pm/V}$ (average of 7 measurements on one sample). The large error is due to the thickness uncertainty. The obtained $\chi^{(2)}_{ZZZ}$ value is close to the value of $\approx 160\,\mathrm{pm/V}$ reported for a bulk crystal (see figure 5.3). We also detected SHG for BNA on oxidized silicon, but the roughness of the unpolished backside made $\chi^{(2)}$ quantification difficult. Our SHG measurements indicate that the crystals have a preferential in-plane orientation, namely with their Z or c axis parallel to the pulling direction. In integrated waveguide based devices, the nonlinear tensor element $\chi^{(2)}_{ZZZ}$ can be addressed using optical TE modes and in-plane RF electric fields for electro-optic modulation.

To avoid the non-uniformity associated with the drop casting technique, the exploration of alternative deposition techniques such as spin coating, spray coating [64], ultrasonic substrate vibration-assisted drop casting [65], organic vapor phase deposition (OVPD) [66], and thermal evaporation [50] might prove useful. To fill in the gaps between the crystalline ribbons, an extra layer of BNA can be evaporated on top. Under the right conditions, the underlying BNA crystals can

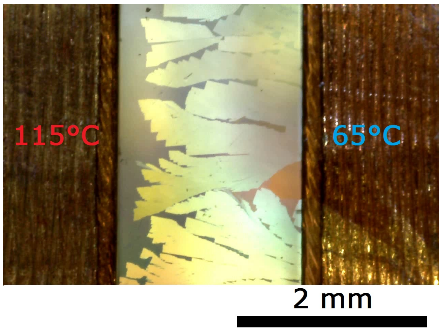

Figure 5.23: Image taken with the Dino-Lite microscope of a sample on the homebuilt tool. On the left you can see the hot stage and on the right the cold stage. In the gap, growing BNA crystals can be seen. A glass substrate was used for this sample. The tool parameters are: $T_{hot} = 115\,°\mathrm{C}$, $T_{cold} = 65\,°\mathrm{C}$, and $v = 0.7\,\mu\mathrm{m\,s^{-1}}$. The growth started from a seed. The glass cover was treated with FDTS.

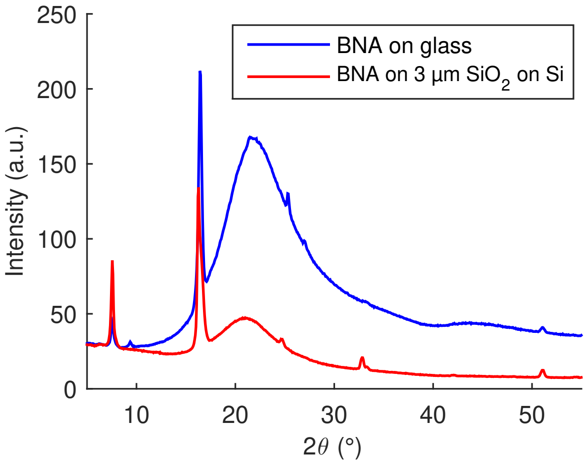

Figure 5.24: XRD θ-2θ scans (utilizing Cu K_α radiation) of BNA crystalline thin films grown on a glass substrate (blue) and an silicon substrate with $3\,\mu\mathrm{m}$ of wet oxide (red). The crystalline films were grown on the homebuilt tool using the following parameters: $T_{hot} = 115\,°\mathrm{C}$, $T_{cold} = 65\,°\mathrm{C}$, and $v = 0.7\,\mu\mathrm{m\,s^{-1}}$. The growth started from a seed.

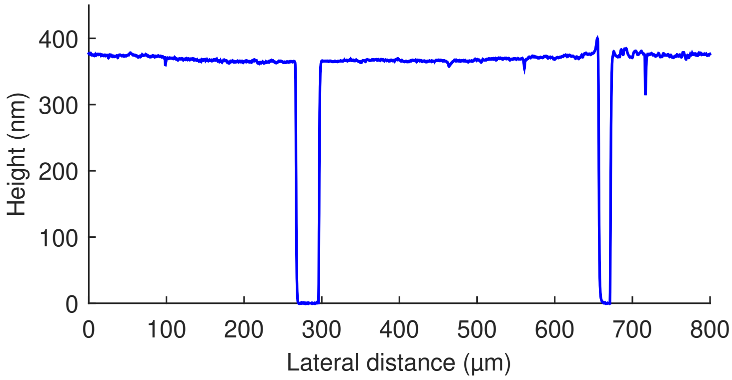

Figure 5.25: Surface profile of a crystalline BNA thin film. The film was grown on an oxidized silicon substrate (oxide thickness of 3 µm) utilizing the homebuilt tool with following parameters: $T_{hot} = 115\,°\mathrm{C}$, $T_{cold} = 65\,°\mathrm{C}$, and $v = 0.7\,\mu\mathrm{m\,s^{-1}}$. The growth started from a polycrystalline seed.

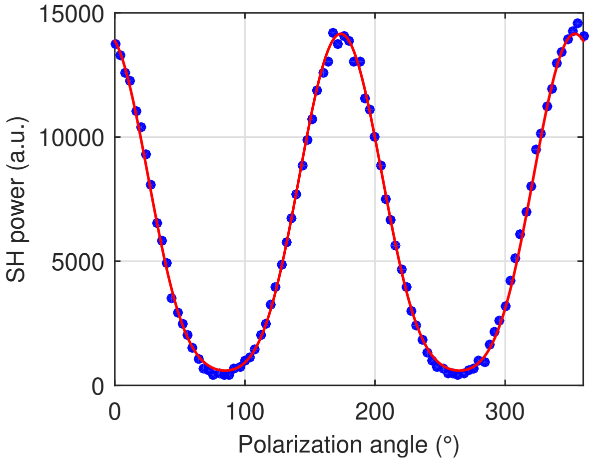

Figure 5.26: Measurement (blue dots) and fitting (red line) of the SH power for normal incidence and varying input polarization (0° corresponds to the electric field of the incident laser beam being normal to the optical table; for 90° it is parallel to the optical table). The PBSC in front of the detector is oriented with its transmission axis normal to the optical table. The measured BNA crystals are grown on a glass substrate using the homebuilt tool (parameters: $T_{hot} = 115\,°\mathrm{C}$, $T_{cold} = 65\,°\mathrm{C}$, $v = 0.7\,\mu\mathrm{m\,s^{-1}}$, starting from seed). For the SHG measurement, the sample is placed in the sample holder such that the long side of the BNA crystals (i.e. direction parallel to the pulling direction) is normal to the table.

act as templates for epitaxial growth [67]. The use of mechanical polishing, as is done for bulk BNA crystals [10, 49], is also an interesting approach to get smooth, uniform films. A possible alternative for the glass cover is to deposit a thin layer of SiO_2 (or another transparent material with a high melting point that can easily be deposited) on top of the BNA film. This layer of SiO_2 can for instance be deposited by vacuum evaporation where the substrate temperature is kept low (at a pressure of $5 \times 10^{-6}\,\mathrm{Torr}$, BNA begins to evaporate at $70\,°\mathrm{C}$ [50]). A thin capping layer of SiO_2 has been shown to prevent dewetting of molten metal films [68].

5.5 Conclusions

We have demonstrated the growth of crystalline BNA thin films with a large $\chi^{(2)}$ nonlinearity. These films were grown on amorphous substrates with substrate temperatures not exceeding $115\,°\mathrm{C}$. This makes them suitable for integration on silicon nitride photonic integrated circuits and allows for back-end integration on a CMOS chip.

In a first approach, the crystalline BNA films were grown by melting the material and slowly cooling it down in the presence of a spatial temperature gradient. The temperature gradient was induced by placing the samples on the edge of a hotplate. This technique resulted in millimeter-sized BNA crystallites with a nonlinearity of $\chi^{(2)}_{ZZZ} = (61 \pm 10)\,\mathrm{pm/V}$, where the Z axis is lying in the film plane and the Y axis is normal to the plane. However, no preferred in-plane orientation of the crystallites was observed.

In a second approach, a new tool was designed inspired by the Bridgman method used for the growth of bulk crystals in the semiconductor industry. The use of this homebuilt tool resulted in BNA crystallites of several millimeters long and hundreds of micrometers wide. Moreover, our X-ray and second-harmonic generation measurements indicate that the crystallites preferentially grow with their Z axis along the sample displacement direction and the Y axis normal to the sample plane. A very large nonlinearity of $\chi^{(2)}_{ZZZ} = (153 \pm 70)\,\mathrm{pm/V}$ was measured.

The growth of highly nonlinear single crystal thin films over large areas opens up numerous possibilities for the realization of integrated $\chi^{(2)}$ devices.

References

[1] A. Hermans, R. Janneck, C. Rolin, S. Clemmen, P. Heremans, J. Genoe, and R. Baets. *Growth of thin film organic crystals with strong nonlinearity for on-chip second-order nonlinear optics*. In Annual Symposium of the IEEE Photonics Society Benelux Chapter, 2018.

[2] A. Hermans, S. Clemmen, R. Baets, J. Genoe, and C. Rolin. *Growth of organic crystalline thin films with strong second- order nonlinearity for integrated optics*. In European Conference on Integrated Optics (ECIO), page W.A3.3, 2019.

[3] Z. Wang, W. Sun, A. Chen, I. Kosilkin, D. Bale, and L. R. Dalton. *Organic electro-optic thin films by simultaneous vacuum deposition and laser-assisted poling*. Optics Letters, 36(15):2853, 2011.

[4] F. Agulló-López, J. Manuel Cabrera, and F. Agulló-Rueda. *Electrooptics: Phenomena, Materials and Applications*. Academic Press, 1994.

[5] R. L. Sutherland. *Handbook of Nonlinear Optics*. Marcel Dekker, Inc., 2nd edition, 2003.

[6] D. N. Nikogosyan. *Nonlinear Optical Crystals: A Complete Survey*. Springer, 2005.

[7] S. R. Marder, J. W. Perry, and C. P. Yakymyshyn. *Organic salts with large second-order optical nonlinearities*. Chemistry of Materials, 6(8):1137, 1994.

[8] F. Pan, G. Knöpfle, Ch. Bosshard, S. Follonier, R. Spreiter, M. S. Wong, and P. Günter. *Electro-optic properties of the organic salt 4-N,N-dimethylamino-4'-N'-methyl-stilbazolium tosylate*. Applied Physics Letters, 69(1):13, 1996.

[9] M. Jazbinsek, L. Mutter, and P. Günter. *Photonic applications with the organic nonlinear optical crystal DAST*. IEEE Journal of Selected Topics in Quantum Electronics, 14(5):1298, 2008.

[10] M. Fujiwara, M. Maruyama, M. Sugisaki, H. Takahashi, S. I. Aoshima, R. J. Cogdell, and H. Hashimoto. *Determination of the d-tensor components of a single crystal of N-benzyl-2-methyl-4-nitroaniline*. Japanese Journal of Applied Physics, 46(4A):1528, 2007.

[11] C. Haffner, W. Heni, D. L. Elder, Y. Fedoryshyn, N. Đorđević, D. Chelladurai, U. Koch, K. Portner, M. Burla, B. Robinson, L. R. Dalton, and J. Leuthold. *Harnessing nonlinearities near material absorption resonances*

for reducing losses in plasmonic modulators. Optical Materials Express, 7(7):2168, 2017.

[12] MolPort. *N-benzyl-2-methyl-4-nitroaniline*. `https://www.molport.com/shop/moleculelink/N-benzyl-2-methyl-4-nitroaniline/2116341?searchtype=text-search&searchkey=47IBPQKPOFENS1D22LRI07`. [Accessed 25 March 2019].

[13] M. G. Kuzyk. *Using fundamental principles to understand and optimize nonlinear-optical materials*. Journal of Materials Chemistry, 19:7444, 2009.

[14] P. Gangopadhyay, D. N. Rao, I. Agranat, and T. P. Radhakrishnan. *Strategic placement of stereogenic centers in molecular materials for second harmonic generation*. Enantiomer: A Journal of Sterochemistry, 7(2-3):119, 2002.

[15] Z. Yang, M. Jazbinsek, B. Ruiz, S. Aravazhi, V. Gramlich, and P. Günter. *Molecular engineering of stilbazolium derivatives for second-order nonlinear optics*. Chemistry of Materials, 19:3512, 2007.

[16] C. Koos, J. Leuthold, W. Freude, M. Kohl, L. Dalton, W. Bogaerts, A. L. Giesecke, M. Lauermann, A. Melikyan, S. Koeber, S. Wolf, C. Weimann, S. Muehlbrandt, K. Koehnle, J. Pfeifle, W. Hartmann, Y. Kutuvantavida, S. Ummethala, R. Palmer, D. Korn, L. Alloatti, P. C. Schindler, D. L. Elder, T. Wahlbrink, and J. Bolten. *Silicon-organic hybrid (SOH) and plasmonic-organic hybrid (POH) integration*. Journal of Lightwave Technology, 34(2):256, 2016.

[17] C. Kieninger, Y. Kutuvantavida, D. L. Elder, S. Wolf, H. Zwickel, M. Blaicher, J. N. Kemal, M. Lauermann, S. Randel, W. Freude, L. R. Dalton, and C. Koos. *Ultra-high electro-optic activity demonstrated in a silicon-organic hybrid modulator*. Optica, 5(6):739, 2018.

[18] C. Kieninger, Y. Kutuvantavida, H. Miura, J. N. Kemal, H. Zwickel, F. Qiu, M. Lauermann, W. Freude, S. Randel, S. Yokoyama, and C. Koos. *Demonstration of long-term thermally stable silicon-organic hybrid modulators at* 85 °C. Optics Express, 26(21):27955, 2018.

[19] H. Hashimoto, Y. Okada, H. Fujimura, M. Morioka, O. Sugihara, N. Okamoto, and R. Matsushima. *Second-harmonic generation from single crystals of N-substituted 4-nitroanilines*. Japanese Journal of Applied Physics, 36:6754, 1997.

[20] O-P. Kwon, B. Ruiz, A. Choubey, L. Mutter, A. Schneider, M. Jazbinsek, V. Gramlich, and P. Günter. *Organic nonlinear optical crystals based on*

configurationally locked polyene for melt growth. Chemistry of Materials, 18:4049, 2006.

[21] B. Ruiz, Z. Yang, V. Gramlich, M. Jazbinsek, and P. Günter. *Synthesis and crystal structure of a new stilbazolium salt with large second-order optical nonlinearity*. Journal of Materials Chemistry, 16(27):2839, 2006.

[22] L. Mutter, F. D. J. Brunner, Z. Yang, M. Jazbinšek, and P. Günter. *Linear and nonlinear optical properties of the organic crystal DSTMS*. Journal of the Optical Society of America B, 24(9):2556, 2007.

[23] O-P. Kwon, S.-J. Kwon, M. Jazbinsek, F. D. J. Brunner, J.-I. Seo, C. Hunziker, A. Schneider, H. Yun, Y.-S. Lee, and P. Günter. *Organic phenolic configurationally locked polyene single crystals for electro-optic and terahertz wave applications*. Advanced Functional Materials, 18:3242, 2008.

[24] H. Figi, L. Mutter, C. Hunziker, M. Jazbinšek, P. Günter, and B. J. Coe. *Extremely large nonresonant second-order nonlinear optical response in crystals of the stilbazolium salt DAPSH*. Journal of the Optical Society of America B, 25(11):1786, 2008.

[25] P.-J. Kim, J.-H. Jeong, M. Jazbinsek, S.-J. Kwon, H. Yun, J.-T. Kim, Y. S. Lee, I.-H. Baek, F. Rotermund, P. Günter, and O-P. Kwon. *Acentric nonlinear optical N-benzyl stilbazolium crystals with high environmental stability and enhanced molecular nonlinearity in solid state*. CrystEngComm, 13:444, 2011.

[26] O-P. Kwon, S.-J. Kwon, M. Jazbinsek, J.-Y. Seo, J.-T. Kim, J.-I. Seo, Y. S. Lee, H. Yun, and P. Günter. *Phenolic polyene crystals with tailored physical properties and very large nonlinear optical response*. Chemistry of Materials, 23:239, 2011.

[27] P.-J. Kim, J.-H. Jeong, M. Jazbinsek, S.-B. Choi, I.-H. Baek, J.-T. Kim, F. Rotermund, H. Yun, Y. S. Lee, P. Günter, and O-P. Kwon. *Highly efficient organic THz generator pumped at near-infrared: quinolinium single crystals*. Advanced Functional Materials, 22:200, 2012.

[28] P.-J. Kim, M. Jazbinsek, J.-H. Jeong, J.-T. Kim, Y. S. Lee, Y.-M. Jung, S. W. Lee, and O-P. Kwon. *New acentric quinolinium crystal with high order parameter for nonlinear optical and electro-optic applications*. CrystEngComm, 14:3633, 2012.

[29] Z. Sun, X. Liu, X. Wang, L. Li, X. Shi, S. Li, C. Ji, J. Luo, and M. Hong. *Engineering of acentric stilbazolium salts with large second-order optical nonlinearity and enhanced environmental stability*. Crystal Growth & Design, 12:6181, 2012.

[30] J. Yin, L. Li, Z. Yang, M. Jazbinsek, X. Tao, P. Günter, and H. Yang. *A new stilbazolium salt with perfectly aligned chromophores for second-order nonlinear optics: 4-N,N-Dimethylamino-4'-N'-methyl- stilbazolium 3-carboxy-4-hydroxybenzenesulfonate*. Dyes and Pigments, 94:120, 2012.

[31] J.-H. Jeong, B.-J. Kang, J.-S. Kim, M. Jazbinsek, S.-H. Lee, S.-C. Lee, I.-H. Baek, H. Yun, J. Kim, Y. S. Lee, J.-H. Lee, J.-H. Kim, F. Rotermund, and O-P. Kwon. *High-power broadband organic THz generator*. Scientific Reports, 3:3200, 2013.

[32] S.-H. Lee, B.-J. Kang, J.-S. Kim, B.-W. Yoo, J.-H. Jeong, K.-H. Lee, M. Jazbinsek, J. W. Kim, H. Yun, J. Kim, Y. S. Lee, F. Rotermund, and O-P. Kwon. *New acentric core structure for organic electrooptic crystals optimal for efficient optical-to-THz Conversion*. Advanced Optical Materials, 3(6):756, 2015.

[33] D. Rezzonico, S. J. Kwon, H. Figi, O. P. Kwon, M. Jazbinsek, and P. Günter. *Photochemical stability of nonlinear optical chromophores in polymeric and crystalline materials*. The Journal of Chemical Physics, 128:124713, 2008.

[34] S. Manetta, M. Ehrensperger, C. Bosshard, and P. Günter. *Organic thin film crystal growth for nonlinear optics: present methods and exploratory developments*. Comptes Rendus Physique, 3:449, 2002.

[35] S.-J. Kwon, C. Hunziker, O-P. Kwon, M. Jazbinsek, and P. Günter. *Large-area organic electro-optic single crystalline thin films grown by evaporation-induced local supersaturation with surface interactions*. Crystal Growth & Design, 9(5):2512, 2009.

[36] M. Jazbinsek, H. Figi, C. Hunziker, B. Ruiz, S.-J. Kwon, O-P. Kwon, Z. Yang, and P. Günter. *Organic electro-optic single crystalline films for integrated optics*. In Proc. SPIE 7774, Linear and Nonlinear Optics of Organic Materials X, page 77740Q, 2010.

[37] K. Tsuda, T. Kondo, F. Saito, T. Kudo, and R. Ito. *New fabrication method of channel optical waveguides of organic crystal using an inorganic photoresist*. Japanese Journal of Applied Physics, 31:L 134, 1992.

[38] C. Hunziker, S.-J. Kwon, H. Figi, M. Jazbinsek, and P. Günter. *Fabrication and phase modulation in organic single-crystalline configurationally locked, phenolic polyene OH1 waveguides*. Optics Express, 16(20):15903, 2008.

[39] A. A. Zakhidov, J. K. Lee, H. H. Fong, J. A. DeFranco, M. Chatzichristidi, P. G. Taylor, C. K. Ober, and G. G. Malliaras. *Hydrofluoroethers as orthogonal solvents for the chemical processing of organic electronic materials*. Advanced Materials, 20:3481, 2008.

[40] S. Liu, A. Al-Shadeedi, V. Kaphle, C. M. Keum, and B. Lüssem. *Patterning organic transistors by dry-etching: the double layer lithography*. Organic Electronics, 45:124, 2017.

[41] H. Figi, M. Jazbinšek, C. Hunziker, M. Koechlin, and P. Günter. *Electro-optic single-crystalline organic waveguides and nanowires grown from the melt*. Optics Express, 16(15):11310, jul 2008.

[42] H. Figi, D. H. Bale, A. Szep, L. R. Dalton, and A. Chen. *Electro-optic modulation in horizontally slotted silicon/organic crystal hybrid devices*. Journal of the Optical Society of America B, 28(9):2291, 2011.

[43] M. Fujiwara, K. Yanagi, M. Maruyama, M. Sugisaki, K. Kuroyanagi, H. Takahashi, S. Aoshima, Y. Tsuchiya, A. Gall, and H. Hashimoto. *Second order nonlinear optical properties of the single crystal of N-benzyl 2-methyl-4-nitroaniline: anomalous enhancement of the* d_{333} *component and its possible origin*. Japanese Journal of Applied Physics, 45(11):8676, 2006.

[44] S. Van Cleuvenbergen, I. Asselberghs, W. Vanormelingen, T. Verbiest, E. Franz, K. Clays, M. G. Kuzyk, and G. Koeckelberghs. *Record-high hyperpolarizabilities in conjugated polymers*. Journal of Materials Chemistry C, 2:4533, 2014.

[45] T. Notake, K. Nawata, H. Kawamata, T. Matsukawa, and H. Minamide. *Solution growth of high-quality organic N-benzyl-2-methyl-4-nitroaniline crystal for ultra-wideband tunable DFG-THz source*. Optical Materials Express, 2(2):119, 2012.

[46] K. Thirupugalmani, M. Venkatesh, S. Karthick, K. K. Maurya, N. Vijayan, A. K. Chaudhary, and S. Brahadeeswaran. *Influence of polar solvents on growth of potentially NLO active organic single crystals of N-benzyl-2-methyl-4-nitroaniline and their efficiency in terahertz generation*. CrystEngComm, 19:2623, 2017.

[47] R. Kalaivanan and K. Srinivasan. *Synthesis, growth and characterization of organic nonlinear optical material: N-benzyl-2-methyl-4-nitroaniline (BNA)*. Optics & Laser Technology, 90:27, 2017.

[48] K. Piela, I. Turowska-Tyrk, M. Drozd, and M. M. Szostak. *Polymorphism and cold crystallization in optically nonlinear N-benzyl-2-methyl-4-nitroaniline crystal studied by X-ray diffraction, calorimetry and Raman spectroscopy*. Journal of Molecular Structure, 991:42, 2011.

[49] T. Notake, M. Takeda, T. Hosobata, Y. Yamagata, and H. Minamide. *Ultra-precise processing and Maker fringe measurements of organic N-benzyl-2-methyl-4-nitroaniline crystal*. In International Conference on Infrared, Millimeter, and Terahertz Waves (IRMMW-THz), 2018.

[50] W. Sun, Z. Wang, A. Chen, I. Kosilkin, D. Bale, and L. R. Dalton. *Electro-optic thin films of organic nonlinear optic molecules aligned through vacuum deposition*. Optics Express, 19(12):11189, 2011.

[51] D. Korn, M. Jazbinsek, R. Palmer, M. Baier, L. Alloatti, H. Yu, W. Bogaerts, G. Lepage, P. Verheyen, P. Absil, P. Guenter, C. Koos, W. Freude, and J. Leuthold. *Electro-optic organic crystal silicon high-speed modulator*. IEEE Photonics Journal, 6(2):2700109, 2014.

[52] R. Janneck, P. Heremans, J. Genoe, and C. Rolin. *Influence of the surface treatment on the solution coating of single-crystalline organic thin-Films*. Advanced Materials Interfaces, 5:1800147, 2018.

[53] G. Schweicher, N. Paquay, C. Amato, R. Resel, M. Koini, S. Talvy, V. Lemaur, J. Cornil, Y. Geerts, and G. Gbabode. *Towards single crystal thin films of terthiophene by directional crystallization using a thermal gradient*. Crystal Growth & Design, 11:3663, 2011.

[54] G. Gbabode, M. Delvaux, G. Schweicher, J. W. Andreasen, M. M. Nielsen, and Y. H. Geerts. *Unique crystal orientation of poly(ethylene oxide) thin films by crystallization using a thermal gradient*. Macromolecules, 50:5877, 2017.

[55] C. Kasap and P. Capper, editors. *Springer Handbook of Electronic and Photonic Materials*. Springer, 2006.

[56] C. Y. Liu and A. J. Bard. *In-situ regrowth and purification by zone melting of organic single-crystal thin films yielding significantly enhanced optoelectronic properties*. Chemistry of Materials, 12(8):2353, 2000.

[57] C.-Y. Liu and A. J. Bard. *Increased photo- and electroluminescence by zone annealing of spin-coated and vacuum-sublimed amorphous films producing crystalline thin films*. Applied Physics Letters, 83(26):5431, 2003.

[58] C. Ye, L. Zhang, G. Fu, A. Karim, T. Kyu, A. L. Briseno, and B. D. Vogt. *Controlled directional crystallization of oligothiophenes using zone annealing of preseeded thin films*. ACS Applied Materials & Interfaces, 7:23008, 2015.

[59] P. Fesenko, C. Rolin, R. Janneck, S. P. Bommanaboyena, H. Gaethje, P. Heremans, and J. Genoe. *Determination of crystal orientation in organic thin films using optical microscopy*. Organic Electronics, 37:100, 2016.

[60] L. Gránásy, T. Pusztai, G. Tegze, J. A. Warren, and J. F. Douglas. *Growth and form of spherulites*. Physical Review E, 72:011605, 2005.

[61] S. Horike, Y. Koshiba, M. Misaki, and K. Ishida. *Crystal growth of rubrene in ionic liquids by vacuum vapor deposition*. Japanese Journal of Applied Physics, 53:05FT03, 2014.

[62] L. Yu, M. R. Niazi, G. O. Ngongang Ndjawa, R. Li, A. R. Kirmani, R. Munir, A. H. Balawi, F. Laquai, and A. Amassian. *Programmable and coherent crystallization of semiconductors*. Science Advances, 3:e1602462, 2017.

[63] P. Zaumseil. *High-resolution characterization of the forbidden Si 200 and Si 222 reflections*. Journal of Applied Crystallography, 48:528, 2015.

[64] M. Eslamian. *Spray-on thin film PV solar cells: advances, potentials and challenges*. Coatings, 4:60, 2014.

[65] M. Eslamian and F. Zabihi. *Ultrasonic substrate vibration-assisted drop casting (SVADC) for the fabrication of photovoltaic solar cell arrays and thin-film devices*. Nanoscale Research Letters, 10:462, 2015.

[66] S. R. Forrest, P. E. Burrows, A. Stroustrup, D. Strickland, and V. S. Ban. *Intense second harmonic generation and long-range structural ordering in thin films of an organic salt grown by organic vapor phase deposition*. Applied Physics Letters, 68(10):1326, 1995.

[67] R. Janneck, N. Pilet, S. P. Bommanaboyena, B. Watts, P. Heremans, J. Genoe, and C. Rolin. *Highly crystalline C8-BTBT thin-film transistors by lateral homo-epitaxial growth on printed templates*. Advanced Materials, 29:1703864, 2017.

[68] J. E. Kline and J. P. Leonard. *Suppression of dewetting phenomena during excimer laser melting of thin metal films on* SiO_2. Thin Solid Films, 488:306, 2005.

6

Conclusions and perspectives

Second-order nonlinear optical effects are used in a variety of devices such as frequency-doubled lasers, optical parametric oscillators and amplifiers, some terahertz radiation sources, quantum light sources, and high-speed electro-optic modulators. Unfortunately, the majority of the available second-order nonlinear devices relies on bulk nonlinear crystals and free-space optical components or on low-index-contrast waveguides (e.g. commercial lithium niobate modulators). Integrating them on a nanophotonic chip would reduce their footprint and increase their speed and energy-efficiency. Moreover, once a high-yield mass fabrication process is established, the cost per device goes down drastically.

The mature, CMOS-compatible silicon photonics platform is a very attractive option to realize these integrated second-order nonlinear devices. While silicon is the conventional waveguide material on this platform, silicon nitride is gaining ground as an alternative CMOS-compatible material [1]. With its large transparency window, covering the visible and near-infrared wavelength range, and small waveguide losses, silicon nitride is a very appealing material. In addition, silicon nitride can be deposited at low temperatures by plasma-enhanced chemical vapor deposition ($<400\,^{\circ}\mathrm{C}$). Low-temperature deposited materials are suitable for the integration of a photonics layer in the back end of line of a CMOS process, thereby enabling monolithic integration of electronic and photonic circuits [2].

The research presented in this thesis is geared towards the integration of second-order nonlinear optical devices in silicon nitride photonic circuits. But, silicon nitride (and also silicon) has a centrosymmetric material structure, which means its second-order nonlinearity vanishes in the electric-dipole approximation. Yet, there have been demonstrations of second-order nonlinear effects in silicon nitride, but it is unclear whether large second-order nonlinearities are achievable in low-loss waveguides [3–11]. In this thesis we focused on other second-order nonlinear optical materials which can be integrated with silicon nitride PICs. All of the investigated materials were deposited at low temperatures which makes them suitable for back-end photonic integration on a CMOS chip. The following materials were treated: ABC-type nanolaminates, zinc oxide, zinc sulfide, and *N*-benzyl-2-methyl-4-nitroaniline (BNA). The ABC-type nanolaminates, zinc oxide, and zinc sulfide were deposited by atomic layer deposition (ALD). ALD is a low-temperature, conformal film growth technique that provides thickness control at the monolayer level. The organic BNA films were grown by a combination of drop casting and recrystallization from the melt (BNA melts at $105\,^{\circ}\mathrm{C}$).

ABC-type nanolaminates

We have demonstrated that a material with an effective bulk $\chi^{(2)}$ nonlinearity can be created from three centrosymmetric materials A, B, and C by combining them into a non-centrosymmetric ABC-type nanolaminate. ABC-type nanolaminates with individual layer thickness below $1\,\mathrm{nm}$ were grown by ALD. In second-harmonic generation experiments at a fundamental wavelength of $800\,\mathrm{nm}$, a second-order nonlinearity of $\chi^{(2)}_{zzz} = 1.2\,\mathrm{pm/V}$ was observed for an $In_2O_3/TiO_2/Al_2O_3$ nanolaminate with individual layer thicknesses of approximately $0.9\,\mathrm{nm}$. The constituent oxides are transparent over the visible and near-infrared wavelength range. Several other combinations of oxides were tested, with no signs of improvement in $\chi^{(2)}$. Unfortunately, the observed second-order nonlinearity is still quite small and likely insufficient for the realization of efficient integrated $\chi^{(2)}$ devices.

The $\chi^{(2)}$ nonlinearity of atomic layer deposited ABC-type nanolaminates increases with decreasing thickness of the ABC period up to certain point, whereafter it goes down. This limit is thought to be related to the disappearing of the material interfaces due to not having closed films. Also layer intermixing can be a limiting factor. Not considering fabrication issues, the ultimate limit in layer thickness is a monolayer of material, which we are already quite close to. Therefore, not a lot can be gained on this part.

To get order of magnitude improvements in $\chi^{(2)}$ nonlinearity, the use of highly nonlinear organic molecules in nanolaminates could be an interesting approach. With the recent developments in atomic and molecular layer deposition, organic or inorganic-organic $\chi^{(2)}$ nanolaminates can be explored further.

Zinc oxide and zinc sulfide

The $\chi^{(2)}$ properties of back-end CMOS-compatible atomic layer deposited zinc oxide and zinc sulfide have been explored. ALD ZnO and ZnS thin films have been investigated in second-harmonic generation experiments and silicon nitride based electro-optic ring modulators with ALD ZnO and ZnS overlays have been demonstrated.

For PE-ALD ZnO films on a $6\,\mathrm{nm}$ ALD Al_2O_3 seed layer, $\chi^{(2)}$ nonlinearities similar to those of ZnO single crystals have been observed ($|\chi^{(2)}_{zzz}| = 15\,\mathrm{pm/V}$ at $\lambda_\omega = 800\,\mathrm{nm}$). The $\chi^{(2)}$ tensor components are signicantly larger than those reported for optimized TH-ALD ZnO/Al_2O_3 nanolaminates ($|\chi^{(2)}_{zzz}| = 4\,\mathrm{pm/V}$ at $\lambda_\omega = 800\,\mathrm{nm}$) [12]. For pure PE-ALD ZnO films, where no Al_2O_3 seed layer is present, we find a $|\chi^{(2)}_{zzz}|$ value comparable to that of the optimized TH-ALD ZnO/Al_2O_3 nanolaminate. The control over the magnitude of the $\chi^{(2)}$ nonlinearity by the presence or absence of a nanometer-thickness Al_2O_3 layer can open up possibilities for quasi-phase-matched second-order nonlinear optical processes. Also for PET-ALD ZnO and TH-ALD ZnS, the addition of a Al_2O_3 seed layer led to an enhancement in $\chi^{(2)}$ nonlinearity.

The propagation loss in SiN waveguides with ZnO and ZnS overlays has been estimated from ring resonator transmission measurements. For PE-ALD ZnO overlays, a fairly large loss of approximately $11\,\mathrm{dB/cm}$ has been estimated. For high resistivity PET-ALD ZnO, this goes down to about $5\,\mathrm{dB/cm}$. For TH-ALD ZnS, losses in the range 3 to $9\,\mathrm{dB/cm}$ were observed. The presence of a ZnO or ZnS overlay increases the loss compared to a bare SiN waveguide ($\alpha \approx 1\,\mathrm{dB/cm}$).

Electro-optic modulation measurements in silicon nitride based ring modulators indicated $V_\pi L$ products down to $4\,\mathrm{V\,m}$ when using ZnO overlays and $20\,\mathrm{V\,m}$ for ZnS overlays. For the SiN/ZnS ring modulators, modulation speeds over 1 GHz were reached, where we were limited by the cavity photon lifetime and the resistance-capacitance time constant. For the SiN/ZnO rings, the bandwidth was limited to $\approx 100\,\mathrm{MHz}$. Free charge carriers could play a role in the refractive index modulation mechanism. To investigate their role and extend the bandwidth, a more in-depth material exploration is required, possibly including annealing treatments and depositions at different temperatures to alter the film's resistivity [13]. Up to a factor 8 reduction in $V_\pi L$ is possible by simply increasing the ALD layer thickness, reducing the SiN thickness, and choosing a more optimal electrode configuration. Even larger improvements are possible when using transparent conducting oxide electrodes placed very close to the waveguide core [14], or by using nanoplasmonic SiN slot waveguides [15].

Concerning performance, the SiN/ZnO and SiN/ZnS platforms are not as good as the recently developed $LiNbO_3$-on-insulator [16] and PZT-on-SiN platforms [17], both also being transparent in the visible to near-infrared wavelength range. For $LiNbO_3$-on-insulator, $V_\pi L$ products down to $2\,\mathrm{V\,cm}$ have been reported (with $\alpha \approx 0.2\,\mathrm{dB/cm}$) [16] and losses as low as $2.7\,\mathrm{dB/m}$ [18]. Moreover, periodic poling of lithium niobate can be utilized for quasi-phase matching of $\chi^{(2)}$ processes, as has been demonstrated for second-harmonic generation in $LiNbO_3$-on-insulator waveguides [19, 20]. In PZT-on-SiN ring modulators, $V_\pi L$ products of $3.2\,\mathrm{V\,cm}$ have been measured and propagation losses down to $1\,\mathrm{dB/cm}$ [17]. However, the LiNbO$_3$-on-insulator technology requires expensive substrates prepared by wafer bonding. For PZT, the deposition involves annealing at a temperature of $620\,^\circ\mathrm{C}$. Therefore, these technologies are not suitable for monolithic integration on CMOS based on back-end deposited photonics, as opposed to low-temperature atomic layer deposited zinc oxide and zinc sulfide.

BNA

We have demonstrated the growth of organic crystalline BNA thin films with a large $\chi^{(2)}$ nonlinearity. These films were grown on amorphous substrates with substrate temperatures not exceeding $115\,^\circ\mathrm{C}$.

The general fabrication process is as follows. The first step consists of the drop casting of a BNA in toluene solution on an oxidized silicon or glass substrate. A glass cover is placed on top of the BNA thin film to avoid dewetting in subsequent processing steps. Next, the BNA thin film is molten and recrystallized. Two different crystallization methods have been investigated.

In a first approach, the crystalline BNA films were grown by melting the material and slowly cooling it down in the presence of a spatial temperature gradient. The temperature gradient was induced by placing the samples on the edge of a hotplate. This technique resulted in millimeter-sized BNA crystallites with a nonlinearity of $\chi^{(2)}_{ZZZ} = (61 \pm 10)\,\mathrm{pm/V}$ (measured in second-harmonic generation experiments in thin films at a fundamental wavelength of $1550\,\mathrm{nm}$), where the Z axis is lying in the film plane and the Y axis is normal to the plane. However, no preferred in-plane orientation of the crystallites was observed.

In a second approach, a new tool was designed inspired by the Bridgman method used for the growth of bulk crystals in the semiconductor industry. The use of this homebuilt tool resulted in BNA crystallites of several millimeters long and hundreds of micrometers wide. Moreover, our X-ray and second-harmonic generation measurements indicate that the crystallites preferentially grow with their Z axis along the sample displacement direction and the Y axis normal to the sample plane. A very large nonlinearity of $\chi^{(2)}_{ZZZ} = (153 \pm 70)\,\mathrm{pm/V}$ was measured in second-harmonic generation measurements. For LiNbO$_3$, the largest $\chi^{(2)}$ tensor component is only $54\,\mathrm{pm/V}$ [21], and for PZT, values of $40\,\mathrm{pm/V}$ have been measured (in second-harmonic generation experiments) [22].

To avoid the non-uniformity associated with the drop casting technique, the exploration of alternative deposition techniques such as spin coating, spray coating [23], ultrasonic substrate vibration-assisted drop casting [24], organic vapor phase deposition (OVPD) [25], and thermal evaporation [26] might prove useful. To fill in the gaps between the crystalline ribbons, an extra layer of BNA can be evaporated on top. Under the right conditions, the underlying BNA crystals can act as templates for epitaxial growth [27]. The use of mechanical polishing, as is done for bulk BNA crystals [28, 29], is also an interesting approach to get smooth, uniform films. A possible alternative for the glass cover is to deposit a thin layer of SiO_2 (or another transparent material with a high melting point that can easily be deposited) on top of the BNA film. This layer of SiO_2 can for instance be deposited by vacuum evaporation where the substrate temperature is kept low (at a pressure of $5 \times 10^{-6}\,\mathrm{Torr}$, BNA begins to evaporate at $70\,^{\circ}\mathrm{C}$ [26]). A thin capping layer of SiO_2 has been shown to prevent dewetting of molten metal films [30].

Also for the lithographic patterning of BNA films, multiple routes can be explored. We can use a water soluble inorganic photoresist [31], or first apply a protection layer on the BNA films (e.g. evaporated SiO_2 or a spin coated layer of water dissolved polyvinyl alcohol) and use low-temperature baked SU-8 as a photoresist [32]. Alternatively, photoresists based on fluorous solvents can be used as these are benign to many organic materials [33, 34]. The capibility of patterning BNA films is very useful to achieve phase matching in hybrid SiN/BNA waveguides. Using a modal phase matching scheme, highly efficient second-harmonic generation in hybrid $LiNbO_3/TiO_2$ waveguides has already been demonstrated [35].

The growth of highly nonlinear organic single crystal thin films over large areas is a promising route for the realization of integrated $\chi^{(2)}$ devices.

References

[1] A. Rahim, E. Ryckeboer, A. Z. Subramanian, S. Clemmen, B. Kuyken, A. Dhakal, A. Raza, A. Hermans, M. Muneeb, S. Dhoore, Y. Li, U. Dave, P. Bienstman, N. Le Thomas, G. Roelkens, D. Van Thourhout, P. Helin, S. Severi, X. Rottenberg, and R. Baets. *Expanding the silicon photonics portfolio with silicon nitride photonic integrated circuits*. Journal of Lightwave Technology, 35(4):639, 2017.

[2] Y. H. D. Lee and M. Lipson. *Back-end deposited silicon photonics for monolithic integration on CMOS*. IEEE Journal of Selected Topics in Quantum Electronics, 19(2):8200207, 2013.

[3] J. S. Levy, M. A. Foster, A. L. Gaeta, and M. Lipson. *Harmonic generation in silicon nitride ring resonators.* Optics express, 19(12):11415, 2011.

[4] T. Ning, H. Pietarinen, O. Hyvärinen, J. Simonen, G. Genty, and M. Kauranen. *Strong second-harmonic generation in silicon nitride films*. Applied Physics Letters, 100(16):161902, 2012.

[5] E. F. Pecora, A. Capretti, G. Miano, and L. Dal Negro. *Generation of second harmonic radiation from sub-stoichiometric silicon nitride thin films*. Applied Physics Letters, 102:141114, 2013.

[6] A. Kitao, K. Imakita, I. Kawamura, and M. Fujii. *An investigation into second harmonic generation by Si-rich* SiN_x *thin films deposited by RF sputtering over a wide range of Si concentrations*. Journal of Physics D: Applied Physics, 47:215101, 2014.

[7] S. Miller, Y.-H. D. Lee, J. Cardenas, A. L. Gaeta, and M. Lipson. *Electro-optic effect in silicon nitride*. In Conference on Lasers and Electro-Optics (CLEO), page SF1G.4, 2015.

[8] M. W. Puckett, R. Sharma, H. H. Lin, M. H. Yang, F. Vallini, and Y. Fainman. *Observation of second-harmonic generation in silicon nitride waveguides through bulk nonlinearities*. Optics Express, 24(15):16923, 2016.

[9] K. Koskinen, R. Czaplicki, A. Slablab, T. Ning, A. Hermans, B. Kuyken, V. Mittal, G. S. Murugan, T. Niemi, R. Baets, and M. Kauranen. *Enhancement of bulk second-harmonic generation from silicon nitride films by material composition*. Optics Letters, 42(23):5030, 2017.

[10] A. Billat, D. Grassani, M. H. P. Pfeiffer, S. Kharitonov, T. J. Kippenberg, and C.-S. Brès. *Large second harmonic generation enhancement in* Si_3N_4 *waveguides by all-optically induced quasi-phase-matching*. Nature Communications, 8:1016, 2017.

[11] M. A. G. Porcel, J. Mak, C. Taballione, P. J. M. van der Slot, and K.-J. Boller. *Photo-induced second-order nonlinearity in stoichiometric silicon nitride waveguides*. Optics Express, 25(26):33143, 2017.

[12] A. Wickberg, C. Kieninger, C. Sürgers, S. Schlabach, X. Mu, C. Koos, and M. Wegener. *Second-harmonic generation from ZnO/Al_2O_3 nanolaminate optical metamaterials grown by atomic-layer deposition*. Advanced Optical Materials, 4:1203, 2016.

[13] T. Tynell and M. Karppinen. *Atomic layer deposition of ZnO: a review*. Semiconductor Science and Technology, 29:043001, 2014.

[14] G. Xu, Z. Liu, J. Ma, B. Liu, S.-T. Ho, L. Wang, P. Zhu, T. J. Marks, J. Luo, and A. K. Y. Jen. *Organic electro-optic modulator using transparent conducting oxides as electrodes*. Optics Express, 13(19):7380, 2005.

[15] A. Raza, S. Clemmen, P. Wuytens, M. Muneeb, M. Van Daele, J. Dendooven, C. Detavernier, A. Skirtach, and R. Baets. *ALD assisted nanoplasmonic slot waveguide for on-chip enhanced Raman spectroscopy*. APL Photonics, 3:116105, 2018.

[16] C. Wang, M. Zhang, X. Chen, M. Bertrand, A. Shams-Ansari, S. Chandrasekhar, P. Winzer, and M. Lončar. *Integrated lithium niobate electro-optic modulators operating at CMOS-compatible voltages*. Nature, 562:101, 2018.

[17] K. Alexander, J. P. George, J. Verbist, K. Neyts, B. Kuyken, D. Van Thourhout, and J. Beeckman. *Nanophotonic Pockels modulators on a silicon nitride platform*. Nature Communications, 9:3444, 2018.

[18] M. Zhang, C. Wang, R. Cheng, A. Shams-Ansari, and M. Lončar. *Monolithic ultra-high-Q lithium niobate microring resonator*. Optica, 4(12):1536, 2017.

[19] L. Chang, Y. Li, N. Volet, L. Wang, J. Peters, and J. E. Bowers. *Thin film wavelength converters for photonic integrated circuits*. Optica, 3(5):531, 2016.

[20] C. Wang, C. Langrock, A. Marandi, M. Jankowski, M. Zhang, B. Desiatov, M. M. Fejer, and M. Lončar. *Ultrahigh-efficiency wavelength conversion in nanophotonic periodically poled lithium niobate waveguides*. Optica, 5(11):1438, 2018.

[21] D. N. Nikogosyan. *Nonlinear Optical Crystals: A Complete Survey*. Springer, 2005.

[22] K. Alexander. *Integrated Silicon Nitride Photonics with Highly Nonlinear Thin Films and 2D Materials: Properties and Devices*. PhD thesis, Ghent University, 2018.

[23] M. Eslamian. *Spray-on thin film PV solar cells: advances, potentials and challenges*. Coatings, 4:60, 2014.

[24] M. Eslamian and F. Zabihi. *Ultrasonic substrate vibration-assisted drop casting (SVADC) for the fabrication of photovoltaic solar cell arrays and thin-film devices*. Nanoscale Research Letters, 10:462, 2015.

[25] S. R. Forrest, P. E. Burrows, A. Stroustrup, D. Strickland, and V. S. Ban. *Intense second harmonic generation and long-range structural ordering in thin films of an organic salt grown by organic vapor phase deposition*. Applied Physics Letters, 68(10):1326, 1995.

[26] W. Sun, Z. Wang, A. Chen, I. Kosilkin, D. Bale, and L. R. Dalton. *Electro-optic thin films of organic nonlinear optic molecules aligned through vacuum deposition*. Optics Express, 19(12):11189, 2011.

[27] R. Janneck, N. Pilet, S. P. Bommanaboyena, B. Watts, P. Heremans, J. Genoe, and C. Rolin. *Highly crystalline C8-BTBT thin-film transistors by lateral homo-epitaxial growth on printed templates*. Advanced Materials, 29:1703864, 2017.

[28] M. Fujiwara, M. Maruyama, M. Sugisaki, H. Takahashi, S. I. Aoshima, R. J. Cogdell, and H. Hashimoto. *Determination of the d-tensor components of a single crystal of N-benzyl-2-methyl-4-nitroaniline*. Japanese Journal of Applied Physics, 46(4A):1528, 2007.

[29] T. Notake, M. Takeda, T. Hosobata, Y. Yamagata, and H. Minamide. *Ultra-precise processing and Maker fringe measurements of organic N-benzyl-2-methyl-4-nitroaniline crystal*. In International Conference on Infrared, Millimeter, and Terahertz Waves (IRMMW-THz), 2018.

[30] J. E. Kline and J. P. Leonard. *Suppression of dewetting phenomena during excimer laser melting of thin metal films on* SiO_2. Thin Solid Films, 488:306, 2005.

[31] K. Tsuda, T. Kondo, F. Saito, T. Kudo, and R. Ito. *New fabrication method of channel optical waveguides of organic crystal using an inorganic photoresist*. Japanese Journal of Applied Physics, 31:L 134, 1992.

[32] C. Hunziker, S.-J. Kwon, H. Figi, M. Jazbinsek, and P. Günter. *Fabrication and phase modulation in organic single-crystalline configurationally locked, phenolic polyene OH1 waveguides*. Optics Express, 16(20):15903, 2008.

[33] A. A. Zakhidov, J. K. Lee, H. H. Fong, J. A. DeFranco, M. Chatzichristidi, P. G. Taylor, C. K. Ober, and G. G. Malliaras. *Hydrofluoroethers as orthogonal solvents for the chemical processing of organic electronic materials*. Advanced Materials, 20:3481, 2008.

[34] S. Liu, A. Al-Shadeedi, V. Kaphle, C. M. Keum, and B. Lüssem. *Patterning organic transistors by dry-etching: the double layer lithography*. Organic Electronics, 45:124, 2017.

[35] R. Luo, Y. He, H. Liang, M. Li, and Q. Lin. *Semi-nonlinear nanophotonic waveguides for highly efficient second-harmonic generation*. Laser & Photonics Reviews, 13(3):1800288, 2019.

A

Transfer matrix formalism for second-harmonic generation in a multilayer medium

In this appendix, a model for SHG in a stack of thin films is presented that can handle anisotropic media with arbitrarily oriented principal axes. The model is based on a transfer matrix method that accounts for all of the reflections of the fundamental and SH waves. The method was developed by D. S. Bethune [1] and is summarized in this appendix. The considered geometry is sketched in figure A.1. From the knowledge of the incident wave at frequency ω, the layer thicknesses, the dielectric tensors and the second-order susceptibility tensor(s), the transmitted and reflected waves at frequency 2ω can be calculated. The model is applicable for a low SH conversion efficiency (i.e. no pump depletion). The transfer matrix method allows for convenient numerical implementation (we have implemented it in MATLAB) and easy addition or removal of layers. In a first step, the electric field distribution at the fundamental frequency ω throughout the multilayer medium is determined. In a second step, the knowledge of the fields at frequency ω is used to calculate the bound waves at the SH frequency 2ω in the nonlinear layer(s) (i.e. solution of inhomogeneous wave equation, see section 3.1). In a final step, the free waves at frequency 2ω (i.e. solution of homogeneous wave equation) are determined taking into account all of the boundary conditions.

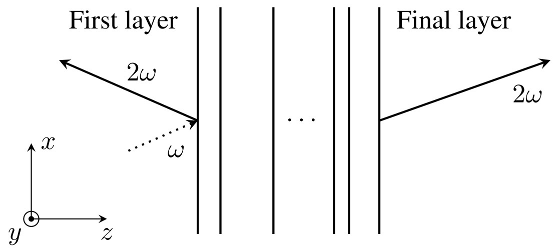

Figure A.1: Second-harmonic generation in a multilayer medium.

A.1 Determination of the fields at the fundamental frequency

Consider a monochromatic plane wave with frequency ω incident on a multilayer medium (see figure A.1). The z axis is normal to the layers and the xz plane forms the plane of incidence. Layer i has a thickness d_i and a dielectric tensor ϵ_i (and $\mu_i = 1$). Usually the dielectric tensor of a certain material is known in its principal axes. If these principal dielectric axes do not coincide with the xyz axes shown in figure 3.4, a coordinate transformation needs to be done to determine ϵ_i in the xyz system. Assuming the SH conversion efficiency is low, the wave equation in layer i at frequency ω is given by

$$\nabla \times (\nabla \times \mathbf{E}_{\omega,i}(\mathbf{r})) - \frac{\omega^2}{c^2}\epsilon_i(\omega)|\mathbf{E}_{\omega,i}(\mathbf{r}) = 0 \tag{A.1}$$

For a plane wave with wave vector $\mathbf{k}_{\omega,i}$ this takes the form

$$\left(n_{\omega,i}^2 I - \mathbf{n}_{\omega,i}\mathbf{n}_{\omega,i} - \epsilon_i(\omega)\right)|\mathbf{E}_{\omega,i} = 0 \tag{A.2}$$

where $\mathbf{n}_{\omega,i} = \frac{\mathbf{k}_{\omega,i}}{k_0}$ (with $k_0 = \frac{\omega}{c}$), $n_{\omega,i}^2 = \mathbf{n}_{\omega,i} \cdot \mathbf{n}_{\omega,i}$, and I the identity matrix of size 3. Furthermore, we can express $\mathbf{n}_{\omega,i}$ as

$$\mathbf{n}_{\omega,i} = \frac{k_{\omega,i,x}}{k_0}\mathbf{e}_x + \frac{k_{\omega,i,z}}{k_0}\mathbf{e}_z = \kappa\mathbf{e}_x + N_{\omega,i}\mathbf{e}_z \tag{A.3}$$

The x component of the wave vector, and consequently κ, stays constant throughout the stack of films (as a consequence of the boundary conditions for electromagnetic fields). Since the incident wave is known, κ is also known. For a non-zero solution $\mathbf{E}_{\omega,i}$ of equation A.2 to exist, the determinant of the bracketed matrix on the left-hand side must be zero. From this condition, the allowed values of $N_{\omega,i}$ for a given layer can be determined. Expansion of the determinant gives a fourth-order polynomial in $N_{\omega,i}$

$$\sum_{n=0}^{4} a_n N_{\omega,i}^n = 0 \tag{A.4}$$

with

$$\begin{aligned} a_0 &= \kappa^2 \left(\kappa^2 \epsilon_{xx} - \epsilon_{xx}\epsilon_{yy} - \epsilon_{xx}\epsilon_{zz} + \epsilon_{xy}^2 + \epsilon_{zx}^2\right) + \epsilon_{xx}\epsilon_{yy}\epsilon_{zz} \\ &\quad + 2\epsilon_{xy}\epsilon_{yz}\epsilon_{zx} - \epsilon_{xx}\epsilon_{yz}^2 - \epsilon_{yy}\epsilon_{zx}^2 - \epsilon_{zz}\epsilon_{xy}^2 \qquad \text{(A.5)} \\ a_1 &= 2\kappa \left(\kappa^2 \epsilon_{zx} + \epsilon_{xy}\epsilon_{yz} - \epsilon_{yy}\epsilon_{zx}\right) \qquad \text{(A.6)} \\ a_2 &= \kappa^2 \left(\epsilon_{xx} + \epsilon_{zz}\right) - \epsilon_{xx}\epsilon_{zz} - \epsilon_{yy}\epsilon_{zz} + \epsilon_{yz}^2 + \epsilon_{zx}^2 \qquad \text{(A.7)} \\ a_3 &= 2\kappa\epsilon_{zx} \qquad \text{(A.8)} \\ a_4 &= \epsilon_{zz} \qquad \text{(A.9)} \end{aligned}$$

The solutions of equation A.4 are labeled $N_{\omega,i}^{(m)}$, with $m = 1, \ldots, 4$. For each $N_{\omega,i}^{(m)}$, there is a corresponding eigenvector $\mathbf{u}_{\omega,i}^{(m)}$

$$[\mathbf{n}_{\omega,i}\mathbf{n}_{\omega,i} + \epsilon_i(\omega)]\,|\mathbf{u}_{\omega,i}^{(m)} = n_{\omega,i}^2\mathbf{u}_{\omega,i}^{(m)} \qquad \text{(A.10)}$$

We normalize the eigenvectors such that $\mathbf{u}_{\omega,i}^{(m)} \cdot (\mathbf{u}_{\omega,i}^{(m)})^* = 1$. In the case of degenerate solutions $N_{\omega,i}^{(m)}$ (e.g. for an optically isotropic medium), a pair of orthonormal eigenvectors can be chosen. The electric field $\mathbf{E}_{\omega,i}(\mathbf{r})$ can now be written as

$$\mathbf{E}_{\omega,i}(\mathbf{r}) = \sum_{m=1}^{4} E_{\omega,i}^{(m)}\mathbf{u}_{\omega,i}^{(m)} e^{-j\kappa k_0 x - jN_{\omega,i}^{(m)}k_0(z-z_i)} \qquad \text{(A.11)}$$

where z_i corresponds to the z coordinate of the left boundary of layer i. The corresponding $\mathbf{B}_{\omega,i}(\mathbf{r})$ field is given by the right-hand side of equation A.11 after replacing $\mathbf{u}_{\omega,i}^{(m)}$ by $\frac{1}{c}(\mathbf{n}_{\omega,i}^{(m)} \times \mathbf{u}_{\omega,i}^{(m)})$. Now, we have all the necessary tools to calculate $N_{\omega,i}^{(m)}$ and $\mathbf{u}_{\omega,i}^{(m)}$ for each layer. But we still need to relate the amplitudes $E_{\omega,i}^{(m)}$ to the amplitude of the incident plane wave in layer 1. This will be done through a transfer matrix approach.

The 4×1 vector $\mathbb{E}_{\omega,i}$ is defined where row m corresponds to the amplitude $E_{\omega,i}^{(m)}$. Consider the interface between layer i and j. $\mathbb{E}_{\omega,i}$ and $\mathbb{E}_{\omega,j}$ are related as

$$\Phi_{\omega,i}\mathbb{E}_{\omega,i} = M_{\omega,ij}\mathbb{E}_{\omega,j} \qquad \text{(A.12)}$$

where $\Phi_{\omega,i}$ is a 4×4 diagonal matrix, called propagation matrix, with diagonal elements

$$\Phi_{\omega,i,mm} = e^{-jN_{\omega,i}^{(m)}k_0 d_i} \qquad \text{(A.13)}$$

$M_{\omega,ij}$ is the transfer matrix that relates the amplitude vector at the right boundary of layer i ($\Phi_{\omega,i}\mathbb{E}_{\omega,i}$) to the amplitude vector at the left boundary of layer j ($\mathbb{E}_{\omega,j}$). $M_{\omega,ij}$ can be derived from the continuity relations for the tangential components of the $\mathbf{E}$ and $\mathbf{B}$ fields across an interface. For a layer j, the tangential components of the $\mathbf{E}$ and $\mathbf{B}$ fields can be related to the amplitude vector $\mathbb{E}_{\omega,j}$ by the matrix $\Pi_{\omega,j}$

$$\begin{pmatrix} E_{\omega,x}(z=z_j) \\ cB_{\omega,y}(z=z_j) \\ E_{\omega,y}(z=z_j) \\ -cB_{\omega,x}(z=z_j) \end{pmatrix} = \Pi_{\omega,j}\mathbb{E}_{\omega,j} \tag{A.14}$$

where the mth column of $\Pi_{\omega,j}$ is given by

$$\begin{matrix} \Pi_{\omega,j,1m} \\ \Pi_{\omega,j,2m} \\ \Pi_{\omega,j,3m} \\ \Pi_{\omega,j,4m} \end{matrix} = \begin{matrix} u^{(m)}_{\omega,j,x} \\ N^{(m)}_{\omega,j} u^{(m)}_{\omega,j,x} - \kappa u^{(m)}_{\omega,j,z} \\ u^{(m)}_{\omega,j,y} \\ N^{(m)}_{\omega,j} u^{(m)}_{\omega,j,y} \end{matrix} \tag{A.15}$$

The boundary conditions can now be expressed as

$$\Pi_{\omega,i}\Phi_{\omega,i}\mathbb{E}_{\omega,i} = \Pi_{\omega,j}\mathbb{E}_{\omega,j} \tag{A.16}$$

and consequently $M_{\omega,ij}$ is given by

$$M_{\omega,ij} = \Pi^{-1}_{\omega,i}\Pi_{\omega,j} \tag{A.17}$$

and $M^{-1}_{\omega,ij} = M_{\omega,ji}$. Now, an overall transfer matrix T_ω can be constructed relating the amplitude vector $\mathbb{E}_{\omega,f}$ (with layer f the final layer in figure A.1) to the amplitude vector $\mathbb{E}_{\omega,1}$ of the first layer (which is as a single exception defined just to the left of the layer 1/layer 2 interface with z coordinate z_2; in other words, $z_1 = z_2$ in equation A.11 for layer 1)

$$\begin{aligned} \mathbb{E}_{\omega,f} &= M_{\omega,f(f-1)}\Phi_{\omega,f-1}M_{\omega,(f-1)(f-2)}\Phi_{\omega,f-2}\cdots M_{\omega,21}\mathbb{E}_{\omega,1} \\ &= T_\omega\mathbb{E}_{\omega,1} \end{aligned} \tag{A.18}$$

As a convention, we order the components of $\mathbb{E}_{\omega,i}$ such that $E^{(1)}_{\omega,i}$ and $E^{(3)}_{\omega,i}$ are the amplitudes of the forward propagating modes (i.e. energy flow towards positive z) and $E^{(2)}_{\omega,i}$ and $E^{(4)}_{\omega,i}$ are the amplitudes of the backward propagating modes. From the Poynting vector it can be found that the quantity

$$\mathrm{Re}\left(N^{(m)}_{\omega,i} - u^{(m)}_{\omega,i,z}(\mathbf{n}_{\omega,i}\cdot(\mathbf{u}^{(m)}_{\omega,i})^*)\right) \tag{A.19}$$

is positive for forward propagating modes and negative for backward propagating modes.

From the knowledge of the incident wave amplitudes $E^{(1)}_{\omega,1}$ and $E^{(3)}_{\omega,1}$, the electric field in every layer can be calculated. The approach is as follows. Four overall reflection coefficients and transmission coefficients for the entire thin film stack are defined according to

$$\begin{pmatrix} t^{(1,1)} \\ 0 \\ t^{(3,1)} \\ 0 \end{pmatrix} = T_\omega \begin{pmatrix} 1 \\ r^{(2,1)} \\ 0 \\ r^{(4,1)} \end{pmatrix} \tag{A.20}$$

and

$$\begin{pmatrix} t^{(1,3)} \\ 0 \\ t^{(3,3)} \\ 0 \end{pmatrix} = T_\omega \begin{pmatrix} 0 \\ r^{(2,3)} \\ 1 \\ r^{(4,3)} \end{pmatrix} \tag{A.21}$$

where $r^{(n,m)}$ and $t^{(n',m)}$ are the reflection and transmission coefficients, respectively, for an incident wave in mode m into mode n of layer 1 and into mode n' of layer f. After some algebra, we find

$$\begin{aligned} r^{(2,1)} &= \frac{T_{\omega,24}T_{\omega,41} - T_{\omega,21}T_{\omega,44}}{D} \\ r^{(4,1)} &= \frac{T_{\omega,21}T_{\omega,42} - T_{\omega,22}T_{\omega,41}}{D} \\ r^{(2,3)} &= \frac{T_{\omega,24}T_{\omega,43} - T_{\omega,23}T_{\omega,44}}{D} \\ r^{(4,3)} &= \frac{T_{\omega,23}T_{\omega,42} - T_{\omega,22}T_{\omega,43}}{D} \end{aligned} \tag{A.22}$$

with $D = T_{\omega,22}T_{\omega,44} - T_{\omega,24}T_{\omega,42}$ ($T_{\omega,mn}$ denotes the element of the matrix T_ω on row m in column n). From these reflection coefficients and the given incident wave amplitudes $E^{(1)}_{\omega,1}$ and $E^{(3)}_{\omega,1}$, the amplitude vector $\mathbb{E}_{\omega,j}$ of any layer can be determined

$$\mathbb{E}_{\omega,j} = L_{\omega,j1} \begin{pmatrix} E^{(1)}_{\omega,1} \\ r^{(2,1)}E^{(1)}_{\omega,1} + r^{(2,3)}E^{(3)}_{\omega,1} \\ E^{(3)}_{\omega,1} \\ r^{(4,1)}E^{(1)}_{\omega,1} + r^{(4,3)}E^{(3)}_{\omega,1} \end{pmatrix} \tag{A.23}$$

where $L_{\omega,j1} = M_{\omega,j(j-1)}\Phi_{\omega,j-1}M_{\omega,(j-1)(j-2)} \cdots \Phi_{\omega,2}M_{\omega,21}$.

A.2 Bound waves at the second-harmonic frequency

Once the fields at frequency ω are known, the bound waves in the layers with a non-vanishing second-order polarization can be determined. In these nonlinear layers, the wave equation at frequency 2ω is given by

$$\nabla \times (\nabla \times \mathbf{E}_{2\omega}(\mathbf{r})) - \frac{4\omega^2}{c^2}\epsilon(2\omega)|\mathbf{E}_{2\omega}(\mathbf{r}) = \frac{4\omega^2}{\epsilon_0 c^2}\mathbf{P}^{(2)}_{2\omega}(\mathbf{r}) \tag{A.24}$$

For simplicity, the subscripts j, indicating the layer number, are left out. In the electric-dipole approximation, $\mathbf{P}^{(2)}_{2\omega}(\mathbf{r})$ is given by

$$\mathbf{P}^{(2)}_{2\omega}(\mathbf{r}) = \epsilon_0 \frac{1}{2} \chi^{(2)}(-2\omega; \omega, \omega) | \mathbf{E}_\omega(\mathbf{r}) \mathbf{E}_\omega(\mathbf{r}) \tag{A.25}$$

where $\chi^{(2)}(-2\omega; \omega, \omega)$ needs to be considered in the xyz coordinate system. As $\mathbf{E}_\omega(\mathbf{r})$ in each layer j is the sum of four modes, $\mathbf{P}^{(2)}_{2\omega}(\mathbf{r})$ will contain terms with different bound wave vectors $\mathbf{k}_s$

$$\mathbf{k}_s = 2\kappa k_0 \mathbf{e}_x + (N^{(m)}_{\omega,j} + N^{(n)}_{\omega,j}) k_0 \mathbf{e}_z \tag{A.26}$$

where m and n can take any value from 1 to 4. We write the part of the second-order polarization corresponding to one such wave vector $\mathbf{k}_s$ as $\mathbf{P}^{(2)}_s(\mathbf{r})$. Now, we look for plane wave solutions of equation A.24 with wave vector $\mathbf{k}_s$ (these are called bound waves, see also section 3.1). For each $\mathbf{k}_s$, we can write the following equation

$$\left(n_s^2 I - \mathbf{n}_s \mathbf{n}_s - \epsilon(2\omega) \right) | \mathbf{E}_s = \frac{1}{\epsilon_0} \mathbf{P}^{(2)}_s \tag{A.27}$$

where $\mathbf{n}_s = \frac{\mathbf{k}_s}{k_{s0}} = \kappa_s \mathbf{e}_x + N_s \mathbf{e}_z$ (with $k_{s0} = \frac{2\omega}{c}$) and $n_s^2 = \mathbf{n}_s \cdot \mathbf{n}_s$. The bound wave $\mathbf{E}_s$ can be determined by finding the eigenvalues and eigenvectors of the bracketed matrix on the left-hand side of equation A.27. The eigenvalues are denoted by $\lambda^{(q)}$ (with $q = 1, 2, 3$) and the (normalized) eigenvectors by $\mathbf{s}^{(q)}$. Using these eigenvalues and eigenvector, equation A.27 can be solved for $\mathbf{E}_s$ in layer j

$$\begin{aligned} \mathbf{E}_s &= \sum_{q=1}^{3} \mathbf{s}^{(q)} \frac{\mathbf{s}^{(q)} \cdot \mathbf{P}^{(2)}_s}{\epsilon_0 \lambda^{(q)}} \\ &= \sum_{q=1}^{3} E^{(q)}_s \mathbf{s}^{(q)} e^{-j\kappa_s k_{s0} x - j N_s k_{s0}(z - z_j)} \end{aligned} \tag{A.28}$$

The corresponding field $\mathbf{B}_s$ can be found from $\mathbf{B}_s = \frac{\mathbf{n}_s \times \mathbf{E}_s}{c}$. In analogy with the previous section, we define a 3×1 vector $\mathbb{E}_s$ where row q is given by $E^{(q)}_s$. Also a 3×3 propagation matrix $\Phi_s = e^{-jN_s k_{s0} d_j} I$ is defined.

A.3 Free waves at the second-harmonic frequency

With the bound waves known, the determination of the free waves at the second-harmonic frequency remains. These free waves satisfy equation A.2, but evaluated at frequency 2ω

$$\left(n^2_{2\omega,i} I - \mathbf{n}_{2\omega,i} \mathbf{n}_{2\omega,i} - \epsilon_i(2\omega) \right) | \mathbf{E}_{2\omega,i} = 0 \tag{A.29}$$

where $\mathbf{n}_{2\omega,i} = \frac{\mathbf{k}_{2\omega,i}}{k_{s0}} = \kappa_s \mathbf{e}_x + N_{2\omega,i}\mathbf{e}_z$. Because of the boundary conditions for electromagnetic fields, the x component of the free wave vector is equal to the x component of the bound wave vector. Similar to section A.1, the four allowed values for $N_{2\omega,i}^{(m)}$ and the corresponding eigenvectors $\mathbf{u}_{2\omega,i}^{(m)}$ can be determined. Also the vector $\mathbb{E}_{2\omega,i}$, containing the amplitudes $E_{2\omega,i}^{(m)}$, the propagation matrix $\Phi_{2\omega,i}$, and the transfer matrix $M_{2\omega,ij} = \Pi_{2\omega,i}^{-1}\Pi_{2\omega,j}$ can be defined.

Now, $\mathbb{E}_{2\omega,i}$ needs to be linked to $\mathbb{E}_s$ so we can determine the amplitudes of the free waves. For the free waves, we have constructed matrices $\Pi_{2\omega,i}$ to give us the tangential components of the electric and magnetic fields. Similarly, we can construct a matrix Π_s to give us the tangential components for the bound waves. Consider equation A.14, but now evaluated at frequency 2ω and the right-hand side replaced by $\Pi_s\mathbb{E}_s$. It can be seen that the qth column of Π_s is given by

$$\begin{matrix} \Pi_{s,1q} \\ \Pi_{s,2q} \\ \Pi_{s,3q} \\ \Pi_{s,4q} \end{matrix} = \begin{matrix} s_x^{(q)} \\ N_s s_x^{(q)} - \kappa_s s_z^{(q)} \\ s_y^{(q)} \\ N_s s_y^{(q)} \end{matrix} \tag{A.30}$$

Consider three layers which are numbered (from left to right) i, j and k, with a bound wave in layer j represented by $\mathbb{E}_s$. The boundary conditions at the interface between layer i and j give us

$$\Pi_{2\omega,i}\Phi_{2\omega,i}\mathbb{E}_{2\omega,i} = \Pi_{2\omega,j}\mathbb{E}_{2\omega,j} + \Pi_s\mathbb{E}_s \tag{A.31}$$

and at the interface between layer j and k

$$\Pi_{2\omega,j}\Phi_{2\omega,j}\mathbb{E}_{2\omega,j} + \Pi_s\Phi_s\mathbb{E}_s = \Pi_{2\omega,k}\mathbb{E}_{2\omega,k} \tag{A.32}$$

After some matrix manipulations, we can eliminate $\mathbb{E}_{2\omega,j}$ and find the expression

$$\mathbb{E}_{2\omega,k} = M_{2\omega,kj}\Phi_{2\omega,j}\left(M_{2\omega,ji}\Phi_{2\omega,i}\mathbb{E}_{2\omega,i} + S_j\right) \tag{A.33}$$

where S_j is given by

$$\begin{aligned} S_j &= \left(\Phi_{2\omega,j}^{-1}M_{js}\Phi_s - M_{js}\right)\mathbb{E}_s \\ &= \Delta\Phi_j M_{js}\mathbb{E}_s \end{aligned} \tag{A.34}$$

with $M_{js} = \Pi_{2\omega,j}^{-1}\Pi_s$ and $\Delta\Phi_j$ is a 4×4 diagonal matrix with elements

$$\Delta\Phi_{j,mm} = e^{-j(N_s - N_{2\omega,j}^{(m)})k_{s0}d_j} - 1 \tag{A.35}$$

Finally, the generated fields at frequency 2ω leaving the first and last interfaces can be calculated. We assume that no waves at frequency 2ω are incident on the multilayer medium and the first and final layer have a vanishing nonlinear polarization. Following from equation A.33, we get

$$R_{2\omega,jf}\begin{pmatrix}E^{(1)}_{2\omega,f}\\0\\E^{(3)}_{2\omega,f}\\0\end{pmatrix}-L_{2\omega,j1}\begin{pmatrix}0\\E^{(2)}_{2\omega,1}\\0\\E^{(4)}_{2\omega,1}\end{pmatrix}=S_j \tag{A.36}$$

where

$$R_{2\omega,jf}=\Phi^{-1}_{2\omega,j}M_{2\omega,jk}\Phi^{-1}_{2\omega,k}M_{2\omega,k(k+1)}\cdots\Phi^{-1}_{2\omega,f-1}M_{2\omega,(f-1)f} \tag{A.37}$$

$$L_{2\omega,j1}=M_{2\omega,ji}\Phi_{2\omega,i}M_{2\omega,i(i-1)}\cdots\Phi_{2\omega,2}M_{2\omega,21} \tag{A.38}$$

Multiplying equation A.36 with $L^{-1}_{2\omega,j1}$ gives

$$\overline{T}\begin{pmatrix}E^{(1)}_{2\omega,f}\\0\\E^{(3)}_{2\omega,f}\\0\end{pmatrix}-\begin{pmatrix}0\\E^{(2)}_{2\omega,1}\\0\\E^{(4)}_{2\omega,1}\end{pmatrix}=S_{1j} \tag{A.39}$$

where $\overline{T}=T^{-1}_{2\omega}=L^{-1}_{2\omega,j1}R_{2\omega,jf}$ and $S_{1j}=L^{-1}_{2\omega,j1}S_j$. After some algebra, this gives the result

$$\begin{aligned}&\begin{pmatrix}E^{(1)}_{2\omega,f}\\E^{(2)}_{2\omega,1}\\E^{(3)}_{2\omega,f}\\E^{(4)}_{2\omega,1}\end{pmatrix}\\&=\frac{1}{D'}\begin{pmatrix}\overline{T}_{33}&0&-\overline{T}_{13}&0\\\overline{T}_{33}\overline{T}_{21}-\overline{T}_{23}\overline{T}_{31}&-D'&\overline{T}_{11}\overline{T}_{23}-\overline{T}_{21}\overline{T}_{13}&0\\-\overline{T}_{31}&0&-\overline{T}_{11}&0\\\overline{T}_{33}\overline{T}_{41}-\overline{T}_{43}\overline{T}_{31}&0&\overline{T}_{11}\overline{T}_{43}-\overline{T}_{41}\overline{T}_{13}&-D'\end{pmatrix}S_{1j}\end{aligned} \tag{A.40}$$

Note that so far we have only considered one bound wave $\mathbf{E}_s$ with wave vector $\mathbf{k}_s$ in layer j. To get the complete solution, S_{1j} needs to be calculated for each $\mathbf{k}_s$ in every nonlinear layer present in the stack. All these contributions need to be summed to get one vector S_{1j} which we can insert in equation A.40.

References

[1] D. S. Bethune. *Optical harmonic generation and mixing in multilayer media: extension of optical transfer matrix approach to include anisotropic materials*. Journal of the Optical Society of America B, 8(2):367, 1991.

B

Supplementary information SHG measurements ABC-type nanolaminates

This appendix contains supplementary information to the second-harmonic generation (SHG) measurements on ABC-type nanolaminate thin films presented in subsection 4.2.2.

B.1 Reference measurement BOROFLOAT 33 glass substrate

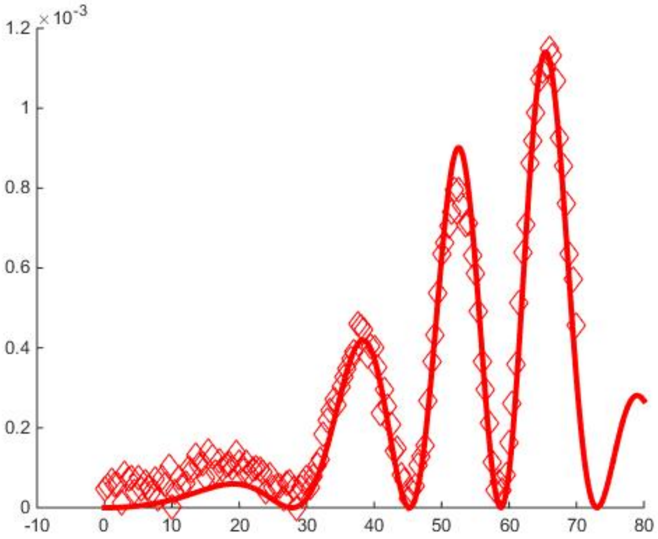

Figure B.1: Reference SHG measurement of a BOROFLOAT® 33 glass substrate using a picosecond laser emitting at a wavelength of $1064\,\mathrm{nm}$.

Figure B.1 shows the reference SHG measurement for a blank BOROFLOAT® 33 substrate ($500\,\mu\mathrm{m}$ thickness) conducted at the Optics Laboratory, Tampere University of Technology by K. Koskinen. The horizontal axis represents the incidence angle ϑ (in degrees) and the vertical axis shows the SH power $P_{2\omega}$ (in arbitrary units). Both the incident fundamental wave and the generated SH wave are p-polarized. Due to the use of a picosecond laser, the temporal walk-off is negligible. Expression B.2 is used to fit the data. The fitted $\chi_s^{(2)}$ values are $\chi_{s,zzz} = 43 \times 10^{-22}\,\mathrm{m}^2/\mathrm{V}$ and $2\chi_{s,xxz} + \chi_{s,zxx} = 18 \times 10^{-22}\,\mathrm{m}^2/\mathrm{V}$ when referenced against quartz with known second-order nonlinearity $\chi_{XXX}^{\mathrm{SiO_2}} = 0.6\,\frac{\mathrm{pm}}{\mathrm{V}}$ [1, 2]. Note that some references mention other $\chi_{XXX}^{\mathrm{SiO_2}}$ values such as $0.8\,\mathrm{pm/V}$ or $0.7\,\mathrm{pm/V}$ (for SHG at a fundamental wavelength of $1.06\,\mu\mathrm{m}$) [3, 4].

B.2 Reference measurement Y-cut quartz

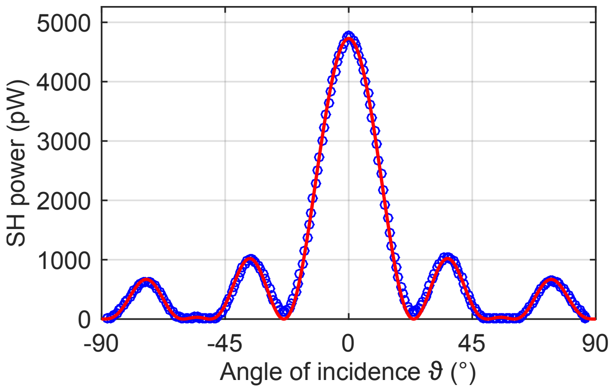

Figure B.2: Reference SHG measurement of a Y-cut quartz plate at a fundamental wavelength of 800 nm using the KIT setup described in 4.2.2.1.

Figure B.2 shows a typical SHG calibration measurement and fit of a Y-cut quartz plate. The p-polarized SH power is recorded as a function of the angle of incidence ϑ for p-polarized fundamental beam with an excitation power $P_{\omega,\mathrm{in}} = 100\,\mathrm{mW}$. The fringes are known as Maker fringes and arise due to the interference between the free and bound waves (see section 3.1) as the crystal is rotated [5–7]. The theoretical model for the fit is given by equation 4.8. However, it has to be noted that the quartz plate is not supported upon a substrate. This can be accounted for by replacing the refractive index of the substrate by the refractive index of air. The effective susceptibility for the Y-cut quartz crystal reads

$$\begin{aligned}\chi_{\text{eff}}^{p} = \chi_{XXX}^{\mathrm{SiO_2}} \big(&\cos(\Theta_{\mathrm{SiO_2}}) \left(\cos^2(\theta_{\mathrm{SiO_2}}) - \sin^2(\theta_{\mathrm{SiO_2}})\right) \\ &-2\sin(\Theta_{\mathrm{SiO_2}}) \sin(\theta_{\mathrm{SiO_2}}) \cos(\theta_{\mathrm{SiO_2}})\big)\end{aligned} \tag{B.1}$$

with $\chi_{XXX}^{\mathrm{SiO_2}} = 0.6\,\frac{\mathrm{pm}}{\mathrm{V}}$ [1]. There are two free fitting parameters. The first one is the thickness L of the quartz plate which determines the position of the individual Maker fringes. Note that fitting the thickness is a quite common approach in the evaluation of Maker fringe experiments [8]. The second fitting parameter is $\alpha = \frac{1}{A\Delta\tau^2 f_{\mathrm{rep}}^2}$ that is needed for the evaluation of equation 4.8. The fitting results are $L = (119.486 \pm 0.007)\,\mu\mathrm{m}$ and $\alpha = (2.340 \pm 0.007) \times 10^{18}/\mathrm{m}^2$. For three consecutive measurements on different spots of the quartz plate the following mean values and corresponding standard deviations are obtained $L = (119.24 \pm 0.22)\,\mu\mathrm{m}$ and $\alpha = (2.338 \pm 0.015) \times 10^{18}/\mathrm{m}^2$. Since the standard deviations of the fitting results for an individual measurement, as well as for consecutive measurements are negligible it can be assumed that the calibration measurement itself introduces insignificant error on the $\chi^{(2)}$ tensor elements of the nanolaminates. Note that due to the symmetry of the data relative to $\vartheta = 0°$ it can be excluded that the angle of incidence on the sample was calibrated incorrectly. Additionally, due to the good agreement between data and fit in magnitude and position of the individual Maker fringes it can be assumed that the quartz plate is not rotated out of focus during the measurement.

B.3 Comparison of different theoretical models for the glass substrate measurements

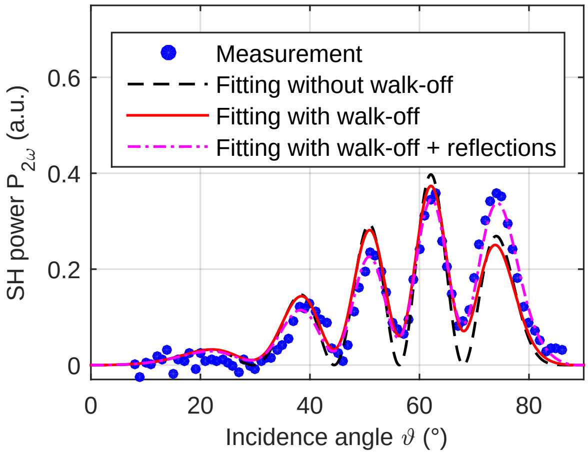

Figure B.3: Comparison of different theoretical models for the fitting of BOROFLOAT® 33 glass substrate SHG measurements (with p-polarized incident laser beam, using UGent setup described in 4.2.2.1).

Figure B.3 shows the SHG measurement and fitting for a blank BOROFLOAT® 33 substrate with known $\chi_s^{(2)}$. For incidence angles larger than 70° there is a clear discrepancy between the fitted curve and the measurement data when reflections are not included. This model without reflections is described by the expression below (and B.4 to include walk-off)

$$\begin{aligned}
A_{2\omega,\mathrm{total}} &= A_{2\omega,\mathrm{front}} + A_{2\omega,\mathrm{back}} \\
&= j\frac{\omega}{2cN_{\mathrm{glass}}\cos\left(\Theta_{\mathrm{glass}}\right)} t^2_{\mathrm{air,glass}} T_{\mathrm{glass,air}} A^2_{\omega,\mathrm{in}} \\
&\quad \left(\chi^{\mathrm{glass}}_{s,xxz}\sin\left(2\theta_{\mathrm{glass}}\right)\cos\left(\Theta_{\mathrm{glass}}\right) + \chi^{\mathrm{glass}}_{s,zxx}\sin\left(\Theta_{\mathrm{glass}}\right)\cos^2\left(\theta_{\mathrm{glass}}\right)\right. \\
&\quad \left. +\chi^{\mathrm{glass}}_{s,zzz}\sin^2\left(\theta_{\mathrm{glass}}\right)\sin\left(\Theta_{\mathrm{glass}}\right)\right) \\
&\quad \left[\exp\left(-j\frac{2\omega N_{\mathrm{glass}}\cos\left(\Theta_{\mathrm{glass}}\right)}{c}L_{\mathrm{glass}}\right)\right. \\
&\quad \left. -\exp\left(-2j\frac{\omega n_{\mathrm{glass}}\cos\left(\theta_{\mathrm{glass}}\right)}{c}L_{\mathrm{glass}}\right)\right]
\end{aligned} \tag{B.2}$$

with similar notations as in 4.2.2.2. This expression can be derived using the slowly varying amplitude approximation presented in section 3.2. It can also be found by taking equation 4.5 and replacing the ABC-type nanolaminate at the front interface with glass.

When extra reflections are included, a good fit is also obtained for the larger angles. This model is given by (and B.4 to include walk-off)

$$\begin{aligned}
A_{2\omega,\mathrm{total}} &= A_{2\omega,\mathrm{front}} + A_{2\omega,\mathrm{back}} \\
&= j\frac{\omega}{2cN_{\mathrm{glass}}\cos\left(\Theta_{\mathrm{glass}}\right)} t^2_{\mathrm{air,glass}} T_{\mathrm{glass,air}} A^2_{\omega,\mathrm{in}} \\
&\quad \left[\left(1-R_{\mathrm{glass,air}}\right)\chi^{\mathrm{glass}}_{s,xxz}\sin\left(2\theta_{\mathrm{glass}}\right)\cos\left(\Theta_{\mathrm{glass}}\right)\right. \\
&\quad +\left(1+R_{\mathrm{glass,air}}\right)\chi^{\mathrm{glass}}_{s,zxx}\sin\left(\Theta_{\mathrm{glass}}\right)\cos^2\left(\theta_{\mathrm{glass}}\right) \\
&\quad \left.+\left(1+R_{\mathrm{glass,air}}\right)\chi^{\mathrm{glass}}_{s,zzz}\sin^2\left(\theta_{\mathrm{glass}}\right)\sin\left(\Theta_{\mathrm{glass}}\right)\right] \\
&\quad \exp\left(-j\frac{2\omega N_{\mathrm{glass}}\cos\left(\Theta_{\mathrm{glass}}\right)}{c}L_{\mathrm{glass}}\right) \\
&\quad -j\frac{\omega}{2cN_{\mathrm{glass}}\cos\left(\Theta_{\mathrm{glass}}\right)} t^2_{\mathrm{air,glass}} T_{\mathrm{glass,air}} A^2_{\omega,\mathrm{in}} \\
&\quad \left[\left(1-r^2_{\mathrm{glass,air}}\right)\chi^{\mathrm{glass}}_{s,xxz}\sin\left(2\theta_{\mathrm{glass}}\right)\cos\left(\Theta_{\mathrm{glass}}\right)\right. \\
&\quad +\left(1-r_{\mathrm{glass,air}}\right)^2\chi^{\mathrm{glass}}_{s,zxx}\sin\left(\Theta_{\mathrm{glass}}\right)\cos^2\left(\theta_{\mathrm{glass}}\right) \\
&\quad \left.+\left(1+r_{\mathrm{glass,air}}\right)^2\chi^{\mathrm{glass}}_{s,zzz}\sin^2\left(\theta_{\mathrm{glass}}\right)\sin\left(\Theta_{\mathrm{glass}}\right)\right] \\
&\quad \exp\left(-2j\frac{\omega n_{\mathrm{glass}}\cos\left(\theta_{\mathrm{glass}}\right)}{c}L_{\mathrm{glass}}\right)
\end{aligned} \tag{B.3}$$

$R_{i,j}$ and $r_{i,j}$ are the Fresnel reflection coefficients (for p-polarized light) propagating from medium i to j. This expression can be derived by considering the electromagnetic boundary conditions in the presence of a polarized sheet at the glass/air interface as described in section 3.3. In fact, the model takes the multiple reflections of the fundamental and SH waves in the interfacial layer with infinitesimal thickness into account. It does not account for the multiple reflections within the thick substrate (so no Fabry-Pérot type resonances). If we take expression B.3 and set the reflection coefficients $r_{\mathrm{glass,air}}$ and $R_{\mathrm{glass,air}}$ to zero, expression B.3 becomes equal to expression B.2.

To include temporal walk-off effects, we model the laser light as $100\,\mathrm{fs}$ (FWHM) sech^2 pulses

$$\begin{aligned} P_{2\omega} = K_2 \int_{-\infty}^{+\infty} \Bigg| & A_{2\omega,\mathrm{front}} \mathrm{sech}^2\left(\frac{t}{\frac{\Delta t}{2\ln(1+\sqrt{2})}}\right) \\ & + A_{2\omega,\mathrm{back}} \mathrm{sech}^2\left(\frac{t+t_{\mathrm{walk-off}}}{\frac{\Delta t}{2\ln(1+\sqrt{2})}}\right) \Bigg|^2 \mathrm{d}t \end{aligned} \tag{B.4}$$

with Δt the FWHM pulse duration and $t_{\mathrm{walk-off}}$ the walk-off time.

B.4 Comparison of different theoretical models for the ABC-type thin film measurements

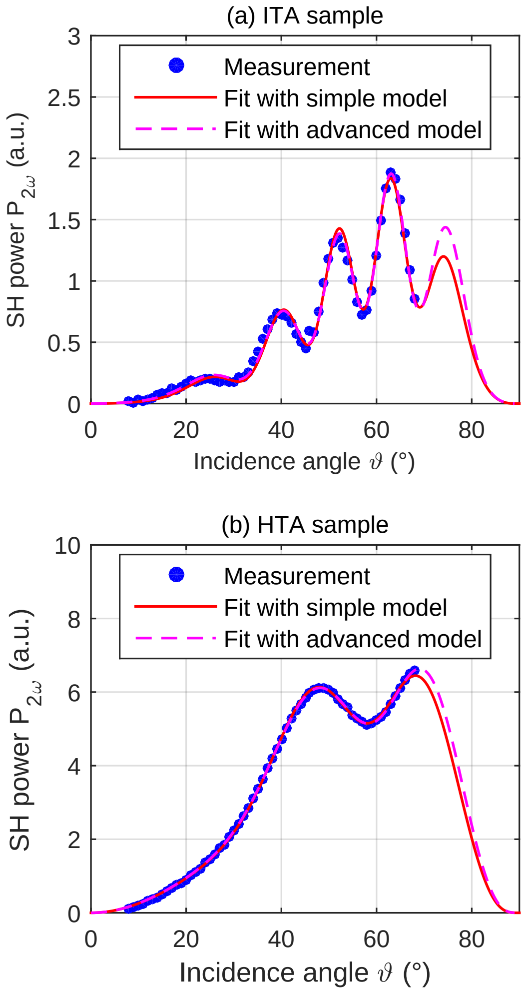

Figure B.4: Comparison of different theoretical models for the fitting of ABC-type nanolaminate SHG measurements (with p-polarized incident laser beam, using UGent setup described in 4.2.2.1). Figure (a) shows the data and fitted curves for UGent's $In_2O_3/TiO_2/Al_2O_3$ nanolaminate (ITA) and (b) for KIT's $HfO_2/TiO_2/Al_2O_3$ nanolaminate (HTA).

Figure B.4(a) shows the measurement and fitting for the ITA sample. The full red line is obtained using the relatively simple model described by equation 4.7. The dashed purple line is the result of fitting with a more advanced model that takes into account the birefringence of the nonlinear film, the multiple reflections inside the nonlinear thin film and the single reflections in the substrate, the finite thickness of the thin film and the temporal walk-off in the substrate. The thin film contribution is modeled according to the transfer matrix formalism described in section 3.4. The matrix formalism is implemented in MATLAB. Though correct and very complete, the matrix formalism is not very transparent and prone to coding errors. For the contribution of the back glass/air interface we used the second term of equation B.3. In the fitting we assume that $\chi^{\mathrm{ABC}}_{xxz} = \chi^{\mathrm{ABC}}_{zxx} = A^{\mathrm{ABC}}_{zx}/3$. This is necessary even for the advanced model. If we do not use this approximation, the relative uncertainties on the off-diagonal components can go above 100% and the results become essentially meaningless. By eliminating one fitting parameter, we can significantly reduce the uncertainty on the final results.

The fitting results are (with standard errors): $A^{\mathrm{ABC}}_{zx} = (0.211 \pm 0.011)\,\mathrm{pm/V}$, $\chi^{\mathrm{ABC}}_{zzz} = (0.974 \pm 0.054)\,\mathrm{pm/V}$ and $L_{\mathrm{glass}} = (498.26 \pm 0.16)\,\mu\mathrm{m}$, for the simple model and $A^{\mathrm{ABC}}_{zx} = (0.2251 \pm 0.0087)\,\mathrm{pm/V}$, $\chi^{\mathrm{ABC}}_{zzz} = (0.800 \pm 0.040)\,\mathrm{pm/V}$ and $L_{\mathrm{glass}} = (498.24 \pm 0.14)\,\mu\mathrm{m}$, for the more advanced model.

The same procedure is repeated for the HTA sample (see figure B.4(b)). The fitting results are (with standard errors): $A^{\mathrm{ABC}}_{zx} = (0.6045 \pm 0.0081)\,\mathrm{pm/V}$, $\chi^{\mathrm{ABC}}_{zzz} = (0.6970 \pm 0.0098)\,\mathrm{pm/V}$ and $L_{\mathrm{glass}} = (170.310 \pm 0.040)\,\mu\mathrm{m}$, for the simple model and $A^{\mathrm{ABC}}_{zx} = (0.5965 \pm 0.0046)\,\mathrm{pm/V}$, $\chi^{\mathrm{ABC}}_{zzz} = (0.634\,63 \pm 0.005\,90)\,\mathrm{pm/V}$ and $L_{\mathrm{glass}} = (169.968 \pm 0.023)\,\mu\mathrm{m}$, for the more advanced model.

The advanced model yields slightly different results, but the discrepancy is within the error margins (standard error and systematic error due to angular uncertainty).

B.5 Interference fringes for s-polarized SH in KIT setup

(a) ITA sample

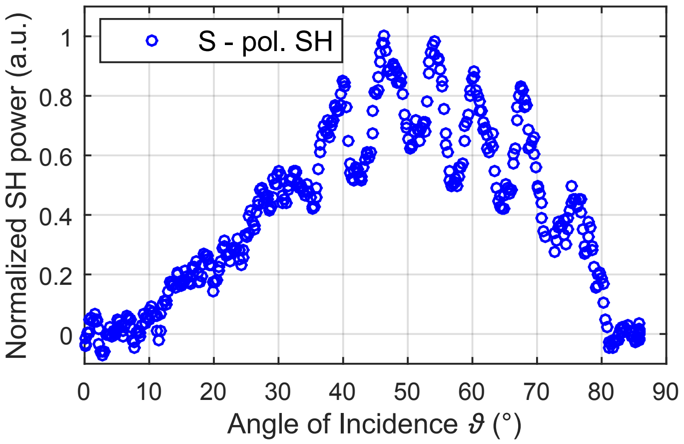

(b) HTA sample

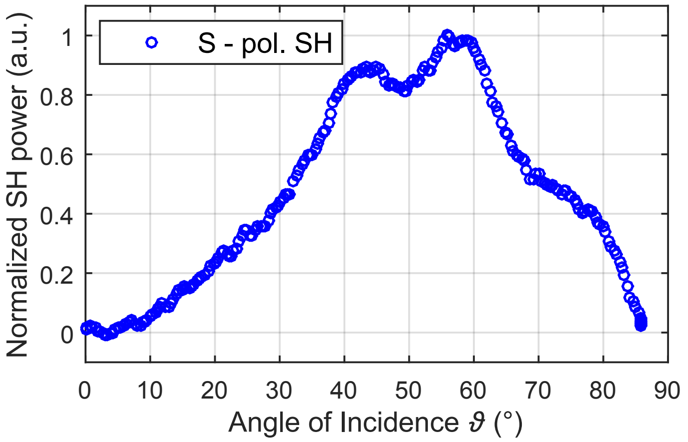

Figure B.5: Interference fringes for s-polarized SH in KIT setup for (a) the ITA sample and (b) the HTA sample.

Figure B.5 displays the normalized s-polarized SH power as a function of the angle of incidence ϑ for fixed pump polarization $\varphi = 45°$ obtained from (a) the ITA sample and (b) the HTA sample. For this measurement configuration only the elements $\chi_{xxz}^{\mathrm{ABC}}$ and $\chi_{s,xxz}^{\mathrm{glass}}$ contribute to the SH power. The very pronounced interference fringes for the ITA sample can explain why the determined values of

χ_{xxz} vary for varying angle of incidence in table 4.5. On the other hand, there are only minor interference fringes for the HTA sample, which results in minor changes in the determined values of χ_{xxz} for the specific angles of incidence.

B.6 Interference fringes for p-polarized SH in KIT setup

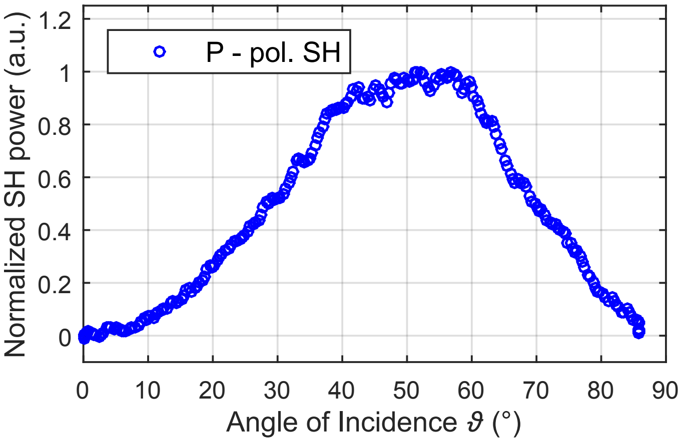

Figure B.6: Interference fringes for p-polarized SH in KIT setup for the HTA sample.

Figure B.6 shows the normalized p-polarized SH power as a function of the angle of incidence ϑ for fixed pump polarization $\varphi = 0°$ obtained from the HTA sample. For this measurement configuration only the elements χ_{zxx}^{ABC} and $\chi_{s,zxx}^{\text{glass}}$ contribute to the SH power. There are no interference fringes visible for the HTA sample. Therefore it can be concluded that $\chi_{s,zxx}^{\text{glass}}$ is much smaller than χ_{zxx}^{ABC}. This finding explains why the determined values for χ_{zxx}^{ABC} for the HTA sample do not vary depending on the angle of incidence, as listed in table 4.5. Unfortunately, a corresponding measurement on the ITA sample could not be performed since the level of generated SH power is too close to the detection limit of the setup.

References

[1] V. G. Dmitriev, G. G. Gurzadyan, and D. N. Nikogosyan. *Handbook of Nonlinear Optical Crystals*. Springer, 3rd edition, 1999.

[2] I. Shoji, T. Kondo, A. Kitamoto, M. Shirane, and R. Ito. *Absolute scale of second-order nonlinear-optical coefficients*. Journal of the Optical Society of America B, 14(9):2268, 1997.

[3] J. R. Pressley, editor. *Handbook of Lasers with Selected Data on Optical Technology*. The Chemical Rubber Co., 1971.

[4] F. J. Rodriguez, F. X. Wang, and M. Kauranen. *Calibration of the second-order nonlinear optical susceptibility of surface and bulk of glass*. Optics Express, 16(12):8704, 2008.

[5] P. D. Maker, R. W. Terhune, M. Nisenoff, and C. M. Savage. *Effects of dispersion and focusing on the production of optical harmonics*. Physical Review Letters, 8(1):21, 1962.

[6] W. N. Herman and L. M. Hayden. *Maker fringes revisited: second-harmonic generation from birefringent or absorbing materials*. Journal of the Optical Society of America B, 12(3):416, 1995.

[7] M. Abe, I. Shoji, J. Suda, and T. Kondo. *Comprehensive analysis of multiple-reflection effects on rotational Maker-fringe experiments*. Journal of the Optical Society of America B, 25(10):1616, 2008.

[8] J. Jerphagnon and S. K. Kurtz. *Maker fringes: a detailed comparison of theory and experiment for isotropic and uniaxial crystals*. Journal of Applied Physics, 41(4):1667, 1970.

C

BBO reference SHG measurements

To calibrate our second-harmonic generation (SHG) measurements performed on the setup illustrated in figure C.1 (a detailed description of the setup can be found in subsection 4.3.2 or section 5.3), a reference measurement on a BBO crystal is conducted before the actual measurements on the sample of interest. The BBO crystal has known linear and nonlinear properties. Therefore, the reference measurement can be used to determine the calibration factor which depends on the laser spot size, pulse duration, etc., (see 4.2.2.2). As these laser properties are not known accurately (and can fluctuate over time), the use of a reference measurement is the preferred approach.

C.1 BBO crystal

Barium borate (BBO) in the β phase is a trigonal uniaxial crystal with 3m point symmetry. From Eksma Optics we have purchased a thin BBO crystal which is optically contacted on a $2\,\mathrm{cm}$ by $2\,\mathrm{cm}$ UV fused silica substrate with a thickness of $500\,\mathrm{\mu m}$. The BBO crystal has a thickness of $65\,\mathrm{\mu m}$ (the lateral dimensions are $1\,\mathrm{cm}$ by $1\,\mathrm{cm}$). The crystal cut is specified by the angles θ and ϕ, which are defined in figure C.2. The z axis is the optic axis of the crystal (also called the optical axis or c axis). The wave vector $\mathbf{k}_1$ indicates the propagation direction for normal incidence, meaning that the front and back side of the thin crystal correspond to cuts along a plane normal to $\mathbf{k}_1$. For our BBO crystal, the angles are given by $\theta = 20.2°$ and $\phi = 90°$. The refractive indices of BBO are given by the following

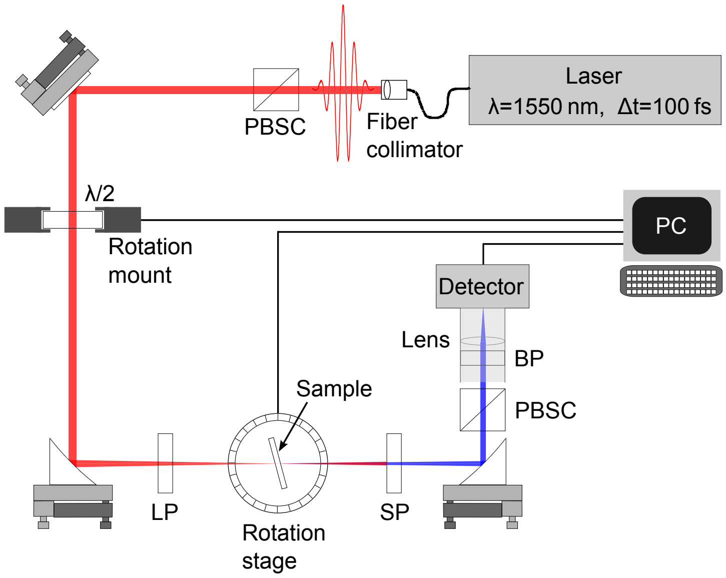

Figure C.1: Setup for SHG measurements. PBSC: polarizing beamsplitter cube, λ/2: half-wave plate, LP: longpass filter, SP: shortpass filter, BP: bandpass filter.

dispersion equations (λ in µm) [1]

$$n_o^2 = 2.7366122 + \frac{0.0185720}{\lambda^2 - 0.0178746} - 0.0143756\lambda^2 \tag{C.1}$$

$$n_e^2 = 2.3698703 + \frac{0.0128445}{\lambda^2 - 0.0153064} - 0.0029129\lambda^2 \tag{C.2}$$

$$\tag{C.3}$$

For the refractive index of the fused silica substrate, the following dispersion equation is used (λ in µm) [2]

$$n^2 - 1 = \frac{0.6961663\lambda^2}{\lambda^2 - 0.0684043^2} + \frac{0.4079426\lambda^2}{\lambda^2 - 0.1162414^2} + \frac{0.8974794\lambda^2}{\lambda^2 - 9.896161^2} \tag{C.4}$$

The angle $\theta = 20.2°$ is chosen to get type I phase matching for second-harmonic generation at a fundamental wavelength of $1550\,\mathrm{nm}$ [3]. As BBO is a negative uniaxial crystal ($n_e < n_o$), type I phase matching is achieved by choosing the ordinary polarization (electric field perpendicular to the plane containing the wave vector $\mathbf{k}_1$ and the optic axis, indicated by the o direction in figure C.2) for the fundamental wave and extraordinary polarization (electric field in the plane containing the wave vector $\mathbf{k}_1$ and the optic axis) for the second-harmonic wave.

For BBO, we assume the following values of the d coefficients at a fundamental wavelength of $1.064\,\mu\mathrm{m}$: $d_{22} = 2.2\,\mathrm{pm/V}$, $d_{33} = \pm 0.04\,\mathrm{pm/V}$, $d_{31} =$

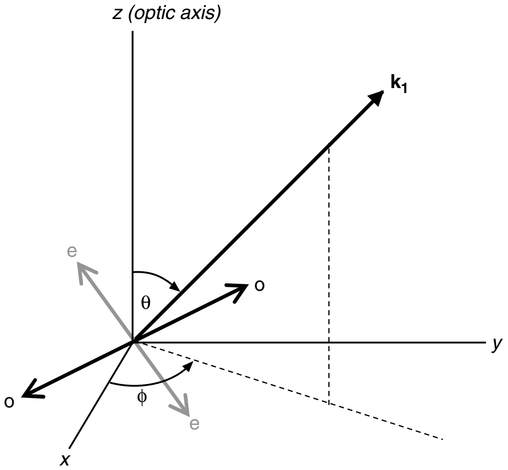

Figure C.2: Definition of the angles θ and ϕ in a uniaxial crystal. Figure reproduced from [4].

$-0.04\,\mathrm{pm/V}$, and $d_{15} = -0.03\,\mathrm{pm/V}$ [5, 6]. For our measurements, these d coefficients were converted to a fundamental wavelength of $1550\,\mathrm{nm}$ utilizing Miller's rule (see section 2.6). To our knowledge, the sign of d_{33} relative to the other coefficients has not been reported in literature. But, as will be shown in the next section, this has no significant impact on our reference measurement.

C.2 Reference measurement

For our reference measurement, we place the BBO sample in the sample holder such that the plane defined by the optic axis and the substrate normal is perpendicular to the optical table. Next, we measure the SH power as a function of the angle of incidence (see figure C.3). The polarization of the incident laser beam is fixed to p-polarization (electric field parallel to the optical table), while the transmission axis of the polarizing beamsplitter cube in front of the detector is oriented to transmit s-polarized light (transmission axis normal to optical table). So for normal incidence (angle of incidence $\vartheta = 0°$), the fundamental wave has the ordinary polarization and the generated extraordinary SH wave is passed by the polarizing beamsplitter cube, which is the type I phase matching configuration explained above. As we move away from normal incidence, the phase matching condition gets broken. Since the generated SH power for the phase matched case is quite large, we use neutral density filters to attenuate the laser beam and avoid saturation of the detector. For the measurements on the (thin film) samples of interest, these filters are typically removed as the SH signal is much smaller. The optical density

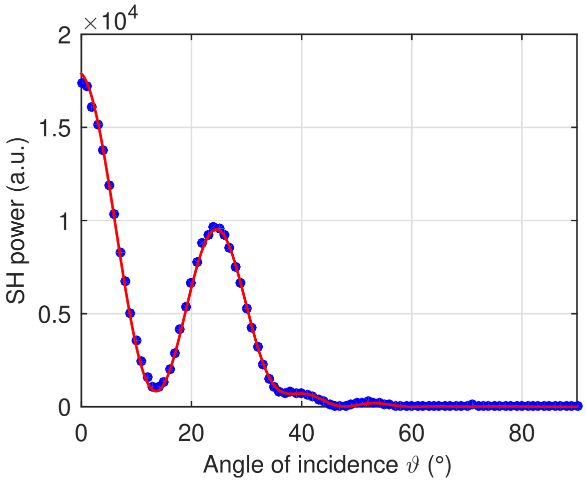

Figure C.3: BBO reference second-harmonic generation measurement. The blue dots represent the measurement data and the red line the fitted curve.

of the neutral density filters (specified by the manufacturer) is then included in the calibration factor.

For the fitting of the measurement data in figure C.3, the calibration factor and the BBO thickness are used as fitting parameters. When changing d_{33} from $-0.04\,\mathrm{pm/V}$ to $0.04\,\mathrm{pm/V}$, the calibration factor only increases by 0.04%, and the fitted thickness changes from $66.48\,\mu\mathrm{m}$ to $66.47\,\mu\mathrm{m}$. So clearly, the unknown sign of d_{33} has no signification impact on the calibration.

A modified version of the transfer matrix model presented in appendix A is used for the fitting (see next section). The modified model does not take into account the multiple reflections (and associated interference effects) of the fundamental and SH waves in the material stack. Figure C.4 compares the model from appendix A (in black) and the modified version without multiple reflections (in red) for our BBO sample, assuming identical calibration factors, thicknesses and material properties. In the black curve we see some (minor) interference fringes which do not seem to appear in our measurements (see figure C.3). This can be attributed to two things: the BBO layer is thicker than the coherence length of the laser and, due to the finite beam size (laser spot diameter of approximately $0.03\,\mathrm{mm}$), the reflections do not overlap for sufficiently large incidence angles. In these two cases the reflections do not add coherently (while coherent addition is assumed in the model presented in appendix A). If we estimate the coherence length of the laser as the pulse duration times the speed of light in the medium (i.e. calculating the pulse length), we get a value of $20\,\mu\mathrm{m}$. This is indeed smaller than the BBO thickness of $65\,\mu\mathrm{m}$. Also, for incidence angles larger than $\approx 25^\circ$, the

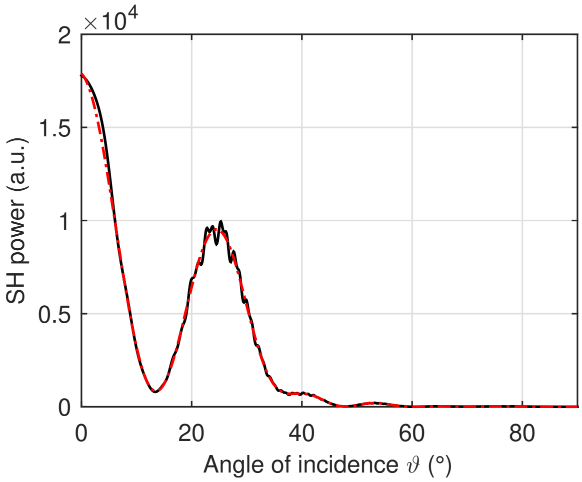

Figure C.4: Comparison of the model presented in appendix A, including multiple reflections in the BBO layer (black), and a modified version of this model where the multiple reflections are neglected (red).

separation (in the transverse direction) between the beams corresponding to two consecutive reflections is larger than the laser spot diameter. Therefore, we choose to work with a model that neglects the multiple reflections. Although in this particular case it makes little difference which model is used, as there is very little discrepancy between the black and red curve in figure C.4 (the refractive index contrasts between the layers are small, so reflections are small).

C.3 Modified transfer matrix formalism

Here, we will briefly go over the changes that were made to the transfer matrix formalism presented in appendix A. As already discussed above, these changes were made to neglect the multiple reflections in the material stack.

Firstly, the procedure to calculate the fields at the fundamental frequency has been changed. The relationship between the electric fields in layer 1 and layer 2 can be written as

$$\begin{pmatrix} E^{(1)}_{\omega,2} \\ 0 \\ E^{(3)}_{\omega,2} \\ 0 \end{pmatrix} = M_{\omega,21} \begin{pmatrix} E^{(1)}_{\omega,1} \\ E^{(2)}_{\omega,1} \\ E^{(3)}_{\omega,1} \\ E^{(3)}_{\omega,1} \end{pmatrix} \tag{C.5}$$

where we have set $E^{(2)}_{\omega,2} = E^{(4)}_{\omega,2} = 0$ as we neglect the reflections. Since the incident wave is known, $E^{(1)}_{\omega,1}$ and $E^{(3)}_{\omega,1}$ are known, and we can solve the set of equations to find $E^{(1)}_{\omega,2}$ and $E^{(3)}_{\omega,2}$. Similarly, we can write for the boundary between layers 2 and 3

$$\begin{pmatrix} E^{(1)}_{\omega,3} \\ 0 \\ E^{(3)}_{\omega,3} \\ 0 \end{pmatrix} = M_{\omega,32}\Phi_{\omega,2} \begin{pmatrix} E^{(1)}_{\omega,2} \\ E^{(2)}_{\omega,2} \\ E^{(3)}_{\omega,2} \\ E^{(3)}_{\omega,2} \end{pmatrix} \tag{C.6}$$

This set of equations can now be solved to find $E^{(1)}_{\omega,3}$ and $E^{(3)}_{\omega,3}$. This procedure is repeated until the electric field at the fundamental frequency is calculated for all the nonlinear layers.

Also for the propagation of the SH waves, some changes have been made. Consider three layers which are numbered (from left to right) i, j and k, with a bound wave in the nonlinear layer j represented by $\mathbb{E}_s$. The boundary conditions at the interface between layer i and j give us

$$\Pi_{2\omega,i}\Phi_{2\omega,i}\mathbb{E}_{2\omega,i} = \Pi_{2\omega,j}\mathbb{E}_{2\omega,j} + \Pi_s\mathbb{E}_s \tag{C.7}$$

which we can rewrite as

$$\begin{pmatrix} 0 \\ E^{(2)}_{2\omega,i} \\ 0 \\ E^{(4)}_{2\omega,i} \end{pmatrix} = \Phi^{-1}_{2\omega,i}M_{2\omega,ij} \begin{pmatrix} E^{(1)}_{2\omega,j} \\ 0 \\ E^{(3)}_{2\omega,j} \\ 0 \end{pmatrix} + \Phi^{-1}_{2\omega,i}\Pi^{-1}_{2\omega,i}\Pi_s\mathbb{E}_s \tag{C.8}$$

where we have set $E^{(1)}_{2\omega,i} = E^{(3)}_{2\omega,i} = E^{(2)}_{2\omega,j} = E^{(4)}_{2\omega,j} = 0$. This set of equations can be solved to find $E^{(1)}_{2\omega,j}$ and $E^{(3)}_{2\omega,j}$. Now, consider the interface between layer j and k

$$\Pi_{2\omega,j}\Phi_{2\omega,j}\mathbb{E}_{2\omega,j} + \Pi_s\Phi_s\mathbb{E}_s = \Pi_{2\omega,k}\mathbb{E}_{2\omega,k} \tag{C.9}$$

This can be rewritten as

$$\begin{pmatrix} E^{(1)}_{2\omega,j} \\ E^{(2)}_{2\omega,j} \\ E^{(3)}_{2\omega,j} \\ E^{(4)}_{2\omega,j} \end{pmatrix} + \Phi^{-1}_{2\omega,j}\Pi^{-1}_{2\omega,j}\Pi_s\Phi_s\mathbb{E}_s = \Phi^{-1}_{2\omega,j}M_{2\omega,jk} \begin{pmatrix} E^{(1)}_{2\omega,k} \\ 0 \\ E^{(3)}_{2\omega,k} \\ 0 \end{pmatrix} \tag{C.10}$$

Since $E^{(1)}_{2\omega,j}$ and $E^{(3)}_{2\omega,j}$ are now known, we can use this set of equations to find $E^{(1)}_{2\omega,k}$ and $E^{(3)}_{2\omega,k}$. Next, the boundary conditions can be written down and the fields calculated for the interfaces between layer k and $k+1$, layer $k+1$ and $k+2$, etc. until the SH fields in the final layer are known.

References

[1] Eksma Optics. *Specifications BBO*. `http://eksmaoptics.com/nonlinear-and-laser-crystals/nonlinear-crystals/beta-barium-borate-bbo-crystals/`. [Accessed 7 June 2019].

[2] I. H. Malitson. *Interspecimen comparison of the refractive index of fused silica*. Journal of the Optical Society of America, 55(10):1205, 1965.

[3] R. W. Boyd. *Nonlinear Optics*. Academic Press, 3rd edition, 2008.

[4] G. New. *Introduction to Nonlinear Optics*. Cambridge University Press, 2011.

[5] I. Shoji, H. Nakamura, K. Ohdaira, T. Kondo, R. Ito, T. Okamoto, K. Tatsuki, and S. Kubota. *Absolute measurement of second-order nonlinear-optical coefficients of* β*-*BaB_2O_4 *for visible to ultraviolet second-harmonic wavelengths*. Journal of the Optical Society of America B, 16(4):620, 1999.

[6] D. N. Nikogosyan. *Nonlinear Optical Crystals: A Complete Survey*. Springer, 2005.